Università Degli Studi Di Padova

Sede Amministrativa: Università degli Studi di Padova

Sede Consorziata: Istituto Veneto di Medicina Molecolare (VIMM), Via Orus 2, 35129 Padova.

Dipartimento di Scienze Biomediche Sperimentali

Scuola di Dottorato di Ricerca in: **Bioscienze**

Indirizzo: **Neurobiologia**

Ciclo: **XX**

Ca^{2+} dynamics in inner ear health and disease

Direttore della Scuola: Ch.mo Prof. Tullio Pozzan

Supervisore: Ch.mo Prof. Fabio Mammano

_____

Dottorando: Mario Bortolozzi

_____

DATA CONSEGNA TESI

31 gennaio 2008

Key words:
Calcium signaling, calcium ATPases, PMCA2 pumps, mutant mice, fluorescent ion indicators, flash photolysis, endogenous buffers, voltage dependent channels, reaction-diffusion equations, numerical simulations, gap junctions, single pore permeability

Mario Bortolozzi

Padova University, Department of Experimental Biomedical Sciences Viale G.Colombo 3, 35121 Padova, Italy.

Venetian Institute of Molecular Medicine (VIMM), Via G.Orus 2, 35129 Padova, Italy.

E-mail: mario.bortolozzi@.unipd.it

mario.bortolozzi@.gmail.com

Considerate la vostra semenza:
fatti non foste a viver come bruti,
ma per seguir virtute e canoscenza

Dante, “Inferno” XXVI

Sommario

Lo ione calcio (Ca^{2+}) svolge un ruolo di fondamentale importanza nell'apparato uditivo per la trasduzione del segnale uditivo e vestibolare, trasferendo informazione sia all'apice delle cellule ciliate, attraverso un esiguo numero di canali di meccano-trasduzione sulle stereocilia, che alla base, dove regola la trasmissione sinaptica. L'approccio genetico si sta dimostrando di fondamentale importanza per svelare le basi molecolari di azione del Ca^{2+} nel controllo di questi importanti processi. Nella fattispecie si è visto che l'assenza o la mutazione della pompa calcio PMCA2 delle stereocilia causa sordità e perdita di equilibrio. Per comprendere l'importanza fisiologica di tali difetti genetici, abbiamo studiato l'estrusione del Ca^{2+} da parte della pompa nelle cellule ciliate di colture organotipiche dell'orecchio interno di topi neonati. Gli esperimenti di microscopia confocale di fluorescenza del calcio hanno mostrato che la dissipazione di transienti Ca^{2+} nelle stereocilia, evocati tramite fotoliberazione citosolica, era significativamente compromessa nel topo knockout della PMCA2 come pure nei mutanti Deafwaddler e Oblivion. Variazioni della concentrazione citosolica di Ca^{2+} ($[Ca^{2+}]_i$) possono alterare i fini meccanismi di trasduzione del segnale, rendendo $[Ca^{2+}]_i$ un fondamentale parametro fisiologico da studiare per la comprensione dei meccanismi della sordità. Confrontando i nostri dati sperimentali di fluorescenza con quelli derivati dalle simulazioni numeriche di tipo Monte Carlo, abbiamo fornito un metodo innovativo per ricavare l'effettiva $[Ca^{2+}]_i$ in microdomini intracellulari che altrimenti sarebbero inaccessibili all'osservazione diretta. L'analisi dati effettuata tramite tale modello indica che le variazioni di $[Ca^{2+}]_i$, nella zona basolaterale della cellula ciliata e durante trasmissione sinaptica, sono principalmente controllate dai tamponi endogeni del Ca^{2+} sia a brevi (< 1 micrometro) che a lunghe distanze (decine di micrometri) dalle zone attive presinaptiche. Abbiamo inoltre stimato quantitativamente le concentrazioni e cinetiche dei tamponi e delle pompe del Ca^{2+} nelle cellule ciliate vestibolari di rana. Altri modelli matematici sono stati applicati con successo nel corso del lavoro di tesi per studiare la permeabilità ai secondi messaggeri dei canali gap junction, i quali mettono in comunicazione le cellule di supporto dell'organo di Corti. Infatti è noto che un passaggio ridotto dell'AMP ciclico e dell'inositolo 1,4,5-trisfosfato è associato a neuropatie periferiche e sordità (rispettivamente). Il nostro modello permetterebbe di quantificare, tramite opportuni esperimenti, difetti di accoppiamento metabolico fra cellule adiacenti e di valutare l'eventuale interdipendenza fra diffusione intercellulare e svariate vie di segnale.

Abstract

Ca^{2+} acts as a fundamental signal transduction element in the inner ear, delivering information about sound acceleration and gravity through a small number of mechano-transduction channels in the hair cell stereocilia as far as to the ribbon synapse, where it drives neurotransmission. The genetic approach is proving fundamental in unravelling the molecular basis of Ca^{2+} function in the control of these key cellular processes. Ablation or missense mutations of the PMCA2 Ca^{2+}-pump of stereocilia cause deafness and loss of balance. To investigate the physiological significance of these genetic defects, we studied PMCA2 Ca^{2+}-extrusion in hair cells of utricle organotypic cultures from neonatal mice inner ear. Confocal Ca^{2+} imaging showed that the dissipation of stereociliary Ca^{2+} transients, induced by cytosolic photoliberation, was compromised by various degrees in PMCA2 knockout mice as well as in the mutant *deafwaddler* and *Oblivion* mice. Alteration of the intracellular Ca^{2+} concentration ($[Ca^{2+}]_i$) can trouble the finely tuned control mechanisms of signal transduction, thus resulting $[Ca^{2+}]_i$ as a fundamental physiological parameter to be investigated in the comprehension of deafness mechanisms. By comparing our experimental fluorescence data with those derived from Monte Carlo numerical simulations, we provided a novel method to effectively deconvolve $[Ca^{2+}]_i$ within cytoplasmic microdomains that would otherwise remain inaccessible to direct observation. Data analysis performed within this environment indicates that changes of hair cell basolateral $[Ca^{2+}]_i$ during synaptic transmission are primarily controlled by the endogenous Ca^{2+} buffers at both short (< 1 micron) and long (tens of microns) distances from the presynaptic active zones. Furthermore, we provided quantitative estimates of concentration and kinetics of the endogenous Ca^{2+}-buffers and Ca^{2+}-ATPases in frog vestibular hair cells. We successfully applied mathematical models also in the study of channel permeability to second messengers of gap junctions, intercellular channels connecting supporting cells of the organ of Corti. In particular, it's known that defective permeation of cAMP or inositol 1,4,5-trisphosphate through gap junction channels is associated with peripheral neuropathies and deafness, respectively. Our model permits quantification of defects of metabolic coupling and can be used to investigate interdependence of intercellular diffusion and cross-talk between diverse signaling pathways.

Index

Acknowledgements

Ringrazio con affetto il prof. Fabio Mammano per i risultati che assieme abbiamo conseguito in questi tre anni di dottorato e per l'attenzione che, da buon maestro, ha avuto alla mia formazione di neo-scienziato. La sua passione e la sua dedizione per la ricerca sono stati per me e sono tuttora un esempio positivo e un punto di riferimento.

Introduction

Inner ear pathologies affect our senses of hearing and balance, resulting the most common sensorineural disorder in humans. It has been estimated that more than 275 million people worldwide have moderate to profound hearing loss in both ears (2005 estimate by the World Health Organization, http://www.who.int/mediacentre/factsheets/fs300/en). The principal causes for hearing loss are genetic disposition, aging, noise exposure, certain infections, and ototoxic drugs. Balance disorders have similar causes, with infections or inflammations of the labyrinth or the vestibular nerve probably being the predominant reasons. In Italy, 1–2 children in 1,000 are born with partial to profound compromise of auditory function and 25,000 children under age 10 have problems in verbal communication caused by hearing deficits (http://www.associazioneairs.it/html/il_bambino.HTM). Genetic causes account for around half of the cases of prelingual hearing impairment, and the identification of more than 120 independent genes for deafness has provided profound new insights into the pathophysiology of hearing, as well as many unexpected surprises [1]. Most cases of genetic deafness result from mutations at a single locus, but an increasing number of examples are being recognized in which recessive mutations at two loci are involved. For example, digenic interactions are now known to be an important cause of deafness in individuals who carry a single mutation at the Connexin-26 (gap-junction protein) locus along with a deletion involving the functionally related Connexin-30 locus [2].

Despite all the information provided by animal models and by electrophysiological studies, a notable progress into understanding the sequence of events that occurs in inner ear genetic-based disorders has been lacking. Degeneration and death of sensory hair cells is causal in greater than 80% of individuals with hearing loss and chronic balance disorders [3]. Hair cells are fundamental elements of the inner ear, playing as mechano-electrical converters of sound and acceleration with exquisite temporal fidelity [4, 5] (Figure 1). Mechano-transduction starts in the hair cell bundle, a collection of stepped ranks of actin-filled stereocilia that pivot back and forth in response to motion of the surrounding endoplasmic liquid and also of the tectorial membrane, for the case of cochlear outer hair cells. The bundle positive deflection increases the open probability of mechanically gated ion channels located at or near the tips of stereocilia, resulting in an influx of cations, mostly K^+ but also Ca^{2+}, that depolarizes the hair cell, thereby generating a receptor potential and leading to increased synaptic transmission at the basolateral surface of the cell.

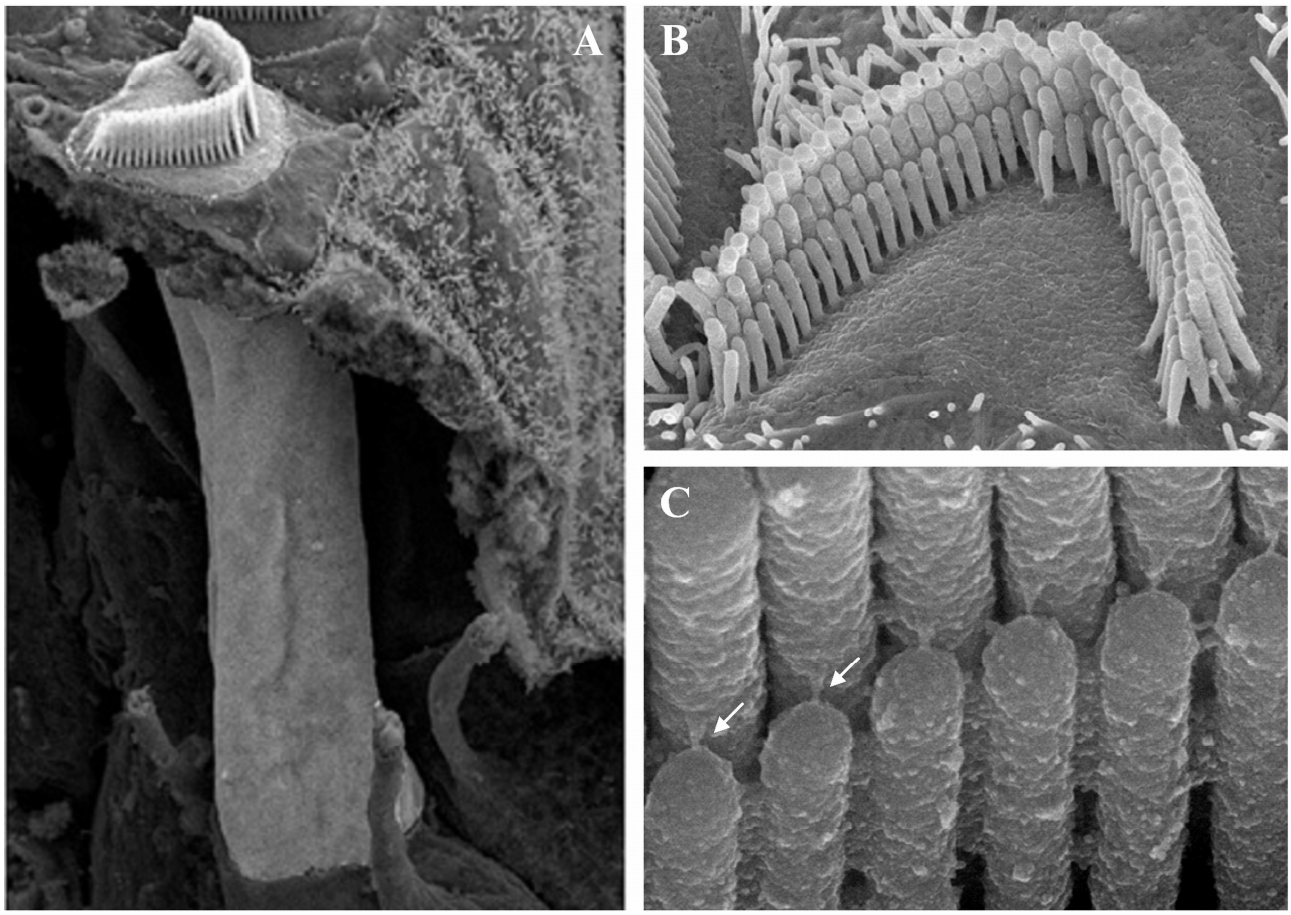

Figure 1. (A) Outer hair cell view from a section of the organ of Corti (Dave Furness courtesy, Keele University, UK). Stepped ranks of stereocilia protruding from the apical surface of the cell (B) are connected by rigid tip-links (C, arrows), responsible to deliver gating force to the mechano-electrical transduction channels.

The afferent synapse is particularly interesting because of its extraordinary capacity for precise and fast relaying of timing and intensity information. This ability depends largely on the mechanisms employed by the hair cell for rapidly modifying the cytosolic free Ca^{2+} concentration ($[Ca^{2+}]_i$) in the vicinity of transmitter release sites (see also Chapter 1). Increases in $[Ca^{2+}]_i$ are brought about by the receptor potential-induced opening of voltage-dependent Ca^{2+} channels that are localized to synaptic active zones, called "hot spots" [5] (Figure 2).

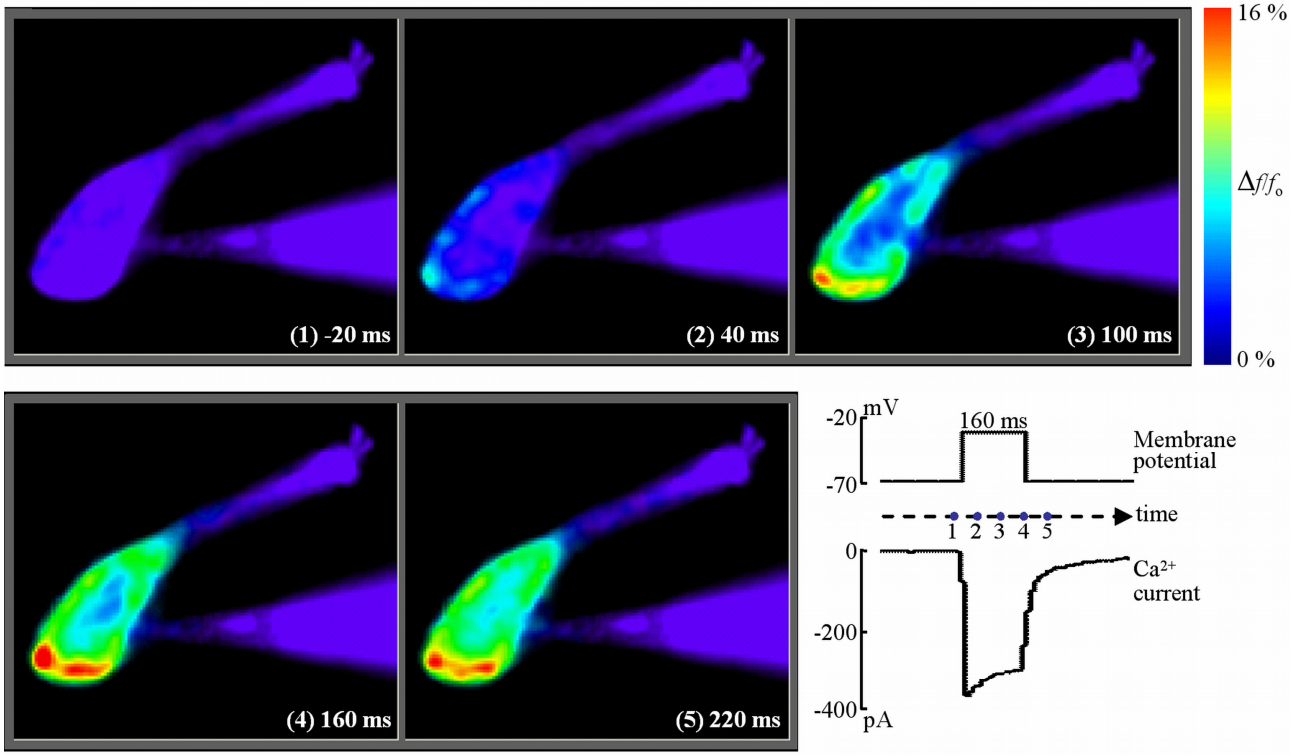

Figure 2. Isolated hair cell from the frog crista ampullaris was contacted by a patch pipette entering from the right and containing the membrane-impermeant Ca^{2+}-sensor Oregon Green 488 BAPTA-1 (Mammano et al. [6]). The hair cell was depolarized for 160 milliseconds, from time zero, eliciting $[Ca^{2+}]_i$ transients near the active presynaptic zones. Fluorescence change ($\Delta f/f_0$) relative to the pre-stimulus level represents $[Ca^{2+}]_i$ variations and is encoded by a pseudo-color scale bar. Inward Ca^{2+} current was measured by using CsCl-based intracellular solution that selectively blocks positive K^+ currents.

A number of mechanisms are used by the hair cell for decreasing $[Ca^{2+}]_i$ during and after mechano-transduction. Among these are simple diffusion of Ca^{2+} away from its site of action, active extrusion by Ca^{2+}-ATPases and Ca^{2+} buffering [7]. In stereocilia, the isoform 2 of the plasma membrane Ca^{2+}-ATPase (PMCA2) pump is the only system that exports back to the apical extracellular fluid, the *endolymph*, Ca^{2+} ions entered through mechano-electrical transduction (MET) channels opened by the hair bundle deflection. In particular, $[Ca^{2+}]_i$ is decreased by the unusual splicing isoform *w/a* of PMCA2 [8]. Ablation or missense mutations of the pump cause deafness and loss of balance, as described for the single point mutations G283S in the deafwaddler (*dfw*) mouse ([9], see Appendix) and the S877F in the Oblivion mouse (unpublished, see Appendix). Only ten base pairs of distance from the *dfw* mutation, the single change G293S in the pump in combination with a substitution, T1999S, in cadherin 23 was found causing hearing loss in a human family [10] (Figure 3).

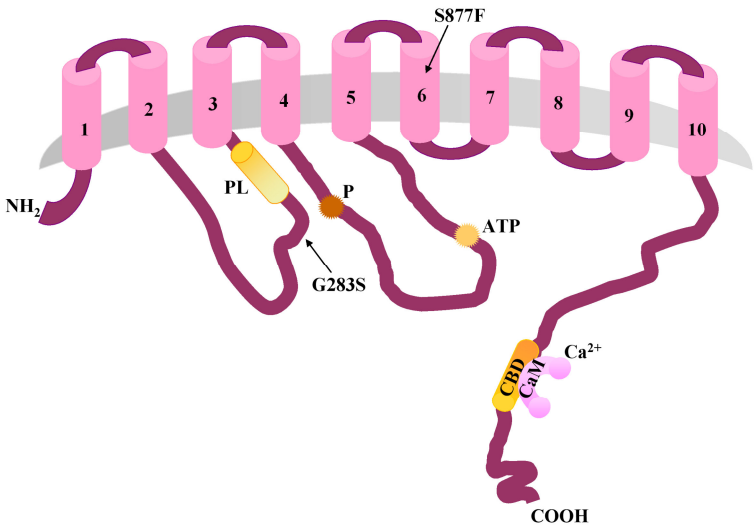

Figure 3. PMCA2 is organized with 10 membrane-spanning segments (TM) and 3 major intracellular domains [11]. The intracellular loop between TM2 and TM3 contains the main site of interaction with activatory acidic phospholipids (PL) and one binding site for the calmodulin (CaM) binding domain (CBD) at the C-terminal. The cytosolic region between TM4 and TM5 contains a second binding site for the CBD and the catalytic domain. The C-terminal tail contains the CBD and isoform specific consensus sites for protein kinases A and C. Phosphorylation (P) increases both the Ca^{2+} affinity and the maximum velocity of the pump. Indicated are also the mutation points of *dfw* and Oblivion mice.

PMCA2 activity in the stereocilia of vestibular hair cells was shown to regulate hair bundle $[Ca^{2+}]_i$ [12], that is vital to hair cell function as $[Ca^{2+}]_i$ is crucial to many aspects of the mechano-transduction process, e.g., the regulation of MET channel adaptation (the process by which hair cells continuously readjust their sensitivity to the ciliary bundle displacements [13, 14]) or the ability to sense small, say nanometrical, deflection of the bundle [15]. Endolymphatic Ca^{2+} concentration is much lower than that of conventional extracellular fluids, a value of 23 micromolars (µM) having been recently measured in mouse cochlea [16]. The *dfw* G283S mutation of the PMCA2 pump lowers the endolymphatic Ca^{2+} concentration to about 6 µM [17]. This value is considerably higher than that necessary for the function of the tip-links, that have an essential role in the deflection of the bundle, whose integrity is preserved at $[Ca^{2+}]_i > 1$ µM [18]. Nevertheless, the *dfw* mouse appears deaf and a number of in vitro studies, for instance in chickens, have shown that the generation of transduction currents requires a minimum of 20 µM extracellular Ca^{2+} and is not elicited in 10 µM [19]. MET currents produced by the deflection of hair bundles require a minimum of 10 µM external Ca^{2+} in bullfrog [20], and adaptation is slowed when extracellular Ca^{2+} is reduced [12, 21, 22]. It must also be considered that the bulk Ca^{2+} concentration in the endolymph needn't correspond to that of the microambient surrounding the hair bundle, which could be substantially higher [12]. It thus appears that the PMCA2 *w/a* pump may be important for Ca^{2+} homeostasis both in the endolymph and in the stereociliary compartment. PMCA should play a more important role in stereocilia than in the soma because the cytoplasmic volume per PMCA molecule is much smaller in stereocilia than in the soma; an equivalent amount of Ca^{2+} therefore should be extruded from stereocilia more rapidly than from the soma.

We are at present involved in the EuroHear Project, supported by funding under the Sixth Research Framework Programme of the European Commission. The EuroHear's strength is in the variety of disciplines that encompass hearing research and the breadth of training in 25 laboratories in 10 European countries. For example, teams that include geneticists, cell biologists and physiologists from France and Germany have discovered that otoferlin is essential for synaptic vesicle exocytosis from the inner hair cell ribbon synapse [23]. Geneticists, neuroscientists, bioinformaticians and cell biologists from France, Belgium, Spain and Israel reported that mutations in Pejvakin cause DFNB59 auditory neuropathy [24]. Our laboratory, directed by prof. Fabio Mammano (Venetian Institute of Molecular Medicine, Padova, Italy), is responsible for the study of the connection between PMCA2 mutations and deafness. In particular, we investigated Ca^{2+} extrusion in hair cells of organotypic cultures of inner ear sensory epithelia from neonatal mice. Confocal Ca^{2+} imaging permitted us to follow the dissipation of Ca^{2+} transients evoked, at the same time, in stereocilia and soma of PMCA2 knockout mice, *dfw* mice (Chapter 2), as well as of a novel strain, Oblivion mice, carrying the single point mutation S877F (Chapter 3). Ca^{2+} transients were generated by ultraviolet (UV) photolysis of intracellular caged calcium (Ca^{2+} bound to NP-EGTA) while $[Ca^{2+}]_i$ changes were determined from the Ca^{2+}-sensor (dye) fluorescence changes of Fluo-4 AM. Data comparison of mutants with wild-type mice evidenced significant and interesting differences, permitting us to formulate a possible explanation of the role played by the mutated PMCA2 pump in hearing loss and balance disorders [10].

Besides Ca^{2+}-ATPases, key parameters for controlling $[Ca^{2+}]_i$ in hair cell stereocilia and soma are endogenous Ca^{2+}-buffers [7, 25]. Although it is possible that the buffering capacity of the stereocilia and that of the soma are distinct, experiments indicate that both hair bundles and basolateral membranes contain significant amounts (a few millimolars, mM) of Ca^{2+}-buffers [25-28]. Mobile buffers are believed to hasten the decline of the presynaptic $[Ca^{2+}]_i$ after closure of Ca^{2+} channels, sharpening the timing of synaptic transmission [7, 29]. The problem of extrapolating the endogenous buffer properties (i.e., concentration, binding kinetics or diffusion coefficient in cytosol) is strictly interdependent with determination of $[Ca^{2+}]_i$ from fluorescence imaging data. The study of $[Ca^{2+}]_i$ dynamics in hair cells typically combines Ca^{2+} dyes, patch clamp and optical microscopy to produce images of the patterns of fluorescence of the Ca^{2+} indicator following various stimulation protocols [30, 31]. In general, extrapolating $[Ca^{2+}]_i$ requires a mathematical model because the only directly observable quantity is a linear combination of the fluorescence emission of free dye and dye bound to Ca^{2+}. We developed a complete tool (user friendly, called *Simulimm*) for the numerical simulation of cellular phenomena involving diffusion, buffering,

extrusion and release of Ca^{2+}. In particular we modelled the buffered diffusion of Ca^{2+} from presynaptic hotspots following depolarization of the hair cell plasma membrane (Chapter 4). Simulimm was developed to investigate $[Ca^{2+}]_i$ dynamics over ~1 s time intervals and distances of the order of the entire cell (20-30 μm) and to directly compare experimental data to simulation results. Simulations were performed by adopting the Monte Carlo method, essentially based upon the repetitive generation of random numbers. This method have been used successfully to study reaction and diffusion processes in biological systems [32-36] and permits to take into account realistic boundary conditions for the reaction-diffusion equations and to alter them with great ease. Simulations took into account also the (poor) axial resolution of the wide field optical apparatus and the operating conditions of the CCD camera used to acquire fluorescence image sequences. Fluorescence traces obtained by computer simulations fitted experimental data extremely well, permitting us to address crucial questions regarding (a) concentrations and dynamics of Ca^{2+} and its unknown buffers in our experiments; (b) the role played by buffers and Ca^{2+}-ATPases in vestibular hair cell soma; (c) the nature of the noise sources affecting the fluorescence signals.

A key aspect of the physiology of sound transduction in the mammalian cochlea is not only Ca^{2+} concentration but the entire ionic composition of the extracellular environment that surrounds the hair cells. Their basolateral surface is bathed in *perilymph*, a fluid with normal extracellular salt composition (high Na^+ and Ca^{2+}, low K^+), but their apical surface is contacted by endolymph, which has a salt composition that resembles intracellular fluids (high K^+, low Na^+ and Ca^{2+}). Another unique feature of the organ of Corti is the very high trans-epithelial potential between the endolymphatic and perilymphatic compartments, which is necessary to trigger the influx of K^+ into hair cells that depolarizes them during sound and acceleration stimulation. K^+ is, in turn, transported into the interstitial space of the organ of Corti, where it is partly taken up by cochlear supporting cells [37]. Hence, connexins Cx26, Cx30 and Cx31, intercellular channels (*gap junctions*) between epithelial cells, are believed to delineate an intercellular pathway to remove the excess K^+ that results from auditory signals, providing a spatial buffering function that is similar to astrocytic gap junctions in the brain (see also Appendix, "Ca^{2+} signaling in the inner ear"). Although the finding that most connexin mutations resulting in a loss of hearing function suggests that it is a deficit of intercellular communication that leads to the pathological phenotype [38], a lingering question has remained unanswered: what is it exactly that needs to be exchanged? Ions? Metabolites? Second messengers? Gap junctions are also permeable to second messengers such as cyclic nucleotides and inositol polyphosphates [39]. In particular, the inositol-1,4,5-trisphosphate ($InsP_3$), which mobilizes intracellular Ca^{2+} when introduced into HeLa cells [40], has long been known to permeate through some types of gap-junction channels [41-44]. A study by Beltramello *et al.*[45] has delivered the

first answer by pinning down the suspect $InsP_3$, thus providing a plausible hypothesis to account for the pathogenesis of DFNB1, the most frequent form of genetic deafness. We now know that all connexins are not made equal; there are differences in size and ionic selectivity, differences in the rules of compatibility between available partners, and distinct gating mechanisms. We investigated the permeability of connexin Cx26 to cAMP and $InsP_3$, two of the most important intercellular messengers, by the use of a mathematical model which was able to provide a quantitative estimate of the single gap junction permeability from the experimental data acquired by our collaborator Victor Hernandez (Chapter 3).

Chapter 1

Ca^{2+} signaling in the inner ear*

Fabio Mammano, Mario Bortolozzi, Saida Ortolano and Fabio Anselmi

Physiology, 2007

1.1. Summary

The inner ear contains delicate sensory receptors that have adapted to detect the minutest mechanical disturbances. Ca^{2+} ions are implicated in all steps of the transduction process, as well as in its regulation by an impressive ensemble of finely tuned feedback control mechanisms. Recent studies have unveiled some of the key players, but things do not sound quite right yet.

1.2. Introduction

At the present, we know that Ca^{2+} presides over both the life and death of cells. Ca^{2+} begins life at fertilization, rules over most of the activities of developing and mature cells (such as muscle contraction, glands and synapses secretion, gene expression in the nucleus) and mediates their demise once the twilight of their life has been reached. In the course of evolution, multicellular organisms have thus developed complex ways of generating and processing informations based on messengers that carry the primary signals to cells (the first messengers) or decode their information inside them (the second messengers). While the first messengers are numerous, the second messengers known today are only about a dozen: as a rule, they are committed, i.e., they only influence a single target function. The exception is Ca^{2+}, which has great versatility and controls a very large list of cellular processes [46]. The evolutionary choice of Ca^{2+} as a universal and versatile intracellular messenger has evidently been dictated by its chemical properties (see [47] for a comprehensive review of the topic). The total concentration of Ca^{2+} within eukaryotic cells can be very high, reaching the mM range. However, Ca^{2+} easily forms complexes with low-molecular weight anions (e.g., phosphates, ATP, aminoacids, acidic phospholipids of membranes) even in the presence of much higher concentrations of other metals, such as Mg^{2+}, the other biologically important and abundant divalent cation. In fact, while charge and dimension of Ca^{2+} makes it an ideal ligand for irregularly shaped binding cavities, Mg^{2+} tends to demand perfectly octahedral binding cavities. In principle, formation of these Ca^{2+}-complexes would be a mean to substantially reduce the total concentration of free Ca^{2+}, an essential requirement for any chemical chosen to act as a messenger. It is indeed self-evident that a messenger must be maintained within cells at very

* For the full text article see the Appendix.

low free concentrations, to avoid prohibitive energy expenditures to achieve the necessary changes in its concentration in the ambient surrounding the signaling targets.

Chapter 2

Defects of plasma membrane calcium pump isoform 2 causing deafness in mice and humans. A functional study of normal and mutated variants*

Ficarella#, R., Di Leva#, F., Bortolozzi#, M., Ortolano#, S., Donaudy, F., Petrillo, M., Carella, M., Lelli, A., Domi, T., Fedrizzi, L., Lim, D., Shull, G.E., Gasparini, P., Brini, M., Mammano, F., Carafoli, E.

PNAS, 2007

2.1. Summary

Ca^{2+} enters the stereocilia of hair cells through mechanoelectrical transduction channels opened by the deflection of the hair bundle and is exported back to endolymph by an unusual splicing isoform (*w/a*) of plasma-membrane calcium-pump isoform 2 (PMCA2). Ablation or missense mutations of the pump cause deafness, as described for the G283S mutation in the deafwaddler (*dfw*) mouse. A deafness-inducing missense mutation of PMCA2 (G293S) has been identified in a human family. The family also was screened for mutations in cadherin 23, which accentuated hearing loss in a previously described human family with a PMCA2 mutation. A T1999S substitution was detected in the cadherin 23 gene of the healthy father and affected son but not in that of the unaffected mother, who presented instead the PMCA2 mutation. The *w/a* isoform was overexpressed in CHO cells. At variance with the other PMCA2 isoforms, it became activated only marginally when exposed to a Ca2_ pulse. The G293S and G283S mutations delayed the dissipation of Ca^{2+} transients induced in CHO cells by InsP3. In organotypic cultures, Ca^{2+} imaging of vestibular hair cells showed that the dissipation of stereociliary Ca^{2+} transients induced by Ca^{2+} uncaging was compromised in the *dfw* and PMCA2 knockout mice, as was the sensitivity of the mechanoelectrical transduction channels to hair bundle displacement in cochlear hair cells.

2.2. Introduction

Ca^{2+} signaling, which is peculiar of hair cells, could have dictated the choice of a PMCA pump with unusual properties: no other cell type is known to eject Ca^{2+} using predominantly the *w/a* splicing variant of the PMCA2. On the molecular/physiological rationale that dictated the choice of the isoform 2 and *w/a* variant little more than speculation is presently possible. Resting stereociliary

* For the full text article see the Appendix.

#These authors have contributed equally.

Ca^{2+} is very low [25, 48], and it thus makes sense to have there a PMCA isoform that can decrease Ca^{2+} to lower concentrations than other isoforms could do [49], and which is able to do so even if insensitive to calmodulin (and presumably to acidic phospholipids). The insensitivity to calmodulin also appears logical, considering that its very high concentration in the stereocilia, 70 μM [50], would produce permanent maximal activation of all isoforms sensitive to it. That said, the molecular role(s) of Ca^{2+} within the hair bundles, and the significance of its interactions with protein targets are only partially understood [15]. The stereocilia are filled with actin, contain unconventional myosins, and also contain cadherin 23 [51], which are all Ca^{2+}-binding proteins. Intuitively, one would think that the reversible complexation of Ca^{2+} by these proteins should have a role in the special physiology of the hair bundle. And the role should be important, considering the unique ways these specialized cell appendices have adopted to control it.

2.3. Methodological widenings

To investigate PMCA2 activity we combined confocal microscopy with UV flash photolysis in hair cells of organotypic cultures of the inner ear utricle from neonatal mice between postnatal day 1 and 4 (P1-P4). The utricle epithelium was dissected and fixed by Cell-Tak to the lateral side of a glass capillary that had been previously glued to a microscope slide by a small drop of Sylgard Silicon Elastomer. This configuration permitted to obtain confocal images of the hair cell along its main axis (Figure 4A). At recording time, cultures were loaded with cell-permeant Ca^{2+}-dye Fluo-4. Fluo-4 fluorescence was excited by the 488-nm line of an argon laser coupled by optic fiber to the microscope. A rapid increase in cytosolic Ca^{2+} was achieved by photorelease of Ca^{2+} from the state caged with nitrophenyl-EGTA. The UV illumination for uncaging covered an area corresponding to a few hair cells, and was generated by a UV (375 nm) laser connected to the microscope through an optical fiber. Fiber output, after recollimation, was reflected off a 400 DCLP dichromatic beam splitter positioned at 45° just above the water-immersion objective lens (Figure 4B).

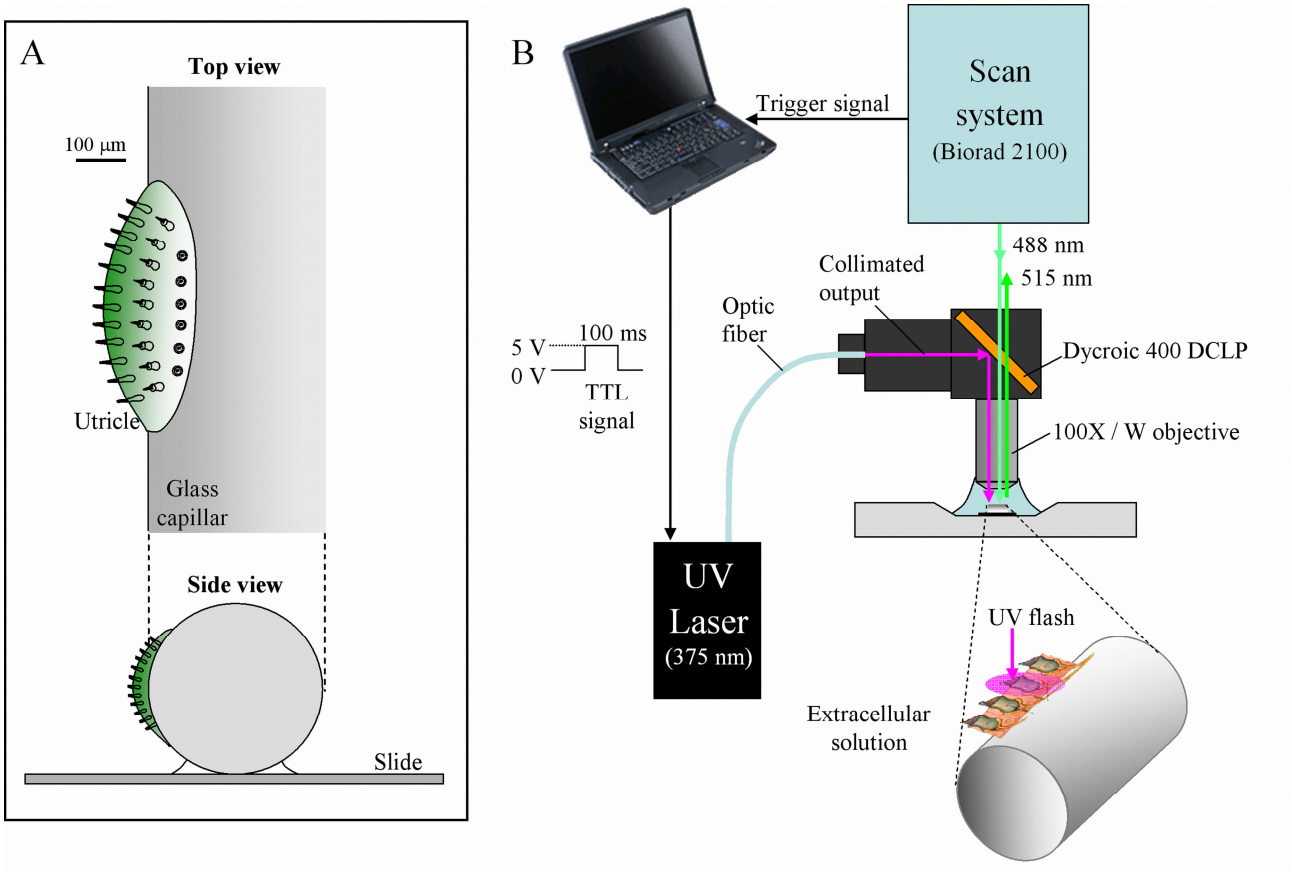

Figure 4. (A) Utricle fixation to the lateral side of a glass capillary permitted us to observe hair cells along their main axis. (B) UV light, controlled by a transistor–transistor logic (TTL) signal generated by a computer connected to the Biorad 2100 scanning system, was delivered for 30–100 ms during the scanning pause (1 s) between a couple of frames during the recording.

Chapter 3

The novel mouse mutation *Oblivion* inactivates the PMCA2 pump and causes progressive hearing loss*

Sarah L. Spiden#, Mario Bortolozzi#, Francesca Di Leva#, Martin Hrabé de Angelis, Helmut Fuchs, Dmitry Lim, Saida Ortolano, Marisa Brini, Neil J. Ingham, Ernesto Carafoli, Fabio Mammano and Karen P. Steel

Submitted to Human Molecular Genetics (January 2008)

3.1. Summary.

We have characterised a new dominantly-inherited mouse mutant, Oblivion (*Obl*), generated by *N*-ethyl-*N*-nitrosourea (ENU) mutagenesis, which may prove useful as an animal model for progressive hearing loss in humans. *Obl*/+ mutants showed hearing impairment with increasing severity from post-natal day (P)20 to P90, and loss of auditory function was followed by a corresponding base to apex progression of hair cell degeneration. *Obl/Obl* mutants were small, showed severe vestibular dysfunction by 2 weeks of age and were completely deaf from birth; sensory hair cells were completely degenerate in the basal turn of the cochlea, although hair cells appeared normal in the apex. We mapped the mutation to chromosome 6. Mutation analysis of *Atp2b2*, a candidate gene, showed a missense mutation (2630C→T) in exon 15, causing a serine to phenylalanine substitution (S877F) in transmembrane domain 6 of the PMCA2 pump, the resident Ca^{2+} pump of hair cell stereocilia. Transmembrane domain mutations in these pumps generally are believed to be incompatible with normal targeting of the protein to the plasma membrane. However, analyses of hair cells in cultured utricular maculae of *Obl/Obl* mice and of the mutant *Obl* pump in model cells showed that the protein was correctly targeted to the plasma membrane. Biochemical and biophysical characterisation showed that the pump had an impaired Ca^{2+} exporting function.

3.2. Methodological widenings

In these experiments we used a combination of flash-photolysis and fast confocal line scan (Figure 5) to investigate PMCA2 activity in hair cells of neonatal Oblivion mice. Utricle preparation and experimental setup were the same as described in Figure 4, but the unchanging apparatus included a

* For the full text article see the Appendix.

#These authors have contributed equally.

337 nm nitrogen pulsed-laser to obtain very rapid (<1 ms) Ca^{2+} uncaging. At recording time, the scan line was positioned along the main axis of the cell (Figure 5 left panel), scanning at ~170 Hz. After reading a baseline, a 4 nanoseconds UV (337 nm) pulse was delivered to uncage Ca^{2+}.

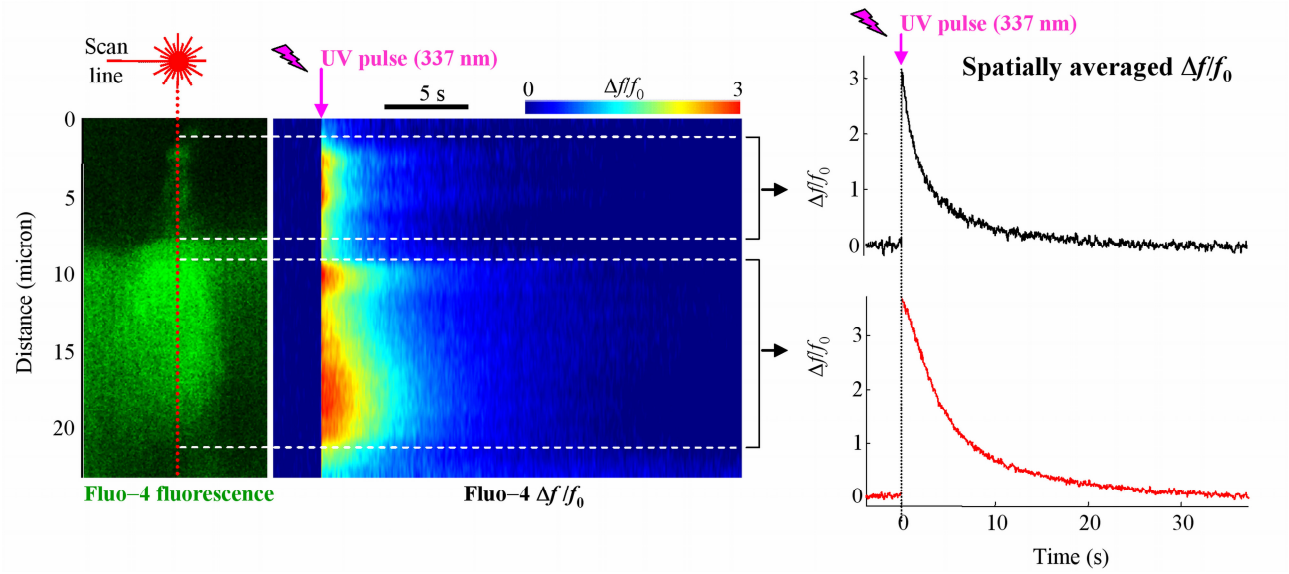

Figure 5. Analysis of a flash photolysis experiment in a utricle hair cell of Oblivion wild-type mouse. Ca^{2+} dynamics in the scanned line (red, left panel) is shown before and after the UV flash, in two dimensions, in the pseudo-color time course (center panel). The two graphics on the right are traces corresponding to the line-averaged time course of the $\Delta f/f_0$ in the stereociliary (up dashed white lines) and in the soma (down dashed white lines) compartments.

Chapter 4

Calcium microdomains at presynaptic active zones of vertebrate hair cells unmasked by stochastic deconvolution*

Mario Bortolozzi, Andrea Lelli and Fabio Mammano

Cell Calcium (in press, January 2008)

4.1. Summary.

Signal transduction by auditory and vestibular hair cells involves an impressive ensemble of finely tuned control mechanisms, strictly dependent on the local intracellular Ca^{2+} concentration ($[Ca^{2+}]_i$). The study of Ca^{2+} dynamics in hair cells typically combines electrophysiological recordings, Ca^{2+}-sensitive fluorescent indicators (dyes), patch clamp and optical microscopy to produce images of the patterns of fluorescence of a Ca^{2+} indicator following various stimulation protocols. Here we describe a novel method that combines fluorescence imaging and numerical simulations to effectively deconvolve Ca^{2+} signals within cytoplasmic microdomains that would otherwise remain inaccessible to direct observation. The method relies on the comparison of experimental data with virtual signals derived from a Monte Carlo reaction—diffusion model based on a realistic reconstruction of the relevant cell boundaries in three dimensions. The model comprises Ca^{2+} entry at individual presynaptic active zones followed by diffusion, buffering, extrusion and release of Ca^{2+}. Our results indicates that changes of the hair cell $[Ca^{2+}]_i$ during synaptic transmission are primarily controlled by the Ca^{2+} endogenous buffers both at short (<1 micron) and at long (tens of microns) distances from the active zones. We provide quantitative estimates of concentration and kinetics of the hair cell endogenous Ca^{2+} buffers and Ca^{2+}-ATPases. We finally show that experimental fluorescence data collected during Ca^{2+} influx are not interpreted correctly if the $[Ca^{2+}]_i$ is estimated by assuming that Ca^{2+} equilibrates instantly with its reactants. In our opinion, this approach is of potentially general interest as it can be easily adapted to the study of Ca^{2+} dynamics in diverse biological systems.

4.2. Introduction

There are several reasons why computer simulations are helpful when exploring Ca^{2+} dynamics. A typical observable variable is dye fluorescence but in principle one may want to access many other

* For the full text article see the Appendix.

variables affecting Ca^{2+} dynamics such as concentration and distribution of endogenous buffers, pumps and receptors. Theoretical approaches involve mathematical models of the classical diffusion-reaction scheme where Ca^{2+}, entering the hair cell, binds to the dye and to one or more endogenous buffers. $[Ca^{2+}]_i$ obeys the reaction diffusion equation and its solutions can be obtained either by applying standard partial differential equation numerical methods or by the Monte Carlo approach, which permits a more realistic description of molecule diffusion and interaction with cell boundaries.

Having obtained good correspondence between simulation and experiment, we are in a position to draw several conclusions concerning cell system properties that are not directly observable. First of all a key parameter for synaptic transmission, i.e., $[Ca^{2+}]_i$ at presynaptic active zones.

Chapter 5

Unitary permeability of gap junction channels to second messengers measured by FRET microscopy and dual whole-cell current recordings*

Victor H. Hernandez#, Mario Bortolozzi#, Vanessa Pertegato, Martina Beltramello, Michele Giarin, Manuela Zaccolo, Sergio Pantano and Fabio Mammano.

Nature Methods, 2007

5.1. Summary.

Gap junction channels assembled from connexin protein subunits mediate intercellular transfer of ions and metabolites. Impaired channel function is implicated in several hereditary human diseases. In particular, defective permeation of cAMP or inositol 1,4,5-trisphosphate ($InsP_3$) through connexin channels is associated with peripheral neuropathies and deafness, respectively. Here we present a method to estimate the permeability of single gap junction channels to second messengers. Using HeLa cells that overexpressed wild-type human connexin 26 (HCx26wt) as a model system, we combined measurements of junctional conductance and fluorescence resonance energy transfer (FRET) emission ratio of biosensors selective for cAMP and $InsP_3$. The unitary permeabilities to cAMP ($47 \cdot 10^{-3} \pm 15 \cdot 10^{-3}$ $\mu m^3/s$) and $InsP_3$ ($60 \cdot 10^{-3} \pm 12 \cdot 10^{-3}$ $\mu m^3/s$) were similar, but substantially larger than the unitary permeability to lucifer yellow (LY; $7 \pm 3 \cdot 10^{-3}$ $\mu m^3/s$), an exogenous tracer. This method permits quantification of defects of metabolic coupling and can be used to investigate interdependence of intercellular diffusion and cross-talk between diverse signaling pathways.

5.2. Introduction

Quantification of the single pore permeability, p_u, was based on the experimental data acquired from Cx26 trasfected HeLa cells by our collaborator Victor Hernandez with a combination of dual patch-clamp recordings of junctional conductance and fluorescence resonance energy transfer (FRET) emission of biosensors selective for cAMP and $InsP_3$ (H30 and LIBRA sensors, respectively). The model provides a method to quantify and compare gap junction permeability to different molecules for wild-type and mutant connexins and, potentially, to answer whether a given molecular intercellular diffusion is of functional importance for the organ of Corti.

---

* For the full text article see the Appendix.

#These authors have contributed equally.

Conclusions

Our study on mutant PMCA2 pumps suggests that the compromised function is not the ability to respond efficiently to a sudden request of hyperactivity, which is any way mediocre even in the normal *w/a* variant of PMCA2. What is compromised is instead the special ability of the *w/a* variant to operate efficiently at the non-activated level, a defect that leads to impaired Ca^{2+} handling in the microambient of the stereocilia, paralleled by a reduction of the endolymphatic Ca^{2+} concentration, as observed in the *dfw* mouse model [16]. We propose that this reduction is a conveyor of doom in that it biases the MET channel toward the full open state. Thus, hair cells become insensitive to bundle displacements and MET currents are replaced by a large standing current that depolarizes the cell plasma membrane eventually resulting in cell death. To verify this conclusion in our future experiments, we built a two-fluid compartment chamber which should permit to vary Ca^{2+} concentration of the fluid surrounding the hair cell bundle from mM to μM values, by leaving unaltered the basolateral (mM range) Ca^{2+} concentration. Several other aspects regarding Ca^{2+} effects on MET function requires further investigation and clarification. For instance, open questions are the relevance of Ca^{2+} accumulation in cytosol of PMCA2 mutant hair cells and how fast is fast adaptation under endolymphatic Ca^{2+} concentrations in wild-type mice. To clarify these points we will combine patch-clamp technique to flash photolysis and hair bundle mechanical stimulation in cochlear hair cells.

Fluorescence experimental data recorded in mice stereocilia will be analyzed with a mathematical model similar to that developed in the study of $[Ca^{2+}]_i$ near presynaptic active zones. Our Monte Carlo simulation code have shown to be a useful "nanoscope" to investigate physiological variables that otherwise would remain inaccessible to direct observation, e.g., Ca^{2+}-ATPase and Ca^{2+}-buffer concentrations and kinetics. In our studies, the traditional Monte Carlo approach, leading to numerical instabilities, was overcome by handling reactant chemical species with greatly different concentrations, e.g., resting $[Ca^{2+}]_i$ (nM range) and endogenous buffers (mM range), by the use, for each simulated species, of a different proportionality factor between real molecules and simulated particles. Furthermore, the direct comparison of experimental and virtual $\Delta f / f_0$ signals permitted us to show that the Ca^{2+}-dye is too slow to describe a fast increase (50 milliseconds duration) of the $[Ca^{2+}]_i$, and the $\Delta f / f_0$ signal represents spatially and temporally low-pass filtered version of the real $[Ca^{2+}]_i$.

In our opinion, a combination of sophisticated experimental techniques and mathematical models appears to be the proper way, sometimes necessary, to investigate the huge complexity of

multicellular living organisms. Furthermore, the large number of human genes implicated in deafness and the increasing number of mouse models with a deafness phenotype indicate that we will still learn a great deal more about hearing from the genetic approach, which will undoubtedly pave the way to therapies for auditory dysfunctions in the years to come.

References

1. Birkenhager R, Aschendorff A, Schipper J, Laszig R. (2007) [Non-syndromic hereditary hearing impairment]. Laryngorhinootologie, 86, 299-309; quiz 310-3.
2. Nance WE. (2003) The genetics of deafness. Ment Retard Dev Disabil Res Rev, 9, 109-19.
3. Cuajungco MP, Grimm C, Heller S. (2007) TRP channels as candidates for hearing and balance abnormalities in vertebrates. Biochim Biophys Acta, 1772, 1022-7.
4. Hudspeth AJ. (1989) How the ear's works work. Nature, 341, 397-404.
5. Parsons TD. (2006) Neurobiology: auditory fidelity. Nature, 444, 1013-4.
6. Lelli A, Perin P, Martini M, Ciubotaru CD, Prigioni I, Valli P, Rossi ML, Mammano F. (2003) Presynaptic calcium stores modulate afferent release in vestibular hair cells. J Neurosci, 23, 6894-903.
7. Roberts WM. (1994) Localization of calcium signals by a mobile calcium buffer in frog saccular hair cells. J Neurosci, 14, 3246-62.
8. Hill JK, Williams DE, LeMasurier M, Dumont RA, Strehler EE, Gillespie PG. (2006) Splice-site A choice targets plasma-membrane Ca2+-ATPase isoform 2 to hair bundles. J Neurosci, 26, 6172-80.
9. Street VA, McKee-Johnson JW, Fonseca RC, Tempel BL, Noben-Trauth K. (1998) Mutations in a plasma membrane Ca2+-ATPase gene cause deafness in deafwaddler mice. Nat Genet, 19, 390-4.
10. Ficarella R, Di Leva F, Bortolozzi M, Ortolano S, Donaudy F, Petrillo M, Melchionda S, Lelli A, Domi T, Fedrizzi L, Lim D, Shull GE, Gasparini P, Brini M, Mammano F, Carafoli E. (2007) A functional study of plasma-membrane calcium-pump isoform 2 mutants causing digenic deafness. Proc Natl Acad Sci U S A, 104, 1516-21.
11. Brini M, Leva FD, Domi T, Fedrizzi L, Lim D, Carafoli E. (2007) Plasma-membrane calcium pumps and hereditary deafness. Biochem Soc Trans, 35, 913-8.
12. Yamoah EN, Lumpkin EA, Dumont RA, Smith PJ, Hudspeth AJ, Gillespie PG. (1998) Plasma membrane Ca2+-ATPase extrudes Ca2+ from hair cell stereocilia. J Neurosci, 18, 610-24.
13. Gillespie PG, Cyr JL. (2004) Myosin-1c, the hair cell's adaptation motor. Annu Rev Physiol, 66, 521-45.
14. Fettiplace R, Ricci AJ. (2003) Adaptation in auditory hair cells. Curr Opin Neurobiol, 13, 446-51.
15. Fettiplace R, Ricci AJ. (2006) Mechanoelectrical transduction in auditory hair cells. In: Vertebrate Hair Cells. Vol. 27 (eds. RA Eatock, RR Fay, AN Popper), pp 154-203. Springer Science Inc., New York.
16. Wood JD, Muchinsky SJ, Filoteo AG, Penniston JT, Tempel BL. (2004) Low endolymph calcium concentrations in deafwaddler2J mice suggest that PMCA2 contributes to endolymph calcium maintenance. J Assoc Res Otolaryngol, 5, 99-110.
17. Wood JD, Muchinsky SJ, Filoteo AG, Penniston JT, Tempel BL. (2004) Low Endolymph Calcium Concentrations in deafwaddler(2J) Mice Suggest that PMCA2 Contributes to Endolymph Calcium Maintenance. J Assoc Res Otolaryngol.
18. Assad JA, Shepherd GM, Corey DP. (1991) Tip-link integrity and mechanical transduction in vertebrate hair cells. Neuron, 7, 985-94.
19. Ohmori H. (1985) Mechano-electrical transduction currents in isolated vestibular hair cells of the chick. J Physiol, 359, 189-217.
20. Corey DP, Hudspeth AJ. (1979) Ionic basis of the receptor potential in a vertebrate hair cell. Nature, 281, 675-7.
21. Assad JA, Hacohen N, Corey DP. (1989) Voltage dependence of adaptation and active bundle movement in bullfrog saccular hair cells. Proc Natl Acad Sci U S A, 86, 2918-22.

22. Ricci AJ, Fettiplace R. (1998) Calcium permeation of the turtle hair cell mechanotransducer channel and its relation to the composition of endolymph. J Physiol, 506 (Pt 1), 159-73.
23. Roux I, Safieddine S, Nouvian R, Grati M, Simmler MC, Bahloul A, Perfettini I, Le Gall M, Rostaing P, Hamard G, Triller A, Avan P, Moser T, Petit C. (2006) Otoferlin, defective in a human deafness form, is essential for exocytosis at the auditory ribbon synapse. Cell, 127, 277-89.
24. Delmaghani S, del Castillo FJ, Michel V, Leibovici M, Aghaie A, Ron U, Van Laer L, Ben-Tal N, Van Camp G, Weil D, Langa F, Lathrop M, Avan P, Petit C. (2006) Mutations in the gene encoding pejvakin, a newly identified protein of the afferent auditory pathway, cause DFNB59 auditory neuropathy. Nat Genet, 38, 770-8.
25. Lumpkin EA, Hudspeth AJ. (1998) Regulation of free Ca2+ concentration in hair-cell stereocilia. J Neurosci, 18, 6300-18.
26. Edmonds B, Reyes R, Schwaller B, Roberts WM. (2000) Calretinin modifies presynaptic calcium signaling in frog saccular hair cells. Nat Neurosci, 3, 786-90.
27. Heller S, Bell AM, Denis CS, Choe Y, Hudspeth AJ. (2002) Parvalbumin 3 is an abundant Ca2+ buffer in hair cells. J Assoc Res Otolaryngol, 3, 488-98.
28. Baird RA, Steyger PS, Schuff NR. (1997) Intracellular distributions and putative functions of calcium-binding proteins in the bullfrog vestibular otolith organs. Hear Res, 103, 85-100.
29. Rispoli G, Martini M, Rossi ML, Mammano F. (2001) Dynamics of intracellular calcium in hair cells isolated from the semicircular canal of the frog. Cell Calcium, 30, 131-40.
30. Issa NP, Hudspeth AJ. (1994) Clustering of Ca2+ channels and Ca(2+)-activated K+ channels at fluorescently labeled presynaptic active zones of hair cells. Proc Natl Acad Sci U S A, 91, 7578-82.
31. Tucker T, Fettiplace R. (1995) Confocal imaging of calcium microdomains and calcium extrusion in turtle hair cells. Neuron, 15, 1323-35.
32. Saxton MJ. (1994) Anomalous diffusion due to obstacles: a Monte Carlo study. Biophys J, 66, 394-401.
33. Saxton MJ. (1996) Anomalous diffusion due to binding: a Monte Carlo study. Biophys J, 70, 1250-62.
34. Kruk PJ, Korn H, Faber DS. (1997) The effects of geometrical parameters on synaptic transmission: a Monte Carlo simulation study. Biophys J, 73, 2874-90.
35. Gil A, Segura J, Pertusa JA, Soria B. (2000) Monte carlo simulation of 3-D buffered Ca(2+) diffusion in neuroendocrine cells. Biophys J, 78, 13-33.
36. Bennett MR, Farnell L, Gibson WG. (2000) The probability of quantal secretion near a single calcium channel of an active zone. Biophys J, 78, 2201-21.
37. Boettger T, Hubner CA, Maier H, Rust MB, Beck FX, Jentsch TJ. (2002) Deafness and renal tubular acidosis in mice lacking the K-Cl co-transporter Kcc4. Nature, 416, 874-8.
38. Gerido DA, White TW. (2004) Connexin disorders of the ear, skin, and lens. Biochim Biophys Acta, 1662, 159-70.
39. Harris AL. (2001) Emerging issues of connexin channels: biophysics fills the gap. Q Rev Biophys, 34, 325-472.
40. Thomas D, Lipp P, Tovey SC, Berridge MJ, Li W, Tsien RY, Bootman MD. (2000) Microscopic properties of elementary Ca2+ release sites in non-excitable cells. Curr Biol, 10, 8-15.
41. Saez JC, Connor JA, Spray DC, Bennett MV. (1989) Hepatocyte gap junctions are permeable to the second messenger, inositol 1,4,5-trisphosphate, and to calcium ions. Proc Natl Acad Sci U S A, 86, 2708-12.
42. Kam Y, Kim DY, Koo SK, Joe CO. (1998) Transfer of second messengers through gap junction connexin 43 channels reconstituted in liposomes. Biochim Biophys Acta, 1372, 384-8.

43. Niessen H, Willecke K. (2000) Strongly decreased gap junctional permeability to inositol 1,4, 5-trisphosphate in connexin32 deficient hepatocytes. FEBS Lett, 466, 112-4.
44. Niessen H, Harz H, Bedner P, Kramer K, Willecke K. (2000) Selective permeability of different connexin channels to the second messenger inositol 1,4,5-trisphosphate. J Cell Sci, 113 (Pt 8), 1365-72.
45. Beltramello M, Piazza V, Bukauskas FF, Pozzan T, Mammano F. (2005) Impaired permeability to Ins(1,4,5)P3 in a mutant connexin underlies recessive hereditary deafness. Nat Cell Biol, 7, 63-9.
46. Carafoli E, Penniston JT. (1985) The calcium signal. Sci Am, 253, 70-8.
47. Williams RJP. (1999) Calcium:The developing role of its chemistry in biological evolution. In: Calcium as a Cellular Regulator (eds. E Carafoli, CE Klee), pp pages 3-27. Oxford University Press, New York.
48. Denk W, Holt JR, Shepherd GM, Corey DP. (1995) Calcium imaging of single stereocilia in hair cells: localization of transduction channels at both ends of tip links. Neuron, 15, 1311-21.
49. Elwess NL, Filoteo AG, Enyedi A, Penniston JT. (1997) Plasma membrane Ca2+ pump isoforms 2a and 2b are unusually responsive to calmodulin and Ca2+. J Biol Chem, 272, 17981-6.
50. Walker RG, Hudspeth AJ, Gillespie PG. (1993) Calmodulin and calmodulin-binding proteins in hair bundles. Proc Natl Acad Sci U S A, 90, 2807-11.
51. El-Amraoui A, Petit C. (2005) Usher I syndrome: unravelling the mechanisms that underlie the cohesion of the growing hair bundle in inner ear sensory cells. J Cell Sci, 118, 4593-603.

Appendix

Ca^{2+} signaling in the inner ear, Physiology (2007).
Fabio Mammano, Mario Bortolozzi, Saida Ortolano and Fabio Anselmi.

Defects of plasma membrane calcium pump isoform 2 causing deafness in mice and humans. A functional study of normal and mutated variants, PNAS (2007)
Ficarella, R., Di Leva, F., Bortolozzi, M., Ortolano, S., Donaudy, F., Petrillo, M., Carella, M., Lelli, A., Domi, T., Fedrizzi, L., Lim, D., Shull, G.E., Gasparini, P., Brini, M., Mammano, F., Carafoli, E.

The novel mouse mutation *Oblivion* inactivates the PMCA2 pump and causes progressive hearing loss, submitted to Human Molecular Genetics (January 2008).
Sarah L Spiden, Mario Bortolozzi, Francesca Di Leva, Martin Hrabé de Angelis, Helmut Fuchs, Dmitry Lim, Saida Ortolano, Marisa Brini, Neil J. Ingham, Ernesto Carafoli, Fabio Mammano and Karen P Steel

Calcium microdomains at presynaptic active zones of vertebrate hair cells unmasked by stochastic deconvolution, Cell Calcium (in press, January 2008).
Mario Bortolozzi, Andrea Lelli and Fabio Mammano

Unitary permeability of gap junction channels to second messengers measured by FRET microscopy and dual whole-cell current recordings, Nature Methods (2007).
Victor H. Hernandez, Mario Bortolozzi, Vanessa Pertegato, Martina Beltramello, Michele Giarin, Manuela Zaccolo, Sergio Pantano and Fabio Mammano.

PHYSIOLOGY 22: 131–144, 2007; 10.1152/physiol.00040.2006

Ca^{2+} Signaling in the Inner Ear

Fabio Mammano,[1–3] Mario Bortolozzi,[1] Saida Ortolano,[1,3] and Fabio Anselmi[2]

[1]Istituto Veneto di Medicina Molecolare, Fondazione per la Ricerca Biomedica Avanzata, Padova; [2]Centro Interdipartimentale per lo Studio dei Segnali Cellulari, and [3]Dipartimento di Fisica "G.Galilei", Università di Padova, Padova, Italy
fabio.mammano@unipd.it

The inner ear contains delicate sensory receptors that have adapted to detect the minutest mechanical disturbances. Ca^{2+} ions are implicated in all steps of the transduction process, as well as in its regulation by an impressive ensemble of finely tuned feedback control mechanisms. Recent studies have unveiled some of the key players, but things do not sound quite right yet.

Sensory transduction in the inner ear (FIGURE 1) is the job of hair cells that are grouped into three types of sensory epithelia. The organ of Corti is the epithelium of the mammalian cochlea (hearing); the maculae and the cristae are the epithelia of the vestibular system (balance). The epithelia are polarized in that sensory hair cells as well as nonsensory (supporting) cells are divided into apical and basolateral domains. Diffusion of proteins between these subcellular domains is prevented by tight junctions between neighboring cells, which also serve to insulate endolymph, an extracellular fluid low in Na^+ and Ca^{2+} but rich in K^+, from perilymph, the normal extracellular fluid that bathes the basolateral membrane of the cells (FIGURE 1A).

Mechanical stimuli that can be ultimately ascribed to sound, for the cochlea, or acceleration, for the vestibular system, are applied to the hair cell mechanoreceptor organelle, composed of 20–300 actin-filled stiff microvilli, called the stereocilia, that reach into endolymph from the cell's apical surface and are arranged in three to four rows of increasing height. Stimulation of sensory transduction results in an increased flux of K^+ from endolymph through the hair cells, for hair bundle deflection modulates the open probability of specialized cation-selective mechanosensitive transduction (MET) channels found in the stereocilia (FIGURES 1A AND 2A). By altering the ratio of apical to basolateral membrane impedance, MET channel opening (closing) decreases (increases) the potential difference across the basolateral membrane of the hair cell. The ensuing graded receptor potential (i.e., the analog modulation of the hair cell resting potential) follows the movements of the stereocilia. Electrical activity in the hair cell is signaled to the central nervous system by afferent fibers of the acoustic or vestibular nerve that synapse to several active zones in the cell basolateral membrane.

With few exceptions, hair cells of the vestibular system in all animals respond to subacoustic frequencies, rarely in excess of a few tens of Hertz, whereas distinct mechanisms have evolved in the auditory periphery to extract sound frequency information over a far broader range. Thus, in the mammalian cochlea primed by sound, hydromechanical interactions excite specific vibration patterns on the basilar membrane, the elastic structure that supports the organ of Corti (FIGURE 1A). Basilar membrane vibrations are enhanced by a physiologically vulnerable mechanism, known as the cochlear amplifier, permitting frequency discrimination with ~1% accuracy over a range that, in humans, covers seven octaves from 40 Hz to 18 kHz. Frequency limits are species specific, and in other mammals the upper boundary may extend beyond a dazzling 100 kHz. In a subset of these frequencies, what might rightfully be defined as the energetic miracle of sound perception enables the detection of just-audible sounds corresponding to pressure changes as small as ~20 μPa (hearing threshold), i.e., 1 part in 5×10^9 of the static atmospheric pressure. At 1 kHz, these minute pressure changes are reciprocally related to air density fluctuations that alter the mean intermolecular distances by ~8 pm, about 1/10 of an atom's diameter. The sensitivity of the human ear is such that, under ideally quiet conditions in a still atmosphere, a 1-W source emitting sound waves at 3.5 kHz could in principle be heard at a distance of 564 km! Indeed, it has been proposed that yodeling, now a type of folk music, was developed as a method of communication between relatively distant mountain peaks of the Swiss Alps.

Though hair cells are the sensors for hearing and balance, several other cell types play essential roles for maintaining the environment necessary for optimal function of the inner ear. For example, vestibular and cochlear endolymph is secreted, respectively, by dark cells and by marginal cells of the stria vascularis. The stria is additionally responsible for maintaining cochlear endolymph at a potential of +80 to +100 mV (the so-called endochlear potential, or EP) relative to perilymph (FIGURE 1A), thus increasing the driving force for K^+. MET channel activation causes the hair cell to release K^+ ions that are either dispersed into perilymph or taken up by adjacent supporting cells and eventually returned to the stria vascularis. In this complex scenario of vertebrate inner ear, Ca^{2+} ions play numerous and fundamental roles. Here, we summarize the common aspects of transduction that are influenced by Ca^{2+} in vestibular and auditory hair cells, including MET function and neurotransmitter release. In the second part, we concentrate on the auditory periphery, reviewing the control exerted by Ca^{2+} on the cochlear amplifier and ion homeostasis in endolymph.

1548-9213/05 8.00

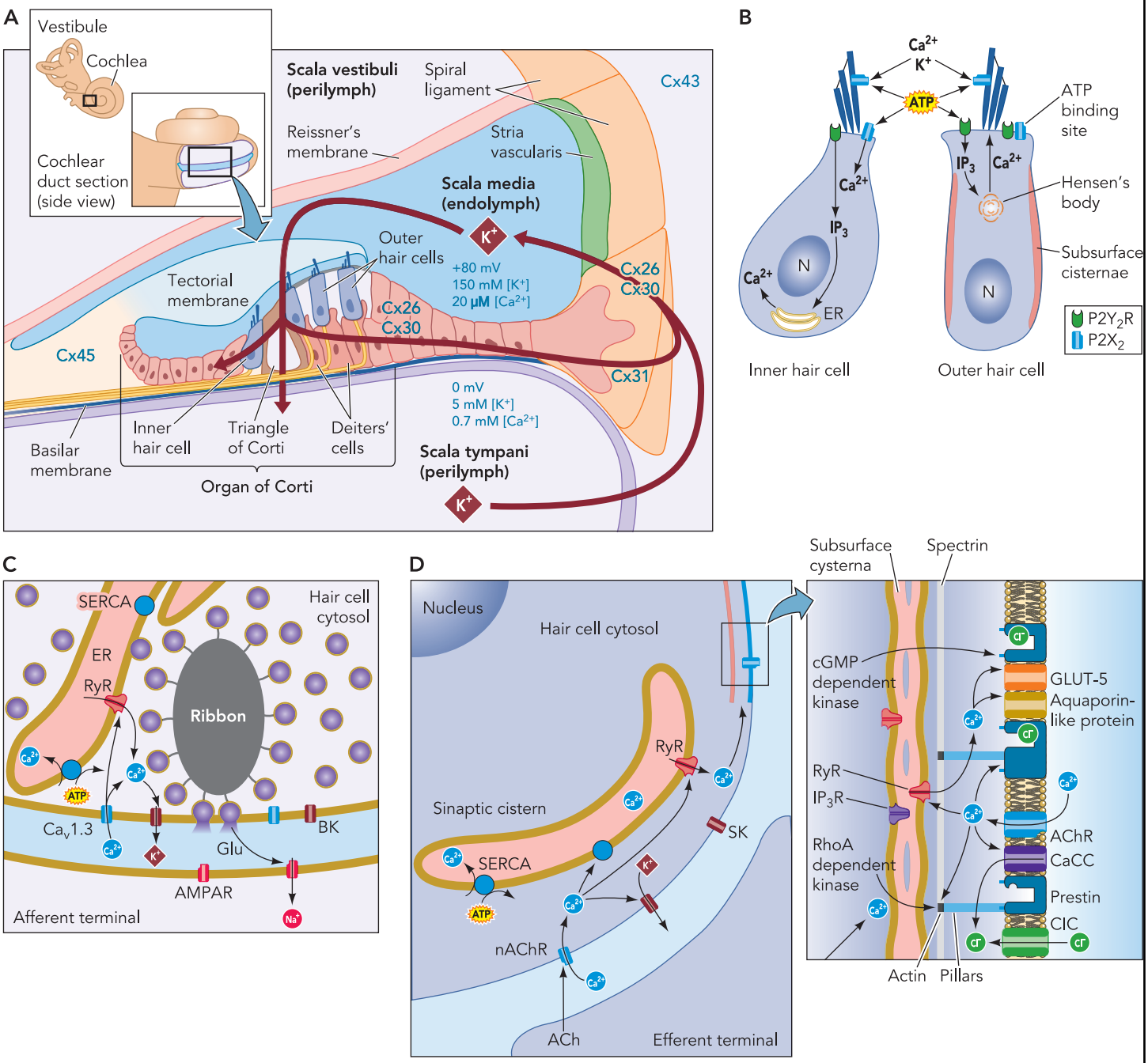

FIGURE 1. **Schematic view of selected Ca^{2+} signaling processes in the inner ear**

A: scheme of the inner ear (*inset*). Endolymphatic (blue) and stria vascularis (SV) compartments are delimited by a tight junction network. Perilymph bathes the rest of the cochlea. Scala media is separated from scala vestibuli by the Reissner's membrane (RM). The organ of Corti rests on the basilar membrane (BM), surmounted by the tectorial membrane (TM). The SV borders the spiral ligament at the lateral wall of the cochlear duct. The organ of Corti hosts sensory inner (IHC) and outer (OHC) hair cells. IHCs mechanotransduction is activated by the fluid viscous drag applied to their stereocilia by the oscillation of the TM. *B*: P2R expression in hair cells. P2YR are associated with release of Ca^{2+} from intracellular stores [endoplasmic reticulum (ER) or Hensen's body], whereas P2XR are localized on the stereocilia of the hair cells, in proximity of the MET channels, as well as in the apical cell surface. *C*: afferent (ribbon) synapse. $[Ca^{2+}]_i$ concentration at the afferent ribbon synapse of the hair cell indirectly controls the activation of glutamate receptors (AMPARs) at the postsynaptic terminal. $[Ca^{2+}]_i$ increase is amplified by CICR from tubular shaped ER extending to within 50 nm of the plasma membrane, close to the ribbon (see Ref. 100). *D*: efferent synapse and CICR. The inhibitory hyperpolarizing potassium current at the OHC efferent synapse is mediated by SK-type Ca^{2+}-activated potassium channels. This mechanism is supplemented and modulated by CICR from a synaptic cistern facing plasma membrane acetylcholine receptors (nAChRs). *Inset*: ACh influences OHC electromotility also by activating Ca^{2+}-dependent signaling pathways mediated by protein kinases that target cytoskeletal and prestin proteins. Function of prestin is influenced by intracellular anion concentrations, in particular Cl^- controlled by Ca^{2+}-dependent (CaCC) and voltage-dependent (e.g., ClC-2) chloride channels. OHC cell volume and turgor is regulated by Ca^{2+}-dependent phosphorylation of an aquaporin-like protein and/or a GLUT-5 sugar carrier, both voltage dependent and located in the lateral plasma membrane.

Ca^{2+} Modulation of Mechanotransduction in Hair Cells

As mentioned in the introduction, hair bundle deflection opens MET channels (FIGURE 2A), one of the few ion channels not yet conclusively identified (6, 26). Stereocilia in hair bundles are organized into rows of graded heights, forming precisely uniform staircase patterns (103). Stimuli that are sensed by hair cells as excitatory deflect a hair bundle toward its tallest stereocilia, thus increasing tension in the tip link, an extracellular filament stretched between the tops of stereocilia in adjacent rows (28, 85). Application of the Ca^{2+} chelator BAPTA to reduce the extracellular calcium concentration ($[Ca^{2+}]_o$) to submicromolar levels cuts the tip links and eliminates transduction (3). Tip-link tension is thought to be conveyed to MET channels through unidentified elastic elements, termed gating springs (78), mechanically in series with the tip links (28, 56). Values of up to two channels per tip link have been estimated for the mammalian cochlea (6), in accord with previous results in nonmammalian vertebrates (36, 76, 133).

Even though K^+ ions carry most of the transduction current, MET channels are highly permeable to Ca^{2+} (43). At the tens of micromolar $[Ca^{2+}]_o$ found in endolymph (12, 27), Ca^{2+} ions carry ~10% of the total MET current (134). But, to complicate matters, it appears that Ca^{2+} ions can both permeate and block the transducer channels (134) by binding with millimolar affinity at a site presumably located halfway through the membrane electric field (40). These and several other observations led to the conclusion that endolymph composition is specialized to allow a compromise between the largest monovalent current and the largest Ca^{2+} influx (43). From a physiological point of view, the key question is the role of Ca^{2+} ions admitted into the stereocilia through MET channels. The most obvious answer is that elevated stereociliary Ca^{2+} levels promote MET channel closure through adaptation, a negative-feedback mechanism that involves a shift of the sensitive range of the MET process (42, 78) (see http://www.rockefeller.edu/labheads/hudspeth/graphicalSimulations.php). Because it is accompanied by the restoration of sensitivity to transient stimuli, adaptation has been postulated to depend on an active motor that readjusts tension in the gating springs (2, 77), whose stiffness may in turn be Ca^{2+} dependent (20). But adaptation is a complex phenomenon in which at least two phases, both Ca^{2+} dependent, can be distinguished on the basis of their different kinetics and mechanical correlates (44, 71, 163). In different species and different epithelia, slow adaptation has a time constant (τ_A) of 10–100 ms (55), whereas fast adaptation in turtle auditory hair cells has millisecond τ_A (at 2.8 mM $[Ca^{2+}]_o$) (135), scaling down to sub-millisecond values in rodents (at 1.5 mM $[Ca^{2+}]_o$) (6, 87, 89). It has been suggested that fast adaptation is mediated by Ca^{2+} entering through the MET channel to shut it by binding at a site on the channel itself or a closely associated intracellular component (20, 29, 136, 163) and that this may tune the channel for small displacements around a resting position that is continually readjusted by slow adaptation (42). However, the calcium-binding site for channel block is thought to be distinct from that mediating fast adaptation (40). The alternative proposal is that of a unified mechanism for both fast and slow adaptation (73, 151) that involves the operation of an adaptation-motor complex formed by myosin-1c (Myo1c) (55), one of the several unconventional myosin isoforms of the stereocilia (43, 65). Myo1c in this scheme interacts in a Ca^{2+}-dependent manner with the rigid cross-linked actin filaments at the core of the stereocilia to adjust the force delivered by the tip link to the MET channel (FIGURE 2). In addition, phosphatidylinositol 4,5-bisphosphate (PIP2) binds directly to the IQ domains of Myo1c, regulating the motor activity, and consequently also transduction and adaptation (70). Ca^{2+} may also influence the activity of MET channels in an indirect way, i.e., via cAMP, because the rise in stereociliary $[Ca^{2+}]$ can activate a Ca^{2+}-calmodulin-activated type I adenyl cyclase of the hair cells (37, 54, 135) followed by activation of protein kinase A and phosphorylation of relevant targets. In summary, adaptation *1*) provides a transient response to slow or static stimuli, emphasizing changes in force; *2*) positions the transduction element in the most sensitive part of its activation curve to maximize responsiveness, both during development and during physiological stimuli; and *3*) prevents saturation of the transducer with larger stimuli (20).

Despite the staggering amount of heroically accumulated data on MET function, several aspects require further investigation and clarification. For instance, in virtually all types of hair cells studied so far, fast and slow adaptation are readily discriminated only for low-amplitude stimuli delivered (in the excitatory direction) under millimolar $[Ca^{2+}]_o$. Indeed, fast adaptation seemingly requires a well-defined range of stereociliary Ca^{2+} levels, but whether this range occurs under physiological conditions in vivo remains an open question. Thus, at 100 μM $[Ca^{2+}]_o$, MET currents of hair cells from mouse utricular macula or bullfrog saccular macula show negligible adaptation (20, 72), consistent with single MET channel recordings of frog auditory hair cells at 50 μM $[Ca^{2+}]_o$ or +80 mV holding potential (133). For larger displacements of the hair bundle, the time course of decline in the MET current slows down considerably, suggesting a prevalence of the slow component of adaptation (44). But MET current kinetics slow down also when the driving force for Ca^{2+} entry is reduced either by depolarizing the hair cell or by reducing $[Ca^{2+}]_o$ from nonphysiological millimolar levels to values between 20 and 100 μM that better approximate those found in endolymph (43). Furthermore, reducing $[Ca^{2+}]_o$ to near endolymphatic values in auditory hair cells of turtles

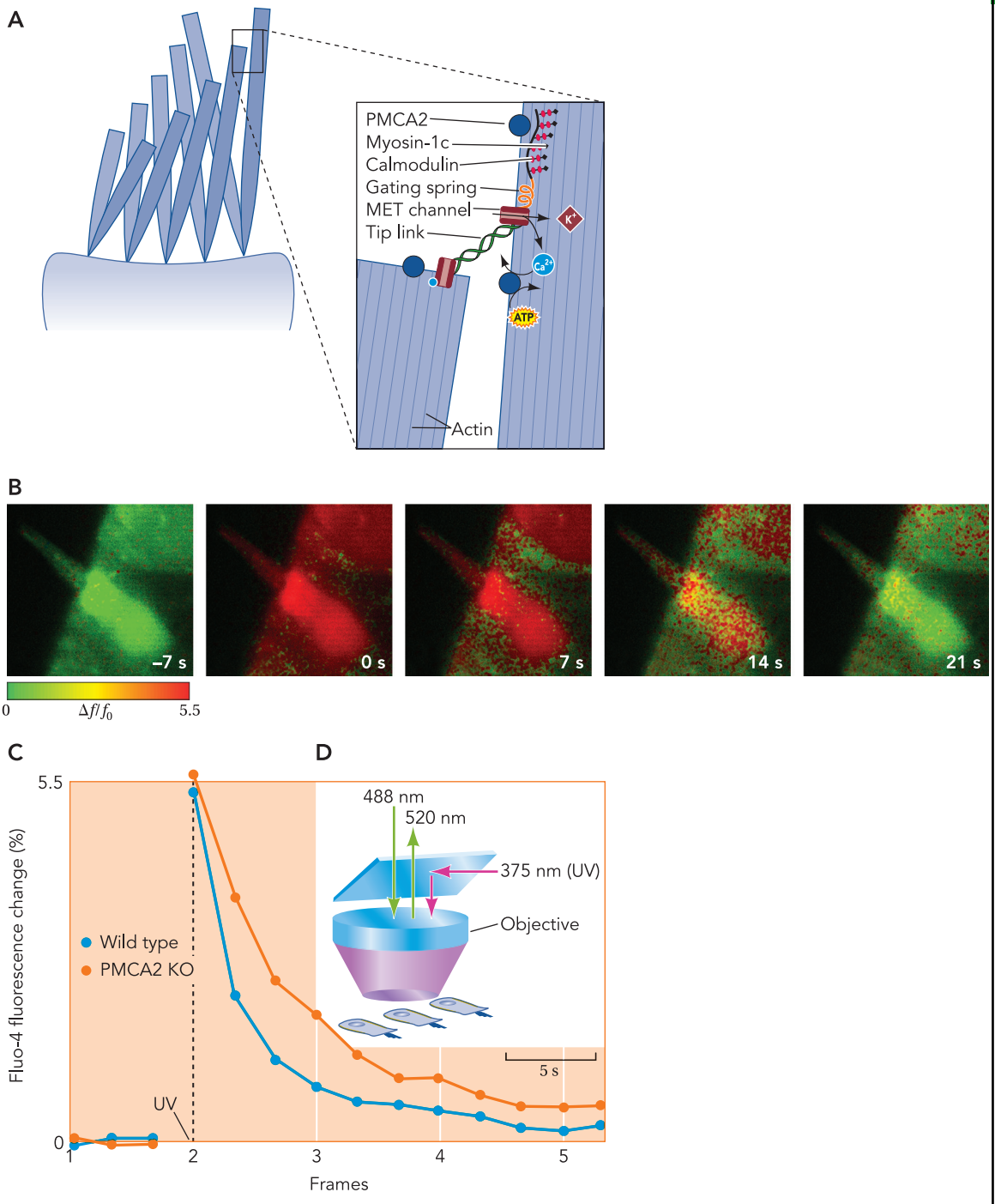

FIGURE 2. **Ca^{2+} dynamics at the apical pole of the hair cell**
A: mechanotransduction and calcium pumps. In this model, Myo1c of the adaptation-motor complex interacts, in a Ca^{2+}-calmodulin-dependent manner, with the rigid cross-linked actin filaments at the core of the stereocilia to adjust the force delivered by the tip link to the MET channel. The elastic component of the motor is represented by an intracellular gating spring connected to the MET channel. Ca^{2+} levels are returned to baseline by the ejection activity of the calcium pump (PMCA2 *w/a*). *B*: time sequence of confocal images before and after UV photolysis of caged Ca^{2+} in hair cells from a mouse utricle culture at *postnatal day 2* (P2). Timing relative to the onset of the 100-ms UV light pulse is shown on each numbered frame. Ca^{2+} concentration changes probed by Fluo-4 emission signal are encoded by the color scale bar beneath frame n.1. *C*: comparing time course of stereociliary fluorescence ratio changes evoked by Ca^{2+} photoliberation in a wild-type control (blue trace) and a PMCA2 KO mouse (red trace, corresponding to the frames in *B*); arrowheads below time axis show time of frame capture. *D*: methods. Fluo-4 fluorescence was excited by the 488-nm line of an argon laser, and fluorescence emission was selected around 520 nm. The UV illumination covered an area of ~5,000 μm^2, comprising a few hair cells, and was generated by a 375-nm laser light beam, reflected off a 400 DCLP dichromatic beam splitter positioned at 45 degrees just above the microscope objective lens. See Ref. 45. Note: the otolith organs (utricle and saccule) respond to translational head movements (linear accelerations) or to the orientation of the head relative to gravity.

and rodents results in doubling the unitary conductance, from 100 to 150 pS to 200 to 300 pS, and slowing of MET channel activation kinetics (6, 133). Interestingly, when turtle explants are exposed to 70 μM $[Ca^{2+}]_o$, the typical (multi)exponential decay of the MET current evoked by step displacements of the hair bundle evolves into damped current oscillations at frequencies comprised between 58 and 230 Hz, in the lower fraction of the animal's auditory range (134, 135). Under some conditions, the damping becomes negligible, and the turtle MET currents oscillate continuously in a limit-cycle mode (43), as found in other lower vertebrates in relation to low-frequency spontaneous hair bundle oscillations (110).

Clearly, fast adaptation ought to be most compelling for the mammalian cochlea, in which auditory information with frequency content in the kilohertz range is transmitted to the brain by the inner hair cells (IHCs) via synapses onto afferent terminals of the auditory nerve (41). It has been known for decades that when the mammalian ear is stimulated by sound with precisely defined frequency (pure tones, up to ~3.5 or 5.0 kHz depending on the species) the firing activity on the auditory nerve is cyclically and precisely concentrated only in one-half of the stimulating sinusoid, a phenomenon known as phase locking (1, 112). But rat IHCs, maintained at room temperature (19–22°C) at a potential of –80 mV, show level-dependent fast adaptation with shortest τ_A of ~0.5 ms (for the smallest stimuli in 1.5 mM $[Ca^{2+}]_o$, both at the 4- and 14-kHz frequency points sampled in this study (6). τ_A should be considerably shorter, of the order of 60–70 μs, when corrected for the environmental conditions in vivo (as done in Ref. 89 for OHCs). Therefore, if the properties of IHC MET channels are indeed invariant along the cochlea (6), during each cycle of, say, a 1-kHz tone, adaptation would be expected to impart a significant and Ca^{2+}-dependent (i.e., level-dependent) distortion to the transduction current and, consequently, receptor potential and afferent firing. Instead, published period histograms of phase-locked firing activity, evoked by pure tones around 1 kHz, track remarkably well the (half-wave rectified) stimulus waveform. In particular, they are symmetric around the peak firing probability over a wide range of input sound levels (1), in accord with the undistorted shape of the phasic (a.c.) receptor potential component (30, 124). In conclusion, it seems difficult to escape the questions of *1*) how fast is fast adaptation under physiological (endolymphatic) $[Ca^{2+}]_o$ in vivo and *2*) what of it is not an artifact due to the highly artificial recording conditions that are commonly employed?

Whatever the answer to these pressing questions, we now have a fairly clear picture of the fate undergone by Ca^{2+} entering through MET channels. It is rapidly bound by endogenous buffers within the stereocilia (63, 137) to be eventually shuttled back to endolymph by the plasma membrane Ca^{2+} ATPases (PMCAs) that are expressed at high density in the stereocilia (~2,000/μm^2) (134, 162, 164, 165). Ablation of the PMCA2 gene causes deafness and balance disorders in mice (93), associated to reduction of the Ca^{2+} extrusion rate (FIGURE 2, B–D). The extrusion task is performed by the *w/a* splicing isoform of PMCA2 (60, 61, 69). The choice of this unusual variant of the otherwise very efficient PMCA2 is surprising, given that this isoform is probably less responsive to the two natural PMCA activators, calmodulin and acidic phospholipids, and should be unable to rapidly enhance its activity in response to a sudden Ca^{2+} increase (14). It is also thought that PMCAs create an ambient of higher extracellular Ca^{2+} in the immediate proximity of the hair bundle (165), possibly with the complicity of the acellular structures overlying the hair cells in the cochlea (FIGURE 1A) (147) and, particularly, in the vestibular system (109) where PMCAs would also contribute to the formation and maintenance of the otoliths in the otolithic membranes (93) (structures in the saccule or utricle comprised of a combination of a gelatinous matrix and calcium carbonate crystals; the inertia of these small particles causes them to stimulate hair cells when the head accelerates). Furthermore, a mutation in the PMCA2 pump in the deaf waddler (*dfw*) mouse (G283S, downstream of the phospholipids binding domain in the loop connecting transmembrane domains 2 and 3) has been found to cause recessively inherited deafness (152). A mutation next to the active site of the pump (V586M) was later found to depress activity of the pump and to increase loss of hearing in heterozygous human patients that also carried a homozygous mutation in cadherin 23 (CDH23) (146), a member of the rapidly growing complement of stereocilia proteins (56). An unrelated T1999S substitution in the CDH23 gene has been recognized as a precondition for the development of a deafness phenotype in a human family when associated to a missense mutation of PMCA2, G293S, close to the *dfw* site (45). As discussed in detail in Ref. 127, an increasing number of other proteins have been found to be associated with hereditary hearing loss, the most common sensory deficit in humans (see the Hereditary Hearing Loss Homepage, http://webh01.ua.ac.be/hhh/), and their analysis is proving essential for the understanding of sensory transduction in the normal ear.

"Clearly, fast adaptation ought to be most compelling for the mammalian cochlea..."

Ca^{2+} Control of Synaptic Function

As mentioned above, MET current flowing into the apex of hair cells (and shaped by adaptation?) produces a

graded receptor potential at the cell basolateral membrane. Therefore, the hair cell can be functionally subdivided into apical and basal compartments, devoted to mechanoelectrical transduction and synaptic dialogue with afferent (and efferent) nerve fibers, respectively (52). At the afferent synapses of all hair cells, glutamate release is triggered by Ca^{2+} influx through L-type voltage-gated calcium channels ($Ca_V1.3$) clustered at such active zones ("hot spots") together with BK-type (Ca^{2+}-sensitive) voltage gated K^+ channels (116). Estimates of the total number of Ca^{2+} channels of these ~300-nm diameter micro- or nano-domains have been obtained in frog saccular hair cells [~90 channels for each of the ~20 active zones (138)] and mouse inner hair cells (IHCs) [~80 for 10–20 active zones (13)]. Domains of presynaptic Ca^{2+} are spatiotemporally restricted by the presence of mobile, proteinaceous Ca^{2+} buffers, calretinin, calbindin, and parvalbumin, which have been found in a variety of cochlear and vestibular hair cells with concentration in the millimolar range (63). However, discrepancies regarding both the amount and kinetic properties of such buffers in different hair cells suggest that their exact role and scope of function need to be analyzed further.

The afferent synapse of both vestibular and auditory hair cells is of the ribbon type (51, 120) (FIGURE 1C)

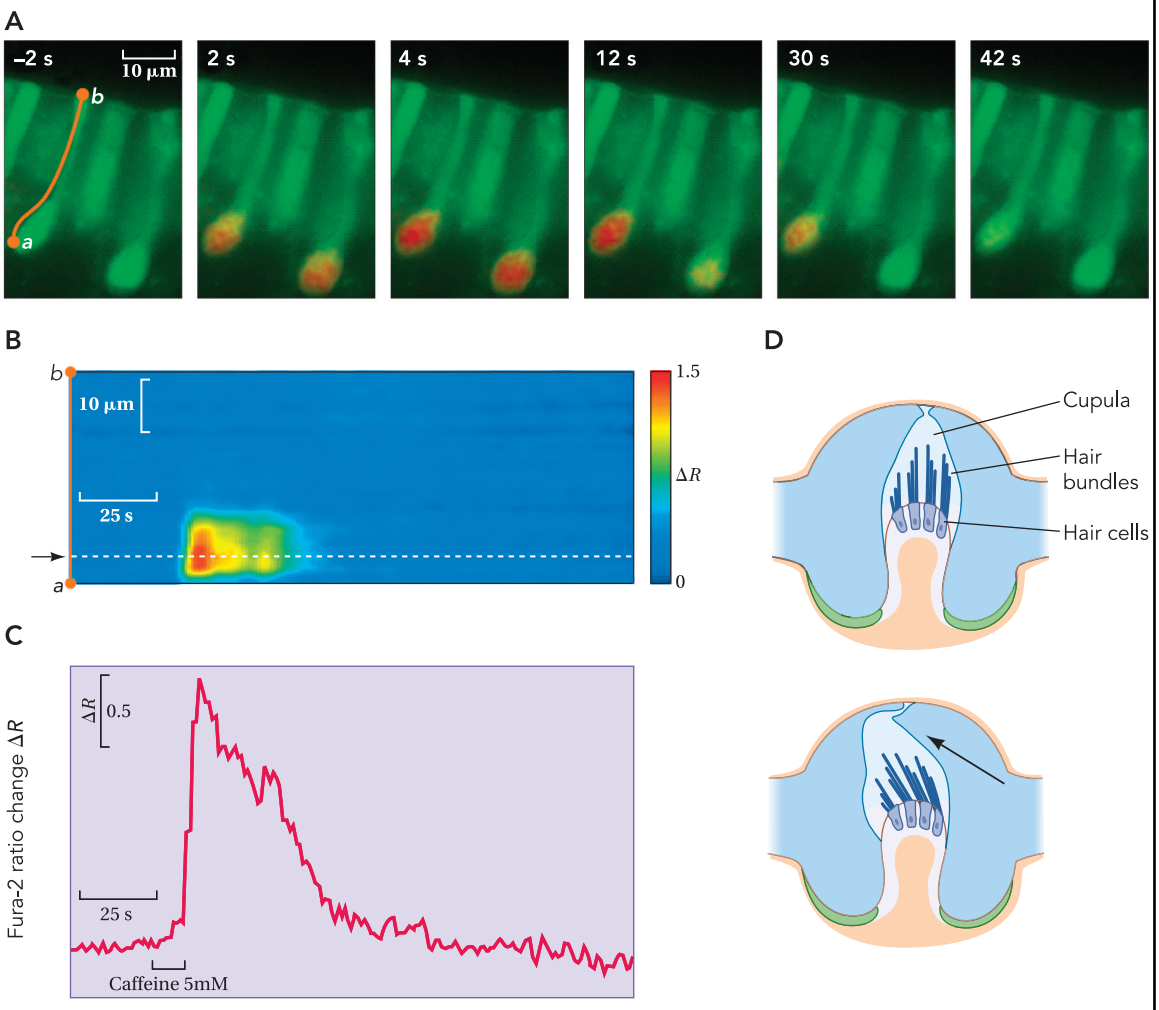

FIGURE 3. **Ca^{2+} stores at the synaptic pole of the hair cells**
A: time course of Ca^{2+} responses evoked by caffeine application (5 mM, 10 s) on hair cells in a slice of frog *Crista Ampullaris* loaded with fura 2-AM. *B*: pseudo-line-scan representation of fluorescence intensity changes ΔR. Abscissas represent time, and ordinates are distance along the line (*a*–*b*) superimposed on the cell in *A*. *C*: response analyzed at the point marked by the black arrow in *B*. See Ref. 99. *D*: schematic representation of the semicircular canal and crista ampullaris. *Top*: within each ampulla, the hair cells and their supporting cells lie embedded in a saddle-shaped neuroepithelial ridge, the crista, which extends across the base of the ampulla. Type I hair cells are concentrated in central regions of the crista, and type II hair cells are more numerous in peripheral areas. Arising from the crista and completely enveloping the stereocilia of the hair cells is a gelatinous structure, the cupula. The latter attaches to the roof and walls of the ampulla, forming a fluid-tight partition that has the same specific density as that of endolymph. *Bottom*: rotational head movements produce angular accelerations that cause the endolymph in the membranous ducts to be displaced so that the cupula is pushed to one side or the other. These cupular movements displace the stereocilia (and kinocilium) of the hair cells in the same direction.

and operates under stringent Ca^{2+} control conditions (8), and even more so in the auditory system where the establishment and maintenance of accurate phase relationship with sound stimuli relay on fast and tonic simultaneous multi-vesicular release (57, 86). Accurate and reliable timing of afferent discharge underlies the phenomenon of phase locking, discussed above, as well as the localization of sound sources in space, which requires discriminating time differences in the arrival of sound down to tens of microseconds (113). At any instant, only about 100 vesicles are tethered to the synaptic "ribbon" (or "dense body") of IHCs, and about 14 of these are docked to the plasma membrane (101, 142), constituting the "readily releasable" pool (115). The presynaptic Ca^{2+} current that closely follows the membrane potential (79) is directly proportional to vesicle release (83, 145). This linear relationship extends across the synapse to the postsynaptic current; therefore, the postsynaptic glutamate AMPA receptors faithfully transmit the information conveyed by the hair cell receptor potential (86). In higher frequency cells, overall higher frequencies of vesicle release are obtained primarily as a result of a greater number of synapses, whereas the lower Ca^{2+} entry per synapse may prevent postsynaptic receptor saturation (154). The Ca^{2+}-dependence of release is non-saturating and independent of hair cell frequency, suggesting that release, not refilling, is the rate-limiting factor (145). This conclusion is supported by the rapid, 1.9 vesicle per millisecond resupply that enables temporally precise and sustained release rates, two orders of magnitude higher than those of conventional synapses (62). How the ribbon replenishes its pool of vesicles, concentrating them at the site of Ca^{2+} influx, remains unclear (52, 120). Although the microtubule motor protein KIF3A was identified on the ribbon (117), evidence accumulates against an active "conveyor belt" for the resupply mechanism (67, 125). Interestingly, vesicles of the ribbon synapse lack synapsins as well as synaptotagmin 1 and 2, which are considered the Ca^{2+} sensors for vesicle fusion in neurons and neuroendocrine cells (140), whereas the core fusion complex contains some components in common with other synapses: SNARE proteins (syntaxin 1, synaptobrevin 1, and SNAP-25); the ribbon structural component RIBEYE; Bassoon and Piccolo, contributing to the anchoring of the ribbon at the active zone (120).

In addition to Ca^{2+} flowing through plasma membrane voltage-gated channels, it has been proposed that the increase of cytoplasmic free calcium concentration ($[Ca^{2+}]_i$) can also depend (or be amplified) by Ca^{2+} released from a presynaptic endoplasmic reticulum network of tubules and cysternae lying only a few tens of nanometers from the hair cell plasma membrane (25, 100, 141, 149) (FIGURE 1C). The mechanism of release depends on a caffeine and ryanodine sensitive Ca^{2+} channel through the mechanism of calcium-induced calcium release, CICR (FIGURE 3). An antagonistic concentration of ryanodine reduced afferent nerve fiber activity both in frog vestibular hair cells (99) and in mammalian IHC (7). In rat cochlear hair cells, CICR may be mediated by type I and II ryanodine receptors (RyR1–2) (59, 114). In IHCs, the highest levels of RyR1 labeling were observed over an area of rough endoplasmic reticulum that sits in the cytoplasmic region beneath the nucleus (59), supporting the conclusion that CICR enhances neurotransmitter release at the afferent region (57, 90). It has also been evidenced that RyRs and BK-type (Ca^{2+}-sensitive) voltage-gated potassium channels, co-localized mainly at the extrasynaptic apical neck of the IHCs, filter the receptor potential, and in turn depress neurotransmission in extreme conditions of enhanced Ca^{2+} accumulation that may occur during sound overstimulation or ischemia (7).

Recently, transient receptor potential ion channels (TRPC) have been characterized as a novel Ca^{2+} entry pathway in cochlear OHCs (132). TRPCs represent a superfamily of nonselective cation channels that have a particular significance in sensory systems (21). The OHC Ca^{2+} entry current is activated by the lowering of cytosolic Ca^{2+} levels and displays biophysical and pharmacological properties consistent with channels incorporating TRPC3 subunits. The TRPC-mediated Ca^{2+} entry channels may also be directly activated by DAG to complement G protein-coupled receptor-mediated release of stored Ca^{2+} (132).

The Cochlear Amplifier and Its Regulation by Ca^{2+}

As early as 1948, there were suggestions that an active mechanism might be necessary to explain the exquisite sensitivity and frequency resolving powers of the cochlea (58). It is now amply documented that a vulnerable active process known as cochlear amplifier (34) enhances up to a thousand-fold the vibrations of the basilar membrane (139) and is thus key to the perception of low-level sounds (107), as well as to other facets of sound processing performed by the cochlea (118, 119) (see The Cochlea Homepage, http://vimm.it/cochlea). This is the job of the outer hair cells (OHCs) (41), in which synaptic function is eclipsed by electromotility, a feature of these receptor/actuators that has no analog in any other cell of the body (15). The source of the electromotile cell length variations in OHCs is prestin (FIGURE 1D, *INSET*), an 81-kDa protein similar to pendrin and other members of the sulfate-anion transporter family but uniquely packed in the OHC lateral plasma membrane at a density of several thousand per square micron (31). Prestin, in contrast to enzymatic-activity-based motors, is a direct voltage-to-force converter that uses cytoplasmic Cl^- and HCO_3^- anions as extrinsic sensors for the receptor potential (122) and can operate at

microsecond rates (up to a frequency of, at least, 70 kHz) (46). The cell membrane fraction containing the prestin motor is a significant voltage-dependent contributor to the cell axial stiffness (66), together with the cytoskeletal cortical lattice and subsurface cisterns (121, 158). The OHC motor function can be modulated by numerous signaling pathways (47), some of which are Ca^{2+} dependent (48, 49), and, due to the strategic location of OHCs in the organ of Corti (FIGURE 1A), any change of OHC mechanical properties, particularly somatic length and axial stiffness, is bound to profoundly affect cochlear mechanics. On a slow time scale, OHC stiffness is controlled by phosphorylation of both cytoskeletal and prestin proteins. The polymerization state of cortical cytoskeleton filaments might be affected by activation of RhoA kinases under the control of intracellular Ca^{2+}, resulting in a stiffness increase (64, 166). Furthermore, OHC electromotility can be modulated by cGMP-dependent protein kinase acting at two prestin phosphorylation sites, as indicated by experiments performed in prestin-transfected cells (35). As mentioned above, prestin's function is influenced by intracellular anion concentrations, in particular by $[Cl^-]$, which may be regulated by Ca^{2+}-dependent and voltage-dependent chloride channels. Finally, water or sugar balance, influencing cell volume and turgor, can be regulated by a Ca^{2+}-dependent phosphorylation of an aquaporin-like protein and/or a GLUT-5 sugar carrier, both voltage dependent and located in the lateral plasma membrane (47) (FIGURE 1D, *INSET*).

A Ca^{2+}-dependent decrease of OHC axial stiffness was observed following the application of acetylcholine (ACh) to the cell basal pole (32). This is related to OHCs being the target of olivocochlear fibers that carry efferent inhibitory feedback from the brain (50) (FIGURE 1D). The efferent synapse uses a Ca^{2+}-permeable excitatory ACh receptor (75) to evoke both fast ionotropic and slow metabotropic responses (48). The fast response is a hyperpolarizing potassium current mediated by small-conductance Ca^{2+}-activated potassium channels (SK2) (123). The slow component, occurring with a delay of ~10 s, mediates an increase in the motile response of isolated unloaded OHCs, attributed to the activation of Ca^{2+}-/calmodulin-dependent phosphorylation of unspecified cytoskeletal proteins (153). OHC efferent synapses rely on the CICR mechanism (39), which is mediated by RyR1 receptors of a "synaptoplasmic" cistern at the postsynaptic site (104) (FIGURE 1D). It could be speculated that ACh triggers some sort of intracellular Ca^{2+} wave propagating in the proximity of the plasma membrane from the base of the cell to the lateral wall, via CICR from subsurface cisternae located beneath the cortical cytoskeleton. However, this phenomenon has not yet been experimentally demonstrated (47). The ensuing decrease in the global axial stiffness of the cell should exert an inhibitory effect on the OHC amplification mechanism in the organ of Corti (32). The biochemical pathway targeting OHC stiffness either after ACh application or following the increase of $[Ca^{2+}]_i$ appears to share a currently uncharacterized common mechanism (49). OHC axial stiffness decreases in response to increases of $[Ca^{2+}]_i$ (49) that also trigger cell elongation with consequent circumferential contraction, known as "Ca^{2+}-dependent slow motility" (24, 130). In summary, current data strongly argue for a crucial role of prestin-dependent amplification of mechanical stimuli in the mammalian cochlea (18, 19, 33, 102, 105, 143). The relevance for amplification of Ca^{2+}-dependent hair bundle movements, identified in rat OHCs as mechanical correlates of fast adaptation (17, 87) similar to those of nonmammalian vertebrates that lack prestin (110, 111), remains highly controversial (82, 88).

Other Ca^{2+} Signaling Pathways that Impact Inner Ear Function and Sound Perception

Extracellular signaling by nucleotides has long been associated with sensory systems, where ATP acts as a co-transmitter and/or neuromodulator (156). In both endolymphatic and perilymphatic compartments, basal level of extracellular ATP is maintained in the low nanomolar range by the action of ectonucleotidases (159). Even minimal departures from this level signal important changes to purinergic receptors (P2R) that play multiple important roles in sensory transduction and neurotransmission, consistent with the widespread expression of ATP gated ion channels (P2XR) and G-protein coupled receptors (P2YR) on inner ear cells, including cochlear hair cells (74). In most cases, Ca^{2+} ions are key intermediates in the ATP-evoked signaling cascades. Thus application of ATP to guinea pig IHC results in a rapid production of NO, presumably via ATP increase in $[Ca^{2+}]_i$. This in turn leads to a cGMP-PKG-dependent inhibition of the ATP-induced Ca^{2+} elevation in these cells (148). In OHCs, focal application of ATP to the hair bundle determines a biphasic increase in $[Ca^{2+}]_i$ (106). Initially, Ca^{2+} enters the cell apex through P2X ionotropic channels. Because it opens a pathway for K^+ ions (FIGURE 1B) in parallel to MET channels (FIGURE 2A), this process has been proposed to mediate a humoral modulation of mechanotransduction (75). But other mechanisms may be activated by the second phase of the ATP-evoked Ca^{2+} response, due to IP_3-induced Ca^{2+} release from internal stores mediated by PLC-coupled P2YR. In guinea pig OHCs, the release site coincides with the system of endoplasmic reticulum membranes and mitochondria known as Hensen's body, located at the base of the hair bundle. Ca^{2+} released in this region, beneath the cuticular plate that supports the hair bundle, effectively bypasses the clearance mechanism of the stereocilia and potentially influences mechanotransduction by mod-

ulation of unconventional myosin isoenzymes and actin-binding proteins involved in maintaining bundle integrity (106). Besides Myo1c, at least two other myosin isoforms, myosin VIIa and XVa, are found in the stereocilia and may alter bundle mechanics by acting on the attachment sites of the later links that hold the bundle together. Tropomyosin in the stereociliary rootlets, at the level of the cuticular plate, may also be involved in this process (38). In summary, myosin, tropomyosin, and actin together regulate the stiffness of bundle and cuticular plate under the control of Ca^{2+} binding proteins whose action is in turn regulated by Ca^{2+} pumps and buffers that control the concentration of intracellular Ca^{2+} at the apical pole of the hair cell, as explained in the relevant section above. Importantly, cochlear models indicate that even minimal disturbance to the mechanotransduction process may significantly alter the motor output of the cochlear amplifier, which operates at the threshold of spontaneous oscillations (107, 118, 119). Indeed, the estimated P2X-mediated conductance of hair cells must be minimal with respect to the one calculated for the Reissner's membrane (FIGURE 1A) because *1*) measurements of cochlear partition resistance (CoPR) in guinea pig endolymphatic compartment show that activation of hair cell P2XR has negligible influence on EP modulation and *2*) the EP value following ATP administration in the endolymph is not significantly altered in kanamicin treated animals lacking OHCs (157). Finally, mechanotransduction may be also affected by reduction of EP brought about by ATP stimulation of marginal cells in the gerbil stria vascularis, which determines a metabotropic Ca^{2+}-dependent inhibition of K^+ channel KCNE1 via $P2Y_4R$ (108).

Gap-Junction Coupling and Ca^{2+} Signaling in the Cochlear Duct

The homeostatic regulation of EP and endolymphatic K^+ levels, key prerequisites for the maintenance of MET function, require K^+ recirculation through the stria vascularis (FIGURE 1A) that houses a dense capillary network, supporting the high metabolic rate of this compartment (131). K^+ recirculation in the inner ear has been recently reviewed in this Journal (68). Briefly, K^+ released from cochlear hair cells following mechanotransduction (84) has been initially proposed to diffuse into scala tympani perilymph before entering the lateral wall of the cochlea (168). Here, it is taken up by fibrocytes in the spiral ligament, a densely vascularized endosteum at the outer limits of the cochlear canals, which is covered by the stria vascularis toward the cochlear duct. The stria vascularis in turn comprises basal, intermediate, and marginal cells. Gap-junction channels interconnect the fibrocytes of the spiral ligament and also medial and intermediate cells of the stria vascularis (22). Therefore, it has been proposed that intercellular transport across the gap junction network of this connective tissue participates in K^+ recirculation. After reaching the stria vascularis, K^+ ions are released by intermediate cells into the strial luminal site and are finally taken up by strial marginal cells to be secreted back into endolymph (81, 160, 161).

The fraction of K^+ being lost to perilymph due to MET channel activation is unknown, but disruption of the K-Cl cotransporters Kcc4 and Kcc3, which causes deafness in mice (10, 11), indicates that active K^+ uptake by the Deiter's cells and other supporting cells of the organ of Corti is essential to cochlear ion homeostasis. These cells belong in distinct gap junction networks formed by nonsensory epithelial cells (22, 80), including interdental cells of the spiral limbus, inner sulcus cells, organ of Corti supporting cells, outer sulcus cells, and cells within the root processes of the spiral ligament (92). Therefore, immediately after being released from the hair cells, a substantial proportion of the K^+ ions is likely to be taken up into these syncytia that may be an integral part of the recycle scheme (91).

In the organ of Corti, most gap-junction channels are assembled from connexin (Cx) protein subunits, primarily connexin 26 (Cx26, *GJB2* gene) and co-localized Cx30 (*GJB6*) (92, 98). Mouse models confirmed that both connexins are essential for cochlear function and cell survival (23, 94, 155), and the complex deafness DFNB1 locus (13q11-q12) has been shown to contain both gap-junction genes. Deafness-causing mutations have been reported in two other connexin genes, Cx31 (*GJB3*) and Cx43 (*GJA1*) (22); however, DFNB1 mutations are responsible for about half of all cases of human deafness in countries surrounding the Mediterranean Sea. In particular, over 50 causative mutations in *GJB2* have been shown to account for the vast majority of prelingual hearing impairment in most populations (see The Connexin-deafness homepage, http://davinci.crg.es/deafness/). DFNB1 is thus almost as frequent as cystic fibrosis (128). Yet deafness associated with mutations in the Cx26 gene may not solely depend on the loss of K^+ coupling and K^+ recirculation. Collectively, secondary messengers and small metabolites are deemed to be the molecular constituents that are directly passed from one cell to another: important molecules include cAMP, cGMP, IP_3, adenosine, ADP, and ATP, to name only a few (97). Indeed, Cx26 channels carrying the deafness-related V84L substitution present normal localization and similar conductance to wild-type protein (16), but significantly impaired permeability to IP_3 (4). Furthermore, direct injection of IP_3 in cochlear supporting cells of neonatal rat organotypic cultures generates a wave of calcium that spreads throughout the tissue and is suppressed when junctional channels (or unapposed Cx hemichannels facing scala media) are blocked by acidification with CO_2 (4). IP_3 permeability defects (167) may interfere with K^+ recycle function, because K^+/Cl^- efflux from supporting cells (10) may be, directly or indirectly, controlled by Ca^{2+}.

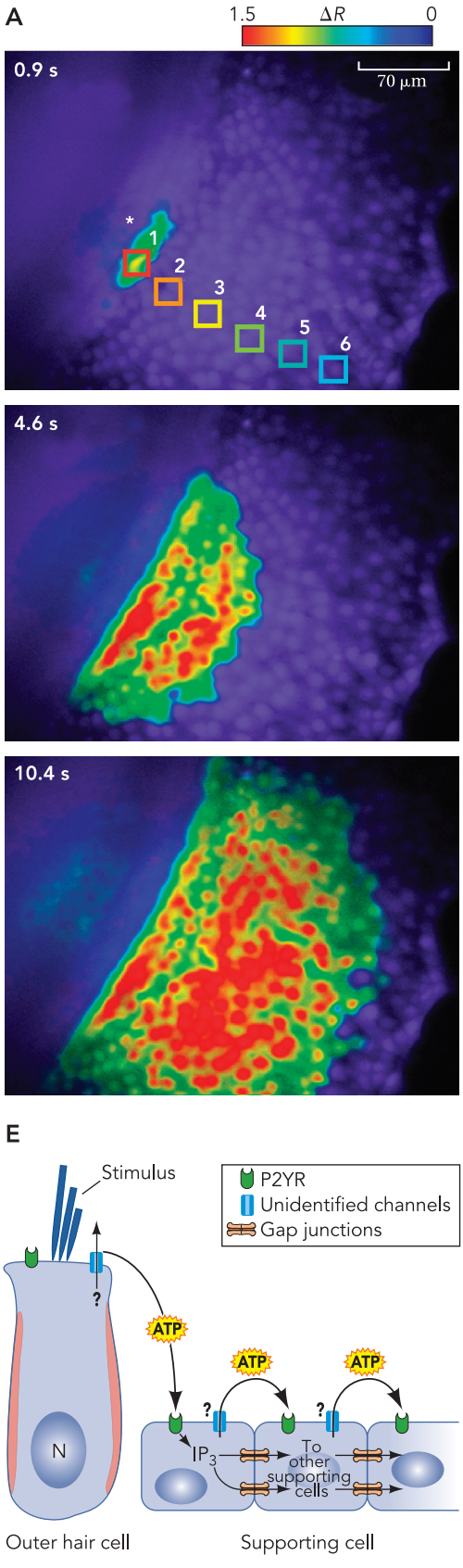

FIGURE 4. **Ca^{2+} waves in the organ Corti**
A: one representative experimental record, showing Ca^{2+} transient responses in fura 2-loaded supporting cells following focal ATP application (50 ms, 4 μM) to OHCs. Shown are pseudocolor images of the Ca^{2+} wave spreading at three different time points. *B*: $[Ca^{2+}]_i$ profiles from the regions of interest (ROIs) superimposed over six selected supporting cells in *A* (*top*). *C*: distance of wave-front points from the point of stimulus application (white asterisk) vs. time; wave speed is estimated by the slope of the least square linear fit (solid line). *D*: the amplitude of mean fura 2 ratio signal vs. distance shows no significant attenuation of the $[Ca^{2+}]_i$ response with distance from the point source, implicating an active mechanism of propagation. *E*: proposed mechanism of Ca^{2+} wave propagation. ATP release following hair cell stimulation induces an auto-sustained spreading of the signal in adjacent supporting cells, determined by further release of ATP into endolymph through an unidentified channel and concurrent IP_3 diffusion through gap-junction channels. *F*: IP_3 diffusion through gap junctions. The differently colored ribbons represent alpha-helices in the transmembrane portion of the six connexin proteins forming the connexon. See Ref. 9.

Pharmacological dissection indicates that ATP, acting through a highly sensitive purinergic-/IP_3-mediated signaling pathway, is the principal paracrine mediator implicated in the propagation of waves through supporting and epithelial cells (129) (FIGURE 4). Interestingly, Ca^{2+} waves generated by brief (50–200 ms) application of low doses of ATP (4–1 μM) from a puff pipette are identical to Ca^{2+} waves evoked by mechanical stimulation of hair cells, mimicking in vitro the effects of sound over-stimulation (53). A fundamental step is ATP release at the endolymphatic surface of the epithelium, which triggers adjacent cell responses (FIGURE 4E). Based on connexin expression models and inhibition by blockers, connexin hemichannels have been proposed as a diffusion pathway for the release of extracellular messengers, including ATP (5). This is the case of retinal pigment epithelium where ATP is released in the extracellular space through Cx43 hemichannels, with pore opening controlled by spontaneous elevations of intracellular Ca^{2+} (126). But transmission of Ca^{2+}-related signals may exploit alternative nonvesicular release mechanisms, along with IP_3 diffusion through gap junctions (4, 144) (FIGURE 4F). Thus anion channels, pannexins, and $P2X_7$ receptors have all been proposed as conduits for ATP to the extracellular milieu in other systems (150). The significance of Ca^{2+} wave propagation through the cochlear tissue, as well as that of oscillations in intracellular Ca^{2+} concentration levels (95, 96), are intimately connected to the role of Ca^{2+} in the control of key cellular processes. The extraordinary sensitivity to ATP of cochlear neonatal culture suggests that spreading of intracellular calcium through the syncitium is an essential component for the perception of sound and is potentially involved in sound-induced gene expression (53).

Conclusions

Ca^{2+} acts as a fundamental signal transduction element in the inner ear, delivering information about sound acceleration and gravity through the small number of hair cell MET channels to the ribbon synapse, thus driving neurotransmission. Ca^{2+} is also a second messenger that induces conformational changes in effector molecules regulating the sensitivity of the cochlear amplifier and inner ear fluid homeostasis. Several aspects regarding Ca^{2+} effects on MET function require further investigation and clarification. For instance, open questions are *1*) how fast is fast adaptation under endolymphatic Ca^{2+} concentrations (i.e., in vivo), and *2*) what is the relevance for amplification of Ca^{2+}-dependent hair bundle movements, mechanical correlates of fast adaptation? Other interesting problems regard Ca^{2+} dynamics near the ribbon synapse and the way in which the dense body replenishes its pool of vesicles, concentrating them at the site of Ca^{2+} influx. Is Ca^{2+} implicated in yet unidentified mechanisms driving ribbon dynamics? The genetic approach is proving fundamental in unraveling the molecular basis of Ca^{2+} function in the control of key cellular processes. It has recently provided interesting advances about cochlear K^+ recycle function and the role of Ca^{2+} waves propagation through the supporting cell network. Calcium wave spreading throughout the cells of the auditory periphery, following mechanical stimulation of hair cells, suggests the possibility of a link between wave generation and sound propagation. Although many of the molecular effectors of wave spreading have been identified, the explanation of the physiological significance of this phenomenon requires additional research efforts. Furthermore, the large number of human genes implicated in deafness and the increasing number of mouse models with a deafness phenotype indicate that we will still learn a great deal more about hearing from the genetic approach, which will undoubtedly pave the way to therapies for auditory dysfunctions in the years to come. ■

We thank Tullio Pozzan for critically reading the manuscript and Pascal Martin for helpful discussions.

This review was supported by the FP6 program of the European Union (FP6 Integrated Project EUROHEAR, LSHG-CT-20054-512063) and the Telethon Foundation (Projects GGP04169 and GGP02043).

References

1. Anderson DJ, Rose JE, Hind JE, Brugge JF. Temporal position of discharges in single auditory nerve fibers within the cycle of a sine-wave stimulus: frequency and intensity effects. *J Acoust Soc Am* 49, *Suppl* 2: 1131, 1971.
2. Assad JA, Corey DP. An active motor model for adaptation by vertebrate hair cells. *J Neurosci* 12: 3291–3309, 1992.
3. Assad JA, Shepherd GM, Corey DP. Tip-link integrity and mechanical transduction in vertebrate hair cells. *Neuron* 7: 985–994, 1991.
4. Beltramello M, Piazza V, Bukauskas FF, Pozzan T, Mammano F. Impaired permeability to Ins(1,4,5)P3 in a mutant connexin underlies recessive hereditary deafness. *Nat Cell Biol* 7: 63–69, 2005.
5. Bennett MV, Contreras JE, Bukauskas FF, Saez JC. New roles for astrocytes: gap junction hemichannels have something to communicate. *Trends Neurosci* 26: 610–617, 2003.
6. Beurg M, Evans MG, Hackney CM, Fettiplace R. A large-conductance calcium-selective mechanotransducer channel in mammalian cochlear hair cells. *J Neurosci* 26: 10992–11000, 2006.
7. Beurg M, Hafidi A, Skinner LJ, Ruel J, Nouvian R, Henaff M, Puel JL, Aran JM, Dulon D. Ryanodine receptors and BK channels act as a presynaptic depressor of neurotransmission in cochlear inner hair cells. *Eur J Neurosci* 22: 1109–1119, 2005.
8. Beutner D, Voets T, Neher E, Moser T. Calcium dependence of exocytosis and endocytosis at the cochlear inner hair cell afferent synapse. *Neuron* 29: 681–690, 2001.
9. Bicego M, Beltramello M, Melchionda S, Carella M, Piazza V, Zelante L, Bukauskas FF, Arslan E, Cama E, Pantano S, Bruzzone R, D'Andrea P, Mammano F. Pathogenetic role of the deafness-related M34T mutation of Cx26. *Hum Mol Genet* 15: 2569–2587, 2006.
10. Boettger T, Hubner CA, Maier H, Rust MB, Beck FX, Jentsch TJ. Deafness and renal tubular acidosis in mice lacking the K-Cl co-transporter Kcc4. *Nature* 416: 874–878, 2002.

11. Boettger T, Rust MB, Maier H, Seidenbecher T, Schweizer M, Keating DJ, Faulhaber J, Ehmke H, Pfeffer C, Scheel O, Lemcke B, Horst J, Leuwer R, Pape HC, Volkl H, Hubner CA, Jentsch TJ. Loss of K-Cl co-transporter KCC3 causes deafness, neurodegeneration and reduced seizure threshold. *EMBO J* 22: 5422–5434, 2003.

12. Bosher SK, Warren RL. Very low calcium content of cochlear endolymph, an extracellular fluid. *Nature* 273: 377–378, 1978.

13. Brandt A, Khimich D, Moser Few CaV1 T.3. channels regulate the exocytosis of a synaptic vesicle at the hair cell ribbon synapse. *J Neurosci* 25: 11577–11585, 2005.

14. Brini M, Coletto L, Pierobon N, Kraev N, Guerini D, Carafoli E. A comparative functional analysis of plasma membrane Ca^{2+} pump isoforms in intact cells. *J Biol Chem* 278: 24500–24508, 2003.

15. Brownell WE, Spector AA, Raphael RM, Popel AS. Micro- and nanomechanics of the cochlear outer hair cell. *Annu Rev Biomed Eng* 3: 169–194, 2001.

16. Bruzzone R, Veronesi V, Gomes D, Bicego M, Duval N, Marlin S, Petit C, D'Andrea P, White TW. Loss-of-function and residual channel activity of connexin26 mutations associated with non-syndromic deafness. *FEBS Lett* 533: 79–88, 2003.

17. Chan DK, Hudspeth AJ. Ca^{2+} current-driven nonlinear amplification by the mammalian cochlea in vitro. *Nat Neurosci* 8: 149–155, 2005.

18. Cheatham MA, Huynh KH, Gao J, Zuo J, Dallos P. Cochlear function in Prestin knockout mice. *J Physiol* 560: 821–830, 2004.

19. Cheatham MA, Zheng J, Huynh KH, Du GG, Gao J, Zuo J, Navarrete E, Dallos P. Cochlear function in mice with only one copy of the prestin gene. *J Physiol* 569: 229–241, 2005.

20. Cheung EL, Corey DP. Ca^{2+} changes the force sensitivity of the hair-cell transduction channel. *Biophys J* 90: 124–139, 2006.

21. Clapham DE. TRP channels as cellular sensors. *Nature* 426: 517–524, 2003.

22. Cohen-Salmon M. Connexins responsible for hereditary deafness: the tale unfolds. In: *Gap Junctions in Development and Disease*, edited by Winterhager E. Heidelberg, Germany: Springer-Verlag, 2005, p. 111–134.

23. Cohen-Salmon M, Ott T, Michel V, Hardelin JP, Perfettini I, Eybalin M, Wu T, Marcus DC, Wangemann P, Willecke K, Petit C. Targeted ablation of connexin26 in the inner ear epithelial gap junction network causes hearing impairment and cell death. *Curr Biol* 12: 1106–1111, 2002.

24. Coling DE, Bartolami S, Rhee D, Neelands T. Inhibition of calcium-dependent motility of cochlear outer hair cells by the protein kinase inhibitor, ML-9. *Hear Res* 115: 175–183, 1998.

25. Collin T, Marty A, Llano I. Presynaptic calcium stores and synaptic transmission. *Curr Opin Neurobiol* 15: 275–281, 2005.

26. Corey DP. What is the hair cell transduction channel? *J Physiol* 576: 23–28, 2006.

27. Corey DP, Hudspeth AJ. Kinetics of the receptor current in bullfrog saccular hair cells. *J Neurosci* 3: 962–976, 1983.

28. Corey DP, Sotomayor M. Hearing: tightrope act. *Nature* 428: 901–903, 2004.

29. Crawford AC, Evans MG, Fettiplace R. The actions of calcium on the mechano-electrical transducer current of turtle hair cells. *J Physiol* 434: 369–398, 1991.

30. Dallos P. Neurobiology of cochlear inner and outer hair cells: intracellular recordings. *Hear Res* 22: 185–198, 1986.

31. Dallos P, Fakler B. Prestin, a new type of motor protein. *Nat Rev Mol Cell Biol* 3: 104–111, 2002.

32. Dallos P, He DZ, Lin X, Sziklai I, Mehta S, Evans BN. Acetylcholine, outer hair cell electromotility, and the cochlear amplifier. *J Neurosci* 17: 2212–2226, 1997.

33. Dallos P, Zheng J, Cheatham MA. Prestin and the cochlear amplifier. *J Physiol* 576: 37–42, 2006.

34. Davis H. An active process in cochlear mechanics. *Hear Res* 9: 79–90, 1983.

35. Deak L, Zheng J, Orem A, Du GG, Aguinaga S, Matsuda K, Dallos P. Effects of cyclic nucleotides on the function of prestin. *J Physiol* 563: 483–496, 2005.

36. Denk W, Holt JR, Shepherd GM, Corey DP. Calcium imaging of single stereocilia in hair cells: localization of transduction channels at both ends of tip links. *Neuron* 15: 1311–1321, 1995.

37. Drescher MJ, Khan KM, Beisel KW, Karadaghy AA, Hatfield JS, Kim SY, Drescher AJ, Lasak JM, Barretto RL, Shakir AH, Drescher DG. Expression of adenylyl cyclase type I in cochlear inner hair cells. *Brain Res Mol Brain Res* 45: 325–330, 1997.

38. El-Amraoui A, Petit C. Usher I syndrome: unravelling the mechanisms that underlie the cohesion of the growing hair bundle in inner ear sensory cells. *J Cell Sci* 118: 4593–4603, 2005.

39. Evans MG, Lagostena L, Darbon P, Mammano F. Cholinergic control of membrane conductance and intracellular free Ca^{2+} in outer hair cells of the guinea pig cochlea. *Cell Calcium* 28: 195–203, 2000.

40. Farris HE, LeBlanc CL, Goswami J, Ricci AJ. Probing the pore of the auditory hair cell mechanotransducer channel in turtle. *J Physiol* 558: 769–792, 2004.

41. Fettiplace R, Hackney CM. The sensory and motor roles of auditory hair cells. *Nat Rev Neurosci* 7: 19–29, 2006.

42. Fettiplace R, Ricci AJ. Adaptation in auditory hair cells. *Curr Opin Neurobiol* 13: 446–451, 2003.

43. Fettiplace R, Ricci AJ. Mechanoelectrical transduction in auditory hair cells. In: *Vertebrate Hair Cells*, edited by Eatock RA, Fay RR, and Popper AN. New York: Springer Science, 2006, p. 154–203.

44. Fettiplace R, Ricci AJ, Hackney CM. Clues to the cochlear amplifier from the turtle ear. *Trends Neurosci* 24: 169–175, 2001.

45. Ficarella R, Di Leva F, Bortolozzi M, Ortolano S, Donaudy F, Petrillo M, Carella M, Lelli A, Domi T, Fedrizzi L, Lim D, Shull GE, Gasparini P, Brini M, Mammano F, Carafoli E. A functional study of plasma membrane calcium pump isoform 2 mutants causing digenic deafness. *PNAS*. In press.

46. Frank G, Hemmert W, Gummer AW. Limiting dynamics of high-frequency electromechanical transduction of outer hair cells. *Proc Natl Acad Sci USA* 96: 4420–4425, 1999.

47. Frolenkov GI. Regulation of electromotility in the cochlear outer hair cell. *J Physiol* 576: 43–48, 2006.

48. Frolenkov GI, Mammano F, Belyantseva IA, Coling D, Kachar B. Two distinct Ca^{2+}-dependent signaling pathways regulate the motor output of cochlear outer hair cells. *J Neurosci* 20: 5940–5948, 2000.

49. Frolenkov GI, Mammano F, Kachar B. Regulation of outer hair cell cytoskeletal stiffness by intracellular Ca^{2+}: underlying mechanism and implications for cochlear mechanics. *Cell Calcium* 33: 185–195, 2003.

50. Fuchs P. The synaptic physiology of cochlear hair cells. *Audiol Neurootol* 7: 40–44, 2002.

51. Fuchs PA. Time and intensity coding at the hair cell's ribbon synapse. *J Physiol* 566: 7–12, 2005.

52. Fuchs PA, Glowatzki E, Moser T. The afferent synapse of cochlear hair cells. *Curr Opin Neurobiol* 13: 452–458, 2003.

53. Gale JE, Piazza V, Ciubotaru CD, Mammano F. A mechanism for sensing noise damage in the inner ear. *Curr Biol* 14: 526–529, 2004.

54. Geleoc GS, Corey DP. Modulation of mechanoeletrical transduction by protein kinase A in utricular hair cells of neonatal mice. *Assoc Res Otolaryngol Abst* 24: 242, 2001.

55. Gillespie PG, Cyr JL. Myosin-1c, the hair cell's adaptation motor. *Annu Rev Physiol* 66: 521–545, 2004.

56. Gillespie PG, Dumont RA, Kachar B. Have we found the tip link, transduction channel, and gating spring of the hair cell? *Curr Opin Neurobiol* 15: 389–396, 2005.

57. Glowatzki E, Fuchs PA. Transmitter release at the hair cell ribbon synapse. *Nat Neurosci* 5: 147–154, 2002.

58. Gold Hearing T2nd. The physical basis of the action of the cochlea. *Proc R Soc Lond B Biol Sci* 135: 492–498, 1948.

59. Grant L, Slapnick S, Kennedy H, Hackney C. Ryanodine receptor localisation in the mammalian cochlea: an ultrastructural study. *Hear Res* 219: 101–109, 2006.

60. Grati M, Aggarwal N, Strehler EE, Wenthold RJ. Molecular determinants for differential membrane trafficking of PMCA1 and PMCA2 in mammalian hair cells. *J Cell Sci* 119: 2995–3007, 2006.

61. Grati M, Schneider ME, Lipkow K, Strehler EE, Wenthold RJ, Kachar B. Rapid turnover of stereocilia membrane proteins: evidence from the trafficking and mobility of plasma membrane Ca^{2+}-ATPase 2. *J Neurosci* 26: 6386–6395, 2006.

62. Griesinger CB, Richards CD, Ashmore JF. Fast vesicle replenishment allows indefatigable signalling at the first auditory synapse. *Nature* 435: 212–215, 2005.

63. Hackney CM, Mahendrasingam S, Penn A, Fettiplace R. The concentrations of calcium buffering proteins in mammalian cochlear hair cells. *J Neurosci* 25: 7867–7875, 2005.

64. Hall A, Nobes CD. Rho GTPases: molecular switches that control the organization and dynamics of the actin cytoskeleton. *Philos Trans R Soc Lond B Biol Sci* 355: 965–970, 2000.

65. Hasson T, Gillespie PG, Garcia JA, MacDonald RB, Zhao Y, Yee AG, Mooseker MS, Corey DP. Unconventional myosins in inner-ear sensory epithelia. *J Cell Biol* 137: 1287–1307, 1997.

66. He DZ, Jia S, Dallos P. Prestin and the dynamic stiffness of cochlear outer hair cells. *J Neurosci* 23: 9089–9096, 2003.

67. Heidelberger R. Adenosine triphosphate and the late steps in calcium-dependent exocytosis at a ribbon synapse. *J Gen Physiol* 111: 225–241, 1998.

68. Hibino H, Kurachi Y. Molecular and physiological bases of the K+ circulation in the mammalian inner ear. *Physiology Bethesda* 21: 336–345, 2006.

69. Hill JK, Williams DE, LeMasurier M, Dumont RA, Strehler EE, Gillespie PG. Splice-site A choice targets plasma-membrane Ca^{2+}-ATPase isoform 2 to hair bundles. *J Neurosci* 26: 6172–6180, 2006.

70. Hirono M, Denis CS, Richardson GP, Gillespie PG. Hair cells require phosphatidylinositol 4,5-bisphosphate for mechanical transduction and adaptation. *Neuron* 44: 309–320, 2004.

71. Holt JR, Corey DP. Two mechanisms for transducer adaptation in vertebrate hair cells. *Proc Natl Acad Sci USA* 97: 11730–11735, 2000.

72. Holt JR, Corey DP, Eatock RA. Mechanoelectrical transduction and adaptation in hair cells of the mouse utricle, a low-frequency vestibular organ. *J Neurosci* 17: 8739–8748, 1997.

73. Holt JR, Gillespie SK, Provance DW, Shah K, Shokat KM, Corey DP, Mercer JA, Gillespie PG. A chemical-genetic strategy implicates myosin-1c in adaptation by hair cells. *Cell* 108: 371–381, 2002.

74. Housley GD. Physiological effects of extracellular nucleotides in the inner ear. *Clin Exp Pharmacol Physiol* 27: 575–580, 2000.

75. Housley GD, Greenwood D, Ashmore JF. Localization of cholinergic and purinergic receptors on outer hair cells isolated from the guinea-pig cochlea. *Proc Biol Sci* 249: 265–273, 1992.

76. Howard J, Hudspeth AJ. Compliance of the hair bundle associated with gating of mechanoelectrical transduction channels in the bullfrog's saccular hair cell. *Neuron* 1: 189–199, 1988.

77. Howard J, Hudspeth AJ. Mechanical relaxation of the hair bundle mediates adaptation in mechanoelectrical transduction by the bullfrog's saccular hair cell. *Proc Natl Acad Sci USA* 84: 3064–3068, 1987.

78. Hudspeth AJ, Gillespie PG. Pulling springs to tune transduction: adaptation by hair cells. *Neuron* 12: 1–9, 1994.

79. Hudspeth AJ, Lewis RS. A model for electrical resonance and frequency tuning in saccular hair cells of the bull-frog, Rana catesbeiana. *J Physiol* 400: 275–297, 1988.

80. Jagger DJ, Forge A. Compartmentalized and signal-selective gap junctional coupling in the hearing cochlea. *J Neurosci* 26: 1260–1268, 2006.

81. Jentsch TJ. Neuronal KCNQ potassium channels: physiology and role in disease. *Nat Rev Neurosci* 1: 21–30, 2000.

82. Jia S, He DZ. Motility-associated hair-bundle motion in mammalian outer hair cells. *Nat Neurosci* 8: 1028–1034, 2005.

83. Johnson SL, Marcotti W, Kros CJ. Increase in efficiency and reduction in Ca^{2+} dependence of exocytosis during development of mouse inner hair cells. *J Physiol* 563: 177–191, 2005.

84. Johnstone BM, Patuzzi R, Syka J, Sykova E. Stimulus-related potassium changes in the organ of Corti of guinea-pig. *J Physiol* 408: 77–92, 1989.

85. Kachar B, Parakkal M, Kurc M, Zhao Y, Gillespie PG. High-resolution structure of hair-cell tip links. *Proc Natl Acad Sci USA* 97: 13336–13341, 2000.

86. Keen EC, Hudspeth AJ. Transfer characteristics of the hair cell's afferent synapse. *Proc Natl Acad Sci USA* 103: 5537–5542, 2006.

87. Kennedy HJ, Crawford AC, Fettiplace R. Force generation by mammalian hair bundles supports a role in cochlear amplification. *Nature* 433: 880–883, 2005.

88. Kennedy HJ, Evans MG, Crawford AC, Fettiplace R. Depolarization of cochlear outer hair cells evokes active hair bundle motion by two mechanisms. *J Neurosci* 26: 2757–2766, 2006.

89. Kennedy HJ, Evans MG, Crawford AC, Fettiplace R. Fast adaptation of mechanoelectrical transducer channels in mammalian cochlear hair cells. *Nat Neurosci* 6: 832–836, 2003.

90. Kennedy HJ, Meech RW. Fast Ca2+ signals at mouse inner hair cell synapse: a role for Ca^{2+}-induced Ca^{2+} release. *J Physiol* 539: 15–23, 2002.

91. Kikuchi T, Adams JC, Miyabe Y, So E, Kobayashi T. Potassium ion recycling pathway via gap junction systems in the mammalian cochlea and its interruption in hereditary nonsyndromic deafness. *Med Electron Microsc* 33: 51–56, 2000.

92. Kikuchi T, Kimura RS, Paul DL, Adams JC. Gap junctions in the rat cochlea: immunohistochemical and ultrastructural analysis. *Anat Embryol (Berl)* 191: 101–118, 1995.

93. Kozel PJ, Friedman RA, Erway LC, Yamoah EN, Liu LH, Riddle T, Duffy JJ, Doetschman T, Miller ML, Cardell EL, Shull GE. Balance and hearing deficits in mice with a null mutation in the gene encoding plasma membrane Ca^{2+}-ATPase isoform 2. *J Biol Chem* 273: 18693–18696, 1998.

94. Kudo T, Kure S, Ikeda K, Xia AP, Katori Y, Suzuki M, Kojima K, Ichinohe A, Suzuki Y, Aoki Y, Kobayashi T, Matsubara Y. Transgenic expression of a dominant-negative connexin26 causes degeneration of the organ of Corti and non-syndromic deafness. *Hum Mol Genet* 12: 995–1004, 2003.

95. Lagostena L, Ashmore JF, Kachar B, Mammano F. Purinergic control of intercellular communication between Hensen's cells of the guinea-pig cochlea. *J Physiol* 531: 693–706, 2001.

96. Lagostena L, Mammano F. Intracellular calcium dynamics and membrane conductance changes evoked by Deiters' cell purinoceptor activation in the organ of Corti. *Cell Calcium* 29: 191–198, 2001.

97. Laird DW. Life cycle of connexins in health and disease. *Biochem J* 394: 527–543, 2006.

98. Lautermann J, ten Cate WJ, Altenhoff P, Grummer R, Traub O, Frank H, Jahnke K, Winterhager E. Expression of the gap-junction connexins 26 and 30 in the rat cochlea. *Cell Tissue Res* 294: 415–420, 1998.

99. Lelli A, Perin P, Martini M, Ciubotaru CD, Prigioni I, Valli P, Rossi ML, Mammano F. Presynaptic calcium stores modulate afferent release in vestibular hair cells. *J Neurosci* 23: 6894–6903, 2003.

100. Lenzi D, Runyeon JW, Crum J, Ellisman MH, Roberts WM. Synaptic vesicle populations in saccular hair cells reconstructed by electron tomography. *J Neurosci* 19: 119–132, 1999.

101. Liberman MC. Efferent synapses in the inner hair cell area of the cat cochlea: an electron microscopic study of serial sections. *Hear Res* 3: 189–204, 1980.

102. Liberman MC, Gao J, He DZ, Wu X, Jia S, Zuo J. Prestin is required for electromotility of the outer hair cell and for the cochlear amplifier. *Nature* 419: 300–304, 2002.

103. Lin HW, Schneider ME, Kachar B. When size matters: the dynamic regulation of stereocilia lengths. *Curr Opin Cell Biol* 17: 55–61, 2005.

104. Lioudyno M, Hiel H, Kong JH, Katz E, Waldman E, Parameshwaran-Iyer S, Glowatzki E, Fuchs PA. A "synaptoplasmic cistern" mediates rapid inhibition of cochlear hair cells. *J Neurosci* 24: 11160–11164, 2004.

105. Liu XZ, Ouyang XM, Xia XJ, Zheng J, Pandya A, Li F, Du LL, Welch KO, Petit C, Smith RJ, Webb BT, Yan D, Arnos KS, Corey D, Dallos P, Nance WE, Chen ZY. Prestin, a cochlear motor protein, is defective in non-syndromic hearing loss. *Hum Mol Genet* 12: 1155–1162, 2003.

106. Mammano F, Frolenkov GI, Lagostena L, Belyantseva IA, Kurc M, Dodane V, Colavita A, Kachar B. ATP-Induced Ca^{2+} release in cochlear outer hair cells: localization of an inositol triphosphate-gated Ca^{2+} store to the base of the sensory hair bundle. *J Neurosci* 19: 6918–6929, 1999.

107. Mammano F, Nobili R. Biophysics of the cochlea: linear approximation. *J Acoust Soc Am* 93: 3320–3332, 1993.

108. Marcus DC, Sunose H, Liu J, Bennett T, Shen Z, Scofield MA, Ryan AF. Protein kinase C mediates P2U purinergic receptor inhibition of K^+ channel in apical membrane of strial marginal cells. *Hear Res* 115: 82–92, 1998.

109. Marquis RE, Hudspeth AJ. Effects of extracellular Ca^{2+} concentration on hair-bundle stiffness and gating-spring integrity in hair cells. *Proc Natl Acad Sci USA* 94: 11923–11928, 1997.

110. Martin P, Bozovic D, Choe Y, Hudspeth AJ. Spontaneous oscillation by hair bundles of the bullfrog's sacculus. *J Neurosci* 23: 4533–4548, 2003.

111. Martin P, Hudspeth AJ. Active hair-bundle movements can amplify a hair cell's response to oscillatory mechanical stimuli. *Proc Natl Acad Sci USA* 96: 14306–14311, 1999.

112. Moller AR. Frequency selectivity of phase-locking of complex sounds in the auditory nerve of the rat. *Hear Res* 11: 267–284, 1983.

113. Moore DR. Anatomy and physiology of binaural hearing. *Audiology* 30: 125–134, 1991.

114. Morton-Jones RT, Cannell MB, Jeyakumar LH, Fleischer S, Housley GD. Differential expression of ryanodine receptors in the rat cochlea. *Neuroscience* 137: 275–286, 2006.

115. Moser T, Beutner D. Kinetics of exocytosis and endocytosis at the cochlear inner hair cell afferent synapse of the mouse. *Proc Natl Acad Sci USA* 97: 883–888, 2000.

116. Moser T, Neef A, Khimich D. Mechanisms underlying the temporal precision of sound coding at the inner hair cell ribbon synapse. *J Physiol* 576: 55–62, 2006.

117. Muresan V, Lyass A, Schnapp BJ. The kinesin motor KIF3A is a component of the presynaptic ribbon in vertebrate photoreceptors. *J Neurosci* 19: 1027–1037, 1999.

118. Nobili R, Mammano F. Biophysics of the cochlea. II: Stationary nonlinear phenomenology. *J Acoust Soc Am* 99: 2244–2255, 1996.

119. Nobili R, Vetesnik A, Turicchia L, Mammano F. Otoacoustic emissions from residual oscillations of the cochlear basilar membrane in a human ear model. *J Assoc Res Otolaryngol* 4: 478–494, 2003.

120. Nouvian R, Beutner D, Parsons TD, Moser T. Structure and function of the hair cell ribbon synapse. *J Membr Biol* 209: 153–165, 2006.

121. Oghalai JS, Patel AA, Nakagawa T, Brownell WE. Fluorescence-imaged microdeformation of the outer hair cell lateral wall. *J Neurosci* 18: 48–58, 1998.

122. Oliver D, He DZ, Klocker N, Ludwig J, Schulte U, Waldegger S, Ruppersberg JP, Dallos P, Fakler B. Intracellular anions as the voltage sensor of prestin, the outer hair cell motor protein. *Science* 292: 2340–2343, 2001.

123. Oliver D, Klocker N, Schuck J, Baukrowitz T, Ruppersberg JP, Fakler B. Gating of Ca^{2+}-activated K^+ channels controls fast inhibitory synaptic transmission at auditory outer hair cells. *Neuron* 26: 595–601, 2000.

124. Palmer AR, Russell IJ. Phase-locking in the cochlear nerve of the guinea-pig and its relation to the receptor potential of inner hair-cells. *Hear Res* 24: 1–15, 1986.

125. Parsons TD, Sterling Synaptic ribbon P. Conveyor belt or safety belt? *Neuron* 37: 379–382, 2003.

126. Pearson RA, Dale N, Llaudet E, Mobbs P. ATP released via gap junction hemichannels from the pigment epithelium regulates neural retinal progenitor proliferation. *Neuron* 46: 731–744, 2005.

127. Petit C. From deafness genes to hearing mechanisms: harmony and counterpoint. *Trends Mol Med* 12: 57–64, 2006.

128. Petit C, Levilliers J, Hardelin JP. Molecular genetics of hearing loss. *Annu Rev Genet* 35: 589–646, 2001.

129. Piazza V, Ciubotaru CD, Gale JE, Mammano F. Purinergic signalling and intercellular Ca^{2+} wave propagation in the organ of Corti. *Cell Calcium* 41: 77–86, 2006.

130. Puschner B, Schacht J. Calmodulin-dependent protein kinases mediate calcium-induced slow motility of mammalian outer hair cells. *Hear Res* 110: 251–258, 1997.

131. Raphael Y, Altschuler RA. Structure and innervation of the cochlea. *Brain Res Bull* 60: 397–422, 2003.

132. Raybould NP, Jagger DJ, Kanjhan R, Greenwood D, Laslo P, Hoya N, Soeller C, Cannell MB, Housley GD. TRPC-like conductance mediates restoration of intracellular Ca^{2+} in cochlear outer hair cells in the guinea pig and rat. *J Physiol* 579: 101–113, 2007.

133. Ricci AJ, Crawford AC, Fettiplace R. Tonotopic variation in the conductance of the hair cell mechanotransducer channel. *Neuron* 40: 983–990, 2003.

134. Ricci AJ, Fettiplace R. Calcium permeation of the turtle hair cell mechanotransducer channel and its relation to the composition of endolymph. *J Physiol* 506: 159–173, 1998.

135. Ricci AJ, Fettiplace R. The effects of calcium buffering and cyclic AMP on mechano-electrical transduction in turtle auditory hair cells. *J Physiol* 501: 111–124, 1997.

136. Ricci AJ, Kennedy HJ, Crawford AC, Fettiplace R. The transduction channel filter in auditory hair cells. *J Neurosci* 25: 7831–7839, 2005.

137. Ricci AJ, Wu YC, Fettiplace R. The endogenous calcium buffer and the time course of transducer adaptation in auditory hair cells. *J Neurosci* 18: 8261–8277, 1998.

138. Roberts WM, Jacobs RA, Hudspeth AJ. Colocalization of ion channels involved in frequency selectivity and synaptic transmission at presynaptic active zones of hair cells. *J Neurosci* 10: 3664–3684, 1990.

139. Robles L, Ruggero MA. Mechanics of the mammalian cochlea. *Physiol Rev* 81: 1305–1352, 2001.

140. Safieddine S, Wenthold RJ. SNARE complex at the ribbon synapses of cochlear hair cells: analysis of synaptic vesicle- and synaptic membrane-associated proteins. *Eur J Neurosci* 11: 803–812, 1999.

141. Saito K. Fine structure of the sensory epithelium of guinea-pig organ of Corti: subsurface cisternae and lamellar bodies in the outer hair cells. *Cell Tissue Res* 229: 467–481, 1983.

142. Saito K. Fine structure of the sensory epithelium of the guinea pig organ of Corti: afferent and efferent synapses of hair cells. *J Ultrastruct Res* 71: 222–232, 1980.

143. Santos-Sacchi J, Song L, Zheng J, Nuttall AL. Control of mammalian cochlear amplification by chloride anions. *J Neurosci* 26: 3992–3998, 2006.

144. Scemes E, Giaume C. Astrocyte calcium waves: what they are and what they do. *Glia* 54: 716–725, 2006.

145. Schnee ME, Lawton DM, Furness DN, Benke TA, Ricci AJ. Auditory hair cell-afferent fiber synapses are specialized to operate at their best frequencies. *Neuron* 47: 243–254, 2005.

146. Schultz JM, Yang Y, Caride AJ, Filoteo AG, Penheiter AR, Lagziel A, Morell RJ, Mohiddin SA, Fananapazir L, Madeo AC, Penniston JT, Griffith AJ. Modification of human hearing loss by plasma-membrane calcium pump PMCA2. *N Engl J Med* 352: 1557–1564, 2005.

147. Shah DM, Freeman DM, Weiss TF. The osmotic response of the isolated, unfixed mouse tectorial membrane to isosmotic solutions: effect of Na^+, K^+, and Ca^{2+} concentration. *Hear Res* 87: 187–207, 1995.

148. Shen J, Harada N, Nakazawa H, Yamashita T. Involvement of the nitric oxide-cyclic GMP pathway and neuronal nitric oxide synthase in ATP-induced Ca^{2+} signalling in cochlear inner hair cells. *Eur J Neurosci* 21: 2912–2922, 2005.

149. Spicer SS, Thomopoulos GN, Schulte BA. Novel membranous structures in apical and basal compartments of inner hair cells. *J Comp Neurol* 409: 424–437, 1999.

150. Spray DC, Ye ZC, Ransom BR. Functional connexin "hemichannels": a critical appraisal. *Glia* 54: 758–773, 2006.

151. Stauffer EA, Scarborough JD, Hirono M, Miller ED, Shah K, Mercer JA, Holt JR, Gillespie PG. Fast adaptation in vestibular hair cells requires myosin-1c activity. *Neuron* 47: 541-553, 2005.

152. Street VA, McKee-Johnson JW, Fonseca RC, Tempel BL,. and Noben-Trauth K. *Mutations in a plasma membrane Ca2+-ATPase gene cause deafness in deafwaddler mice Nat Genet* 19: 390-394, 1998.

153. Sziklai I, Szonyi M, Dallos P. Phosphorylation mediates the influence of acetylcholine upon outer hair cell electromotility. *Acta Otolaryngol (Stockh)* 121: 153-156, 2001.

154. Taschenberger H, Leao RM, Rowland KC, Spirou GA,. and von Gersdorff H. *Optimizing synaptic architecture and efficiency for high-frequency transmission Neuron* 36: 1127-1143, 2002.

155. Teubner B, Michel V, Pesch J, Lautermann J, Cohen-Salmon M, Sohl G, Jahnke K, Winterhager E, Herberhold C, Hardelin JP, Petit C, Willecke K. Connexin30 (Gjb6)-deficiency causes severe hearing impairment and lack of endocochlear potential. *Hum Mol Genet* 12: 13-21, 2003.

156. Thorne PR, Housley GD. Purinergic signalling in sensory systems. *Semin Neurosci* 8: 233-246, 1996.

157. Thorne PR, Munoz DJ, Housley GD. Purinergic modulation of cochlear partition resistance and its effect on the endocochlear potential in the Guinea pig. *J Assoc Res Otolaryngol* 5: 58-65, 2004.

158. Tolomeo JA, Steele CR, Holley MC. Mechanical properties of the lateral cortex of mammalian auditory outer hair cells. *Biophys J* 71: 421-429, 1996.

159. Vlajkovic SM, Thorne PR, Housley GD, Munoz DJ, Kendrick IS. Ecto-nucleotidases terminate purinergic signalling in the cochlear endolymphatic compartment. *Neuroreport* 9: 1559-1565, 1998.

160. Wangemann P. K(+) cycling and its regulation in the cochlea and the vestibular labyrinth. *Audiol Neurootol* 7: 199-205, 2002.

161. Wangemann P. K+ cycling and the endocochlear potential. *Hear Res* 165: 1-9, 2002.

162. Wood JD, Muchinsky SJ, Filoteo AG, Penniston JT, Tempel BL. Low endolymph calcium concentrations in deafwaddler2J mice suggest that PMCA2 contributes to endolymph calcium maintenance. *J Assoc Res Otolaryngol* 5: 99-110, 2004.

163. Wu YC, Ricci AJ, Fettiplace R. Two components of transducer adaptation in auditory hair cells. *J Neurophysiol* 82: 2171-2181, 1999.

164. Wu YC, Tucker T, Fettiplace R. A theoretical study of calcium microdomains in turtle hair cells. *Biophys J* 71: 2256-2275, 1996.

165. Yamoah EN, Lumpkin EA, Dumont RA, Smith PJ, Hudspeth AJ, Gillespie PG. Plasma membrane Ca2+-ATPase extrudes Ca2+ from hair cell stereocilia. *J Neurosci* 18: 610-624, 1998.

166. Zhang M, Kalinec GM, Urrutia R, Billadeau DD, Kalinec F. ROCK-dependent and ROCK-independent control of cochlear outer hair cell electromotility. *J Biol Chem* 278: 35644-35650, 2003.

167. Zhang Y, Tang W, Ahmad S, Sipp JA, Chen P, Lin X. Gap junction-mediated intercellular biochemical coupling in cochlear supporting cells is required for normal cochlear functions. *Proc Natl Acad Sci USA* 102: 15201-15206, 2005.

168. Zidanic M, Brownell WE. Fine structure of the intracochlear potential field. *I The silent current Biophys J* 57: 1253-1268, 1990.

A functional study of plasma-membrane calcium-pump isoform 2 mutants causing digenic deafness

R. Ficarella*, F. Di Leva†, M. Bortolozzi‡, S. Ortolano‡, F. Donaudy*, M. Petrillo*, S. Melchionda§, A. Lelli‡, T. Domi†, L. Fedrizzi†, D. Lim‡, G. E. Shull¶, P. Gasparini*‖, M. Brini†**, F. Mammano‡**††, and E. Carafoli‡**

*Telethon Institute of Genetics and Medicine, 80131 Naples, Italy; Departments of †Biochemistry, Experimental Veterinary Sciences, and ††Physics, University of Padua, 35121 Padua, Italy; ‡Venetian Institute of Molecular Medicine, 35129 Padua, Italy; §Unit of Medical Genetics, Instituto di Ricovero e Cura a Carattere Scientifico, Casa Sollievo della Sofferenza, 71013 San Giovanni Rotondo, Italy; ¶Department of Molecular Genetics, University of Cincinnati, Cincinnati, OH 45221; and ‖Unit of Medical Genetics, Department of Reproductive Science and Development, Instituto di Ricovero e Cura a Carattere Scientifico-Burlo Garofalo, University of Trieste, 34127 Trieste, Italy

Communicated by Harald Reuter, University of Bern, Bern, Switzerland, November 13, 2006 (received for review September 20, 2006)

Ca^{2+} enters the stereocilia of hair cells through mechanoelectrical transduction channels opened by the deflection of the hair bundle and is exported back to endolymph by an unusual splicing isoform (*w/a*) of plasma-membrane calcium-pump isoform 2 (PMCA2). Ablation or missense mutations of the pump cause deafness, as described for the G283S mutation in the deafwaddler (*dfw*) mouse. A deafness-inducing missense mutation of PMCA2 (G293S) has been identified in a human family. The family also was screened for mutations in cadherin 23, which accentuated hearing loss in a previously described human family with a PMCA2 mutation. A T1999S substitution was detected in the cadherin 23 gene of the healthy father and affected son but not in that of the unaffected mother, who presented instead the PMCA2 mutation. The *w/a* isoform was overexpressed in CHO cells. At variance with the other PMCA2 isoforms, it became activated only marginally when exposed to a Ca^{2+} pulse. The G293S and G283S mutations delayed the dissipation of Ca^{2+} transients induced in CHO cells by $InsP_3$. In organotypic cultures, Ca^{2+} imaging of vestibular hair cells showed that the dissipation of stereociliary Ca^{2+} transients induced by Ca^{2+} uncaging was compromised in the *dfw* and PMCA2 knockout mice, as was the sensitivity of the mechanoelectrical transduction channels to hair bundle displacement in cochlear hair cells.

hereditary hearing loss | mutations | calcium homeostasis | calcium transport

The receptive organelle of sensory hair cells in the mammalian cochlea, the stereocilia bundle, protrudes from the cell's apical surface. Inner hair cells transduce mechanical vibrations into electrical signals that are eventually transmitted to the brain to be transformed into hearing signals (1), whereas outer hair cells (OHCs) (2) amplify the vibrations of the basilar membrane (3). Mechanical stimuli that are detected as excitatory deflect a hair bundle, thus increasing tension in the tip link, a filament stretched between the tops of stereocilia. This tension is conveyed to mechanosensitive transduction (MET) channels that open to allow ions into the cell (4). The apical surface of hair cells is bathed in endolymph, which is rich in K^+ but low in Na^+ and Ca^{2+} (5). K^+ carries most the transduction current, but MET channels are Ca^{2+} selective, i.e., Ca^{2+} influx is significant even at the low Ca^{2+} levels of the endolymph, which are much lower than those of other extracellular fluids (6–10): 20–23 μM in the rodent cochlea (11, 12), 200–250 μM in the vestibular system, possibly because of the presence there of calcium carbonate crystals (13, 14). Approximately 10% of the MET current may actually be carried by Ca^{2+} ions (15). Ca^{2+} entering through MET channels is rapidly sequestered by buffers in the stereocilia (16, 17) and is shuttled back to endolymph by the plasma membrane Ca^{2+} pump (PMCA) (18, 19), which is very concentrated in the stereocilia membrane ($\approx$2,000 per squared micrometer) (15, 19–21). The PMCA is assumed to increase Ca^{2+} in the immediate proximity of the hair bundle (19), possibly with the complicity of the acellular structures overlying the hair cells in the cochlea (22) and, particularly, in the vestibular system (14), where the pump also would contribute to the formation and maintenance of the otoconia (23).

Of the four basic isoforms of the PMCA pump,‡‡ two (PMCA1 and PMCA4) operate in all tissues and two (PMCA2 and PCMA3) operate in specialized tissues, such as muscle and, especially, brain (24, 25). All four isoforms display splice variants caused by the insertion of alternative exons at site A in the cytosolic loop connecting transmembrane domains 2 and 3 and at site C in the C-terminal tail of the pump. Alternative splicing is peculiarly complex in PMCA2 because it involves the insertion of up to three novel exons at site A and of two at site C. The A-site insertions are in-frame, creating variant *w* when three exons are inserted (the normal variant without site-A inserts is termed *z*). The insert at site C creates instead a novel stop codon, leading to the truncation of the pump (variants *a* and *b* being the normal full-length pump). The site-C insertions eliminate approximately half of the calmodulin binding domain; those at site A occur next to a domain that binds activatory acidic phospholipids, which, however, also bind to the calmodulin binding domain (26). As expected, the site-C insertions lower the affinity of PMCA pumps for calmodulin (27) but do not compromise the activation by acidic phospholipids, which is alternative to that by calmodulin (28). The site-A insertion, in contrast, could impair the activation by acidic phospholipids, particularly in the C-terminally truncated pump variants, in which the C-terminal phospholipid binding domain also is compromised.

Several splice variants of the four PMCAs have been detected in cochlear cDNAs (29), the C-terminally truncated PMCA2*a* being the only isoform detected in the stereocilia of hair cells (30). PMCA1*b* prevails instead in basolateral membranes. Recent work has shown that the truncated isoform in the stereocilia of OHCs is also spliced at site A and is thus the *w/a* variant (31). It is plausible

Author contributions: R.F., F.D.L., M. Bortolozzi, and S.O. contributed equally to this work; P.G., M. Brini, F.M., and E.C. designed research; R.F., F.D.L., M. Bortolozzi, S.O., F.D., M.P., S.M., A.L., T.D., L.F., and D.L. performed research; G.E.S. contributed new reagents/analytic tools; F.D.L., M. Bortolozzi, A.L., P.G., M. Brini, F.M., and E.C. analyzed data; and P.G., M. Brini, F.M., and E.C. wrote the paper.

The authors declare no conflict of interest.

Abbreviations: OHC, outer hair cell; MET, mechanosensitive transduction; PMCA, plasma-membrane Ca^{2+} pump; KO, knockout; P*n*, postnatal day *n*.

**To whom correspondence may be addressed. E-mail: marisa.brini@unipd.it, ernesto.carafoli@unipd.it, or fabio.mammano@unipd.

‡‡In this article, we have used the PMCA isoform nomenclature featuring only small italic letters because it has become the most widely accepted of the two existing nomenclatures and because it saves space.

This article contains supporting information online at www.pnas.org/cgi/content/full/0609775104/DC1.

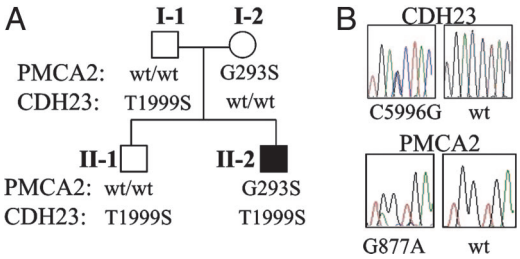

Fig. 1. Association of digenic mutations of PMCA2 and CDH23 with hearing loss. (*A*) Pedigree of an Italian family. Black symbols denote the family members affected. Genotypes of PMCA2 and CDH23 are indicated for each individual. (*B*) Representative chromatogram of CDH23 C5996G and PMCA2 G877A, respectively, which were identified from the family.

to assume that the choice of this unusual variant of the PMCA (32) was dictated by the special Ca^{2+} homeostasis demands of the ambient in which the pump must operate.

Mutations of PMCA2 have been recently shown to induce recessively inherited deafness (33). A G283S mutation replaced a conserved G [supporting information (SI) Fig. 5] downstream of the phospholipids binding domain of the pump (deafwaddler mouse, *dfw*). A mutation next to the active center (V586M) was later found to depress pump activity and to increase hearing loss in heterozygous patients that also carried a homozygous mutation in cadherin 23 (CDH23) (34). A mutation has now been identified in the human PMCA2 gene that replaces a conserved glycine residue (G293S) 10 residues downstream of the *dfw* mutation.

For the present work, the activity of the recombinant *w/a* variant of the PMCA2 pump was compared in the natural environment of model cells with the other variants of the pump and with the *dfw* pump and the pump carrying the G293S mutation. The *dfw* pump also has been studied biochemically and electrophysiologically in organotypic cultures of mice cochleae and utricles, and the results have been compared with those in WT mice and in mice in which the PMCA2 gene had been ablated (23).

Results

Genetic Analysis of the PMCA2 Mutation. A mutational screening of the PMCA2 gene (GenBank accession no. NM_001001331.1) on samples of 450 subjects coming from different countries identified a missense mutation associated with autosomal dominant hearing loss. The mutated allele was a G→A transition at position 877 in exon 5 of the nucleotide sequence, leading to the replacement of a highly conserved glycine with a serine at position 293 in the cytosolic loop connecting transmembrane domains 2 and 3 (the region in which the mutation G283S of *dfw* maps). The mutated allele was detected in an Italian patient affected by severe bilateral sensorineural hearing impairment without vestibular involvement. Two hundred chromosomes of individuals coming from the same geographical area of the patient were negative for the presence of the mutated allele. The G293S mutation was inherited from the mother who had normal hearing. The father and a brother of the patient, with normal hearing, were negative for the G293S mutation. Considering the recent finding of a contribution of the PMCA2 gene mutation as a modifier of the hearing loss phenotype (34), the whole family was analyzed for the presence of mutations in other genes that are also frequently involved in hereditary hearing loss: connexin 30 (GJB6), myosin 6 (MYO6), and CDH23; mitochondrial DNA was also screened. The screening on the CDH23 gene (GenBank accession no. NM_022124.2) has identified a T→S substitution at position 1999 (C5996G) in the affected son but not in the mother (Fig. 1). This mutated allele, which had already been described in a mutation database as a polymorphism, was inherited by the patient from his healthy father and also was present in the healthy brother (Fig. 1). Negative results were obtained for the other DNA sequences analyzed.

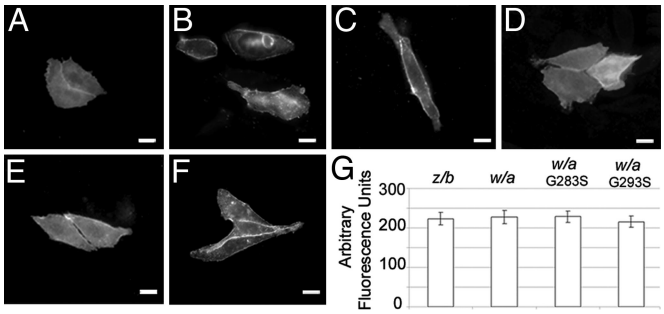

Fig. 2. Immunolocalization of recombinant PMCA2 variants and mutants in transiently transfected CHO cells. (*A–D*) PMCA2 variants *w/b* (*A*), *z/a* (*B*), *z/b* (*C*), and *w/a* (*D*). The interaction with antibody 5F10 was revealed by the Alexa Fluor 488-conjugated secondary antibody. (*E* and *F*) PMCA mutants on the *w/a* construct G283S (*E*) and G293S (*F*) were stained with antibody 2N, and the interaction was visualized by the Alexa Fluor 488-conjugated secondary antibody. The plasma membrane pattern of the overexpressed proteins in representative cells is shown. (*G*) The level of fluorescence in the plasma membrane was quantified as described in *Materials and Methods*. The SDs are indicated by the bars. Immunocytochemistry was performed as described in *Materials and Methods*. (Scale bars, 20 μm.)

Comparative Analysis of the Ca^{2+} Handling Activity of the Splice Variants of PMCA2 and of the Mice and Human Mutants. Mammalian expression plasmids for the *dfw* (G283S) and human (G293S) *w/a* mutants were generated and transfected in CHO cells. Expression plasmids were also prepared for the other PMCA2 splice isoforms *z/b*, *z/a*, *w/b*. Appropriate controls (Western blots and quantitative immunocytochemistry) established that all variants of the pump were expressed at equivalent levels and were correctly delivered to the plasma membrane (Fig. 2 and SI Fig. 6). The transfection routinely yielded 10–15% positive cells, of which 50% had a pure plasma-membrane targeting pattern, i.e., a clear signal at the cell surface (on which quantitative immunofluorescence was performed). In the remainder of the cell population both rim staining and endoplasmic reticulum expression patterns were visible. Because the PMCA units retained in the endoplasmic reticulum are normally inactive (35), they do not influence Ca^{2+} homeostasis. The percentage of cells with unambiguous plasma membrane pattern was obtained by counting hundreds of cells for each transfection experiment. CHO cells were cotransfected with the Ca^{2+}-sensitive photoprotein aequorin (36) and stimulated with ATP, an $InsP_3$-linked agonist that acts on P2Y purinergic receptors. Under the experimented conditions, the height of the Ca^{2+} transient generated by the opening of the $InsP_3$ receptor was controlled primarily by the PMCA pumps, not by the SERCA pump. In some experiments, the latter was silenced with the specific inhibitor 2,5-di-*tert*-butyl-1,4 benzohydroquinone, with marginal changes in the height of the Ca^{2+} peak and in the kinetics of the return of the traces to baseline. Evidently, the activity and/or amount of overexpressed PMCA pump overshadowed those of the native SERCA pump. The postpeak decay kinetics of the traces is expected to be influenced by Ca^{2+} influx through store-operated Ca channels. No efforts were made to eliminate their contribution to the shape of the Ca^{2+} curves because it was felt that the effects would have been the same for all pump variants.

The overexpression of the four splice variants of the pump affected the ability of the cells to handle Ca^{2+} (Fig. 3*A*). The lowering of the Ca^{2+} peak with respect to untransfected cells reflects the ability of the pump to respond with a burst of activation to the sudden arrival of a Ca^{2+} pulse. Two of the splice variants (*z/a* and *w/b*) had essentially the same effect on the Ca^{2+} peak of the

BIOCHEMISTRY

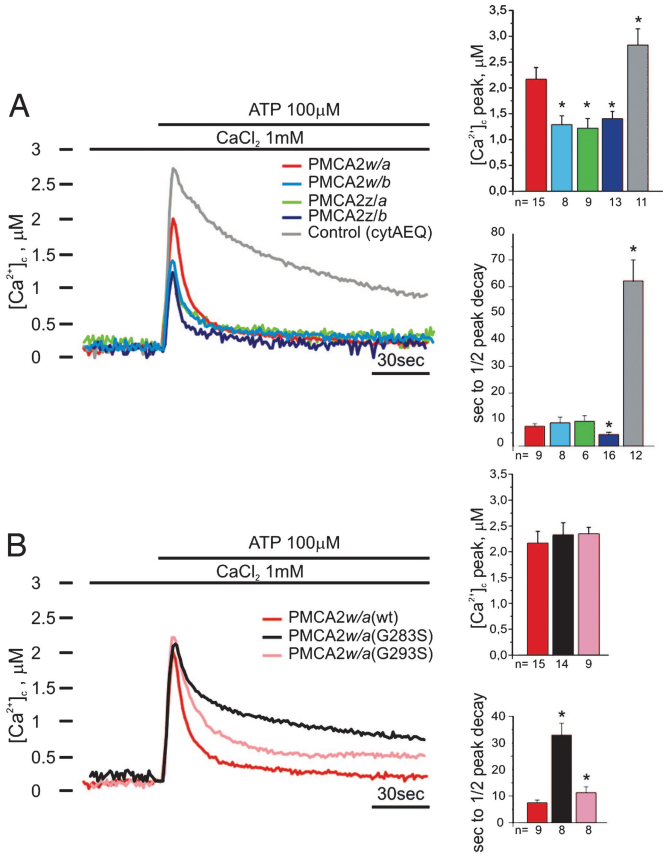

Fig. 3. Activity of recombinant PMCA2 isoforms (*A*) and of the mutated *w/a* isoforms (*B*) in CHO cells. CHO cells were transiently cotransfected with the PMCA2 variants and cytAEQ or with only cytAEQ (as a control). The cells were then perfused with KRB supplemented with $CaCl_2$ (1 mM). We used 100 μM ATP to produce a transient increase of $[Ca^{2+}]_c$. The histograms show the means ± SD of $[Ca^{2+}]_c$ peaks and of the half-peak decay times. The traces are representative of at least eight experiments. *, $P < 0.01$ calculated with respect to PMCA2*w/a*.

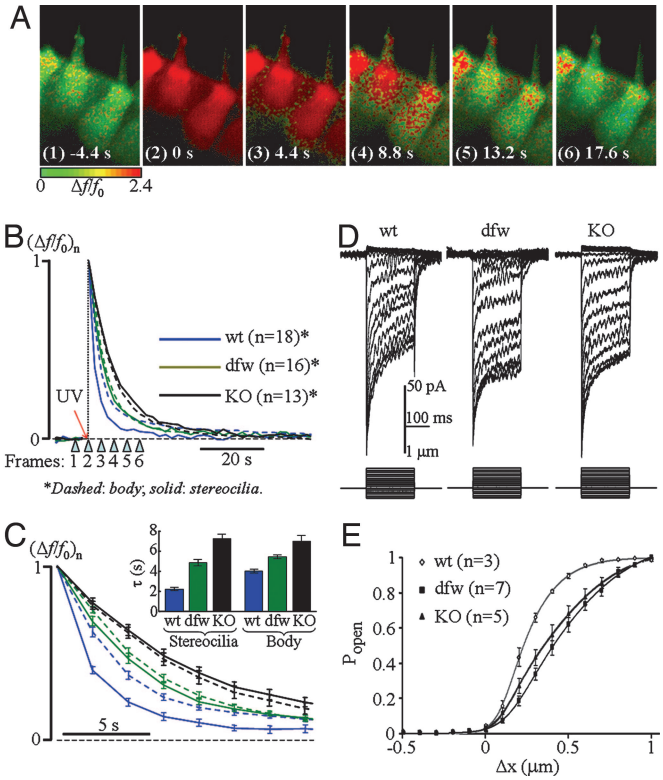

Fig. 4. Ca^{2+} extrusion and MET currents in hair cells of PMCA2 KO and *dfw* mice. (*A*) Time sequence of confocal images before and after UV photolysis of caged calcium in hair cells of an utricle culture (P2) from PMCA2 KO mice. Timing relative to the onset of the 100-ms UV light (375 nm) delivery is shown on each numbered frame. The example of Ca^{2+} concentration change was probed by the $\Delta f/f_0$ signal encoded by the color scale bar beneath frame 1. (*B*) Time course of normalized fluorescence ratio changes $(\Delta f/f_0)_n$ evoked by Ca^{2+} photoliberation. Each data point is averaged over $n > 13$ cells in two to four mice of each type, encoded by colored lines (solid lines, stereocilia; dashed lines, cell body excluding stereocilia) for WT controls (wt, blue traces), *dfw* (green traces), and PMCA2 KO (black traces) mice. The arrowheads below the time axis show the time of frame capture from *A*. (*C*) Same as *B* for the first 15 s after UV application. (*Inset*) Decay time constants τ were derived by a single-exponential fit. The ANOVA test gave $P < 10^{-4}$ and $P = 0.03$ for compatibility of stereociliary τ of WT *dfw* and *dfw* KO, respectively. (*D*) MET currents in OHCs for displacements of the tip of the hair bundle toward or away from the kinocilium. In the stimulus monitor shown at the bottom, positive steps indicate (excitatory) movements toward the highest stereocilia. Inward currents are given as negative relative to the current level in the absence of bundle stimulation at the holding potential, −80 mV. The high-frequency oscillations in the current traces were due to imperfectly cancelled environmental mechanical disturbances. Each response is the average of 10 presentations. (*E*) Plots of peak MET current versus displacement, Δx, of the tip of the hair bundle. Peak current was measured from records like those in *D* expressed as the difference in current relative to that obtained with a large negative displacement, where all transducer channels are assumed to be closed, and peak current was normalized to yield a measure of channel open probability (P_{open}, ordinates). Smooth curves are least-square fits calculated from $P_{open} = 1/(1 + e^{A2(X2-\Delta x)}\cdot(1 + e^{A1(X1-\Delta x)}))$, where A_1, A_2, X_1, and X_2 are fit parameters. For WT, $A_1 = 13.91 \pm 2.35\ \mu m^{-1}$, $A_2 = 7.17 \pm 0.77\ \mu m^{-1}$, $X_1 = 0.14 \pm 0.03\ \mu m$, and $X_2 = 0.20 \pm 0.02\ \mu m$; for *dfw*, $A_1 = 9.85 \pm 1.15\ \mu m^{-1}$, $A_2 = 3.99 \pm 0.43\ \mu m^{-1}$, $X_1 = 0.21 \pm 0.03\ \mu m$, and $X_2 = 0.43 \pm 0.01\ \mu m$; and for KO, $A_1 = 13.79 \pm 1.09\ \mu m^{-1}$, $A_2 = 4.34 \pm 0.19\ \mu m^{-1}$, $X_1 = 0.14 \pm 0.01\ \mu m$, and $X_2 = 0.37 \pm 0.01\ \mu m$.

full-length, nonspliced PMCA2*z/b*, which is a very active PMCA isoform (32) (see histograms on $[Ca^{2+}]_c$ peak in Fig. 3*A*). By contrast, the doubly spliced variant *w/a* was less able to control the peak height; i.e., it reacted less to the incoming Ca^{2+} pulse. However, when the function of the pump became the longer-term control of postpeak Ca^{2+}, i.e., when only nonactivated pumping was presumably required, all variants, including the *w/a*, became equivalent (the *z/b* was slightly more efficient; see histograms on half peak decay time in Fig. 3*A*). Fig. 3*B* shows the same type of experiment on the *dfw* (G283S) and human mutants (G293S), which were expressed in amounts equivalent to those of the other isoforms, and were correctly sorted to the plasma membrane (Fig. 2 and SI Fig. 6). The two mutant pumps were as ineffective as the WT *w/a* in lowering the Ca^{2+} peak (2.2 ± 0.2 μM, $n = 15$ for *w/a*; 2.3 ± 0.2 μM, $n = 14$ for *w/a* G283S; and 2.3 ± 0.1 μM, $n = 9$ for *w/a* G293S). Instead, the declining phase of the Ca^{2+} curve was much slower in the mutant pumps than in the WT *w/a* variant (half peak decay time: 32.9 ± 4.4 s, $n = 8$ for *w/a* G283S; 11.3 ± 2.3 s, $n = 8$ for *w/a* G293S; and 7.4 ± 1.0 s, $n = 9$ for the WT *w/a*). The defect was more pronounced in the *dfw* mutant than in the G293S mutant. The increased severity of the *dfw* mutation was made more evident when the mutations were introduced in the full-length PMCA2 variant (*z/b*). The Ca^{2+} handling defect became even more dramatic in the *dfw* mutant but was less evident in the G293S human mutation (see SI Fig. 7).

Ca^{2+} Homeostasis in the Hair Cells of Cultured Utricles of WT, PMCA2 Knockout (KO), and *dfw* Mice. To investigate pump activity *in situ*, confocal fluorescence imaging was performed on utricle organotypic cultures obtained from postnatal day P0 to P3 mice, observed between P1 and P4. Cultures were coloaded with the single

Table 1. Clearance rate of Ca^{2+} in stereocilia and body of OHCs in WT, *dfw*, and PMCA2 KO mice

Variable	Mouse	Stereocilia	Body
τ, s	WT	2.2 ± 0.2 (n = 18)	4.0 ± 0.3
	dfw	4.8 ± 0.6 (n = 16)	5.4 ± 0.3
	KO	7.2 ± 0.8 (n = 13)	7 ± 1
$(\Delta f/f_0)_{peak}$	WT	1.7 ± 0.2 (n = 18)	3 ± 0.3
	dfw	3.5 ± 0.6 (n = 16)	4 ± 0.4
	KO	2 ± 0.4 (n = 13)	2.3 ± 0.5

Data are shown as means ± SEM. The age of each mouse was between P1 and P4.

wavelength indicator fluo-4 and with *o*-nitrophenyl-EGTA, which released caged Ca^{2+} upon UV light illumination. After obtaining a reading for the baseline fluorescence of the indicator, UV exposure generated a uniform Ca^{2+} transient distributed over the whole cell, which was quantified as $\Delta f/f_0 = (f - f_0)/f_0$, where f is fluorescence at time t and f_0 is prestimulus fluorescence (Fig. 4*A*). In WT mice, the recovery to baseline Ca^{2+} was slightly but significantly ($P < 10^{-4}$) faster in the stereocilia (time constant τ = 2.2 ± 0.2 s, n = 18) than in the corresponding cell body (τ = 4.0 ± 0.3 s, n = 18) (Fig. 4 *B* and *C*, solid and dashed lines for stereocilia and cell body, respectively). This result shows that stereocilia are Ca^{2+} microdomains (17) in which Ca^{2+} gradients generated during mechanotransduction (9) are dissipated independently from the cell body (18). τ was significantly larger in *dfw* than in WT and, particularly, in PMCA2 KO mice. The results in Fig. 4*C Inset* and Table 1 show that ablation of PMCA2, or impairment of its activity, decreased the Ca^{2+} clearing rate of the stereocilia, making it similar to the slower rate of cell soma.

MET Currents in OHCs of WT, PMCA2 KO, and *dfw* Mice. Hair cells detect vibrations of atomic dimensions of the order of 0.2 nm (37) [in the mouse cochlea, their operating range is ≈500 nm (38)]. To assay transduction, organotypic cochlear cultures from P0–P3 mice were studied between P1 and P4 (for details, see *Materials and Methods*). The amplitude and kinetics of the currents in PMCA2 KO and *dfw* mice were qualitatively similar to those of WT controls (Fig. 4*D*). However, the curves relating bundle displacement (X) to channel opening probability, P_{open} (X), in *dfw* and PMCA2 KO mice were shifted positively with respect to controls (Fig. 4*E*). The shift was more pronounced in the KO mice (175 nm) than in the *dfw* mice (117 nm). These results are consistent with those obtained with vanadate, which blocks Ca^{2+} extrusion in auditory hair cells (39) and induces a similar (≈200 nm) shift in the P_{open} (X) curve (40).

Discussion

A number of genes and proteins have been associated with hereditary hearing loss, the most common sensory deficit in humans (41). As discussed in the Introduction, a recent addition to the list is *Atpb2*, encoding the PMCA2 pump, which is specifically expressed in the stereocilia of hair cells. Isoform 2 of the PMCA pump has properties that distinguish it from other PMCA isoforms: When tested in the cellular environment, it is two to three times more active than the two ubiquitous pumps in pumping Ca^{2+} out of the cell (32). In the isolated state, it shows very high calmodulin affinity (K_d, 2–4 nM) (27); i.e., it becomes fully activated under conditions (e.g., calmodulin and/or Ca^{2+} concentration) that would very poorly activate isoforms 1 and 4. PMCA2 also has peculiarly high activity in the absence of activators (42). But the property that distinguishes PMCA2 most clearly is the complexity of alternative splicing. The stereocilia of the OHCs contain a splice variant (*w/a*) that has high basal Ca^{2+} ejection activity but fails to respond with rapid activation to the sudden arrival of a Ca^{2+} load. As mentioned above, these properties evidently satisfy the Ca^{2+} homeostasis demands of the endolymph and of the stereocilia. Even if Ca^{2+} in the endolymph is very low, the recently measured value of 23 μM (12) is considerably higher than that necessary for the integrity of the tip links, which is compromised only below 1 μM Ca^{2+} (43). In fact, even the inactivating *dfw* mutation lowers the endolymph Ca^{2+} concentration only to ≈6 μM (12). However, a number of *in vitro* studies have shown that the generation of MET currents, for instance, in chickens, requires a minimum of 20 μM extracellular Ca^{2+} and is not elicited at 10 μM (7). Other studies have shown that MET currents require a minimum of 10 μM external Ca^{2+} in bullfrog (6), and adaptation, the process by which hair cells continuously readjust their sensitivity to the ciliary bundle displacements (44, 45), is slowed when extracellular Ca^{2+} is reduced (15, 19, 46, 47).

Within the stereocilia, the control of Ca^{2+} is vital to a number of aspects of the mechanotransduction process, e.g., the regulation of adaptation (44, 45), the ability to sense the deflection of the ciliary bundle with high sensitivity (37), and the breaking and regeneration of tip links (48). As mentioned above, these peculiar functions of the Ca^{2+} signal have in all likelihood dictated the choice of the PMCA2*w/a* isoform. Because resting stereociliary Ca^{2+} is very low (9, 18), it makes sense to control it with a pump variant that decreases Ca^{2+} to lower concentrations than other isoforms (27), even if it is insensitive to calmodulin (and, presumably, to acidic phospholipids). The relative insensitivity of the *w/a* pump to calmodulin makes good sense, given that its very high concentration in the stereocilia (70 μM) (49) would produce permanent maximal activation of pump isoforms normally sensitive to it. A comment would also be in order on CDH23, which binds harmonin, an F-actin bundling protein that may anchor it to the actin core of the stereocilia (50). Harmonin also binds myosin VIIa, suggesting a role for the complex harmonin–myosin VIIa, CDH23, in the cohesion of the stereocilia (50). Whether the tripolar complex has any role in the function of PMCA2 is an open question.

The study has shown that the function compromised in the mutated pumps is not the ability to respond to a sudden demand of hyperactivity, which is about the same in the WT *w/a* variant, but the special ability to operate efficiently at the nonactivated level. The mutations impair the longer-term export of Ca^{2+}, in agreement with the measurements of endolymphatic Ca^{2+} levels in the *dfw* mouse model (12), but endolymphatic Ca^{2+} also influences stereociliary Ca^{2+}. By controlling the multiple phases of adaptation, Ca^{2+} influx contributes to setting the resting position of the hair bundle and thus influences the fraction of MET channels open at rest. By increasing Ca^{2+} near the stereocilia tips, the pump augments the probability of blocking MET channels and increases the rate of adaptation. Conversely, lowering Ca^{2+} would reduce the rate of adaptation and increase open probability and channel unitary conductance (51). Even if the low Ca^{2+} levels in *dfw* endolymph preserve tip links (43), under these conditions MET channels will become biased toward the full open state. OHCs containing mutated pumps would therefore become insensitive to bundle displacements, and MET currents would be replaced by a large standing current that would permanently depolarize the cells' state. Eventually, Ca^{2+} loading via voltage-gated channels in the basolateral membrane and/or excitotoxic effects would doom OHCs. In the vestibular system, the cell fate may be delayed, albeit only temporarily, by the Ca^{2+} buffering action of the otoconia.

Materials and Methods

Genetic Analysis of Human PMCA Mutations. More than 400 subjects were analyzed for mutations in the PMCA2*a* gene. The inclusion criteria were (*i*) absence of the most common mutations within the GJB2 gene, (*ii*) sensorineural hearing loss, and (*iii*) normal tympanometric evaluation. In all cases, vestibular data were obtained by clinical examination and routine vestibular tests (one or more of the following: caloric, rotatory, optokinetic, swinging torsion, statokinesimetric, and vestibulo-vegetative). The series includes cases

with a variable degree of hearing loss, ranging from mild to profound and with age onset varying from congenital to late onset. Familial records were available in most cases. The majority of patients came from Central and Southern Italy (200), 140 were from Spain, and 54 were from Belgium. After informed consent, peripheral blood was obtained, and DNA was isolated from blood leukocytes according to standard methods. Fifty primer pairs were designed to amplify the 22 coding exons of the PMCA2 gene, including the splice sites and 5′ UTR and 3′ UTR regions. Moreover, 128 primer pairs were designed to amplify 67 coding exons, including the splice site of the CDH23 gene (PCR primer sequences and conditions are available upon request). All amplicons were screened by denaturing HPLC on a WAVE Nucleic Acid Fragment Analysis System HSM (Transgenomic, Omaha, NE) according to the supplier's protocols. Denaturing HPLC data analysis was based on a subjective comparison of sample and reference chromatograms. PCR products showing an abnormal chromatographic profile were directly sequenced on an automated sequencer (ABI 3100; Perkin–Elmer, Wellesley, MA).

Cloning and Expression of PMCA2 Isoforms and of Mutants G283S and G293S. Site-directed mutagenesis was carried out to obtain mutants cloned in the appropriate vector. Both PMCA2*w/a* and PMCA2*z/b* were used as targets, and experiments were performed according to the manufacturer's standard protocol (Stratagene, Cedar Creek, TX). The following primers were used: G283S, tgaactctcagactagcatcatctttacc (forward) and ggtaaagatgatgctagtctgagagttca (reverse); G293S, cctcctgggggctggtagtgaagaggaagagaa (forward) and ttctcttcctcttcactaccagcccccaggagg (reverse).

Immunolocalization of the Expressed Pumps. CHO cells were grown in Ham's F12 medium supplemented with 10% FCS. Before transfection, the cells were seeded onto 13-mm glass coverslips and allowed to grow to 50% of confluence. Transfection with 3 μg of plasmid DNA (or 1.5:1.5 μg in the case of cotransfection) was carried out with a Ca-phosphate procedure (52).

Thirty-six hours after transfection, CHO cells were processed for immunofluorescence. The cells were washed twice with PBS (140 mM NaCl/2 mM KCl/1.5 mM KH_2PO_4/8 mM Na_2HPO_4, pH 7.4), fixed for 20 min in 3.7% formaldehyde, washed three times with PBS, and then incubated for 10 min in PBS supplemented with 50 mM NH_4Cl. The cells were then permeabilized in 0.1% Triton X-100 in PBS, followed by a 1-h wash with 1% gelatin (type IV, from calf skin) in PBS. Cells were then incubated for 1 h at 37°C in a wet chamber with polyclonal isoform-specific PMCA antibody 2N (Affinity BioReagents, Golden, CO) or a monoclonal antibody recognizing all pump isoforms (5F10; Affinity BioReagents) at a 1:100 dilution in PBS. Staining was carried out with Alexa Fluor 488-labeled anti-rabbit or anti-mouse secondary antibodies (Molecular Probes, Carlsbad, CA) at a 1:50 dilution in PBS. After each incubation, cells were washed four times with PBS. Fluorescence was analyzed with an Axiovert microscope (Zeiss, Oberkochen, Germany) equipped with an AxioCam HRm camera (Zeiss). Images were acquired with AxioVision vs30 software (Zeiss).

Membrane Fluorescence Computation. Immunocytochemistry was performed to quantify the expressed pump proteins in the plasma membrane of transfected cells. CHO cells transfected with the constructs expressing the PMCA2 variants and mutants were stained with the 2N antibody. Cells were imaged on a spinning disk confocal microscope (Ultraview; Perkin–Elmer) by using a ×60 oil-immersion objective at a 1.4 N.A. (PlanApo; Nikon, Tokyo, Japan). Regions of interest were selected by applying an edge-finding (Sobel) digital filter, thus limiting the analysis to plasma membrane areas. The total fluorescence intensity in membrane-delimiting regions of interest was quantified with software developed in our laboratory. For each construct, fluorescence was averaged over a total of 50 cells in three different slides.

Ca^{2+} Measurements with Recombinant Aequorin. Transfected cytAEQ was reconstituted by incubating CHO cells for 1–3 h with 5 μM coelenterazine in DMEM supplemented with 1% FCS at 37°C in a 5% CO_2 atmosphere. Additions to the KRB medium (1 mM $CaCl_2$/100 μM ATP) were made as specified in the figure legends. The experiments were terminated by lysing the cells with 100 μM digitonin in a hypotonic Ca^{2+}-rich solution (10 mM $CaCl_2$ in H_2O) to discharge the remaining aequorin pool. Briefly, a 13-mm round coverslip with the transfected cells was placed in a perfused thermostated chamber in close proximity to a low-noise photomultiplier, with a built-in amplifier discriminator. The output of the discriminator was captured by a Thorn-EMI photon-counting board and stored in an IBM-compatible computer for further analyses. Luminescence was calibrated off-line into $[Ca^{2+}]$ values by using a computer algorithm based on the Ca^{2+} response curve of WT aequorin (36).

Data are reported as means ± SD. Statistical differences were evaluated by Student's two-tailed *t* test for unpaired samples. A *P* value of <0.01 was considered statistically significant.

Organotypic Cultures of Utricles and Cochleae. Sensory epithelia of utricle or cochleae were excised from PMCA2 KO, *dfw*, or WT mice. Organs were dissected from mice between P1 and P4. The care and use of the animals were approved by the Animal Care and Use Committee of the University of Padua. The otic capsule was opened medially, and the endolymphatic compartment of the utricle was cut open. The otolithic membrane was removed after 15 min of incubation in dissection saline to which 0.1 g/liter bacterial subtilisin protease (type XXIV; Sigma–Aldrich, St. Louis, MO) had been added. Dissection saline was composed of Hank's balanced salt solution (HBSS, catalog no. H6648; Sigma–Aldrich) with 10 mM Hepes, 10.000 units/liter penicillin and 25 μg/liter fungizone. HBSS contained 0.4 g/liter KCl, 0.06 g/liter KH_2PO_4 (anhydrous), 0.35 g/liter $NaHCO_3$, 8.0 g/liter NaCl, 0.048 g/liter Na_2HPO_4 (anhydrous), and 1 g/liter D-glucose. The cultures were preserved for 1 day at 37°C in a complete medium of 95% DMEM/Ham's F-12 (1:1) (1×, liquid, with L-glutamine, without Hepes; GIBCO, Carlsbad, CA) and 5% FBS.

Fluorescence Imaging and UV Photolysis of Caged Ca^{2+}. To obtain images of the hair cell along its main axis, the utricle epithelium was fixed at culture time by Cell-Tak (mixed to 90% $NaHCO_3$; BD Biosciences, Bedford, MA) to the lateral side of a glass ball (≈2 mm in diameter) that was previously glued to a microscope slide by a small drop of Sylgard Silicon Elastomer (Dow Corning, Wiesbaden, Germany). At recording time, cultures were loaded with 10 μM cell-permeant Fluo-4 for 50 min at 37°C in DMEM (Invitrogen) supplemented with 10 μM cell-permeant *o*-nitrophenyl-EGTA AM (Invitrogen), 25 μM sulfinpyrazone and Pluronic F-127 (0.1% wt/vol). For deesterification, cultures were transferred to a chamber mounted on the stage of a confocal imaging setup [a Radiance 2100 (Bio-Rad, Hercules, CA) incorporating a Nikon Eclipse E600FN microscope] and superfused for 20 min with a medium composed of HBSS supplemented with 4.4 g/liter glucose and 2 mM anhydrous $CaCl_2$ (pH 7.4, Osm 330). Experiments were performed with a ×100 water-immersion objective with a N.A. of 1.00 (LUMPlanFl; Olympus, Tokyo, Japan). Fluo-4 fluorescence was excited by the 488-nm line of an argon laser coupled by fiber optics to the microscope. Fluorescence emission was selected ≈528 nm by using a narrow-band interference filter (D528/50m; Chroma Technology, Brattleboro, VT). A rapid increase in cytosolic Ca^{2+} was achieved by photorelease of Ca^{2+} from the caged state (*o*-nitrophenyl-EGTA bound to Ca^{2+}). The UV illumination for uncaging covered an area of ≈5,000 μm^2, comprising a few hair cells, and was generated by a 375-nm laser (an LCDU12/7342 at a maximum power of 8 mW; Power Technology, Little Rock, AR) connected to the microscope through a 600-μm-diameter optical fiber. Fiber output was placed in the focal plane of a UV-

transparent positive lens, and the recollimated light beam was reflected off of a 400 DCLP dichromatic beam splitter (Chroma) positioned at 45° just above the microscope objective lens. UV light, controlled by a transistor–transistor logic signal generated by the Bio-Rad 2100 at the end of each frame, was delivered for 50–100 ms during the scanning pause (≈1 s) between the 15th and 16th frames. Images were acquired with a resolution of 512 × 512 pixels by scanning at 512 lines per second under control of Bio-Rad Laser Sharp software. All data were analyzed offline on a personal computer with the Matlab 7.0 (MathWorks, Natick, MA) software environment.

Mechanical Stimulation of Hair Cells. Experiments were performed on OHC of the first row of the mid-apical turn of the organ of Corti. Bundles were deflected with a stiff glass pipette mounted on a piezoelectric bimorph with submillisecond rise times (10–90%) in response to prefiltered (1 kHz) square command steps supplied by the A/D-D/A interface (Digidata 1322; Axon Instruments, Foster City, CA). The tip of the pipette was fire-polished to fit the V-shape of the hair cell stereocilia bundle.

Electrophysiological Recordings on Hair Cells. The sensory epithelium was transferred to an experimental chamber placed on the stage of an upright microscope (Olympus BX51W) equipped with differential interference contrast optics and viewed with the LumPlanFL ×100 water objective. Extracellular solutions were continuously superfused at 5 ml/min with a medium containing 144 mM NaCl, 0.7 mM NaH_2PO4, 5.8 mM KCl, 1.3 mM $CaCl_2$, 0.9 mM $MgCl_2$, 5.6 mM D-glucose, and 10 mM Hepes-NaOH (adjusted to pH 7.4). The recording pipettes contained a standard intracellular solution that included 140 mM KCl, 0.5 mM EGTA-KOH, 3.5 mM $MgCl_2$, 2.5 mM MgATP, and 5 mM Hepes-KOH (pH 7.4). The recording pipettes were pulled with resistances of 3–5 MΩ from R-6 soda lime glass (Garner Glass, Claremont, CA) and had series resistance of 8–12 MΩ when sealed to cells. Recordings were made from hair cells in the intact epithelium in the whole-cell, tight-seal mode of the patch-clamp technique by using an Axopatch 200B patch-clamp amplifier (Axon Instruments). Transduction (MET) currents were recorded from cells held at −80 mV, filtered at 1 kHz with an 8-pole Bessel filter (Axon Instruments), digitized at 4 kHz with a 12-bit acquisition board (Digidata 1322) and pClamp 9.2 software (both from Axon Instruments), and stored on a hard disk.

We thank Ms. Sabrina Facciolo for skilled technical assistance and Dr. E. E. Strehler (Mayo Clinic, Rochester, MN) for the donation of PMCA2 clones. This work was supported by the European Union FP6 Integrated Project EUROHEAR, LSHG-CT-20054-512063 (to F.M. and E.C.), Telethon Foundation Project GGP04169 (to M. Brini and F.M.), and the Italian Ministry of University and Research (Project of Key National Research 2005 to M. Brini and Fund for Basic Research 2001 to E.C.).

1. Fuchs PA (2005) *J Physiol* 566:7–12.
2. Lim DJ (1986) *Hear Res* 22:117–146.
3. Fettiplace R, Hackney CM (2006) *Nat Rev Neurosci* 7:19–29.
4. Corey DP, Sotomayor M (2004) *Nature* 428:901–903.
5. Anniko M, Wroblewski R (1986) *Hear Res* 22:279–293.
6. Corey DP, Hudspeth AJ (1979) *Nature* 281:675–677.
7. Ohmori H (1985) *J Physiol* 359:189–217.
8. Lumpkin EA, Marquis RE, Hudspeth AJ (1997) *Proc Natl Acad Sci USA* 94:10997–11002.
9. Denk W, Holt JR, Shepherd GM, Corey DP (1995) *Neuron* 15:1311–1321.
10. Jorgensen F, Kroese AB (1995) *Acta Physiol Scand* 155:363–376.
11. Bosher SK, Warren RL (1978) *Nature* 273:377–378.
12. Wood JD, Muchinsky SJ, Filoteo AG, Penniston JT, Tempel BL (2004) *J Assoc Res Otolaryngol* 5:99–110.
13. Corey DP, Hudspeth AJ (1983) *J Neurosci* 3:962–976.
14. Marquis RE, Hudspeth AJ (1997) *Proc Natl Acad Sci USA* 94:11923–11928.
15. Ricci AJ, Fettiplace R (1998) *J Physiol* 506:159–173.
16. Hackney CM, Mahendrasingam S, Penn A, Fettiplace R (2005) *J Neurosci* 25:7867–7875.
17. Ricci AJ, Wu YC, Fettiplace R (1998) *J Neurosci* 18:8261–8277.
18. Lumpkin EA, Hudspeth AJ (1998) *J Neurosci* 18:6300–6318.
19. Yamoah EN, Lumpkin EA, Dumont RA, Smith PJ, Hudspeth AJ, Gillespie PG (1998) *J Neurosci* 18:610–624.
20. Crouch JJ, Schulte BA (1995) *Hear Res* 92:112–119.
21. Wu YC, Tucker T, Fettiplace R (1996) *Biophys J* 71:2256–2275.
22. Shah DM, Freeman DM, Weiss TF (1995) *Hear Res* 87:187–207.
23. Kozel PJ, Friedman RA, Erway LC, Yamoah EN, Liu LH, Riddle T, Duffy JJ, Doetschman T, Miller ML, Cardell EL, Shull GE (1998) *J Biol Chem* 273:18693–18696.
24. Carafoli E, Santella L, Branca D, Brini M (2001) *Crit Rev Biochem Mol Biol* 36:107–260.
25. Guerini D, Coletto L, Carafoli E (2005) *Cell Calcium* 38:281–289.
26. Brodin P, Falchetto R, Vorherr T, Carafoli E (1992) *Eur J Biochem* 204:939–946.
27. Elwess NL, Filoteo AG, Enyedi A, Penniston JT (1997) *J Biol Chem* 272:17981–17986.
28. Niggli V, Adunyah ES, Penniston JT, Carafoli E (1981) *J Biol Chem* 256:395–401.
29. Crouch JJ, Schulte BA (1996) *Hear Res* 101:55–61.
30. Dumont RA, Lins U, Filoteo AG, Penniston JT, Kachar B, Gillespie PG (2001) *J Neurosci* 21:5066–5078.
31. Hill JK, Williams DE, LeMasurier M, Dumont RA, Strehler EE, Gillespie PG (2006) *J Neurosci* 26:6172–6180.
32. Brini M, Coletto L, Pierobon N, Kraev N, Guerini D, Carafoli E (2003) *J Biol Chem* 278:24500–24508.
33. Street VA, McKee-Johnson JW, Fonseca RC, Tempel BL, Noben-Trauth K (1998) *Nat Genet* 19:390–394.
34. Schultz JM, Yang Y, Caride AJ, Filoteo AG, Penheiter AR, Lagziel A, Morell RJ, Mohiddin SA, Fananapazir L, Madeo AC, Penniston JT, Griffith AJ (2005) *N Engl J Med* 352:1557–1564.
35. Brini M, Bano D, Manni S, Rizzuto R, Carafoli E (2000) *EMBO J* 19:4926–4935.
36. Brini M, Marsault R, Bastianutto C, Alvarez J, Pozzan T, Rizzuto R (1995) *J Biol Chem* 270:9896–9903.
37. Fettiplace R, Ricci AJ (2006) in *Vertebrate Hair Cells*, eds Eatock RA, Fay RR, Popper AN (Springer, New York), Vol 27, pp 154–203.
38. Beurg M, Evans MG, Hackney CM, Fettiplace R (2006) *J Neurosci* 26:10992–11000.
39. Tucker T, Fettiplace R (1995) *Neuron* 15:1323–1335.
40. Wu YC, Ricci AJ, Fettiplace R (1999) *J Neurophysiol* 82:2171–2181.
41. Petit C (2006) *Trends Mol Med* 12:57–64.
42. Hilfiker H, Guerini D, Carafoli E (1994) *J Biol Chem* 269:26178–26183.
43. Assad JA, Shepherd GM, Corey DP (1991) *Neuron* 7:985–994.
44. Gillespie PG, Cyr JL (2004) *Annu Rev Physiol* 66:521–545.
45. Fettiplace R, Ricci AJ (2003) *Curr Opin Neurobiol* 13:446–451.
46. Assad JA, Hacohen N, Corey DP (1989) *Proc Natl Acad Sci USA* 86:2918–2922.
47. Eatock RA, Corey DP, Hudspeth AJ (1987) *J Neurosci* 7:2821–2836.
48. Zhao Y, Yamoah EN, Gillespie PG (1996) *Proc Natl Acad Sci USA* 93:15469–15474.
49. Walker RG, Hudspeth AJ, Gillespie PG (1993) *Proc Natl Acad Sci USA* 90:2807–2811.
50. Boeda B, El-Amraoui A, Bahloul A, Goodyear R, Daviet L, Blanchard S, Perfettini I, Fath KR, Shorte S, Reiners J, *et al*. (2002) *EMBO J* 21:6689–6699.
51. Ricci AJ, Crawford AC, Fettiplace R (2003) *Neuron* 40:983–990.
52. Rizzuto R, Brini M, Bastianutto C, Marsault R, Pozzan T (1995) *Methods Enzymol* 260:417–428.

The novel mouse mutation *Oblivion* inactivates the PMCA2 pump and causes progressive hearing loss

Sarah L Spiden[1,2 #], Mario Bortolozzi[3 #], Francesca Di Leva[4 #], Martin Hrabé de Angelis[5], Helmut Fuchs[5] , Dmitry Lim[3], Saida Ortolano[3], Neil J. Ingham[1], Marisa Brini[4*], Ernesto Carafoli[3*], Fabio Mammano[3,6*] and Karen P Steel[1,2*]

1. Wellcome Trust Sanger Institute, Genome Campus, Hinxton, Cambridge, CB10 1SA, UK.
2. MRC Institute of Hearing Research, University Park, Nottingham, NG7 2RD, UK.
3. Venetian Institute of Molecular Medicine (VIMM), Padua, Italy
4. Department of Biochemistry and Department of Experimental Veterinary Sciences, University of Padua, Padua, Italy
5. Helmholtz Zentrum München, GmbH, Institute of Experimental Genetics, Neuherberg, Germany.
6. Department of Physics, University of Padua, Padua, Italy

#The authors wish it to be known that the first 3 authors (Spiden, Bortolozzi & Di Leva) should be regarded as joint first auhors.
*Joint senior authors.

Correspondence should be addressed to Professor. Karen .P. Steel, Wellcome Trust Sanger Institute, Genome Campus, Hinxton, Cambridge CB10 1SA, UK.
Tel: (44) 1223 495379. Fax: (44) 1223 494840. E-mail: kps@sanger.ac.uk

Abstract

We have characterised a new dominantly-inherited mouse mutant, Oblivion (*Obl*), generated by *N*-ethyl-*N*-nitrosourea (ENU) mutagenesis, which may prove useful as an animal model for progressive hearing loss in humans. *Obl*/+ mutants showed hearing impairment with increasing severity from post-natal day (P)20 to P90, and loss of auditory function was followed by a corresponding base to apex progression of hair cell degeneration. *Obl/Obl* mutants were small, showed severe vestibular dysfunction by 2 weeks of age and were completely deaf from birth; sensory hair cells were completely degenerate in the basal turn of the cochlea, although hair cells appeared normal in the apex. We mapped the mutation to chromosome 6. Mutation analysis of *Atp2b2*, a candidate gene, showed a missense mutation (2630C→T) in exon 15, causing a serine to phenylalanine substitution (S877F) in transmembrane domain 6 of the PMCA2 pump, the resident Ca^{2+} pump of hair cell stereocilia. Transmembrane domain mutations in these pumps generally are believed to be incompatible with normal targeting of the protein to the plasma membrane. However, analyses of hair cells in cultured utricular maculae of *Obl/Obl* mice and of the mutant *Obl* pump in model cells showed that the protein was correctly targeted to the plasma membrane. Biochemical and biophysical characterisation showed that the pump had an impaired Ca^{2+} exporting function.

Introduction

PMCA2 is one of four isoforms of the plasma membrane Ca^{2+} pumps of mammalian cells (1); (2). The expression of PMCA2 and PMCA3 is largely restricted to brain and muscle, whereas PMCA1 and 4 are ubiquitously expressed. PMCA2 and PMCA3 are more active in exporting Ca^{2+} than the ubiquitous isoforms (3), probably due to their higher affinity for the activator calmodulin. PMCA2, however, is peculiar in its very high activity even in the absence of calmodulin (4); (5). In the ear, PMCA2 is expressed at high levels in outer hair cell stereocilia and apical membranes and at moderate levels in inner hair cell stereocilia and in the spiral ganglion (6); (7); (8); (9); (10). It actively extrudes Ca^{2+} that has entered the hair cell during mechanoelectrical transduction (11). This maintains the low intracellular levels of Ca^{2+} and may create a relatively higher concentration of Ca^{2+} in the endolymph surrounding the stereocilia, contributing to the maintenance of the electrochemical gradient needed for transduction to occur (11). Bulk concentration of Ca^{2+} in mammalian cochlear endolymph is estimated at ~20 μM (12). PMCA2 is also important in maintaining sufficient extracellular Ca^{2+} in the vestibular system for the formation of the otoconia, the calcium carbonate crystals needed for sensing gravity and acceleration (13).

Transcripts for PMCA2 undergo alternative splicing at two sites. Site A is closer to the N-terminus and site C closer to the C-terminus. In the PMCA2 variant expressed in stereocilia (14); (15), the splicing introduces three exons at site A, generating variant *w*, and two novel exons at site C, generating variant *a*. The C-site insert leads to a truncated pump that contains only about half of the original calmodulin binding domain (5); (4). The doubly inserted *w/a* variant, seen in stereocilia, has an unusually limited

ability to increase activity rapidly when challenged with a Ca^{2+} pulse, but has about the same high non-stimulated activity as the full-length *z/b* variant (16).

The Oblivion (*Obl*) mutant was identified as a new mouse mutant with progressive hearing loss from a large scale ENU mutagenesis screen (17). The aim of this screen is to provide new models for deafness, especially progressive deafness which is common in the human population, and to identify the genes and underlying pathology in these new mutants. Here we report that the progressive hearing loss in *Obl*, which may be a good model for the human condition 3sp- syndrome, is due to a missense mutation in the gene *Atp2b2,* encoding PMCA2. We describe the hearing impairment and hair cell pathology in the mutants, the dysfunction of Ca^{2+} export by the mutated PMCA2 pump cloned and overexpressed in model cells and in cultures of utricles from the mutant mice.

Results

Progressive hearing loss in Oblivion mutants

Obl/+ heterozygotes have a normal Preyer reflex at one month old, but by two months only 58% offspring from *Obl*/+ x +/+ matings showed a Preyer reflex (Supplementary Table I), suggesting progressive hearing loss in *Obl*/+ mice. No vestibular defect, indicated by head-tossing or circling behaviour, was seen in these heterozygotes, although no detailed analysis of vestibular function was performed.

To measure auditory thresholds, auditory brainstem responses (ABR), a reflection of cochlear and brainstem neural activity, were recorded in P20, P59-62 and P89-91 mice (Figure 1). ABRs of wild-type mice showed an improvement in thresholds below 12kHz from P20 to P59-62, perhaps indicative of maturation of the auditory system. From P20 to P89-91, wild type mice showed mild and progressive elevations of thresholds above 12kHz.

Obl/+ mice demonstrated a severe and age-related progressive hearing loss. *Obl*/+ mice showed significantly raised thresholds at all frequencies, compared to age-matched wild-type controls (t-test, $p<0.05$), of up to 60-70dB or more. In contrast to the Preyer reflex tests, even at P20, *Obl*/+ showed large threshold elevations. At P59-62, the heterozygotes showed further threshold elevations which were most severe at higher frequencies, above 18kHz. By P89-91, high frequency losses were compounded by severe losses across the entire range measured. This indicated a progressive hearing loss in *Obl*/+ mice, demonstrated by threshold elevations at P20 followed by further losses of high to low frequencies from P59-62 to P89-91. The improvement of low frequency (3-6kHz) ABR thresholds between P20 and P59-62 may indicate maturation of the

developing auditory system between these ages. Thresholds then start to deteriorate by P89-91.

Progression of hearing loss may be accelerated on a mixed genetic background (CAP recordings; data not shown). As the *Atp2b2* gene is known to show epistatic interaction with the *ahl* variant of the *Cdh23* gene, we developed a genotyping tool for the *ahl* mutation. All backcross mice carried either one or no copies of the recessive *ahl* allele, suggesting that the putative effect of the change in genetic background on CAP thresholds was not mediated by *ahl* (Supplementary Materials).

Obl/Obl homozygous mutants show a very severe hearing and vestibular phenotype and are significantly smaller (10.5g, SD 2.02) than age and sex matched *Obl*/+ littermates (17.3g, SD 2.11; *t*-test, $p<0.05$, 31-34 days old). They (a) fail to develop a Preyer reflex; (b) fall from side to side whilst walking; (c) are unable to right themselves; and (d) curl towards their belly when lifted by their tail and do not display a reaching response when lowered towards a surface. Homozygotes also show hind limb stiffness and appear ataxic, which are not general features of vestibular dysfunction.

Structure of the inner ear

The gross morphology of the middle ear ossicles and inner ear appeared normal in Oblivion mutants. Scanning electron microscopy in mutants at 3-4 months of age showed degeneration of hair cells, with the basal turn more severely affected than the apex, and outer hair cells (OHCs) more affected than inner hair cells (IHCs), a pattern that is commonly reported in damaged cochleas (Figures 2 and 3). *Obl/Obl* homozygotes were more severely affected than heterozygotes. However, there were many remaining hair cells with relatively normal appearance in the mutants, including a

W-shaped arrangement of stereocilia, especially in the apical turn. Stereocilia fusion was seen in some, an early indicator of hair cell degeneration. At P20, no significant hair cell loss was detected in *Obl*/+ mutants compared to their littermate controls (Figure 3A and 3B), despite the fact that these mice did show significantly raised CAP thresholds (Figure 1B). Hair cell counts from the basal and middle turns at P75 showed no significant OHC degeneration in the middle turn and no significant IHC loss throughout the cochlea in *Obl*/+ heterozygotes (Figures 3A-D). By P121, there was significant OHC and IHC loss in basal and middle turns in *Obl*/+ (Figures 3E and 3F). This suggests that the hair cell loss seen in these mutants is a secondary consequence of the hair cell not functioning correctly, rather than being the primary cause of raised thresholds in *Obl*/+ mutants.

In *Obl/Obl* mutants at P30 there was highly variable hair cell degeneration, both within and between animals. In some regions there was scattered hair cell loss with a pattern similar to that seen in heterozygotes (Figures 2G and 2H), while some regions towards the base there was complete degeneration of the organ of Corti with a complete absence of specialised cells, including supporting cells such as pillar cells (Figure 2I).

Mapping and identification of the Oblivion mutation

Obl/+ mutants on a C3HeB/FeJ background were outcrossed to C57BL/6J and mutant F1 progeny were backcrossed to the original C3HeB/FeJ strain. Backcross litters were assessed for absence of a Preyer reflex and a genome-wide scan was performed on their DNA using 60 polymorphic microsatellite markers. We identified a region of linkage on chromosome 6 (Fig 4A) between markers *D6Mit104* and *D6Mit218*, corresponding to a physical distance of 16Mb. This region contained a good candidate gene: *Atp2b2*.

Genomic DNA was used to sequence the 19 coding exons of the gene, including the splice sites. We identified a C/T heterozygous peak in *Obl/+* mutants, suggesting a C→T transition (2630C→T) in exon 15 of *Atp2b2*, predicted to change a serine to a phenylalanine (S877F; Figure 4) in the mutant allele. This change was also confirmed by a restriction test assay that was used to genotype the colony. This assay was used to screen 19 inbred strains for the *Obl* mutation and none were found to have it, suggesting that it is not a common polymorphism. We found non-complementation of *Obl* with the deafwaddler mutant allele, $Atp2b2^{dfw}$, confirming that the missense mutation we found was the pathogenic mutation (Supplementary Materials).

Functional analysis of the mutated PMCA2 pump overexpressed in model cells

To investigate the effects of the serine to phenylalanine change on the functionality of the pump, mammalian expression plasmids for the S877F and the wild type variant of the PMCA2 pump were prepared and expressed in CHO cells. Appropriate controls (Western blotting and quantitative immunocytochemistry) established that the two pump variants were expressed at about the same levels, and were correctly delivered to the plasma membrane (Figure 5). CHO cells were transfected with the Ca^{2+} sensitive photoprotein aequorin (cytAEQ, (3)) and stimulated with ATP, an agonist of purinergic P2Y receptors that produces $InsP_3$ generating a cytosolic Ca^{2+} transient. Under the experimental conditions, the height of the Ca^{2+} peak, and the kinetics of the return of the Ca^{2+} transient to baseline were controlled primarily by the PMCA pump: the much larger amounts of the overexpressed PMCA2 pump overshadowed the endoplasmic reticulum Ca^{2+} pump (SERCA) (see (16)) and the contribution of plasma membrane Ca^{2+} influx channels opened by emptying of intracellular stores to the shaping of the

Ca^{2+} trace was disregarded, as their effect would be the same in the wild type and *Obl* measurements. The *w/a* variant of the PMCA2 pump had poorer ability to react with a burst of activation to the sudden arrival of a Ca^{2+} pulse than the non-inserted (*z/b*) variant (inset of Figure 6), which decreased the height of the Ca^{2+} peak much more sharply than the *w/a* variant. The overexpressed *Obl* pump did not further depress the limited ability of the wild type *w/a* pump to control the height of the Ca^{2+}peak (Figure 6). The mutation, however, severely affected the resting activity of the pump that drove the return of the Ca^{2+} trace to baseline after the peak. The half time of the declining phase was 64.15 ± 3.02 sec (n=6) in control, 6.55 ± 0.72 sec (n=9) in the wild type *w/a* variant and 45.50 ± 5.97 sec (n=4), $p<0.001$, in *Obl*.

Ca^{2+} dynamics in the hair cell stereocilia of wild type, Obl/+ and Obl/Obl mice

To characterize Ca^{2+} dynamics in the stereocilia of hair cells, cultures of immature utricular maculae were obtained from wild type and mutant mice (see Materials and Methods). Ca^{2+}-dependent changes in fluorescence evoked by the photorelease of intracellular caged Ca^{2+} (4 ns single UV pulse) were monitored with a temporal resolution of 6 ms using confocal laser scanning microscopy. Immunofluorescence labelling with isoform specific antibodies showed that PMCA2 was correctly located in the stereocilia of mutant organotypic cultures (Figure 7A). Figure 7B shows a hair cell loaded with Fluo-4. Fluorescence changes in the stereocilia were monitored repeatedly by a line-scan positioned along the hair bundle and extending into the cell soma (dashed line). Time-dependent post UV pulse changes in fluorescence at different parts of the line scan are illustrated in Figure 7C. The time course of the stimulus-evoked changes in fluorescence (ΔF), normalized to basal (pre-stimulus) fluorescence (F_0), are compared

for wild type (*wt*, blue trace) heterozygous Oblivion mice (*Obl/+*, green trace) and homozygous Oblivion mice (*Obl/Obl*, black trace) in Figure 7D. The time courses matched well at the peak, although the $[Ca^{2+}]_i$ transient decayed more slowly for the *Obl/Obl* mice. To highlight the differences, the traces are re-plotted in Figure 7E on an expanded time scale (solid lines), together with their respective confidence intervals (dash-dotted lines). A single exponential fit to the first 10 s of these transients yielded significantly longer decay time constants for the *Obl/+* and *Obl/Obl* cultures: $\tau_{wt} = 2.8 \pm 0.4$ s for *wt*, $\tau_{Obl/+} = 4.2 \pm 1$ s for *Obl/+* mice ($p = 0.02$, if compared to *wt* using the ANOVA test) and $\tau_{Obl/Obl} = 6.9 \pm 1.3$ s for *Obl/Obl* mice ($p < 0.01$). No significant divergence in the early phase (first 2 s) of the decay was found for *Obl/+* mice relative to *wt*, consistent with the lack of evident phenotypic vestibular defects in these mice. At later times, the decay tended to diverge possibly due to the contribution of complex processes such as Ca^{2+}-induced Ca^{2+} release. These contributions were not investigated further.

Discussion

Progressive, age-related hearing loss affects 60% of humans over the age of 70 (18). The condition is a multifactorial disorder to which genetic variation, disease and environmental influences such as acoustic trauma are all contributing factors, making identification of the genes involved in humans difficult. The mouse is an ideal resource to study the genetics of progressive hearing loss due to the possibility of controlling both genetic background and the environment.

The present study has identified a new ENU-induced allele of *Atp2b2*, *Atp2b2*^{Obl} in the *Obl* mouse mutant. This allele contains a C to T missense mutation in exon 15 of *Atp2b2*, causing a non-conservative amino acid substitution of serine by phenylalanine in transmembrane domain 6 of the PMCA2 pump (1); (19). The serine at position 877 is highly conserved in both human and mouse and also between other members of the PMCA family (Figures 4C and 9, Supplementary Material). The S877F mutation is of special interest on at least two accounts. One is the finding that substitutions in the transmembrane residues of the PMCA pump frequently impair its correct plasma membrane targeting (20). However, the mutant *Obl* pump was correctly delivered to the plasma membrane in both the model cells and in native stereocilia. In another *Atp2b2* mutant allele, Wriggle mouse Sagami (*wri)*, a missense mutation in transmembrane domain 4 completely abolished the expression of PMCA2 protein in stereocilia of cochlear hair cells (21). The second reason for interest stems from studies of the SERCA pump of endoplasmic reticulum, considered a model for all P-type pumps. Conserved residues within transmembrane domain 6 of SERCA have been shown to be components of the channel through which Ca^{2+} is translocated (22) and are also present in the PMCA pump.

The *Obl* mutation is the sixth mutation in mouse *Atp2b2* to be reported. In the deafwaddler (*dfw)* mouse a missense mutation in *Atp2b2* leads to a partial loss of function (8) and PMCA2 retains 30% of its Ca^{2+} pumping activity (23). A further four mutations of mouse *Atp2b2* have been described: deafwaddler 2J (dfw^{2J}), deafwaddler 3J (dfw^{3J}), wriggle mouse sagami (*wri*) and a targeted null mutation. Analysis of mRNA transcripts and protein levels suggests that these latter four mutations are all null alleles (13); (24); (21). Homozygotes for these alleles show severe ataxia by 10 days of age as well as profound deafness. The profound deafness and ataxia detected in *Obl* homozygotes is similar to the phenotype of these other known *Atp2b2* null mutants (13); (24); (25). Non-complementation between *Obl* and *dfw* confirmed that these two mouse mutants are likely to be allelic. The mutations identified in the *Atp2b2* gene are shown in Figure 8 (Supplementary Material).

Both the *Obl* and the *dfw* mutations significantly reduce the non-activated Ca^{2+} exporting ability of the PMCA2 protein Observations on organotypic cultures showed that the defect of the pump observed in model cells also reduced its ability to remove the Ca^{2+} produced by UV photolysis in stereocilia. Thus, the *Obl* mutant has lost a significant portion of the non stimulated, longer-term Ca^{2+} exporting ability in respect to the *w/a* PMCA2 pump

In the present work we show that hearing loss in *Obl*/+ mice is detected at P20 and progresses in its severity with increasing age. Threshold shifts of up to 60-70dB were found at frequencies corresponding to the basal and middle turns of the cochlea, where the majority of outer hair cell loss was detected. Analysis of *Obl*/+ mice at P20 showed no OHC or IHC loss despite the fact that they had a significant hearing

impairment, confirming the previous suggestion that although hair cells are present they are not functioning normally (26).

IHC loss was detected in the base and middle of the cochlea in *Obl*/+ mutants at 4 months of age. The early degeneration of the OHCs seen in heterozygous *Obl* (and *dfw*) mice, leading to complete degeneration of the organ of Corti in the base of the cochlea, is similar to that seen in some human patients with age-related hearing loss (27); (28). It is not clear why hair cell dysfunction leads to hair cell degeneration in these mouse mutants, but prolonged abnormal calcium homeostasis may contribute to hair cell death. In *dfw* mice at approximately P60, distortion product otoacoustic emission studies show that PMCA2 is important for the correct functioning of outer hair cells, especially at high frequencies (29). Mice expressing the *Atp2b2*^{dfw2J} allele, **(9)** demonstrated a lowered endocochlear potential and reduced endolymphatic calcium concentration, and thus have a reduced capacity for mechanoelectrical transduction. Taken together, these features may explain why ABR thresholds in *Obl*/+ mice are elevated above controls, but are still recordable. An interesting observation from the ABRs recorded in P59-62 and P89-91 *Obl*/+ mice is that click thresholds are more sensitive than the best tone threshold, by a factor of 15-22dB. Clicks produce a more synchronised activation of a wider region of the basilar membrane compared to tone pips, and this may produce a summation of activity, reflected in lower click-evoked ABR thresholds.

When *Obl* was placed on a mixed C3HeJ/FeB and C57BL/6J background, the progressive hearing loss in heterozygotes seemed more severe (data not shown). Onset and severity of progressive hearing loss seen in heterozygotes of other *Atp2b2* mutant alleles have been shown to vary considerably depending on the genetic background on

which the mutation arose (13); (24); (30); (26); (21). This is due to the presence of modifier alleles, one of which has been identified as the G753A variant of *Cdh23* at the *ahl* locus (also known as modifier of deafwaddler, *mdfw*) (31); (30), although this modifier did not appear to account for the influence of genetic background on Oblivion mutant thresholds. Interactions between heterozygous *Atp2b2* mutations and *Cdh23* mutations have been shown to worsen the progressive hearing loss seen in some human patients. Heterozygous mutations ($ATP2B2^{V586M}$) increase the severity of the progressive hearing loss seen in human patients with mutations in *CDH23* (32). The $ATP2B2^{V586M}$ mutation reduced the level of PMCA2 protein produced by 50%, although on its own it was not sufficient to cause hearing impairment in humans (32). More recently, hearing loss has been reported in a human patient with an $ATP2B2^{G293S}$ mutation and a $CDH23^{T1999S}$ mutation. The parents of the patient carried either the *ATP2B2* or the *CDH23* mutation, but had no hearing impairment (16).

The *ATP2B2* gene has recently been implicated in 3p- syndrome. The syndrome is characterised by developmental delay, growth retardation and craniofacial abnormalities (see **(33)**), which is sometimes, but not always, associated with a severe sensorineural hearing loss. In 3p- syndrome patients with a hearing loss, a deletion in the 3p25.3 locus was mapped to a region containing 18 genes including *ATP2B2*. It is likely that haploinsufficientcy of *ATP2B2* is responsible for the deafness associated with this syndrome (34).

As progressive hearing loss is so common in the human population and we know so little about its molecular basis, identifying other mutations in and modifiers of the *Atp2b2* locus in mouse inbred strains may be of importance in identifying new loci involved in progressive and age-related hearing loss in humans.

Materials and methods

Mice

The founder mouse carrying the Oblivion mutation (gene symbol *Obl*, original identifier DEA14) arose from the ENU mutagenesis program at Munich (17). Mutations were generated by injecting 3 doses of 80-90mg/kg bodyweight of *N*-ethyl-*N*-nitrosourea (ENU) into C3HeB/FeJ males. F1 progeny were screened for a range of phenotypes, including deafness and balance disorders. The founder *Obl*/+ mutant was identified by the absence of a Preyer reflex at 3 months. The mutant colony was maintained on the C3HeB/FeJ background. The care and use of animals was carried out in accordance with UK Home Office regulations and the Animal Care and Use Committee of the University of Padua.

Inner ear clearing and ossicle dissection

Half heads were fixed in Bodian's fixative and cleared with glycerol using a standard protocol. The inner ear was examined for signs of malformation. Middle ear ossicles were dissected out and studied. Six *Obl*/+ mutants and six littermate controls between 3-4 months age were analysed.

Scanning Electron Microscopy

Inner ears were fixed in 2.5% glutaraldehyde in 0.1M sodium cacodylate buffer, the organ of Corti was exposed and samples were processed using the osmium tetroxide-thiocarbohydrazide (OTOTO) method (35). After critical point drying and sputter coating with gold, samples were examined using a Phillips XL30 scanning electron microscope at 10kV or a Hitachi S4800 FE Scanning Electron Microscope at 5 kV.

Initial characterisation was performed on 3 *Obl*/+ and 3 littermate controls at 3-4 months of age. Hair cell degeneration was assessed in the basal turn (20-30% of the total distance from the base of the cochlear duct) and middle turn (55-65% from the base) at 20 (P20), 72-75 and 121 days old. Between 3 and 7 *Obl*/+ and +/+ mice were examined at each age. Hair cells with intact stereocilia bundles were counted over a stretch of at least 200-300 µm of the cochlear duct. Hair bundles that were damaged or showed fusion were still counted as being present. A two tailed T-Test was performed on hair cell counts for each hair cell row in each region at 95% confidence intervals, with the number of cases and standard deviations included in the analysis. A two tailed T-test was carried out on the weights of *Obl/Obl* mutants compared to littermate (*Obl*/+) controls in the same way.

Preyer reflex and auditory brainstem response (ABR)

The Preyer reflex (pinna flick) was detected using a custom-built click box to deliver a calibrated 20 kHz sound burst at 90dB SPL. Up to 88 mice from *Obl*/+ x +/+ matings were tested weekly from 3 to 8 weeks of age, although the numbers of mice at each time-point varied. For ABR recordings, mice were anaesthetised (urethane 2 mg/g) and subcutaneous needle electrodes inserted on the vertex (active), and over the left (reference) and right (ground) bullae. A calibrated sound system was used to deliver free-field click (0.01ms duration) and tone pip (various frequencies from 3 – 42 kHz of 5ms duration, 1ms rise/fall time) stimuli at a range of intensity levels in 3dB (or multiple) steps. Averaged responses to 512 stimuli, presented at 21.1s^{-1}, were analysed and thresholds established as the lowest sound intensity giving a visually-detectable ABR response. ABR recordings were obtained from a total of 61 mice, 28 at P20 (+/+,

n=9; *Obl*/+, n=19), 14 at P59-62 (+/+, n=5; *Obl*/+, n=9) and 19 at P89-91 (+/+, n=5; *Obl*/+, n=14).

Mapping the Obl mutation

Obl/+ mutants on a C3HeB/FeJ background were outcrossed to C57BL/6J wild type females. *Obl*/+ F1 progeny were then backcrossed to +/+ animals from the original C3HeB/FeJ strain. Offspring from these backcross matings were examined at 2 months of age or older (as this is the age at which *Obl*/+ mice on the original genetic background show profound hearing loss) using the Preyer reflex. Tail and pinna tissue collected for DNA preparation. A total of 255 backcross mice were analysed (129 *Obl*/+, 126 +/+). A genome-wide scan was conducted with 60 microsatellite markers approximately 25cM apart, that had been shown to be polymorphic between C3HeB/FeJ and C57BL/6J inbred strains (Supplementary Table II). Additional microsatellite markers used for fine mapping of the *Obl* mutation were: *D6Mit36*; *D6Mit104*; *D6Mit150*; *D6Mit115*; *D6Mit218*; *D6Mit254*. PCR was performed using standard techniques.

Mutation screening and confirmation

Sequence analysis was performed on genomic DNA in *Obl*/+ mutants and littermate controls using primers designed to amplify the coding exons and splice sites of the *Atp2b2* gene. The primer sequences are listed in Supplementary Table III. PCR was performed using standard techniques and products were cleaned using magnetic bead separation (Ampure) and sequenced using BigDye Terminator Cycle sequencing kit (Applied Biosystems). Sequence traces were analysed using Gap4 software (36). To

confirm the mutation identified in exon 15 and for genotyping of the colony, a PCR-based genotype test was designed. The 2630C→T missense mutation did not change a restriction enzyme recognition site, so primers were designed flanking the mutation site that would incorporate a *StyI* recognition site in the wildtype (C) allele, but not in the mutant (T) allele. Primers OblRTF (5'-CTT CTT CTC CCT GCC ACT GTC GTA G) and OblRTR (5'-CCA CCG AGA CAC CGG TCC CGG TTC) were used for PCR. The 111bp PCR product was digested with *StyI* (New England Biolabs) which cuts the wildtype allele giving an 89bp fragment while the mutant allele remains uncut. This genotyping tool was used to establish whether the sequence change in *Obl* DNA was a polymorphism in a total of 17 inbred strains: BALB/C, CBA/Ca, C3HeB/FeJ, DDY/Jc1, 129X1/SvJ, A/J, Bxd-1/Ty, C58/J, CE/J, DA/HuSn, DBA/2J, FL/1Re, LP/J, NON/LtJ, RBG/Dn, St/bJ and SWR/J.

Cloning and mutagenesis of pmRFP-PMCA2 w/a mRFP was amplified from pCDNA3.1/zeo-mRFP (kindly donated by Dr. M. Zaccolo, Padua, Italy) using the following primers, forward: 5'-GC**GCTAGC**ATGGCCTCCTCCGAGGACGTCA-3' and reverse: 5'-GC**AGATCT**GAGGCGCCGGTGGAGTGGCGG-3', bearing restriction sites for NheI and BglII, respectively (in bold). The PCR product was than digested with NheI and BglII and inserted in pEGFP-c1 (Clontech, Palo Alto, CA) digested with NheI and BglII to create pmRFP-c1. PMCA2 *w/a* in pMM2 (kindly provided by Dr. Strehler, Rochester, MN) was excised by independent digestion with SalI-EcoRI and EcoRI-KpnI and inserted into XhoI-KpnI sites of pmRFP-c1 in a three-part ligation reaction resulting in pmRFP-PMCA2wa. The construct was controlled by sequencing. Site-directed mutagenesis was carried out to obtain the mutant cloned in the

appropriate vector. pmRFP-PMCA2w/a was used as target and experiments were performed according to the manufacturer's standard protocol (Stratagene, Cedar Creek, TX) The following primers were used: *Obl* 5' CATCATGGACACATTTGCTTTCCTGGCCCTGGCAACAGAGC 3'(forward) and 5' GCTCTGTTGCCAGGGCCAGGAAAGCAAATGTGTCCATGATG 3'(reverse)

Immunolocalization of the expressed pumps and membrane fluorescence computation

CHO cells were grown in Ham's F12 medium, supplemented with 10% fetal calf serum (FCS). Before transfection, they were seeded onto 13 mm glass coverslips and allowed to grow to 50% confluence. Transfection with 3 μg of plasmid DNA (or 1.5 :1.5 μg in the case of co-transfection) was carried out with a Ca-phosphate procedure (37). Immunocytochemistry quantified the expressed pump proteins in the plasma membrane of transfected cells. CHO cells expressing the PMCA2 variants, were stained with polyclonal isoform-specific PMCA antibody 2N (Affinity Bioreagent, Inc., Golden, CO) or a monoclonal antibody recognizing all pump isoforms (5F10, Affinity Bioreagent, Inc., Golden, CO), at a 1:100 dilution in PBS. Staining was carried out with Alexa 488 labelled anti-rabbit or anti-mouse secondary antibodies (Molecular Probes, Invitrogen Corp., Carlsbad, CA) at a 1:50 dilution in PBS and total fluorescence intensity in membrane was quantified using software developed in the Laboratory as previously described (16). For each construct fluorescence was averaged over a total of 50 cells in 3 different slides.

Ca^{2+} measurements with recombinant aequorin

Transfected cytAEQ were reconstituted by incubating CHO cells for 1–3 h with 5 µM coelenterazine in Dulbecco's modified Eagle's medium (D-MEM) supplemented with 1% FCS, at 37°C in a 5% CO_2 atmosphere. Additions to the KRB medium (1 mM $CaCl_2$, 100 µM ATP) were made as specified in the Figure legends. The experiments and luminescence calibration into [Ca^{2+}] values were carried out according to (38). Data are reported as mean ± SD. Statistical differences were evaluated by Student's 2-tailed t-test for unpaired samples. A p value <0.01 was considered statistically significant.

Preparation of organotypic utricle cultures

To access utricular maculae of wild type or mutant mice between postnatal day 3 (P3) and P4, the otic capsule was opened medially and the endolymphatic compartment of the macula cut open. The otolithic membrane was removed after 15 min incubation in dissection saline to which 0.1 g/l bacterial subtilisin (type XXIV; Sigma-Aldrich, St. Louis, MO) had been added. Dissection saline was composed of Hank's Balanced Salt Solution (HBSS; part number H6648, Sigma-Aldrich) with 10 mM HEPES, 10.000 U/l penicillin and 25 µg/l fungizone. HBSS contained (in g/l): 0.4 KCl, 0.06 KH_2PO_4 (anhydrous), 0.35 $NaHCO_3$, 8.0 NaCl, 0.048 Na_2HPO_4 (anhydrous), 1 D-glucose. The epithelium was fixed by Cell-Tak (BD Biosciences, Bedford, MA), mixed with 90 % $NaHCO_3$, to the lateral side of a glass capillary (1.5 mm diameter, 5 mm length), which had been previously glued to a microscope slide by a small drop of Sylgard Silicon Elastomer (Dow Corning, Wiesbaden, Germany). Cultures were preserved for one day at 37 °C in a complete medium of 95 % D-MEM/Ham's F-12 (1:1) (concentration 1X, liquid form, containing L-glutamine but no HEPES; Gibco, Invitrogen Corp., Carlsbad, CA) and 5 % fetal bovine serum.

Immunolocalization of PMCA2 in the stereocilia of hair cells in utricle cultures

Organotypic cultures dissected from P3 wild type and mutant mice pups were maintained over night at 37 °C in D-MEM/Ham's F-12 (1:1) medium with 5% fetal bovine serum. Tissue preparations were fixed in paraformaldehyde 4% for 20'min at room temperature, rinsed in washing solution (PBS containing BSA 2%) and permeabilised with washing solution containing Triton 0.1% for 1 h at room temperature. Incubation with primary PMCA antibody 2N was carried out overnight at 4°C using a 1:100 dilution in washing solution. FITC-conjugated rabbit anti-IgG antibody (Invitrogen) was used as secondary antibody for pump detection (1:200 dilution in washing solution, 2H r.t.). The preparation was mounted on coverslip and imaged up side down on an inverted spinning disk confocal microscope (Ultraview; Perkin-Elmner) using a 60× oil-immersion objective at a 1.4 N.A. (PlanApo; Nikon, Tokyo, Japan).

Confocal imaging of organotypic utricle cultures

Cultures were loaded with 10 µM cell permeant Fluo-4 AM (Invitrogen) for 50 min at 37 °C in D-MEM supplemented with 10 µM cell permeant NP-EGTA AM (Invitrogen), 25 µM sulfinpyrazone and Pluronic F-127 (0.1 % w/v). For de-esterification, cultures were transferred to an experimental chamber mounted on the stage of a confocal imaging setup (Biorad Radiance 2100) incorporating an upright microscope (Eclipse E600FN, Nikon, Tokyo, Japan) and superfused for 20 min with a medium composed of HBSS supplemented with 4.4 g/l glucose and 2mM anhydrous $CaCl_2$ (pH 7.4, Osm 330). Experiments were performed with a 100× water-immersion objective (N.A. 1.00,

LUMPlanFl, Olympus, Tokyo, Japan) using the same perfusion medium. Fluo-4 fluorescence was excited by the 488 nm line of an argon laser coupled by fiber optics to the confocal microscope. Fluorescence emission was selected around 528 nm using a narrow-band (50 nm) interference filter. Fluorescence images of utricle hair cells in the organotypic cultures were acquired with a resolution of 512 x 512 pixel by scanning at 512 lines per second under control of the Biorad Laser Sharp software. To be retained for subsequent recording, imaged cells had hair bundles extending for their entire length in a single confocal plane (bundle planarity condition), a possibility afforded by having the culture attached to a curved surface.

Confocal line-scan recording and UV photolysis of caged Ca^{2+} in utricular hair cells

Dynamic fluorescence data were acquired in the 'linescan' mode to produce a scan series of fluorescence intensity values, F, measured in the photomultiplier tube PMT units from a value of 0 to a saturating value of 255. Laser intensity and PMT gain were adjusted to accommodate the dynamic range of changes in F. Typical background fluorescence values, measured from regions devoid of obvious cellular structures, were ~1 PMT units, while pre-stimulus (basal) levels, F_0, averaged over the entire length of the hair bundle, were ~8 PMT units. In all experiments pinhole aperture was adjusted to the same value, yielding confocal section with 3 µm thickness. To assay the Ca^{2+} extrusion activity of the PMCAs, an area of ~ 3000 μm^2, comprising a few hair cells in the cultured utricular macula, was exposed to UV radiation generated by an air-cooled 337 nm pulsed nitrogen laser (Model VSL-337ND-S, Spectra Physics, Mountain View, CA, USA) connected to the microscope through a 600 µm ∅ optical fiber. UV light was directed onto the sample by reflection off a 400 DCLP dichromatic beam splitter

(Chroma) positioned at 45° just above the microscope objective lens. A single laser pulse (4 ns) delivering a maximum of 326 μJ of energy (at the laser output) was used to photorelease Ca^{2} from the caged state (NP-EGTA bound to Ca^{2+}) in the brief time interval between the 2500th and the 2501st scan line. In a typical record lasting about 120 s, 20000 consecutive lines were acquired.

Off-line analysis of fluorescence transients

All data were analyzed offline on a personal computer using the Matlab 7.0 (The MathWorks, Inc., Natick, MA) software environment. Data are presented as $\Delta F / F_0$ where $\Delta F = F - F_0$. In these expressions, raw pixel values are spatial averages along the hair bundle. Maximal percent fluorescence changes, $(F_{max} - F_0) / F_0$, were about 280 %. To estimate the slow time constant, τ, of recovery to baseline, transients peaking at $\Delta F_{max,}$ were fitted by a single exponential function during the first 10 s from the UV pulse. Data are given as mean ± standard error of the mean (S.E.M.).

Acknowledgements

We thank Dr Corne Kros for providing *dfw* mice, Dr Agnieszka Rzadzinska for expert advice on scanning electron microscopy, Ms Sabrina Facciolo for skilled technical assistance, Dr Emanuel Strehler for the donation of PMCA2 clones, Dr Manuela Zaccolo for the pCDNA3.1/zeo-mRFP and Ms Michelle Fleming for genotyping the mice used for ABR recordings. This work was supported by the Medical Research Council, Wellcome Trust, Deafness Research UK, the EC (contract numbers: CT97-

2715, QLG2-CT-1999-00988 and EUROHEAR LSHG-CT-20054-512063), the Telethon Foundation of Italy (Project GGP04169) and the Italian Ministry of University and Research (PRIN 2005, FIRB 2001).

Conflict of Interest Statement

The authors declare no conflict of interests associated with this work.

References

1. Carafoli, E. (1992) The Ca^{2+} pump of the plasma membranE. *J. Biol. Chem.,* **267,** 2115-2118.
2. Strehler, E.E. and Zacharias, D.A. (2001) Role of alternative splicing in generating isoform diversity among plasma membrane calcium pumps. *Physiol. Rev.,* **81,** 21-50.
3. Brini, M., Coletto, L., Pierobon, N., Kraev, N., Guerini, D. and Carafoli, E. (2003) A comparative functional analysis of plasma membrane Ca^{2+} pump isoforms in intact cells. *J. Biol. Chem.,* **278,** 24500-24508.
4. Elwess, N.L., Filoteo, A.G., Enyedi, A. and Penniston, J.T. (1997) Plasma membrane Ca^{2+} pump isoforms 2a and 2b are unusually responsive to calmodulin and Ca^{2+}. *J. Biol. Chem.,* **272,** 17981-17986.
5. Hilfiker, H., Guerini, D. and Carafoli, E. (1994) Cloning and expression of isoform 2 of the human plasma membrane Ca^{2+} ATPase. Functional properties of the enzyme and its splicing products. *J. Biol. Chem.,* **269,** 26178-26183.
6. Crouch, J.J. and Schulte, B.A. (1996) Identification and cloning of site C splice variants of plasma membrane Ca-ATPase in the gerbil cochlea. *Hear. Res.,* **101,** 55-61.
7. Furuta, H., Luo, L., Hepler, K. and Ryan, A.F. (1998) Evidence for differential regulation of calcium by outer versus inner hair cells: plasma membrane Ca-ATPase gene expression. *Hear. Res.,* **123,** 10-26.

8. Street, V.A., McKee-Johnson, J.W., Fonseca, R.C., Tempel, B.L. and Noben-Trauth, K. (1998) Mutations in a plasma membrane Ca^{2+}-ATPase gene cause deafness in deafwaddler mice. *Nat. Genet.,* **19,** 390-394.

9. Wood, J.D., Muchinsky, S.J., Filoteo, A.G., Penniston, J.T. and Tempel, B.L. (2004) Low endolymph calcium concentrations in deafwaddler 2J mice suggest that PMCA2 contributes to endolymph calcium maintenance. *J. Assoc. Res. Otolaryngol.,* **5,** 99-110.

10. Dumont, R.A., Lins, U., Filoteo, A.G., Penniston, J.T., Kachar, B. and Gillespie, P.G. (2001) Plasma membrane Ca^{2+}-ATPase isoform 2a is the PMCA of hair bundles. *J. Neurosci.,* **21,** 5066-5078.

11. Yamoah, E.N., Lumpkin, E.A., Dumont, R.A., Smith, P.J., Hudspeth, A.J. and Gillespie, P.G. (1998) Plasma membrane Ca^{2+}-ATPase extrudes Ca^{2+} from hair cell stereocilia. *J. Neurosci.,* **18,** 610-624.

12. Bosher, S.K. and Warren, R.L. (1978) Very low calcium content of cochlear endolymph, an extracellular fluid. *Nature,* **273,** 3770378.

13. Kozel, P.J., Friedman, R.A., Erway, L.C., Yamoah, E.N., Liu, L.H., Riddle, T., Duffy, J.J., Doetschman, T., Miller, M.L., Cardell, E.L. *et al.* (1998) Balance and hearing deficits in mice with a null mutation in the gene encoding plasma membrane Ca^{2+}-ATPase isoform 2. *J. Biol. Chem.,* **273,** 18693-18696.

14. Grati, M., Aggarwal, N., Strehler, E.E. and Wenthold, R.J. (2006) Molecular determinants for differential membrane trafficking of PMCA1 and PMCA2 in mammalian hair cells. *J. Cell. Sci.,* **119,** 2995-3007.

15. Hill, J.K., Williams, D.E., LeMasurier, M., Dumont, R.A., Strehler, E.E. and Gillespie, P.G. (2006) Splice-site A choice targets plasma-membrane Ca^{2+}-ATPase isoform 2 to hair bundles. *J. Neurosci.,* **26,** 6172-6180.

16. Ficarella, R., Di Leva, F., Bortolozzi, M., Ortolano, S., Donaudy, F., Petrillo, M., Melchionda, S., Lelli, A., Domi, T., Fedrizzi, L. *et al.* (2007) A functional study of plasma-membrane calcium-pump isoform 2 mutants causino digenic deafness. *Proc. Natl. Acad. Sci. U.S.A.,* **104,** 1516-1521.

17. Hrabé de Angelis, M.H., Flaswinkel, H., Fuchs, H., Rathkolb, B., Soewarto, D., Marschall, S., Heffner, S., Pargent, W., Wuensch, K., Jung, M. *et al.* (2000) Genome-wide, large-scale production of mutant mice by ENU mutagenesis. *Nat. Genet.,* **25,** 444-447.

18. Davis, A.C. (1989) The prevalence of hearing impairment and reported hearing disability among adults in Great Britain. *Int. J. Epidemiol.,* **18,** 911-917.

19. Guerini, D. and Carafoli, E. (1999) The calcium pumps. In Carafoli, E. and Klee, C.B. (eds.), *Calcium as a cellular regulator*. Oxford University Press, Oxford, pp. 249-278.

20. Guerini, D., Zecca-Mazza, A. and Carafoli, E. (2000) Single amino acid mutations in transmembrane domain 5 confer to the plasma membrane Ca^{2+} pump properties typical of the Ca^{2+} pump of endo(sarco)plasmic reticulum. *J. Biol. Chem.,* **275,** 31361-31368.

21. Takahashi, K. and Kitamura, K. (1999) A point mutation in a plasma membrane Ca^{2+}-ATPase gene causes deafness in Wriggle Mouse Sagami. *Biochem. Biophys. Res. Commun.,* **261,** 773-778.

22. Clarke, D.M., Loo, T.W., Inesi, G. and MacLennan, D.H. (1989) Location of high affinity Ca^{2+}-binding sites within the predicted transmembrane domain of the sarcoplasmic reticulum Ca^{2+}-ATPase. *Nature,* **339,** 476-478.

23. Penheiter, A.R., Filoteo, A.G., Croy, C.L. and Penniston, J.T. (2001) Characterization of the deafwaddler mutant of the rat plasma membrane calcium-ATPase 2. *Hear. Res.,* **162,** 19-28.

24. McCullough, B.J. and Tempel, B. (2004) Haplo-insufficiency revealed in deafwaddler mice when tested for hearing loss and ataxia. *Hear. Res.,* **195,** 90-102.

25. Takahashi, K., Osawa, N., Ohmura, M. and Kitamura, K. (1999) Evaluation of inner ear histology and auditory brainstem response in Wriggle Mouse Sagami. *Acta Otolaryngol.,* **119,** 767-772.

26. Norton, S.J., Tempel, B.L., Steel, K.P. and Rubel, E.W. (1996) Physiological and anatomical status of the deafwaddler (*dfw*) mutant mouse cochlea. *Midwinter Meeting of the Association for Research in Otolaryngology.* p. 82.

27. Johnsson, L.G. and Hawkins, J.E., Jr. (1972) Sensory and neural degeneration with aging, as seen in microdissections of the human inner ear. *Ann. Otol. Rhinol. Laryngol.,* **81,** 179-193.

28. Schuknecht, H.F. and Gacek, M.R. (1993) Cochlear pathology in presbycusis. *Ann. Otol. Rhinol. Laryngol.,* **102,** 1-16.

29. Konrad-Martin, D., Norton, S.J., Mascher, K.E. and Tempel, B.L. (2001) Effects of PMCA2 mutation on DPOAE amplitudes and latencies in deafwaddler mice. *Hearing Research,* **151,** 205-220.

30. Noben-Trauth, K., Zheng, Q.Y., Johnson, K.R. and Nishina, P.M. (1997) *mdfw*: a deafness susceptibility locus that interacts with deaf waddler (*dfw*). *Genomics,* **44,** 266-272.

31. Noben-Trauth, K., Zheng, Q.Y. and Johnson, K.R. (2003) Association of cadherin 23 with polygenic inheritance and genetic modification of sensorineural hearing loss. *Nat. Genet.,* **35,** 21-23.

32. Schultz, J.M., Yang, Y., Caride, A.J., Filoteo, A.G., Penheiter, A.R., Lagziel, A., Morell, R.J., Mohiddin, S.A., Fananapazir, L., Madeo, A.C. *et al.* (2005) Modification of human hearing loss by plasma-membrane calcium pump PMCA2. *N. Engl. J. Med.,* **352,** 1557-1564.

33. Fernandez, T., Morgan, T., Davis, N., Klin, A., Morris, A., Farhi, A., Lifton, R.P. and State, M.W. (2004) Disruption of contactiv 4 (CNTN4) results in developmental delay and other features of 3p deletion syndrome. *Am. J. Human Genet.,* **74,** 1286-1293.

34. McCullough, B.J., Adams, J.C., Shilling, D.J., Feeney, M.P., Sie, K.C.Y. and Tempel, B.L. (2007) 3p- syndrome defines a hearing loss locus in 3p25.3. *Hearing Research,* **224,** 51-60.

35. Hunter-Duvar, I.M. (1978) A technique for preparation of cochlear specimens for assessment with the scanning electron microscope. *Acta Otolaryngol.,* **Suppl 351,** 3-23.

36. Bonfield, J.K., Rada, C. and Staden, R. (1998) Automated detection of point mutations using fluorescent sequence trace subtraction *Nucleic Acids Res.,* **26,** 3404-3409.

37. Rizzuto, R., Brini, M., Bastianutto, C., Marsault, R. and Pozzan, T. (1995) Photoprotein-mediated measurement of calcium ion concentration in mitochondria of living cells. *Methods Enzymol.,* **260,** 417-428.

38. Brini, M., Marsault, R., Bastianutto, C., Alvarez, J., Pozzan, T. and Rizzuto, R. (1995) Transfected aequorin in the measurement of cytosolic Ca^{2+} concentration ($[Ca^{2+}]c$). A critical evaluation. *J. Biol. Chem. ,* **270,** 9896-9903.

39. Lane, P. (1987) New mutants and linkages:deafwaddler (*dfw*). *Mouse newsletters,* **77,** 129.

40. Johnson, K.R., Zheng, Q.Y. and Erway, L.C. (2000) A major gene affecting age-related hearing loss is common to at least ten inbred strains of mice. *Genomics,* **70,** 171-180.

41. Johnson, K.R., Erway, L.C., Cook, S.A., Willott, J.F. and Zheng, Q.Y. (1997) A major gene affecting age-related hearing loss in C57BL/6J mice. *Hear. Res.,* **114,** 83-92.

42. Johnson, K.R. and Zheng, Q.Y. (2002) *Ahl2*, a second locus affecting age-related hearing loss in mice. *Genomics,* **80,** 461-464.

43. Johnson, K.R., Zheng, Q.Y., Bykhovskaya, Y., Spirina, O. and Fischel-Ghodsian, N. (2001) A nuclear-mitochondrial DNA interaction affecting hearing impairment in mice. *Nat. Genet.,* **27,** 191-194.

44. Nemoto, M., Morita, Y., Mishima, Y., Takahashi, S., Nomura, T., Ushiki, T., Shiroishi, T., Kikkawa, Y., Yonekawa, H. and Kominami, R. (2004) *Ahl3*, a third locus on mouse chromosome 17 affecting age-related hearing loss. *Biochem. Biophys. Res. Commun.,* **324,** 1283-1288.

45. Mashimo, T., Erven, A.E., Spiden, S.L., Guenet, J.-L. and Steel, K.P. (2006) Two quantitative trait loci affecting progressive hearing loss in 101/H mice. *Mammalian Genome,* **17,** 841-850.

Legends to Figures

Fig 1

Obl/+ mutants show significantly raised auditory brainstem response (ABR) thresholds compared to wildtype mice at P20 (circles), P59-62 (squares) and P89-91 (triangles). Mean ABR thresholds with standard error bars are given for +/+ mice (filled symbols) and *Obl*/+ mice (open symbols). The dotted line indicates the maximum dB SPL output for the sound system at each frequency. The position along the length of the cochlear duct that best responds to each frequency (represented by % of total distance from the base) is indicated by the frequency place map at the top of the graph.

Fig 2

Analysis of wildtype, *Obl*/+ and *Obl/Obl* organ of Corti by scanning electron microscopy. At 3-4 months, normal animals show three rows of outer hair cells (OHC) and one row of inner hair cells (IHC) in the apex (A), middle (B) and base (C) of the cochlea. *Obl*/+ have extensive OHC loss and some IHC loss in the base of the cochlea (F) and a few missing OHC in the middle of the cochlea (E). The apex appears normal (D). At 1 month of age, the phenotype in the *Obl/Obl* mice is extremely variable. In some regions of the base, middle and apex, the phenotype is similar to that seen in *Obl*/+. However in other parts of the apex (G) and middle (H) regions of the cochlea, there are missing patches of OHCs. In some regions of the base, there is a complete degeneration of the organ of Corti, with no IHC, OHC or supporting cells such as pillar cells present (I). Scale bar = 10mm.

Fig 3

Hair cell counts show that outer hair cell loss in heterozygotes (*Obl*/+) at P75 is present in the base (C) but not the middle (D) of the cochlea. By P121, outer hair cell loss is seen in the base (E) and the middle (F) of the cochlear duct. IHC loss is seen in the base of the cochlea only at later ages (E). This suggests that hair cell loss in *Obl*/+ mutants progresses in a base to apex direction, with OHC loss occurring first and IHC loss later. No OHC or IHC loss was seen in the base (A) or middle (B) regions of the cochlea at P20. Hair cell counts calculated as mean number of hair cells per 100um at P20 (+/+ n=4-7, *Obl*/+ n=7), P72-75 (+/+ n=4, *Obl*/+ n=5) and P121 (+/+ n=3-4, *Obl*/+ n=4-5). Error bars indicate 95% confidence interval, T-test, * P-value <0.05.

Fig 4

Oblivion chromosomal location, mutation and PMCA2 sequence alignment. (A) *Obl* mutation maps to a 16 Mb region on mouse chromosome 6, between *D6Mit104* and *D6Mit218*. Each box represent a marker typed, and each chromosomal arrangement detected shown, with the number of animals possessing that chromosome given underneath. If a marker was not typed then no box is present. (B) Sequence of *Atp2b2* in *Obl*/+ mouse showing the C→T mutation and predicted sequence. (C) Sequence alignment of several PMCA family members showing Ser877 is highly conserved.

Fig 5

Expression and immunolocalization of recombinant PMCA2 pumps in CHO cells. (A) Western blotting analysis. 48h after transfection CHO cells were washed twice with cold PBS buffer and scraped in lysis buffer (Tris-HCl 10mM, EDTA 1mM, PMSF 2mM

and DTT 1mM). After centrifugation at 1000 x g for 5 min, the cells were resuspended in 80 µl of lysis buffer and subjected to three cycles of freeze and thaw. The proteins of the lysates were quantified using the Bradford Reagent (Sigma-Aldrich). 15 µg of proteins were loaded on 10% polyacrylamide gel and transferred to nitrocellulose membranes which were incubated with polyclonal PMCA2 antibody 2N and monoclonal β-actin antibody (Sigma-Aldrich). After incubation with HRP-conjugated secondary antibodies (Santa Cruz Biotechnology, Inc., Santa Cruz, CA), the blots were developed with ECL reagents (Amersham Life Science). The band of ~130kDa corresponds to PMCA2 and the band of ~42kDa to β-actin. (B) Immunolocalization of *wt* and *Obl* PMCA2 in transiently transfected CHO cells. The interaction with 2N antibody was revealed by the AlexaFluor488-conjugated secondary antibody. Upper panel, plasma membrane pattern of the overexpressed pumps (details in Materials and Methods). (A) wild type *w/a* pump. (B) *Obl/Obl* pump. Lower panel, fluorescence level in the plasma membrane quantified as described in Material and Methods. The SDs are indicated by the bars.

Fig 6

Activity of recombinant PMCA2 pumps in CHO cells. Cells were transiently co-transfected with the PMCA2 variants and cytAEQ, or only with cytAEQ (control). They were then perfused with KRB supplemented with 1 mM $CaCl_2$. 100 µM ATP was used to produce a transient Ca^{2+} increase (A). The histograms in B and C show the means SD of Ca^{2+} peaks and the half peak decay times, respectively (n indicates the number of experiments considered for the statistical analysis) * $p<0.01$ calculated with respect to

the wt pump. Inset, Ca^{2+} transients in cells overexpressing the wt *w/a* pump, and the *z/b* pump.

Fig 7

Dissipation of Ca^{2+} transients in utricular hair cells co-loaded with Fluo-4 and caged Ca^{2+}. (A) immunolocalization of the wt and *Obl*/*Obl* PMCA2 pump in the stereocilia of the utricular hair cells (details in Materials and Methods).(B) confocal image of baseline Fluo-4 fluorescence in an organotypic culture of mouse utricular macula. The diagonal dashed line represents the scan line during subsequent data acquisition. The hair bundle is comprised between the top and middle horizontal dotted lines (the latter crosses the cell cuticular plate). The cell soma is comprised within middle and lower lines. (C) in this line-scan image, ordinates are pixel positions along the scan line, abscissa is time and fluorescence transients, $\Delta F / F_0$, evoked by a 4 ns UV pulse (arrow) are color-coded according to the color scale-bar at right. Signals from pixels below the lowermost horizontal dotted line arise from the cell adjacent to the hair cell in (B). (D) fluorescence traces obtained by spatially averaging line-scan pixel signals within the stereociliary compartment of wild type (*wt*, blue solid line), heterozygous (*Obl*/+, green solid line) and homozygous Oblivion mice (*Obl/Obl*, black solid line). Each trace is the population average of n = 6 cells (for *wt* and *Obl/Obl*) or n = 5 cells (for *Obl*/+). The region within the dash-dotted box is shown on a faster time scale in (E). Also shown in (E) are confidence intervals (dash-dotted lines) for the average $\Delta F / F_0$ responses (solid lines).

Abbreviations

ABR Auditory Brainstem Response.

CAP Compound Action Potential

CHO Chinese Hamster Ovary

IHC Inner Hair Cell

OHC Outer Hair Cell

P Post Natal Day

Supplementary Materials

Complementation test between Obl/+ and dfw/dfw

To confirm that the missense mutation identified was causative, a complementation test was carried out between *Obl/+* and *dfw/dfw* mice maintained on a C3H/HeJ background (8). If the Oblivion phenotype is due to mutation of the *Atp2b2* gene, then it would be expected that the two mutations will not complement and the resulting compound heterozygotes from this cross (*Obl/dfw*) would show a phenotype similar to that seen in *Obl* and *dfw* homozygotes. The *dfw* mice used were the original *dfw* allele and homozygotes have a subtle phenotype being deaf and having a slight waddle and head bob (39); (8). The Oblivion homozygote phenotype was much more obvious, with mutants showing severe vestibular dysfunction, falling from side to side, head-tossing, some circling, poor righting reflex and splaying of the hind limbs. This is similar to the phenotype of null alleles of *Atp2b2* (13); (21). Of the 33 mice that were analysed from this complementation test, 1 (3%) showed mild stargazing; 2 (6%) fell to the side when rearing, one of which also curled in a ball when lifted up and 5 (15%) seemed tottery and fell from side to side when walking and curled up in a ball when lifted up. Since *+/dfw* lose their Preyer reflex by about 1-2 months of age, this test was not a useful discriminator for these mice. Compound heterozygote offspring (*dfw*/*Obl*) showed vestibular phenotypes, intermediate between those seen in the two parental (homozygous) mutants, suggesting that they did not complement and therefore the two mutants are allelic. Only 8/33 (24%) offspring showed non-complementation, which is significantly lower than the 50% that was expected. Since *dfw* and *Obl* both arose on the closely-related genetic backgrounds (C3H/FeJ), it is unlikely that genetic background

effects would contribute to this. Another explanantion could be that due to the variation in severity of the phenotype, some mutants displaying mild behaviour such as star-gazing were missed. However the presence of a phenotype in *dfw/Obl* compound heterozygotes does support the suggestion that the Oblivion mutant is another allele of the *deafwaddler* locus.

Genetic modifiers of the dfw allele

As mentioned in the main text, the *Obl*/+ backcross mice (on a mixed C3H/C57 background) showed hearing loss at a much younger age than the *Obl*/+ mice from the original colony (C3H background). This suggests that there may be a modifier of the *Obl*/+ phenotype present in the C57BL/6J background which accelerates the hearing loss seen in the mutants. It has been reported that homozygosity for the *ahl* susceptible allele $Cdh23^{753A}$ at the *ahl*/*mdfw* locus on mouse chromosome 10 predisposes certain inbred strains to age-related hearing loss (40); (41); (31); (30). It has also been reported that mice heterozygous for the *dfw* locus and homozygous for the $Cdh23^{753A}$ allele show early onset hearing loss, suggesting that the *modifier of deafwaddler* (*mdfw*) is $Cdh23^{753A}$ (30). To determine whether the susceptible $Cdh23^{753A}$ allele could explain the increased hearing loss seen in the *Obl*/+ mutants, we typed the backcross for the *Cdh23* SNP (see below for method). All *Obl*/+ mutants carried either one or no $Cdh23^{753A}$ allele but none carried the two copies necessary to confer *ahl* susceptibility, since *ahl* is a recessive trait. Therefore, we presume there must be another modifier of the progressive hearing loss phenotype seen in *Obl*/+ mutants. Other genetic factors that predispose some inbred strains to early-onset age-related hearing loss are ideal

candidates for this such as *ahl2*, *ahl3, Phl1, Phl2* and the mitochondrial mutation *mt-Tr*^{9827ins8} (42); (43); (44); (45).

Genotyping the ahl locus in the backcross mice

To type the backcross mice for the presence or absence of the *ahl* susceptible *Cdh23*^{753A} allele, a restriction enzyme based genotyping test was designed. As the G to A SNP failed to change a restriction site, primers were designed flanking the mutation site that would incorporate a *PstI* recognition site in the susceptible mutant (A) allele, but not in the wildtype, resistant (G) allele. Amplification with cdh23RTF (5'-TAA CAT CTA CGA GCA CTC TCC TGC) and cdh23RTR (5'-TTA TGT GTG GTA CAC ACG GCC AAC G) gave a 194bp product. Digestion of the product with *PstI* cleaves the mutant allele giving an 170bp fragment, while the wildtype allele remains uncut.

Fig 8

Mutations identified to date affecting PMCA2 protein in mice. Three mutations are missense mutations leading to amino acid substitutions (*dfw, wri*, *Obl*), two are small deletions that lead to frame shift mutations and premature truncation of the PMCA2 protein (*dfw*^{2J}, *dfw*^{3J}) and one is a targeted null allele (*Atp2b2*^{tm1Ges}) (13); (24); (8); (21). Adapted from (21).

Fig 9

Alignment of the amino acids residues in transmembrane domain 6 of PMCA isoforms in different species (A) and of PMCAs and other P-type ATPases (B). The similarity

analysis was performed using the ClustalW program. GenBank accession numbers are listed: NP_001674 (*Homo sapiens*), Q9ROK7 (*Mus musculus*), NP_036640 (*Rattus norvegicus*), XP_509257 (*Pan troglodytes*), NP_777121 (*Bos taurus*), NP_999517 (*Sus scrofa*), Q00804 (*Oryctolagus cuniculus*), AAK11272 (*Rana catesbeiana*), AAH77905 (*Xenopus laevis*), AAR28532 (*Procambarus clarkii*), AAK68551 (*Caenorhabditis elegans),* XP_653525 (*Entamoeba histolytica*), EAL62716 (*Dictyostelium discoideum*), NP_001001323 (PMCA1), NP_068768 (PMCA3), NP_001675 (PMCA4), NP_004311 (SERCA1), NP_733765 (SERCA2), NP_777615 (SERCA3), AAF35375 (SPCA1), NP_000693 (Na^+/K^+ ATPase) and AAH31609 (Na^+/K^+ ATPase).

Supplementary Table I:
Progressive hearing loss in litters from *Obl*/+ x +/+ matings

Age (days)	Number mice with Preyer reflex	Number mice without Preyer reflex
23-25	82/82 (100%)	0/82 (0%)
30-31	77/82 (94%)	5/82 (6%)
37-39	58/82 (71%)	24/82 (29%)
45-46	41/66 (62%)	25/66 (38%)
51-52	47/75 (63%)	28/75 (37%)
58	19/33 (58%)	14/33 (42%)

Progressive hearing loss detected in *Obl*/+ mutants starts at 1 month of age (6%), with most being deaf by 2 months of age (42%). 50% offspring from *Obl*/+ X +/+ mating are expected to show phenotype.

Supplementary Table II:
Microsatellite markers polymorphic between C3HeB/FeJ and C57BL/6J

Microsatellite marker	Chromosome	Genetic position
D1Mit21	**1**	33.89 cM
D1Mit415	**1**	53.06 cM
D1Mit445	**1**	75.72 cM
D1Mit353	**1**	90.34 cM
D2Mit237	**2**	28.71 cM
D2Mit128	**2**	49.41 cM
D2Mit59	**2**	60 cM
D2Mit200	**2**	98.36 cM
D3Mit117	**3**	2.35 cM
D3Mit339	**3**	29.25 cM
D3Mit199	**3**	56.1 cM
D4Mit172	**4**	11.23 cM
D4Mit58	**4**	40.62 cM
D4Mit33	**4**	67.6 cM
D4Mit190	**4**	75.4cM
D5Mit345	**5**	0 cM
D5Mit391	**5**	18.3 cM
D5Mit115	**5**	40.01 cM
D5Mit168	**5**	68.65 cM
D6Mit138	**6**	2.35 cM
D6Mit320	**6**	22.38 cM
D6Mit366	**6**	43.69 cM
D6Mit61	**6**	48.16 cM
D6Mit201	**6**	62.94 cM
D7Mit178	**7**	2.78 cM
D7Mit230	**7**	22.45 cM
D7Mit253	**7**	42.55 cM
D8Mit190	**8**	22.69 cM
D8Mit280	**8**	74.11 cM
D9Mit254	**9**	20.14 cM
D9Mit214	**9**	58.79 cM
D10Mit206	**10**	4.47 cM
D10Mit115	**10**	32.47 cM
D10Mit12	**10**	52.5 cM
D10Mit180	**10**	65.22 cM
D11Mit140	**11**	25.73 cM
D11Mit35	**11**	44.74 cM
D11Mit99	**11**	63.21 cM
D12Mit240	**12**	3.3 cM
D12Mit69	**12**	23.88 cM
D12Mit259	**12**	42.92 cM
D12Nds2	**12**	62.46 cM
D13Mit3	**13**	8.96 cM

D13Mit9	**13**	32.44 cM
D13Mit77	**13**	50 cM
D14Mit99	**14**	1.51 cM
D14Mit260	**14**	21.21 cM
D14Mit225	**14**	44.1 cM
D15Mit175	**15**	5.72 cM
D15Mit43	**15**	58.01 cM
D16Mit165	**16**	11.17 cM
D16Mit63	**16**	30.76 cM
D16Mit152	**16**	48 cM
D17Mit113	**17**	2.22 cM
D17Mit238	**17**	30.64 cM
D18Mit22	**18**	8.97 cM
D18Mit187	**18**	32.54 cM
D19Mit59	**19**	0 cM
D19Mit16	**19**	17.16 cM
D19Mit67	**19**	35.25 cM

Supplementary Table III.
Sequencing primers for *Atp2b2*

Primer name	Primer sequence (5'-3')
AtpNE1F	TGCCAAGCTCCCTGATGTGC
AtpNE1R2	AGGCTGCCATCAGAACTGGC
AtpNE2F	TCCTCACCCAGCAGTTCTAAC
AtpNE2R	CTCTACCCATGCAGGTGCAC
Atp3F	TGTGGCAGCTCTTGTCTGCTG
Atp3R	CCAGATCTAGAAGCATGGAGC
Atp4F	CTGTATGCTGTATGCTAGGTAC
Atp4R	GCCAGGGACTACACCAGCGTC
Atp5F	AGACACCTGTTCCTTCTGTTC
Atp5R	GTGGAGTGAACAGATGAATGG
Atp6F	CGTTCTGGCCTCTAGGCTAAC
Atp6R	GGACCATTGGAATCAAGGTAG
Atp7F	CAGAAGCAGTTTAGTGAACATC
Atp7R	CTCAGCTGTGGCTGCTTCAG
Atp8F	CCAGGCAGAAGGTTAAGAGG
Atp8R	CGAGCCAGGTGCTCTGTTATG
Atp9F	CAGTGGCTCCTCTGTGGCGAG
Atp9R	TGCTTAGATCCAGCCTGCATG
Atp10F	TTTGATGACCAAGGTAGGTGG
Atp10R	GAAGGATCCTGATACTGTTAC
Atp11F	GAAGACCTACCTAAGTGATGC
Atp11R	GGCTTCTGTTCAAGCATGCAG
Atp12F	TGCTTGAACAGAAGCCAGCTG
Atp12R	GAGGAAGCTGCGATGCCATG
Atp13F	AGGAAGCCATGCTGAGGCTC
Atp13R	GTGTAGTCCAAGCTGACTATC
Atp14F	GCCATTCACCTCTCCAGCTGC
Atp14R	CAGCCTTTGGTGTGATTCTCC
Atp15F2	TTCTCCCTGCCACTGTCGTAG
Atp15R	CGTTGTTGGCCATGGTATGTC
Atp16F	CGTTCCACACCTGAGCCGGC
Atp16R	GACAGACACGGAGATGGCAC
Atp17F	GTGCCATCTCCGTGTCTGTC
Atp17R	TCACTTCTAGGACCAATCCTG
Atp18F	ATCTTAGCCCTGACCGTTGC
Atp18R	GAGGGTGCATTGGAACTACTG
Atp19F	GGATCCCAGCCGCCTGCGTGC
Atp19R	ATGAGCGTGGCCAGGCGACA

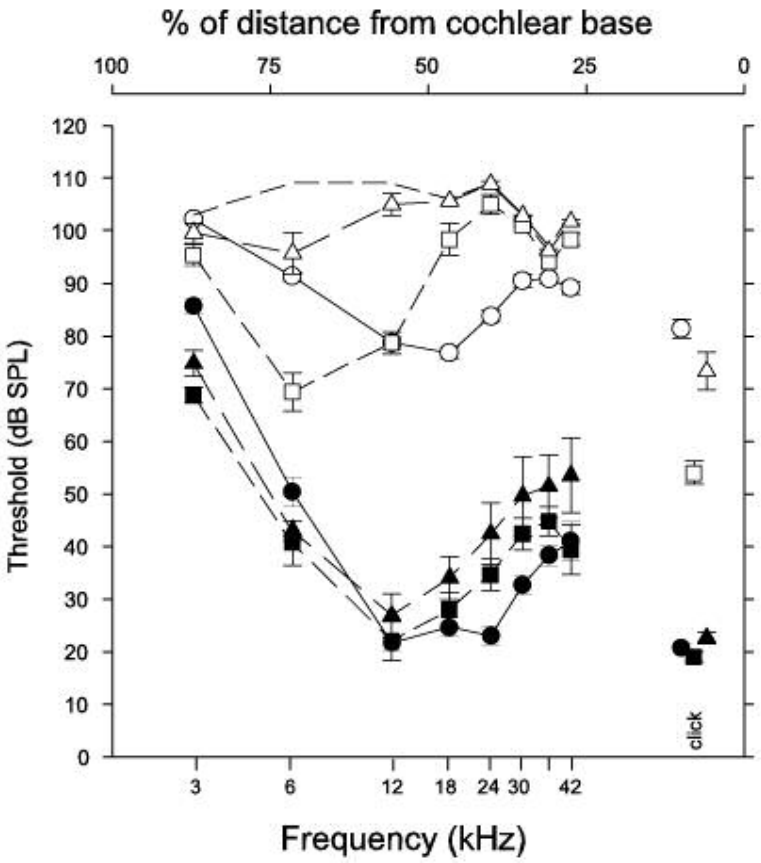

Fig 1: *Obl*/+ mutants show significantly raised auditory brainstem response (ABR) thresholds compared to wildtype mice at P20 (circles), P59-62 (squares) and P89-91 (triangles). Mean ABR thresholds with standard error bars are given for +/+ mice (filled symbols) and *Obl*/+ mice (open symbols). The dotted line indicates the maximum dB SPL output for the sound system at each frequency. The position along the length of the cochlear duct that best responds to each frequency (represented by % of total distance from the base) is indicated by the frequency place map at the top of the graph.
77x113mm (142 x 142 DPI)

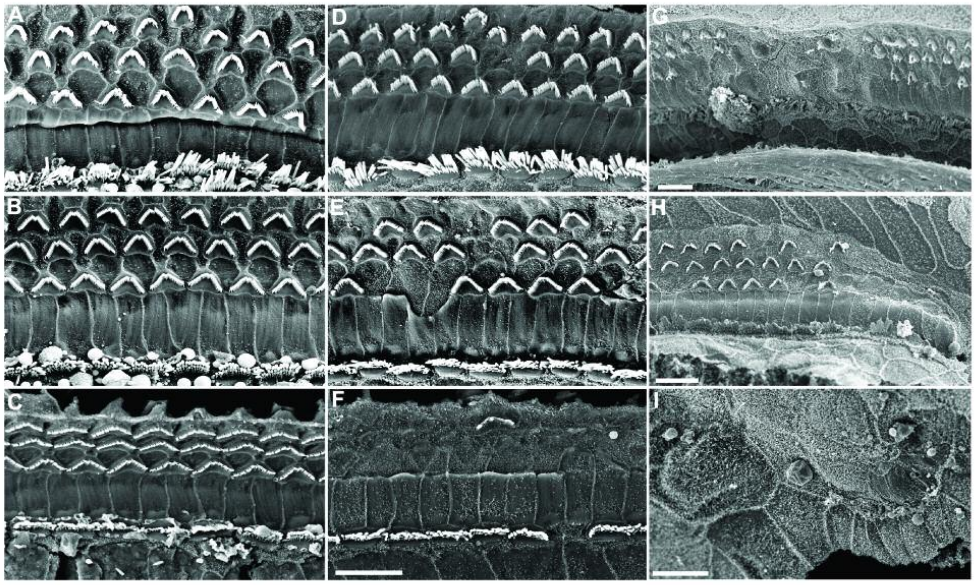

Fig 2: Analysis of wildtype, *Obl/+* and *Obl/Obl* organ of Corti by scanning electron microscopy. At 3-4 months, normal animals show three rows of outer hair cells (OHC) and one row of inner hair cells (IHC) in the apex (A), middle (B) and base (C) of the cochlea. *Obl/+* have extensive OHC loss and some IHC loss in the base of the cochlea (F) and a few missing OHC in the middle of the cochlea (E). The apex appears normal (D). At 1 month of age, the phenotype in the *Obl/Obl* mice is extremely variable. In some regions of the base, middle and apex, the phenotype is similar to that seen in *Obl/+*. However in other parts of the apex (G) and middle (H) regions of the cochlea, there are missing patches of OHCs. In some regions of the base, there is a complete degeneration of the organ of Corti, with no IHC, OHC or supporting cells such as pillar cells present (I). Scale bar = 10mm.

176x114mm (142 x 142 DPI)

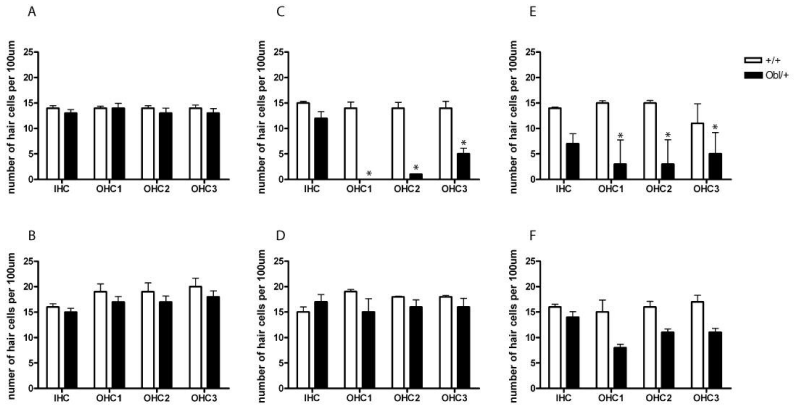

Fig 3: Hair cell counts show that outer hair cell loss in heterozygotes (*Obl*/+) at P75 is present in the base (C) but not the middle (D) of the cochlea. By P121, outer hair cell loss is seen in the base (E) and the middle (F) of the cochlear duct. IHC loss is seen in the base of the cochlea only at later ages (E). This suggests that hair cell loss in *Obl*/+ mutants progresses in a base to apex direction, with OHC loss occurring first and IHC loss later. No OHC or IHC loss was seen in the base (A) or middle (B) regions of the cochlea at P20. Hair cell counts calculated as mean number of hair cells per 100um at P20 (+/+ n=4-7, *Obl*/+ n=7), P72-75 (+/+ n=4, *Obl*/+ n=5) and P121 (+/+ n=3-4, *Obl*/+ n=4-5). Error bars indicate 95% confidence interval, T-test, * P-value <0.05.

208x296mm (142 x 142 DPI)

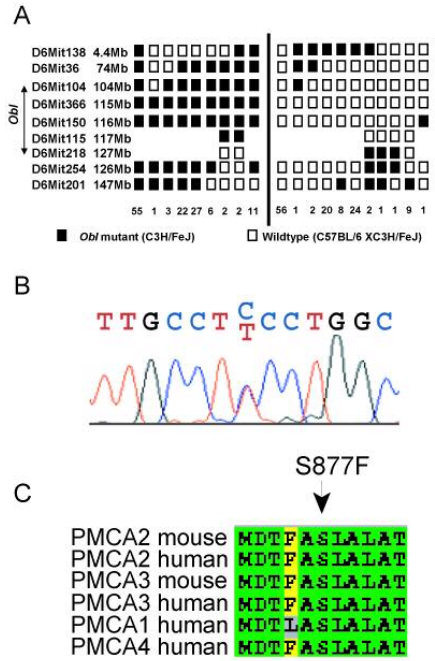

Fig 4: *Oblivion* chromosomal location, mutation and PMCA2 sequence alignment. (A) *Obl* mutation maps to a 16 Mb region on mouse chromosome 6, between *D6Mit104* and *D6Mit218*. Each box represent a marker typed, and each chromosomal arrangement detected shown, with the number of animals possessing that chromosome given underneath. If a marker was not typed then no box is present. (B) Sequence of *Atp2b2* in *Obl*/+ mouse showing the C→T mutation and predicted sequence. (C) Sequence alignment of several PMCA family members showing *Ser877* is highly conserved.
84x199mm (142 x 142 DPI)

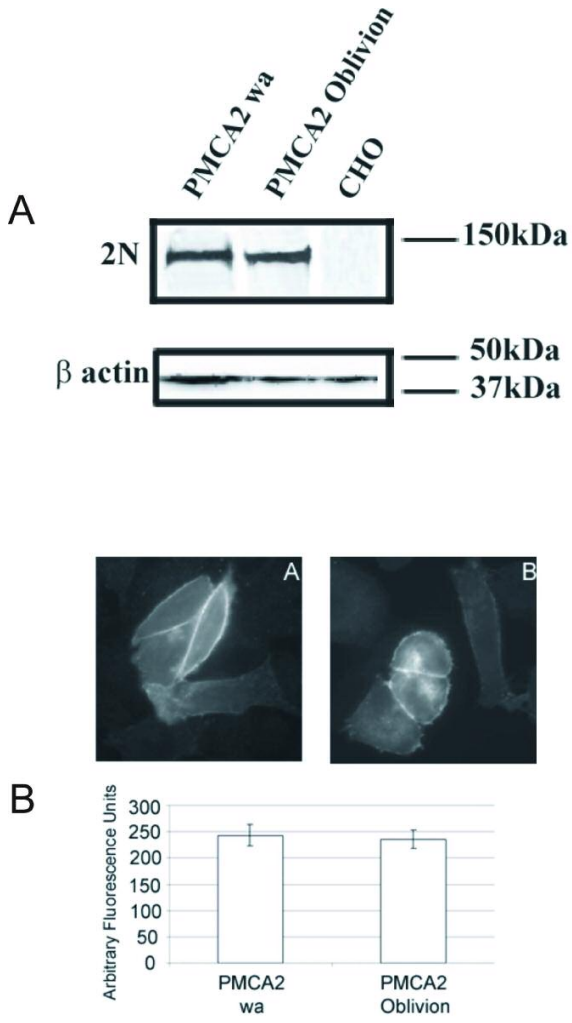

Figure 5

Fig 5: Expression and immunolocalization of recombinant PMCA2 pumps in CHO cells. (A) Western blotting analysis. 48h after transfection CHO cells were washed twice with cold PBS buffer and scraped in lysis buffer (Tris-HCl 10mM, EDTA 1mM, PMSF 2mM and DTT 1mM). After centrifugation at 1000 x g for 5 min, the cells were resuspended in 80 μl of lysis buffer and subjected to three cycles of freeze and thaw. The proteins of the lysates were quantified using the Bradford Reagent (Sigma-Aldrich). 15 μg of proteins were loaded on 10% polyacrylamide gel and transferred to nitrocellulose membranes which were incubated with polyclonal PMCA2 antibody 2N and monoclonal β-actin antibody (Sigma-Aldrich). After incubation with HRP-conjugated secondary antibodies (Santa Cruz Biotechnology, Inc., Santa Cruz, CA), the blots were developed with ECL reagents (Amersham Life Science). The band of ~130kDa corresponds to PMCA2 and the band of

~42kDa to β-actin. (B) Immunolocalization of *wt* and *Obl* PMCA2 in transiently transfected CHO cells. The interaction with 2N antibody was revealed by the AlexaFluor488-conjugated secondary antibody. Upper panel, plasma membrane pattern of the overexpressed pumps (details in Materials and Methods). (A) wild type *w/a* pump. (B) *Obl/Obl* pump. Lower panel, fluorescence level in the plasma membrane quantified as described in Material and Methods. The SDs are indicated by the bars.

146x252mm (142 x 142 DPI)

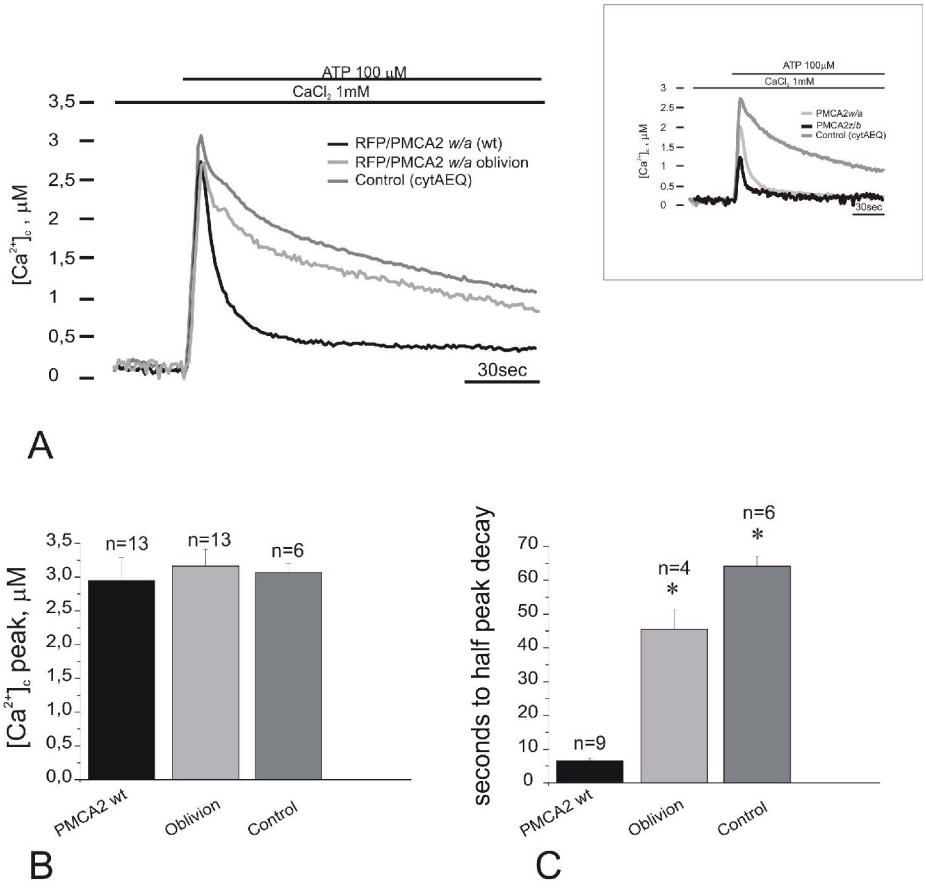

Figure 6

Fig 6: Activity of recombinant PMCA2 pumps in CHO cells. Cells were transiently co-transfected with the PMCA2 variants and cytAEQ, or only with cytAEQ (control). They were then perfused with KRB supplemented with 1 mM CaCl2. 100 µM ATP was used to produce a transient Ca^{2+} increase (A). The histograms in B and C show the means SD of Ca^{2+} peaks and the half peak decay times, respectively (n indicates the number of experiments considered for the statistical analysis) * p<0.01 calculated with respect to the wt pump. Inset, Ca^{2+} transients in cells overexpressing the wt *w/a* pump, and the *z/b* pump.

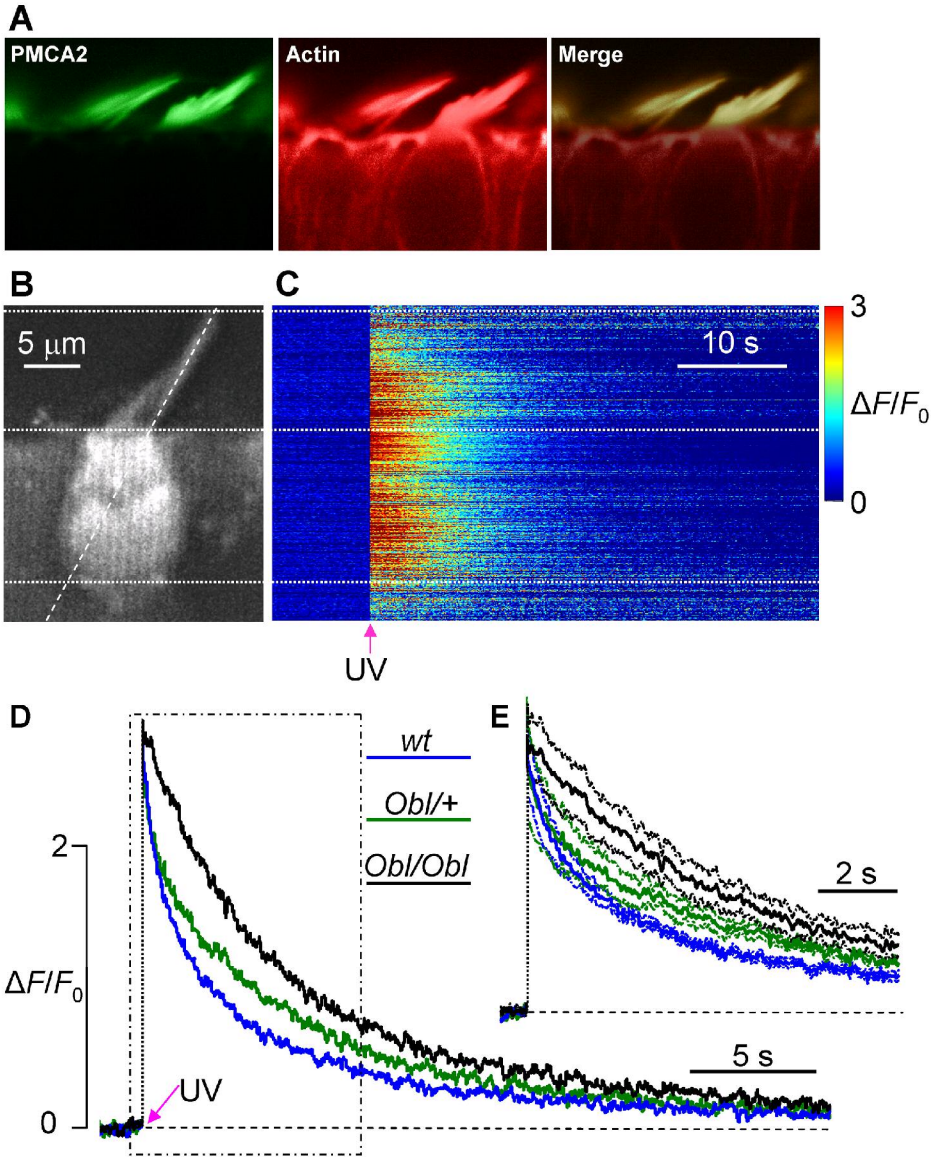

Fig 7: Dissipation of Ca^{2+} transients in utricular hair cells co-loaded with Fluo-4 and caged Ca^{2+}. (A) immunolocalization of the wt and *Obl/Obl* PMCA2 pump in the stereocilia of the utricular hair cells (details in Materials and Methods).(B) confocal image of baseline Fluo-4 fluorescence in an organotypic culture of mouse utricular macula. The diagonal dashed line represents the scan line during subsequent data acquisition. The hair bundle is comprised between the top and middle horizontal dotted lines (the latter crosses the cell cuticular plate). The cell soma is comprised within middle and lower lines. (C) in this line-scan image, ordinates are pixel positions along the scan line, abscissa is time and fluorescence transients, $\Delta F / F0$, evoked by a 4 ns UV pulse (arrow) are color-coded according to the color scale-bar at right. Signals from pixels below the lowermost horizontal dotted line arise from the cell adjacent to the hair cell in (B). (D) fluorescence traces obtained by spatially averaging line-scan pixel signals within the stereociliary compartment of wild type (*wt*, blue solid line), heterozygous (*Obl/+*, green solid line)

and homozygous *Oblivion* mice (*Obl/Obl*, black solid line). Each trace is the population average of n = 6 cells (for *wt* and *Obl/Obl*) or n = 5 cells (for *Obl/+*). The region within the dash-dotted box is shown on a faster time scale in (E). Also shown in (E) are confidence intervals (dash-dotted lines) for the average $\Delta F / F0$ responses (solid lines).
184x216mm (300 x 300 DPI)

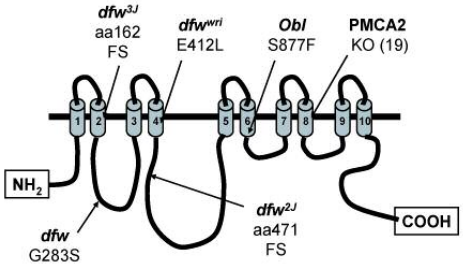

Fig 8: Mutations identified to date affecting PMCA2 protein in mice. Three mutations are missense mutations leading to amino acid substitutions (*dfw*, *wri*, *Obl*), two are small deletions that lead to frame shift mutations and premature truncation of the PMCA2 protein (*dfw*^{2J}, *dfw*^{3J}) and one is a targeted null allele (*Atp2b2*^{tm1Ges}) (13); (24); (8); (21). Adapted from (21).
86x199mm (142 x 142 DPI)

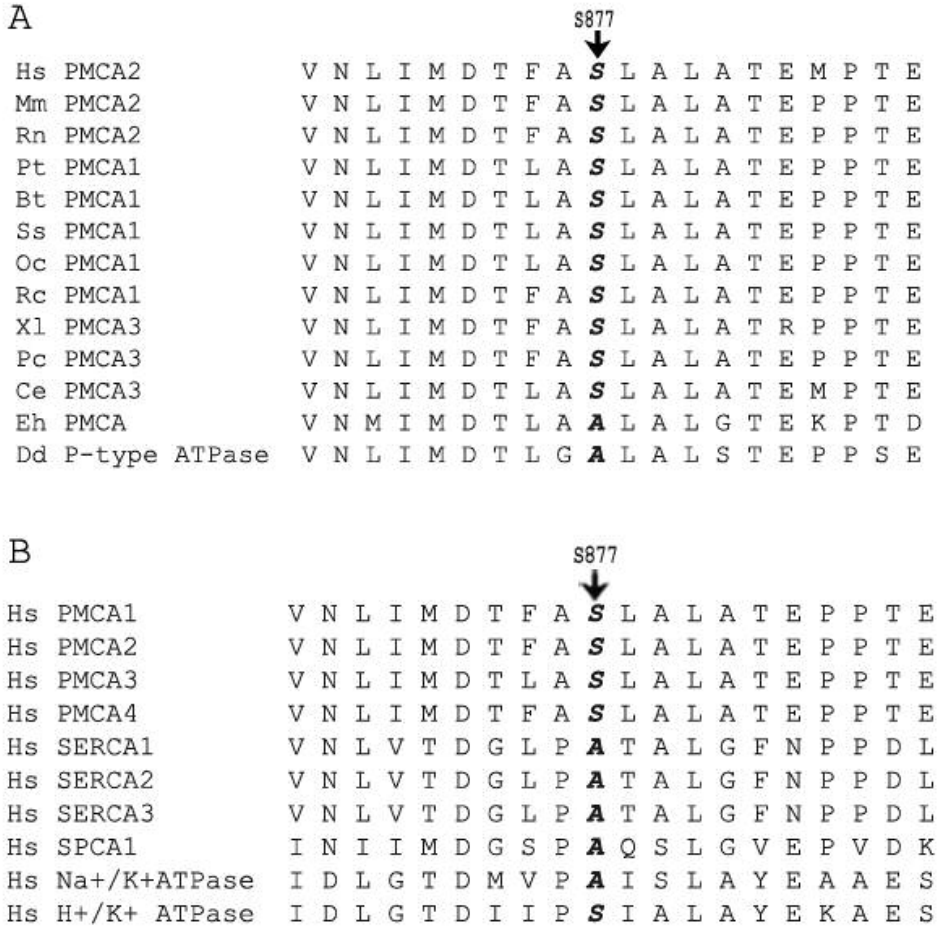

Fig 9: Alignment of the amino acids residues in transmembrane domain 6 of PMCA isoforms in different species (A) and of PMCAs and other P-type ATPases (B). The similarity analysis was performed using the ClustalW program. GenBank accession numbers are listed: NP_001674 (*Homo sapiens*), Q9ROK7 (*Mus musculus*), NP_036640 (*Rattus norvegicus*), XP_509257 (*Pan troglodytes*), NP_777121 (*Bos taurus*), NP_999517 (*Sus scrofa*), Q00804 (*Oryctolagus cuniculus*), AAK11272 (*Rana catesbeiana*), AAH77905 (*Xenopus laevis*), AAR28532 (*Procambarus clarkii*), AAK68551 (*Caenorhabditis elegans*), XP_653525 (*Entamoeba histolytica*), EAL62716 (*Dictyostelium discoideum*), NP_001001323 (PMCA1), NP_068768 (PMCA3), NP_001675 (PMCA4), NP_004311 (SERCA1), NP_733765 (SERCA2), NP_777615 (SERCA3), AAF35375 (SPCA1), NP_000693 (Na^+/K^+ ATPase) and AAH31609 (Na^+/K^+ ATPase).

87x96mm (180 x 180 DPI)

Cell Calcium (2007) **xxx**, xxx–xxx

journal homepage: www.elsevier.com/locate/ceca

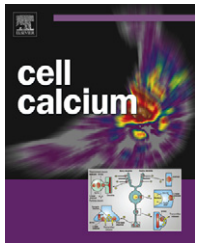

Calcium microdomains at presynaptic active zones of vertebrate hair cells unmasked by stochastic deconvolution

Mario Bortolozzi[a], **Andrea Lelli**[a,1], **Fabio Mammano**[a,b,*]

[a] *Foundation for Advanced Biomedical Research, Venetian Institute of Molecular Medicine, via G. Orus 2, 35129 Padova, Italy*
[b] *Padova University, Department of Physics ''G.Galilei'', via Marzolo 8, 35131Padova, Italy*

Received 31 May 2007; received in revised form 1 November 2007; accepted 8 November 2007

KEYWORDS
Calcium signaling;
Random walk;
Monte Carlo;
Reaction–diffusion equations;
Buffers;
Fluorescent ion indicators;
Law of mass action;
Frog;
Hair cells;
Hotspots;
Voltage-dependent calcium channels;
Calcium ATPases

Summary Signal transduction by auditory and vestibular hair cells involves an impressive ensemble of finely tuned control mechanisms, strictly depending on the local intracellular Ca^{2+} concentration ($[Ca^{2+}]_i$). The study of Ca^{2+} dynamics in hair cells (and many other cell types) typically combines Ca^{2+}-sensitive fluorescent indicators (dyes), patch clamp and optical microscopy to produce images of the patterns of fluorescence of a Ca^{2+} indicator following various stimulation protocols. Here we describe a novel method that combines fluorescence imaging and numerical simulations to effectively deconvolve Ca^{2+} signals within cytoplasmic microdomains that would otherwise remain inaccessible to direct observation. The method relies on the comparison of experimental data with virtual signals derived from a Monte Carlo reaction–diffusion model based on a realistic reconstruction of the relevant cell boundaries in three dimensions. The model comprises Ca^{2+} entry at individual presynaptic active zones followed by diffusion, buffering, extrusion and release of Ca^{2+}. Our results indicates that changes of the hair cell $[Ca^{2+}]_i$ during synaptic transmission are primarily controlled by the endogenous buffers both at short (<1 μm) and at long (tens of microns) distances from the active zones. We additionally provide quantitative estimates of concentration and kinetics of the hair cell endogenous Ca^{2+} buffers and Ca^{2+}-ATPases. We finally show that experimental fluorescence data collected during Ca^{2+} influx are not interpreted correctly if the $[Ca^{2+}]_i$ is estimated by assuming that Ca^{2+} equilibrates instantly with its reactants. In our opinion, this approach is of potentially general interest as it can be easily adapted to the study of Ca^{2+}-related phenomena in diverse biological systems.

* Corresponding author at: Istituto Veneto di Medicina Molecolare (VIMM), via G. Orus 2, 35129 Padova, Italy. Tel.: +39 049 7923 231; fax: +39 049 7923 250.
E-mail address: fabio.mammano@unipd.it (F. Mammano).
[1] Present address: Department of Neuroscience, University of Virginia Medical School, Charlottesville, VA 22908–1392, USA.

0143-4160/$ – see front matter © 2007 Elsevier Ltd. All rights reserved.
doi:10.1016/j.ceca.2007.11.007

Introduction

In sensory cells of the auditory and vestibular systems of vertebrates (hair cells), the $[Ca^{2+}]_i$ increases abruptly following opening of voltage-dependent Ca^{2+} channels in the cell basolateral membrane (reviewed in Ref. [1]). These channels cluster at each presynaptic active zone [2–5], where tens of them cooperate in imposing a ''hotspot'', i.e. a microdomain of elevated $[Ca^{2+}]_i$ [6,7] coincident with the synaptic vesicle release site [4,8–10]. Hair cell afferent synapses are of the ribbon type [11] and, in inner hair cells of the cochlea, are capable of encoding acoustic information over a wide intensity range with high temporal precision over prolonged periods of time [12,13]. Transmitter release and other processes that depend critically on the $[Ca^{2+}]_i$ exploit a number of control mechanisms that affect Ca^{2+} signals within Ca^{2+} microdomains. Besides passive diffusion of Ca^{2+} away from its site of action and buffering by variety of Ca^{2+} binding proteins [14], active control mechanisms include pumping by Ca^{2+}-ATPases (PMCA and SERCA pumps) as well as Ca-induced Ca-release [15,16].

The study of Ca^{2+} dynamics in hair cells typically combines Ca^{2+}-sensitive fluorescent dyes, patch clamp and optical microscopy to produce images of the patterns of fluorescence of a Ca^{2+} indicator following various stimulation protocols [9,10,17,18]. Obviously, optical measurements localize Ca^{2+} microdomains within the limits of optical resolution. Furthermore the measured Ca^{2+} domains reflect the combined Ca^{2+} signaling occurring in the presence of the Ca^{2+} indicator. Although very recently studies of exocytosis have started to benefit from the impressive progress in improving the optical resolution beyond the diffraction limit [19,20], the fast and localized Ca^{2+} signals underlying stimulus-secretion coupling have been (and are still) inaccessible to direct measurements [7]. Even if the required optical resolution were available, extrapolating the $[Ca^{2+}]_i$ from fluorescence imaging data would still require a mathematical model. Indeed, the $[Ca^{2+}]_i$ must be deduced from the only observable quantity that, in the most favorable case, is a linear combination of the fluorescence emission of free dye and dye bound to Ca^{2+}.

The primary aim of this work was to investigate Ca^{2+} dynamics in the hair cell by comparing experimental data to simulation results over ~1 s time intervals, for distances ranging from 0.25 μm to the entire cell (20–30 μm). In previous reports, dynamics were simulated very close to a synaptic site (within a radius of about 1 μm) and for very short periods of time (tens of ms) [8]; others simulated the entire cell volume by modeling plasma membrane with cubic or cylindrical shapes and simplified initial conditions [21,22]. Here, we opted for a different approach, based on Monte Carlo numerical simulations, to describe quantitatively the buffered diffusion of Ca^{2+} from the hotspots following cell depolarization. These types of simulations, which are essentially based upon the repetitive generation of random numbers, have been used to study reaction and diffusion processes in biological systems [23–27].

There are at least two important reasons to adopt a Monte Carlo approach in the hair cell context. First, it eases the simulation of realistic cell geometries, in particular plasma membrane and nuclear membrane. In this work we considered the nuclear membrane to be transparent to Ca^{2+}, but other possibilities would have been easily accommodated into the simulation code. Second, this approach eases the task of adapting the boundary conditions for the reaction diffusion equations to a specific model.

To simulate dye fluorescence dynamics observed in the experiments, we coupled a Monte Carlo model of diffusion processes to differential equations describing Ca^{2+} binding to its buffers, using boundary conditions based on realistic representations of the relevant cell components (membranes, hotspots location, and pumps). Simulations also took into account the (poor) axial resolution of the wide field optical apparatus and the operating conditions of the CCD camera used to acquire sequences of fluorescence images. Computer simulations reproduced experimental data extremely well, permitting us to address crucial questions in regard to (a) concentrations and dynamics of Ca^{2+} and its unknown buffers; (b) the role played by buffers and Ca^{2+}-ATPases in vestibular hair cells; (c) the nature of the noise sources affecting the fluorescence signals.

The dynamics of Ca^{2+} in the all-important stereociliary compartment are not included in the present work and will be analyzed in a future study.

Materials and methods

Cell and tissue preparation

The care and use of the animals reported in this study were approved by Animal Care and Use Committee of the University of Padua. Thin slices were obtained from the posterior semicircular canal of the frog (*Rana esculenta*, 25–30 g body weight) by sectioning the vestibular epithelium through planes parallel to the long axis of the crista using a tissue slicer (Vibroslice™, Campden Instruments Ltd., Sileby, UK), as previously described [28], while bathing the preparation in a solution containing (in mM): 130.4 NaCl, 0.7 NaH_2PO_4, 3 KCl, 5.4 $MgCl_2$, 10 HEPES–NaOH, 6 D-glucose (pH 7.25, 275 mOsm kg^{-1}). Whole crista slices were plated under the microscope and continuously superfused, at 2 ml min^{-1}, with a solution containing (in mM): 135 NaCl, 0.7 NaH_2PO_4, 3 KCl, 1.8 $CaCl_2$, 10 HEPES–NaOH, 6 D-glucose (pH 7.25, 275 mOsm kg^{-1}).

Patch clamp recording and drug delivery

Conventional whole-cell patch-clamp recordings were made under visual control using 1.5 mm o.d. glass capillaries (PG150T-10 Harvard Apparatus Ltd., Edenbridge, UK). Patch pipettes were filled with a CsCl-based intracellular solution containing (in mM): 103 CsCl, 20 TEACl, 2 $MgCl_2$, 1 ATP K^+ salt, 0.1 GTP Na^+ salt, 5 HEPES–CsOH, 0.5 EGTA (pH 7.2, 250 mOsm kg^{-1}) and designed to unmask voltage-dependent Ca^{2+} currents by blocking K^+ currents. Electrical signals were measured with a List EPC-7 patch-clamp amplifier (Heka, Lambrecht, Germany) by sampling current and voltage at 23 kHz using a standard laboratory interface (1401Plus, Cambridge Electronic Design, Cambridge, UK) controlled by customized software.

Please cite this article in press as: M. Bortolozzi, et al., Calcium microdomains at presynaptic active zones of vertebrate hair cells unmasked by stochastic deconvolution, Cell Calcium (2007), doi:10.1016/j.ceca.2007.11.007

Ca^{2+} fluorescence imaging

Fluorescence imaging of intracellular Ca^{2+} was performed as described previously [29]. Briefly, cells were loaded through the patch pipette with 50 μM Oregon Green 488 BAPTA-1 (OGB1) dissolved in the intracellular solution described above. This solution contained also 0.5 mM EGTA to chelate residual Ca^{2+} in our distilled water (estimated at ~5 μM by atomic absorption spectroscopy) and the Ca^{2+} released from the glassware used for solution preparation as well as from the patch pipette itself. [EGTA] was at the lower end of the range commonly used in imaging studies of hair cells (0.5–5.0 mM, see for instance Refs. [9,30]). To minimize the run-down of the Ca^{2+} currents, recordings were taken within 3 min after break-in to the whole-cell configuration. This time interval was generally sufficient to achieve dye loading levels that produced adequate signal-to-noise ratio at the single pixel level in response to a standard stimulus (50–160 ms depolarization to −20 mV). A narrow range of excitation wavelengths was selected around the dye's absorption maximum (494 nm) using an interference filter and a long-pass dichromatic mirror (D480/30x and 515DCXR, Chroma Technology Corporation, Brattleboro, VT, USA). Fluorescence emission, collected with a x60 objective (0.9 N.A., LUMPlanFl W.I., Olympus, Tokyo, Japan), was selected by a second filter (D535/35M, Omega Optical, Brattleboro, VT, USA) to form fluorescence images on a fast (15 MHz readout rate) CCD sensor (IA-D1, DALSA, Ontario, Canada) that was cooled by a peltier device (Marlow Industries, Dallas, TX, USA). The sensor's output was digitized at 12 bit/pixel by customized electronics to produce 128 × 128 pixel images (resolution ~0.5 μm per pixel), recorded in real time to the RAM of a host PC. Fluorescence images were acquired with a mean inter-frame interval of 4.03 ms (frame rate, 248 Hz), including 0.1 ms required for CCD data transfer. All data were analyzed off-line using the Matlab software package (The MathWorks, Inc., Natick, MA, USA) and fluorescence (f) signals were represented as $\Delta f/f_0$, i.e. fluorescence change,

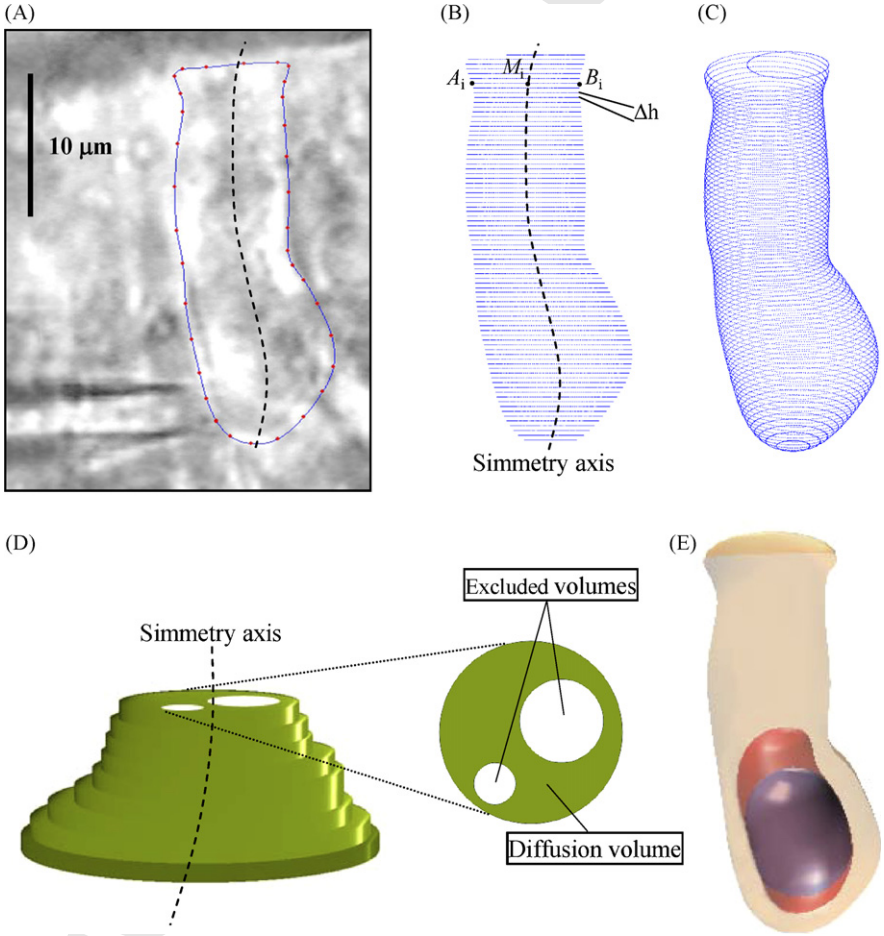

Figure 1 Construction of model cell diffusion boundaries. Starting from a bright field image of the hair cell (A), the contour of the basolateral plasma membrane in the focal plane is highlighted (dotted line) and the cylindrical symmetry axis is computed (dashed line). Thereafter a model of the cell body is constructed (B–C) as a stack of N cylinders (D). The diameter of the ith cylinder is equal to segment $\overline{A_iB_i}$ (panel B) centered on point M_i belonging to the symmetry axis, whereas height equals Δh for all cylinders. The diffusion volume within a cell is, in general, a sub-set of the cell volume comprised between the plasma membrane and intracellular membranes (D, excluded volumes). Endoplasmic reticulum SERCA pumps (E, red zones) are located above and below the nucleus (purple), whereas Ca^{2+} pumps (PMCA) are distributed homogeneously at a density of 1960/μm^2 over the plasma membrane (cutaway is shown).

Please cite this article in press as: M. Bortolozzi, et al., Calcium microdomains at presynaptic active zones of vertebrate hair cells unmasked by stochastic deconvolution, Cell Calcium (2007), doi:10.1016/j.ceca.2007.11.007

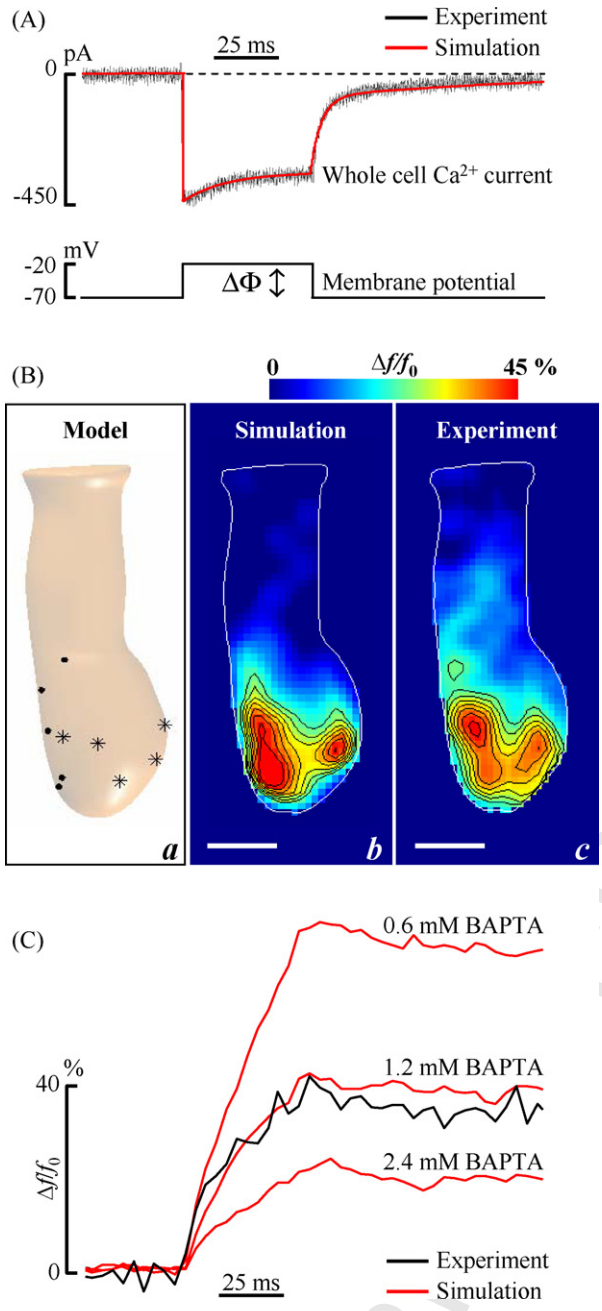

Figure 2 Experimental results vs. numerical simulations. (A) Whole cell Ca^{2+} current (top, black trace) evoked by 50 ms depolarization to −20 mV (bottom trace) for the cell in Fig. 1A; also shown is a fit to the current trace with a multi-exponential function (top, red trace) used as input in all Monte Carlo simulations of this article. (B): sub-panel *a*, model cell showing location of plasma membrane Ca^{2+} channel clusters that give rise to hotspots when the cell is depolarized (asterisks and dots represent hotspots respectively located above and below the focal plane); sub-panel *b*, fluorescence-ratio ($\Delta f/f_0$) pseudo-color image of the simulated cell after ~50 ms from the onset of Ca^{2+} influx; sub-panel *c*, corresponding image of the real cell (see also Supplementary Movie 1, online). The model cell includes 1.2 mM BAPTA as the main Ca^{2+} buffer. Each image is formed by 25 × 60 square pixels, thus pixel side equals 0.5 μm. Scale bars, 5 μm. To mitigate the effect of noise, the two images were filtered digitally through a 3 × 3 pixel median filter followed by a 3 × 3 pixel gaussian filter. No filtering was applied to any of the subsequent figures in this article. (C) $\Delta f/f_0$ mean traces obtained by spatially averaging unfiltered pixel signals over 1 μm² zones centered on each of the 10 hotspots identified in this cell. The experimental $\Delta f/f_0$ trace (black) is compared to simulation results obtained with different concentrations of BAPTA (shown above each red trace).

$\Delta f = f_0 - f_0$, divided by pre-stimulus fluorescence intensity, f_0. Image sequences were typically formed by 100–500 consecutive frames.

As the duration of all present recordings was less than 2 s, fluorescence measurements were not affected appreciably by dye exchange between cell cytoplasm and pipette interior. This was verified in controls whereby the cell was maintained at −70 mV for the duration of the recording. Under these conditions the $\Delta f/f_0$ signal remained stable.

Further methodological information is provided as Supplementary Numerical Methods, online.

Results

Voltage-activate Ca^{2+} currents and associated fluorescence signals were measured from hair cells in acute slices of the frog semicircular canals by whole-cell recordings made with intracellular solutions containing the single-wavelength Ca^{2+}-selective dye OGB1 (50 μM). To minimize washout of endogenous buffers, measurements were obtained within 3 min after break-in to the whole-cell configuration, as previously reported [18]. Imposing a depolarized potential to the patch-clamped hair cell promoted Ca^{2+} influx at selected hotspots located mostly in the lower (synaptic) half of the cell body [17,18].

The buffering power of the hair cell

To determine the spatial and temporal distribution of the $[Ca^{2+}]_i$, we compared experimental data to predictions made by a reaction–diffusion numerical model with realistic boundary conditions (Fig. 1). A detailed model description is provided as Supplementary Numerical Methods, online.

The procedure adopted to determine boundary conditions for the reaction–diffusion model is summarized in Fig. 2. We first estimated the number of active sites, n_{HOT}, by measuring the peak inward Ca^{2+} current, $I_{Ca^{2+},min}$ (Fig. 2A, black top trace), evoked by 50 ms of cell depolarization (bottom trace). The simulated Ca^{2+} influx was determined by fitting the patch-clamp current and equally distributing Ca^{2+} entry between the n_{HOT} hotspots. For the particular experiment in Fig. 2, we set $n_{HOT} = 10 \cong (I_{Ca^{2+},min}/-45\,pA)$, as $I_{Ca^{2+},min} \cong -450$ pA and −45 pA is the mean presumptive peak current at each hotspot [17,21]. Thereafter, hotspot location (Fig. 2B*a*) was inferred iteratively, by trial and error, in the attempt to match the (spatial and temporal) distribution of $\Delta f/f_0$ (Fig. 2B*b*) derived from the Monte Carlo simulations to the experimental $\Delta f/f_0$ (Fig. 2B and Supplementary Movie 1, online). The Ca^{2+} buffering power of the cytoplasm is key parameter for these simulations. Previous work showed that the endogenous buffer in frog saccular hair cells was

Please cite this article in press as: M. Bortolozzi, et al., Calcium microdomains at presynaptic active zones of vertebrate hair cells unmasked by stochastic deconvolution, Cell Calcium (2007), doi:10.1016/j.ceca.2007.11.007

equivalent to [BAPTA] ≅ 1.6 mM [31]. Here, we estimated the BAPTA-equivalent buffering power of frog semicircular canal hair cells by spatially averaging $\Delta f/f_0$ signals over the n_{HOT} hotspots shown in Fig. 2B*a* and comparing experimental data to model predictions obtained by adjusting BAPTA concentration on a trial and error basis (Fig. 2C). Based on this comparison, we suggest that the endogenous buffer in our experiments was equivalent to [BAPTA] ≅ 1.2 mM.

Although this amount of BAPTA provides a reasonable accord between simulation and experiments in the vicinity of the hotspots for time intervals of the order of 100 ms (Fig. 2C), our data indicate that the physical and chemical characteristics of the endogenous buffer depart significantly from those of BAPTA, as shown in Fig. 3A.

Indeed, the predicted buffering action exerted by 1.2 mM BAPTA fails to account for the behavior of the whole cell signal (Fig. 3A, red trace) due to its excessive diffusion speed. We thus examined other possible candidates. In frog vestibular hair cells, the most abundant Ca^{2+} buffers are parvalbumin-3 (12 kDa), calbindin-D_{28K} (28 kDa) and calretinin (29 kDa) [32,33]. Note that the binding kinetics of the latter is similar to those of BAPTA, according to Ref. [32]. A buffer with the same k_{ON} and k_{OFF} of BAPTA and the diffusion coefficient of a 29 kDa protein, here named BAPTA 29 kDa (Fig. 3A, blue solid trace), best fitted the experimental results (black trace) at a concentration of 1.7 mM. The next best candidate appeared to be calbindin-D_{28K} (orange trace, 2 mM), whereas parvalbumin (purple trace, 4 mM), whose kinetics is comparable to those of EGTA (green trace, 4.2 mM), fails to account for the experimental data. To confirm the above conclusions, we examined the time course of $\Delta f/f_0$ at the hotspots. As shown in Fig. 3B, the best fit to the experimental trace is again that provided by BAPTA 29 kDa, closely matched by calbindin-D_{28K}.

This type of analysis permits also to quantify the effects of Ca^{2+} clearance due to PMCA and SERCA pumps. Our simulations indicate that pump contributions are virtually ineffective during Ca^{2+} influx and slowly becomes more relevant (Fig. 3A, solid and dotted blue traces). After 1 s, the decrease of the $\Delta f/f_0$ signal attributable to Ca^{2+} clearance is ~13%, corresponding to ~14% of the total Ca^{2+}-buffer capacity of the cell (see also Supplementary Numerical Methods, online).

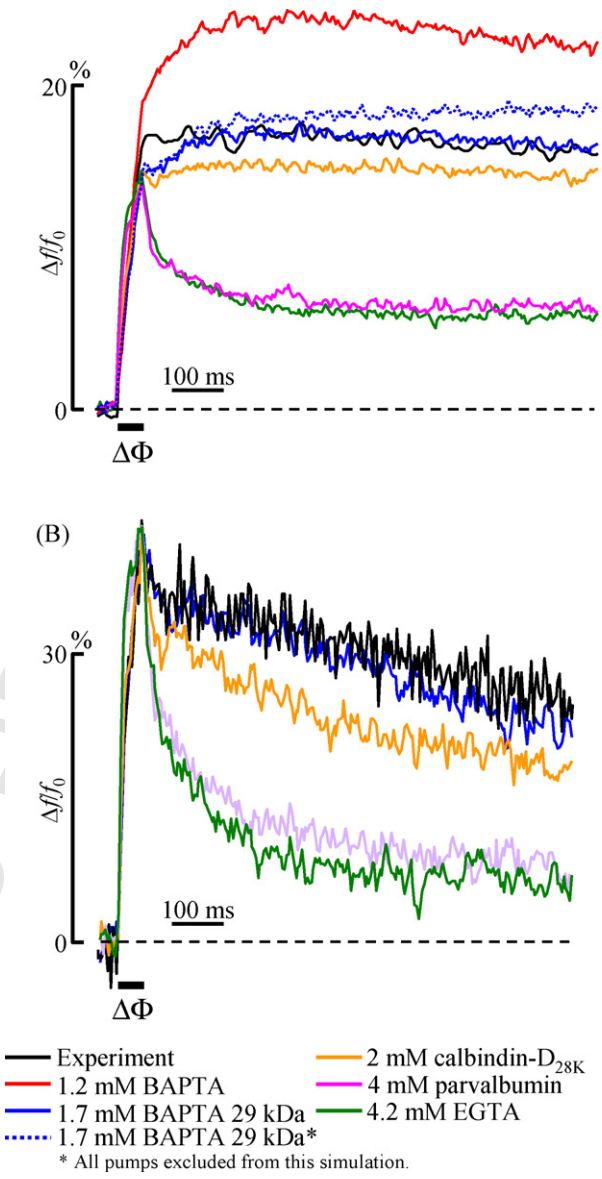

Figure 3 Model fluorescence signals for different Ca^{2+} buffers. (A) The black line is the experimental $\Delta f/f_0$ signal spatially averaged over the whole cell body; colored solid lines are model output for 1.2 mM BAPTA (red), 1.7 mM BAPTA 29 kDa (blue), 2 mM Calbindin-D_{28K} (orange), 4 mM parvalbumin (purple) and 4.2 mM EGTA (green). The dotted blue trace is model output for 1.7 mM BAPTA 29 kDa when all Ca^{2+} pumps are excluded from the simulation. $\Delta\Phi$ (black horizontal bar) corresponds to the 50 ms depolarization imparted to the real cell. (B) $\Delta f/f_0$ traces obtained, as in Fig. 2C, by limiting spatial averaging to pixels covering 1 μm^2 zones centered on the 10 hotspots identified in this cell (see Fig. 2B*a*). The experimental $\Delta f/f_0$ trace (black) is compared to simulation results obtained with 1.7 mM BAPTA 29 kDa (blue), 2 mM Calbindin-D_{28K} (orange), 4 mM parvalbumin (purple) and 4.2 mM EGTA (green).

How fluorescence signals relate to the $[Ca^{2+}]_i$ when equilibrium is perturbed

For a single wavelength dye it is customary to assume that Ca^{2+} is in equilibrium with its reactants and, consequently, the $[Ca^{2+}]_i$ is computed as

$$[Ca^{2+}]_i = k_D \frac{f - f_{min}}{f_{max} - f} \quad (1)$$

where k_D is the dissociation constant of the chemical reaction for Ca^{2+} buffering to the fluorescent dye; f, f_{max} and f_{min} are instantaneous, maximal and minimal dye fluorescence emissions, respectively [34]. In case one simply wishes to estimate the concentration changes, $\Delta[Ca^{2+}]_i$, Eq. (1) can be approximated by

$$\Delta[Ca^{2+}]_i \cong \frac{k\,\Delta f}{f_0} \quad (2)$$

where

$$k = k_D \frac{f_0(f_{max} - f_{min})}{(f_{max} - f_0)^2}. \quad (3)$$

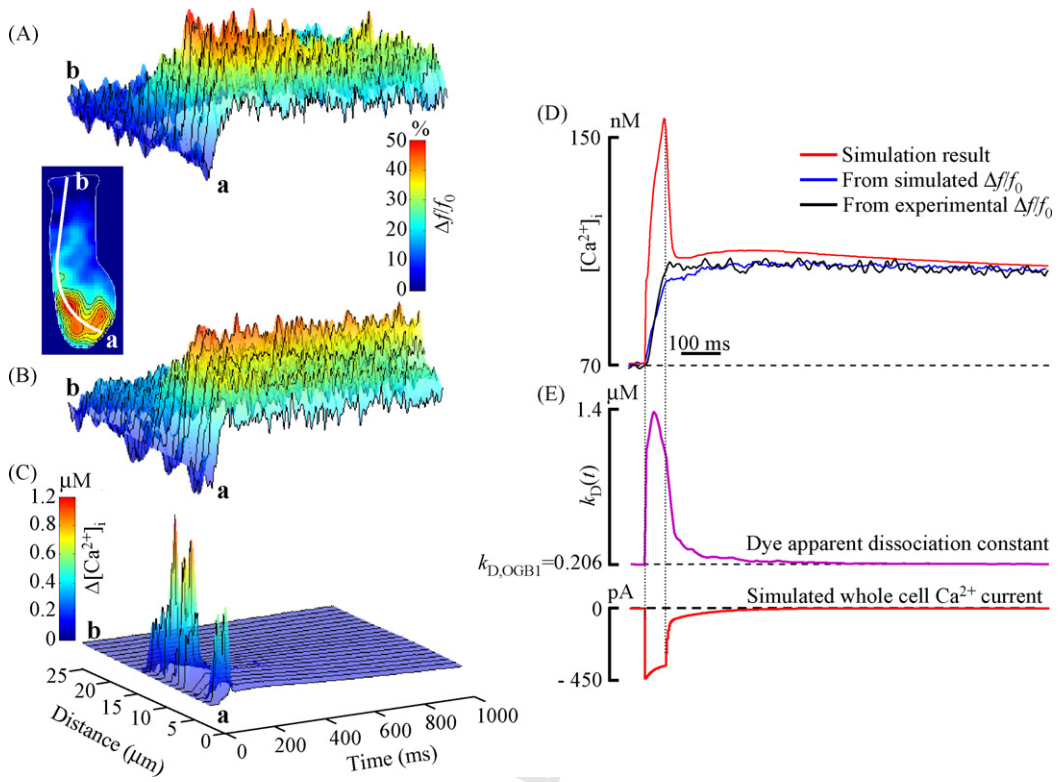

Figure 4 Fluorescence signals vs. cytosolic free Ca^{2+} concentration. (A) Pseudo-line-scan representation of $\Delta f/f_0$ signals obtained from the experiment; abscissae represent time and ordinates are distance along the white line (a to b) passing through a number of hotspots (inset). (B) Simulated $\Delta f/f_0$ signals for a model cell containing 1.7 mM BAPTA 29 kDa (see Fig. 3; see also Supplementary Movies 1–2, online). (C) $\Delta[Ca^{2+}]_i$ changes corresponding to the simulation in (B), obtained by integrating voxel Ca^{2+}-concentrations along the optical (z) axis (D) Time course of the simulated $[Ca^{2+}]_i$, integrated over the entire cell (red trace) and $[Ca^{2+}]_i$ values derived either from the simulated (blue trace) or from the experimental (black trace) $\Delta f/f_0$ whole cell signals, shown in Fig. 3A, based on the law of mass action at equilibrium. (E) Dissociation ''constant'' of the OGB1 dye (top) computed from the local simulated reactant concentrations, averaged over the entire cell volume; bottom: simulated whole cell Ca^{2+} current (same as in Fig. 2A).

However predictions based on Eqs. (1) and (2), which are derived from the law of mass action at equilibrium, break down during Ca^{2+} influx because of the local non-equilibrium of the system. To clarify this crucial issue, we estimated the $\Delta[Ca^{2+}]_i$ from $\Delta f/f_0$ signals by analyzing the model responses for 1.7 mM BAPTA 29 kDa at various points along a line drawn through the cell, intercepting a few hotspots (Fig. 4A–C).

Both measured (Fig. 4A and Supplementary Movie 1, online) and model (Fig. 4B and Supplementary Movie 2, online) $\Delta f/f_0$ signals appear as heavily low-pass filtered versions of the predicted $\Delta[Ca^{2+}]_i$ (Fig. 4C) and are thus inadequate to represent its dynamics. Indeed, the model predicts $\Delta[Ca^{2+}]_i$ values which peak abruptly in the vicinity of the hotspots during Ca^{2+} influx and thereafter decay rapidly in time and space. Fig. 4D compares a simulated $[Ca^{2+}]_i$ trace to those derived from the simulated or experimental whole cell $\Delta f/f_0$ signals, basing on the law of mass action at equilibrium. Finally, Fig. 4E shows that the spatially averaged parameter

$$k_D(t) \equiv \frac{[Ca^{2+}(t)]_i[F(t)]}{[CaF(t)]}, \quad (4)$$

(where $[F(t)]$ and $[CaF(t)]$ are, respectively, concentration of free dye and of Ca^{2+} bound to dye at time t) differs from the equilibrium value $k_{D,\,OGB1} = 0.206\ \mu M$ (dashed line) for as long as the Ca^{2+} current is significantly different from zero. These results indicate unequivocally that equilibrium conditions are heavily perturbed by Ca^{2+} influx even in the presence of millimolar concentrations of the fast buffer BAPTA 29 kDa.

Dependence of the $[Ca^{2+}]_i$ on sequestration and buffering

The analysis of fluorescence data based on our Monte Carlo simulations permits to estimate numerically the dynamics of free Ca^{2+} as well as Ca^{2+} bound to the endogenous buffer (CaB) at all points within the cell.

The spatial distribution of the $\Delta[Ca^{2+}]_i$ extrapolated from the numerical simulations is shown in Fig. 5A for 1.7 mM BAPTA 29 kDa (top panels, see also Supplementary Movie 3, online) or 4 mM parvalbumin (bottom panels). Recall that, at these concentrations, the two buffers are both effective at limiting the peak $\Delta f/f_0$ transients at the hotspots (Fig.3D). However, despite the similarity in the diffusion coefficients of parvalbumin and BAPTA 29 kDa (see Table 1), the $\Delta[Ca^{2+}]_i$ spread is larger with parvalbumin ($k_{ON} = 18.5\ \mu M^{-1}\,s^{-1}$, $k_D = 0.051\ \mu M$) as the main buffer than with BAPTA 29 kDa ($k_{ON} = 500\ \mu M^{-1}\,s^{-1}$, $k_D = 0.192\ \mu M$) during

Please cite this article in press as: M. Bortolozzi, et al., Calcium microdomains at presynaptic active zones of vertebrate hair cells unmasked by stochastic deconvolution, Cell Calcium (2007), doi:10.1016/j.ceca.2007.11.007

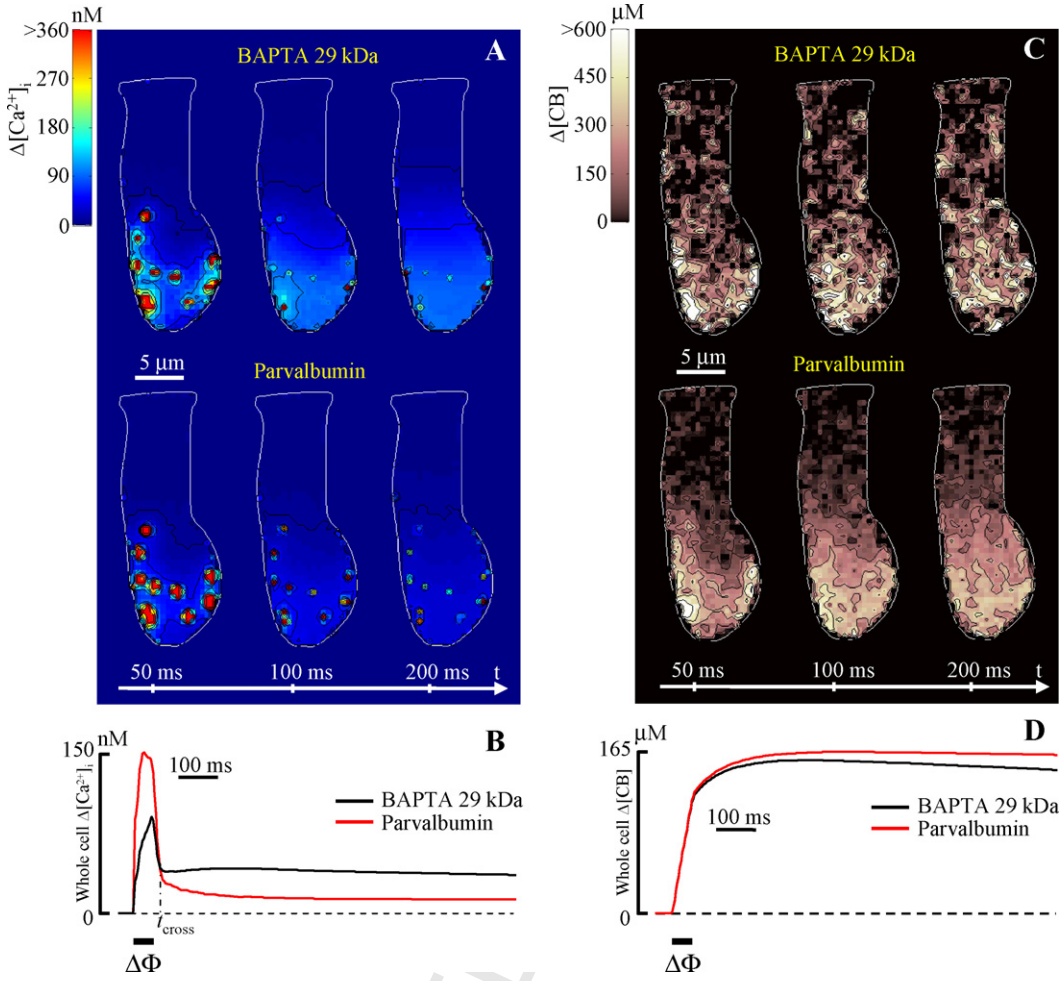

Figure 5 Time course of the extrapolated free Ca^{2+} and Ca^{2+} bound to buffer concentrations ($[Ca^{2+}]_i$ and $[CaB]_i$, respectively). (A) $\Delta[Ca^{2+}]_i$ distributions for the simulations shown in Fig. 3, averaged along the optical (z) axis, 50 ms (left), 100 ms (middle) and 200 ms (right) after the onset of cell depolarization, with 1.7 mM BAPTA 29 kDa (top panels) and 4 mM parvalbumin (bottom panels). (B) $\Delta[Ca^{2+}]_i$ traces obtained by spatially averaging voxel concentrations over the whole cell volume and by further time averaging over periods equal to the CCD camera exposure interval (4.03 ms). (C) Same as (A) for the $\Delta[CaB]$. (D) Same as (B) for the $\Delta[CaB]$. See also Supplementary Movies 3–4, online.

Ca^{2+} influx, when most of the Ca^{2+} (both free and bound) is found near the hotspots. The opposite occurs in the later phase, after diffusion homogenizes the concentration of the various mobile species. Thus, for similar diffusion coefficients, the spatial confinement of the $[Ca^{2+}]_i$ signal afforded by a given buffer depends on the combination of: (1) its total concentration; (2) k_{ON} or k_D, respectively at short and long ranges, as clearly illustrated in Fig. 5B.

Another variable that cannot be monitored directly is CaB. Irrespective of the buffer type, $\Delta[CaB]_i$ tends to decrease over time when the action of the Ca^{2+} pumps becomes appreciable. However, the decrease is notably faster with BAPTA 29 kDa (Fig. 5C, top panels, and Supplementary Movie 4, online) than with parvalbumin (Fig. 5C, bottom panels). This can be explained as an effect of the $[Ca^{2+}]_i$ that, during the recovery phase (i.e. $t > t_{cross}$ in Fig. 5B), remains higher with BAPTA 29 kDa, and thus enhances pump activity, combined with the faster rate at which Ca^{2+} is released from BAPTA 29 kDa due to its 100-fold larger k_{OOF} (Fig. 5D).

A critical issue regards the peak Ca^{2+} levels in the proximity of individual Ca^{2+} channels at the ribbon synapse. Solutions to this problem have been determined under steady-state influx conditions [8]. Fig. 6 illustrates the dependence of the $[Ca^{2+}]_i$ on both spatial and temporal variables within 1.8 μm from a hotspot for the BAPTA 29 kDa buffer at a concentration of 1.7 mM.

For simplicity, hindrance to free space diffusion from the synaptic body was not included in this description. The time course of the $\Delta[Ca^{2+}]_i$ at ~0.4 μm from the hotspot (Fig. 6A, top trace) is compared to the time course of the Ca^{2+} current (bottom trace). The line in Fig. 6B is a fit of the simulation results (points) obtained with the function:

$$\Delta[Ca^{2+}]_i = (42\ \mu M)\frac{e^{-r/(0.19\mu m)}}{r} + 0.08\ \mu M \quad (5)$$

where r is radial distance from the hotspot. A similar equation describes the steady-state $[Ca^{2+}]_i$ distribution in the case of constant Ca^{2+} influx from a point source and unsaturable diffusible Ca^{2+} buffer [31,35] (see Supplementary

Please cite this article in press as: M. Bortolozzi, et al., Calcium microdomains at presynaptic active zones of vertebrate hair cells unmasked by stochastic deconvolution, Cell Calcium (2007), doi:10.1016/j.ceca.2007.11.007

Table 1

Parameter	Value	Description
Calcium		
$M_{Ca^{2+}}$	40.078 kDa	Ca^{2+} atomic weight
$D_{Ca^{2+}}$	440 $\mu m^2\ s^{-1}$	Ca^{2+} diffusion coefficient in cytosol[a]
$[Ca^{2+}]_{i,\ 0}$	70 nM	Initial Ca^{2+} concentration in our simulations
	50–100 nM	Ca^{2+} resting concentration in hair cells [46,47]
BAPTA		
M_{BAPTA}	472.4 kDa	BAPTA atomic weight (Calbiochem data sheet)
D_{BAPTA}	270 $\mu m^2\ s^{-1}$	BAPTA (free or bound) diffusion coefficient in cytosol[a]
$k_{D,\ BAPTA}$	0.192 μM	Dissociation constant for BAPTA [48]
$k_{ON,\ BAPTA}$	500 $\mu M^{-1}\ s^{-1}$	Rate constant for Ca^{2+} binding to BAPTA [21]
$k_{OFF,\ BAPTA}$	96 s^{-1}	Rate constant for Ca^{2+} dissociation from BAPTA (computed as $k_{D,\ BAPTA} \times k_{ON,\ BAPTA}$)
$[BAPTA]_{i,\ TOT}$	1.6 mM	Equivalent endogenous buffer concentration in frog vestibular hair cells [31]
EGTA		
M_{EGTA}	380.4 kDa	EGTA atomic weight (Calbiochem data sheet)
D_{EGTA}	290 $\mu m^2\ s^{-1}$	EGTA (free and bound to Ca^{2+}) diffusion coefficient in cytosol[a]
$k_{D,\ EGTA}$	0.09 μM	Dissociation constant for EGTA [35]
$k_{ON,\ EGTA}$	9.6 $\mu M^{-1}\ s^{-1}$	Rate constant for Ca^{2+} binding to EGTA [35]
$k_{OFF,\ EGTA}$	0.864 s^{-1}	Rate constant for Ca^{2+} dissociation from EGTA (computed as $k_{D,\ EGTA} \times k_{ON,\ EGTA}$)
Calbindin-D_{28K}		
M_{Calb}	28 kDa	Calbindin-D_{28K} atomic weight (EF-Hand calcium protein database).
D_{Calb}	70 $\mu m^2\ s^{-1}$	Calbindin-D_{28K} (free and bound to Ca^{2+}) diffusion coefficient in cytosol[a]
$k_{D,\ Calb}$	0.206 μM	Dissociation constant for calbindin-D_{28K} [49]
$k_{ON,\ Calb}$	55 $\mu M^{-1}\ s^{-1}$	Rate constant for Ca^{2+} binding to calbindin-D_{28K} [49]
$k_{OFF,\ Calb}$	11.3 s^{-1}	Rate constant for Ca^{2+} dissociation from calbindin-D_{28K} (computed as $k_{D,\ Calb} \times k_{ON,\ Calb}$)
$[Calb]_{i,\ TOT}$	Lower than calretinin	Total endogenous concentration of calbindin-D_{28K} in frog saccular hair cells [32]
Parvalbumin		
M_{Parv}	12 kDa	Parvalbumin atomic weight (EF-Hand calcium protein database)
D_{Parv}	90 $\mu m^2\ s^{-1}$	Parvalbumin (free and bound to Ca^{2+}) diffusion coefficient in cytosol[a]
$k_{D,\ Parv}$	0.051 μM	Dissociation constant for parvalbumin [50]
$k_{ON,\ Parv}$	18.5 $\mu M^{-1}\ s^{-1}$	Rate constant for Ca^{2+} binding to parvalbumin (computed as $k_{OFF,\ Parv}/k_{D,\ Parv}$)
$k_{OFF,\ Parv}$	0.95 s^{-1}	Rate constant for Ca^{2+} dissociation from parvalbumin [50]
$[Parv]_{i,\ TOT}$	0.7–3 mM	Total endogenous concentration of parvalbumin in bullfrog saccular hair cells [33]
Calretinin		
M_{Calr}	29 kDa	Calretinin atomic weight (EF-Hand calcium protein database)
D_{Calr}	70 $\mu m^2\ s^{-1}$	Calretinin (free and bound to Ca^{2+}) diffusion coefficient in cytosol[a]
$[Calr]_{i,\ TOT}$	1.2 mM	Total endogenous concentration of calretinin in frog saccular hair cells [32]
Oregon Green 488 BAPTA-1 (OGB1)		
M_{OGB1}	880.3 kDa	OGB1atomic weight (Molecular Probes data sheet)
D_{OGB1}	220 $\mu m^2\ s^{-1}$	OGB1 (free and bound to Ca^{2+}) diffusion coefficient in cytosol[a]
$k_{D,\ OGB1}$	0.206 μM	Dissociation constant for OGB1[51]
$k_{ON,\ OGB1}$	930 $\mu M^{-1}\ s^{-1}$	Rate constant for Ca^{2+} binding to OGB1 (assumed to be equal to k_{ON} of Calcium Green-1 at 30 °C) [52]
$k_{OFF,\ OGB1}$	190 s^{-1}	Rate constant for Ca^{2+} dissociation from OGB1 (computed as $k_{D,\ OGB1} \times k_{ON,\ OGB1}$)
$[OGB1]_{i,\ TOT}$	50 μM	Total cytosolic concentration of OGB1 in our simulations. The same concentration was present in the patch pipette
$\alpha = f_{max}/f_{min}$	5	Measured in our lab for OGB1
	4.3–5.7	Measured for OGB1 in Ref. [51]
Calcium pumps		
$K_{M,\ PMCA}$	0.5 μM	PMCA pump Michaelis constant [53]
V_{max}	0.193 mM s^{-1}	Derived by assuming a PMCA pump density of 1960 molecules μm^{-2} and a maximal turnover rate of $\nu = 100\ s^{-1}$ for a Ca^{2+} pump molecule [21,53]
$K_{M,\ SERCA}$	0.219 μM	SERCA pump Michaelis constant [53]
V_{max}	0.213 mM s^{-1}	Maximum velocity of the SERCA pump used in our simulations

[a] For value computation see Section 9 of Supplementary Numerical Methods, online.

Please cite this article in press as: M. Bortolozzi, et al., Calcium microdomains at presynaptic active zones of vertebrate hair cells unmasked by stochastic deconvolution, Cell Calcium (2007), doi:10.1016/j.ceca.2007.11.007

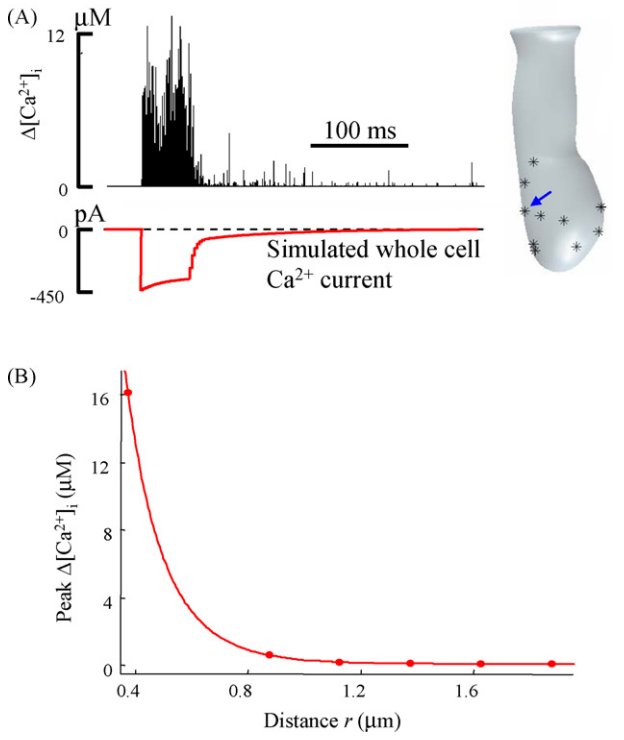

Figure 6 Extrapolated free Ca^{2+} dynamics near a single hotspot during stochastic Ca^{2+} influx in the presence of 1.7 mM BAPTA 29 kDa. (A) Simulated fluctuations of the $\Delta[Ca^{2+}]_i$ (top) in a volume of 0.6 μm^3 around the selected hotspot (blue arrow, right). The simulated whole cell Ca^{2+} current is also shown to highlight the dependence of Ca^{2+} influx probability on current amplitude. (B) Peak $\Delta[Ca^{2+}]_i$ vs. radial distance, r, from the selected hotspot.

Numerical Methods, online). These simulations indicate that the peak $\Delta[Ca^{2+}]_i$ decreases rapidly to sub-μM concentrations within the first micron from a hotspot. Although the $\Delta[Ca^{2+}]_i \cong 15$ μM at $r = 0.4$ μm, it decreases to minus than 100 nM at $r = 1.5$ μm.

Discussion

Advantages and disadvantages of the Monte Carlo approach to the study of Ca^{2+} dynamics

The above results indicate that simulations can be used as a computational nanoscope, which permits to derive images of complex and otherwise inaccessible biomolecular events well below the resolution limit of the optical microscope. We call this type of data processing ''stochastic deconvolution''.

Monte Carlo simulations have been used previously to study reaction and diffusion processes in biological systems [23–25,36–39], including Ca^{2+} dynamics [26,27,40–43]. One advantage of the method here described is the possibility of simulating with great accuracy 3D diffusion in the presence of realistic boundaries. In particular, our algorithm generates particle movements in a continuum without resorting to the use of fix [39] or variable [37] spatial grids.

Combining diffusion with computation of chemical reactions permits a suitable choice of the temporal resolution Δt (step of the random walk), independent from the spatial resolution L, i.e. of the maximal side of voxels in which chemical reactions are computed. The criterion used to minimize computational errors is that, after each step Δt, the net percentage of particles transferred from a given voxels to its neighbors must be small enough to avoid generation of local abrupt concentration changes. This condition becomes critical in the vicinity of Ca^{2+} sources, i.e. near the hotspots. In our computation of chemical reactions, approximations such as rapid buffer [27] or constancy of the total buffer concentration [26] are avoided and replaced by the analytical (up to the fifth order of Taylor's development) solution of the full equations, computed with a fine time step of the order of $\Delta t/25$.

The traditional Monte Carlo approach is confronted with the difficulty of handling reacting chemical species with greatly different concentrations, e.g. free Ca^{2+} (nM range) and endogenous buffer (mM range). The naive approach, in which a unique proportionality constant links molar concentrations to simulated particle numbers, is prone to numerical instabilities because particle counts of low-concentration species may jump abruptly, in a given voxel, from non-zero to zero values and vice versa. In our algorithm, instabilities are avoided by simulating different chemical species with the same (sufficiently large) number of particles, i.e. by using for each species a different proportionality (mapping) factor, χ, between real molecules and simulated particles (for details, see Supplementary Numerical Methods, online). Simulating 1 s of real time with, typically, 1.5×10^5 particles, $\Delta t = 10^{-5}$ s and $L = 0.5$ μm (~10^4 voxels) requires ~48 h on a 1.8 GHz CPU.

Clues to noise, diffusion and buffering from the analysis of $\Delta f/f_0$ traces

Our results show that, at model convergence, simulated and experimental $\Delta f/f_0$ signals are, of course, comparable in magnitude. They are also affected by random fluctuations (noise) of similar amplitude. This came as a surprise since (a) the signal-to-noise ratio in the simulations scales correctly as $\sqrt{N}$, where N is the number of diffusing particles, and (b) the ratio of real dye molecules to simulated particles was $\chi \cong 750$. We conclude that noise in the detection processes and recording apparatus is the dominant factor affecting the quality of the experimental data. It exceeds, by as much as 27-fold, the amplitude of the fluctuations due to the random nature of the diffusion process.

The analysis of $\Delta f/f_0$ near the hotspots permits us to estimate, by trial and error, the concentration and kinetics of the equivalent endogenous Ca^{2+} buffer in the modeled hair cell (Fig. 1). During the first 100 ms from the onset of Ca^{2+} influx, our simulations with 1.2 mM BAPTA as equivalent to the endogenous buffer (Fig. 2) fit well our experimental traces near the hotspots, in good agreement with the results obtained by Roberts [31] in frog saccular hair cells. However, they fail to fit experimental traces away from the hotspots. This discrepancy can be attributed to the diffusion coefficient of BAPTA, which is rather large (270 $\mu m^2 s^{-1}$) compared to the most representative hair cell

Please cite this article in press as: M. Bortolozzi, et al., Calcium microdomains at presynaptic active zones of vertebrate hair cells unmasked by stochastic deconvolution, Cell Calcium (2007), doi:10.1016/j.ceca.2007.11.007

endogenous Ca^{2+} buffers, such as calretinin, calbindin-D_{28K} or parvalbumin, whose diffusion coefficients range from 70 to 100 $\mu m^2 s^{-1}$ (see Table 1). Fitting the experimental $\Delta f/f_0$ signal both over the whole cell (Fig. 3A) and near the hotspots (Fig. 3B) requires a slower diffusion coefficient of $\sim$70 $\mu m^2 s^{-1}$ for the endogenous buffer, corresponding to a 29 kDa molecule, at a concentration of 1.7 mM (this value is also derived, independently, by the procedure described in Supplementary Numerical Methods, online). Our working hypothesis is that this type of buffer, referred to as ''BAPTA 29 kDa'' in this article, has properties compatible with those of calretinin. The latter is thought to be the predominant buffer in frog saccular tall hair cells [32] but, unfortunately, its k_{ON} and k_{OFF} have not been determined experimentally. Buffers with different combinations of k_{ON} and k_{OFF}, namely those of calbindin-D_{28K} and parvalbumin (see Table 1), as well as of EGTA (present in the patch pipette) fail to produce results in agreement with the experimental data (Fig. 3). In particular, neither parvalbumin nor EGTA contribute significantly to the kinetics of $\Delta f/f_0$. In fact, at cell repolarization (when Ca^{2+} influx rapidly declines), the simulated $\Delta f/f_0$ signal decays rapidly both near the hotspots and throughout the rest of the cell body because the $[Ca^{2+}]_i$ is far from being in equilibrium with its buffers. Our results indicate that when the $\Delta f/f_0$ signal, spatially averaged over the whole cell (Fig. 3A), is nearly stationary (apart from a slow decline due to Ca^{2+} clearance by the pumps), it continues to decline near the hotspots (Fig. 3B) due to Ca^{2+} removal by mobile buffers. Our results also indicate that pump contributions become relevant only after cessation of the Ca^{2+} influx. By that time, both dye (Fig. 4E) and endogenous buffer (Fig. 5D) have attained local equilibrium with Ca^{2+}. After this time, the slow recovery of the $[Ca^{2+}]_i$ (and consequently of $\Delta f/f_0$) to the pre-stimulus level, is due only to extrusion by the PMCAs and uptake by the SERCAs into the endoplasmic reticulum. Approximately 1 s after the onset of Ca^{2+} influx, pumps contributed to $\sim$14% of the cell total Ca^{2+}-buffer capacity.

Stochastic deconvolution of Ca^{2+} signals

If Ca^{2+} buffering depended solely to 50 μM OGB1 (Ca^{2+} dye), the mean capture time [35] for Ca^{2+} ions before cell depolarization would be $\tau_{c,F} = 1/([F]k^F_{ON}) \cong 29$ μs; this value would increase during Ca^{2+} influx as [F] is rapidly decreased by Ca^{2+} binding, particularly near the hotspots. In the presence of a fast buffer B, such as BAPTA 29 kDa (1.7 mM), the $[Ca^{2+}]_i$ is controlled primarily by [B] and the mean capture time is dominated by $\tau_{c,B} = 1/([B]k^B_{ON}) \cong 1.6$ μs. Thus the Ca^{2+} dye is too slow to follow the fast increase of the $[Ca^{2+}]_i$ near the hotspots and the $\Delta f/f_0$ signals (Fig. 4A–B) represent spatially and temporally low-pass filtered version of the $[Ca^{2+}]_i$ (Fig. 4C).

$[Ca^{2+}]_i$ peaks at the hotspots were larger with parvalbumin than with BAPTA 29 kDa (Fig. 5A) despite the higher parvalbumin concentration, thus k_{ON} (500 $\mu M^{-1} s^{-1}$ BAPTA vs. 18.5 $\mu M^{-1} s^{-1}$ parvalbumin) is more important than k_D (0.192 μM vs. 0.051 μM) in limiting the Ca^{2+} spread. On the contrary, at longer spatial and temporal ranges, parvalbumin exhibits larger buffering power, thus k_D is more important than k_{ON} as equilibrium is approached (Fig. 5A and B). We conclude that differences in buffer kinetics rebound on different spatial ranges of cytoplasmic Ca^{2+} signaling.

Recently, it has been suggested that exocytosis might be predominantly controlled by one or few Ca^{2+} channels located in nanometer proximity from a vesicle release site [44]. The non-saturation of the Ca^{2+}-sensor for vesicle fusion and the high cooperativity of Ca^{2+} (with 4–5 Ca^{2+} ions needed) render small changes of the local Ca^{2+}-signal highly effective in changing the release probability. Furthermore, it has been determined that surprisingly small (10–25 μM) and brief (<1 ms) local Ca^{2+} signals suffice to achieve the amount and the kinetics of the physiological transmitter release [45]. Our simulations indicate that there is ample scope for fine tuning of the mechanisms underlying exocytosis by a combination of geometrical constraints and buffering power. The approach highlighted here can be seamlessly extended to the investigation of Ca^{2+} dynamics in the submicron distance range, as hinted in Supplementary Fig. 2, online.

Acknowledgements

We thank our colleagues of the Venetian Institute of Molecular Medicine (Padua, Italy), C.D. Ciubotaru for help with computer programming and image processing, S. Pantano for help in the estimation of the cytosolic free calcium diffusion constant and S. Bastianello for helpful comments.

Appendix A. Supplementary data

Supplementary data associated with this article can be found, in the online version, at doi:10.1016/j.ceca.2007.11.007.

References

[1] F. Mammano, M. Bortolozzi, S. Ortolano, F. Anselmi, Ca^{2+} signaling in the inner ear, Physiology (Bethesda) 22 (2007) 131–144.
[2] R.S. Lewis, A.J. Hudspeth, Voltage- and ion-dependent conductances in solitary vertebrate hair cells, Nature 304 (1983) 538–541.
[3] J.J. Art, R. Fettiplace, Variation of membrane properties in hair cells isolated from the turtle cochlea, J. Physiol. 385 (1987) 207–242.
[4] W.M. Roberts, R.A. Jacobs, A.J. Hudspeth, Colocalization of ion channels involved in frequency selectivity and synaptic transmission at presynaptic active zones of hair cells, J. Neurosci. 10 (1990) 3664–3684.
[5] D. Zenisek, V. Davila, L. Wan, W. Almers, Imaging calcium entry sites and ribbon structures in two presynaptic cells, J. Neurosci. 23 (2003) 2538–2548.
[6] M.J. Berridge, Calcium microdomains: organization and function, Cell Calcium 40 (2006) 405–412.
[7] M. Oheim, F. Kirchhoff, W. Stuhmer, Calcium microdomains in regulated exocytosis, Cell Calcium 40 (2006) 423–439.
[8] W.M. Roberts, Localization of calcium signals by a mobile calcium buffer in frog saccular hair cells, J. Neurosci. 14 (1994) 3246–3262.
[9] T. Tucker, R. Fettiplace, Confocal imaging of calcium microdomains and calcium extrusion in turtle hair cells, Neuron 15 (1995) 1323–1335.
[10] N.P. Issa, A.J. Hudspeth, Clustering of Ca^{2+} channels and Ca(2+)-activated K^+ channels at fluorescently labeled presy-

naptic active zones of hair cells, Proc. Natl. Acad. Sci. U.S.A. 91 (1994) 7578–7582.
[11] R. Nouvian, D. Beutner, T.D. Parsons, T. Moser, Structure and function of the hair cell ribbon synapse, J. Membr. Biol. 209 (2006) 153–165.
[12] P.A. Fuchs, Time and intensity coding at the hair cell's ribbon synapse, J. Physiol. 566 (2005) 7–12.
[13] C.B. Griesinger, C.D. Richards, J.F. Ashmore, Fast vesicle replenishment allows indefatigable signalling at the first auditory synapse, Nature 435 (2005) 212–215.
[14] C.M. Hackney, S. Mahendrasingam, A. Penn, R. Fettiplace, The concentrations of calcium buffering proteins in mammalian cochlear hair cells, J. Neurosci. 25 (2005) 7867–7875.
[15] A. Verkhratsky, Physiology and pathophysiology of the calcium store in the endoplasmic reticulum of neurons, Physiol. Rev. 85 (2005) 201–279.
[16] R. Rizzuto, T. Pozzan, Microdomains of intracellular Ca^{2+}: molecular determinants and functional consequences, Physiol. Rev. 86 (2006) 369–408.
[17] G. Rispoli, M. Martini, M.L. Rossi, F. Mammano, Dynamics of intracellular calcium in hair cells isolated from the semicircular canal of the frog, Cell Calcium 30 (2001) 131–140.
[18] A. Lelli, P. Perin, M. Martini, C.D. Ciubotaru, I. Prigioni, P. Valli, M.L. Rossi, F. Mammano, Presynaptic calcium stores modulate afferent release in vestibular hair cells, J. Neurosci. 23 (2003) 6894–6903.
[19] R.J. Kittel, C. Wichmann, T.M. Rasse, W. Fouquet, M. Schmidt, A. Schmid, D.A. Wagh, C. Pawlu, R.R. Kellner, K.I. Willig, S.W. Hell, E. Buchner, M. Heckmann, S.J. Sigrist, Bruchpilot promotes active zone assembly, Ca^{2+} channel clustering, and vesicle release, Science 312 (2006) 1051–1054.
[20] K.I. Willig, S.O. Rizzoli, V. Westphal, R. Jahn, S.W. Hell, STED microscopy reveals that synaptotagmin remains clustered after synaptic vesicle exocytosis, Nature 440 (2006) 935–939.
[21] Y.C. Wu, T. Tucker, R. Fettiplace, A theoretical study of calcium microdomains in turtle hair cells, Biophys. J. 71 (1996) 2256–2275.
[22] J.D. Hall, S. Betarbet, F. Jaramillo, Endogenous buffers limit the spread of free calcium in hair cells, Biophys. J. 73 (1997) 1243–1252.
[23] M.J. Saxton, Anomalous diffusion due to obstacles: a Monte Carlo study, Biophys. J. 66 (1994) 394–401.
[24] M.J. Saxton, Anomalous diffusion due to binding: a Monte Carlo study, Biophys. J. 70 (1996) 1250–1262.
[25] P.J. Kruk, H. Korn, D.S. Faber, The effects of geometrical parameters on synaptic transmission: a Monte Carlo simulation study, Biophys. J. 73 (1997) 2874–2890.
[26] A. Gil, J. Segura, J.A. Pertusa, B. Soria, Monte Carlo simulation of 3D buffered Ca(2+) diffusion in neuroendocrine cells, Biophys. J. 78 (2000) 13–33.
[27] M.R. Bennett, L. Farnell, W.G. Gibson, The probability of quantal secretion near a single calcium channel of an active zone, Biophys. J. 78 (2000) 2201–2221.
[28] S. Masetto, G. Russo, I. Prigioni, Differential expression of potassium currents by hair cells in thin slices of frog crista ampullaris, J. Neurophysiol. 72 (1994) 443–455.
[29] F. Mammano, M. Canepari, G. Capello, R.B. Ijaduola, A. Cunei, L. Ying, F. Fratnik, A. Colavita, An optical recording system based on a fast CCD sensor for biological imaging, Cell Calcium 25 (1999) 115–123.
[30] A.J. Ricci, M. Gray-Keller, R. Fettiplace, Tonotopic variations of calcium signalling in turtle auditory hair cells, J. Physiol. 524 (Pt. 2) (2000) 423–436.
[31] W.M. Roberts, Spatial calcium buffering in saccular hair cells, Nature 363 (1993) 74–76.
[32] B. Edmonds, R. Reyes, B. Schwaller, W.M. Roberts, Calretinin modifies presynaptic calcium signaling in frog saccular hair cells, Nat. Neurosci. 3 (2000) 786–790.
[33] S. Heller, A.M. Bell, C.S. Denis, Y. Choe, A.J. Hudspeth, Parvalbumin 3 is an abundant Ca^{2+} buffer in hair cells, J. Assoc. Res. Otolaryngol. 3 (2002) 488–498.
[34] J.P.Y. Kao, Practical aspects of measuring $[Ca^{2+}]$ with fluorescent indicators, in: R. Nuccitelli (Ed.), A Practical Guide to the Study of Calcium in Living Cells, Academic Press, San Diego, 1994.
[35] E. Neher, Concentration profiles of intracellular calcium in the presence of a diffusible chelator, Exp. Brain Res. 14 (1986) 80–96.
[36] M.R. Riley, H.M. Buettner, F.J. Muzzio, S.C. Reyes, Monte Carlo simulation of diffusion and reaction in two-dimensional cell structures, Biophys. J. 68 (1995) 1716–1726.
[37] T.M. Bartol Jr., B.R. Land, E.E. Salpeter, M.M. Salpeter, Monte Carlo simulation of miniature endplate current generation in the vertebrate neuromuscular junction, Biophys. J. 59 (1991) 1290–1307.
[38] B.P. Olveczky, A.S. Verkman, Monte Carlo analysis of obstructed diffusion in three dimensions: application to molecular diffusion in organelles, Biophys. J. 74 (1998) 2722–2730.
[39] G.R. Stibitz, Calculating diffusion in biological systems by random walks with special reference to gases diffusion in the lung, Respir. Physiol. 7 (1969) 230–262.
[40] J. Segura, A. Gil, B. Soria, Modeling study of exocytosis in neuroendocrine cells: influence of the geometrical parameters, Biophys. J. 79 (2000) 1771–1786.
[41] J.S. Coggan, T.M. Bartol, E. Esquenazi, J.R. Stiles, S. Lamont, M.E. Martone, D.K. Berg, M.H. Ellisman, T.J. Sejnowski, Evidence for ectopic neurotransmission at a neuronal synapse, Science 309 (2005) 446–451.
[42] L. He, X.S. Wu, R. Mohan, L.G. Wu, Two modes of fusion pore opening revealed by cell-attached recordings at a synapse, Nature 444 (2006) 102–105.
[43] M.D. Stern, H. Cheng, Putting out the fire: what terminates calcium-induced calcium release in cardiac muscle? Cell Calcium 35 (2004) 591–601.
[44] A. Brandt, D. Khimich, T. Moser, Few CaV1.3 channels regulate the exocytosis of a synaptic vesicle at the hair cell ribbon synapse, J. Neurosci. 25 (2005) 11577–11585.
[45] R. Schneggenburger, E. Neher, Presynaptic calcium and control of vesicle fusion, Curr. Opin. Neurobiol. 15 (2005) 266–274.
[46] M. Ohtani, G. Devau, J. Lehouelleur, A. Sans, Cholinergic agonists increase intracellular calcium concentration in frog vestibular hair cells, Hear Res. 80 (1994) 167–173.
[47] E.A. Lumpkin, A.J. Hudspeth, Detection of Ca^{2+} entry through mechanosensitive channels localizes the site of mechanoelectrical transduction in hair cells, Proc. Natl. Acad. Sci. U.S.A. 92 (1995) 10297–10301.
[48] R.Y. Tsien, New calcium indicators and buffers with high selectivity against magnesium and protons: design, synthesis, and properties of prototype structures, Biochemistry 19 (1980) 2396–2404.
[49] U.V. Nagerl, D. Novo, I. Mody, J.L. Vergara, Binding kinetics of calbindin-D(28k) determined by flash photolysis of caged Ca(2+), Biophys. J. 79 (2000) 3009–3018.
[50] S.H. Lee, B. Schwaller, E. Neher, Kinetics of Ca^{2+} binding to parvalbumin in bovine chromaffin cells: implications for $[Ca^{2+}]$ transients of neuronal dendrites, J. Physiol. 525 (Pt. 2) (2000) 419–432.
[51] M. Maravall, Z.F. Mainen, B.L. Sabatini, K. Svoboda, Estimating intracellular calcium concentrations and buffering without wavelength ratioing, Biophys. J. 78 (2000) 2655–2667.
[52] M. Eberhard, P. Erne, Calcium binding to fluorescent calcium indicators: calcium green, calcium orange and calcium crimson, Biochem. Biophys. Res. Commun. 180 (1991) 209–215.
[53] E.A. Lumpkin, A.J. Hudspeth, Regulation of free Ca^{2+} concentration in hair-cell stereocilia, J. Neurosci. 18 (1998) 6300–6318.

Please cite this article in press as: M. Bortolozzi, et al., Calcium microdomains at presynaptic active zones of vertebrate hair cells unmasked by stochastic deconvolution, Cell Calcium (2007), doi:10.1016/j.ceca.2007.11.007

SUPPLEMENTARY NUMERICAL METHODS

1 Cell boundary construction

Figure 1A of the Main Text shows an image of the hair cell to be simulated, with the contour of the basolateral plasma membrane drawn in the focal plane. To construct cell boundaries, generalized cylindrical symmetry is assumed for the hair cell, whereby the symmetry axis is a smooth curve lying in the focal plane. To design a three dimensional (3D) model of the membrane, the interpolated two dimensional contours are intersected by a family of N straight lines equally spaced by a distance Δh (typically $\Delta h \cong 0.1$ μm; Figure 1B of the Main Text). The midpoint M_i, $(i = 1,\ldots,N)$ between the two intersection points A_i, B_i of the contour with the *i*–th straight line defines the centroid of a cylinder Γ_i of radius $\rho_i = \overline{A_i B_i}/2$, with axis in the cell contour plane and orthogonal to $A_i B_i$ The collection of such cylinders is assumed to represent the entire cell volume (Figure 1C of the Main Text), with accuracy determined by N. The diffusion volume is, in general, a sub–set of the cell volume comprised between intracellular membranes and the plasma membrane. To define selected sub–volumes with cylindrical sections, a procedure similar to the one just outlined (Figure 1D–E of the Main Text) is applied.

2 Diffusion equation and random walk

According to Fick's second law, the function that describes the concentration C of a set of N identical *molecules* diffusing in a *free, homogeneous and isotropic medium* is

$$C(x,y,z;\Delta t) \equiv \frac{M}{(4\pi D\ \Delta t)^{3/2}} e^{-\frac{(x^2+y^2+z^2)}{4D\ \Delta t}} = \frac{N}{N_A\ \cdot (4\pi D\ \Delta t)^{3/2}} e^{-\frac{(x^2+y^2+z^2)}{4D\ \Delta t}}$$

Equation 1

where C is measured Δt seconds after the onset of diffusion in the point with (x,y,z) coordinates referred to the point source placed in the origin of the Cartesian axes [1]. M is the number of mols, $N_A = 6.022 \cdot 10^{23}$ is Avogadro's number and D is diffusion constant ($\mu m^2\ s^{-1}$).

For $N \to 1$, the function $N_A \cdot C(x,y,z;\Delta t)$ can be interpret as the probability that a single diffusing molecule is found at a point of coordinates (x,y,z). From Equation 1, this equals the product of three independent probabilities P_x, P_y, P_z of a displacement along the axes x, y, z:

$$P_x \equiv \frac{e^{-\frac{x^2}{4D\ \Delta t}}}{(4\pi D\ \Delta t)^{1/2}}\ , P_y \equiv \frac{e^{-\frac{y^2}{4D\ \Delta t}}}{(4\pi D\ \Delta t)^{1/2}}\ , P_z \equiv \frac{e^{-\frac{z^2}{4D\ \Delta t}}}{(4\pi D\ \Delta t)^{1/2}}$$

Equation 2

These probability distributions are normalized Gaussians with variance

$\sigma = \sqrt{2D\ \Delta t}$.

Equation 3

The Monte Carlo algorithm can be exploited to approximate the Brownian motion of the real molecules (*random walk*) with that of a suitable set of *particles*. Typical values used in our simulations are $N \cong 10^5$ for the number of diffusing particles and $\Delta t \cong 10^{-5}$ s for the random walk *time step*. Let (x_0, y_0, z_0) be the coordinates of a particle at time t_0. Δt

seconds later, the new coordinates are $(x, y, z) = (x_0 + \Delta x, y_0 + \Delta y, z_0 + \Delta z)$, where each one of the three spatial increments is computed as $\gamma\sqrt{2D\,\Delta t}$ by the generation of a random number γ (e.g., a number generated by a call to the library function *randn*( ) of Matlab 7.0, The MathWorks, Inc., Natick, MA, USA) with probability Gaussian distribution centered in zero and unit variance. For $\Delta t = 10^{-5}$ s and $D \cong 200$ μm^2 / s, the standard deviation of the P_x, P_y, P_z displacement distributions is $\sigma \cong 63$ nm.

To simulate the constraints imposed on diffusion by internal and external impermeable surfaces, we adopt the following very simple criterion (see also ref. [2]): if the random number triplet $(\Delta x, \Delta y, \Delta z)$ is such that the new position (x, y, z) falls outside the boundaries of the permitted diffusion volume, the particle is left at (x_0, y_0, z_0). Control numerical experiments showed that this choice does not perturb appreciably the dynamics of diffusion within the allowed space and no particle accumulation is observed near the boundaries.

3 Validation of the random walk code

Supplementary Figure 1A, online, compares the C values predicted by Equation 1 for N molecules (of a given chemical species) to simulation results for an equal number of particles that start diffusing at time $t = 0$ in an unconstrained 3D medium from a point source placed in the origin of the Cartesian axes. To perform this comparison, the 3D space is subdivided in a sequence of spherical shells S_i centered at the source location, $\mathbf{r}_0 \equiv (0,0,0)$, with internal radius $R_{i,\text{int}}$ and external radius $R_{i,\text{ext}} = R_{i,\text{int}} + \Delta R$, where $i = 0,1,2,3,\ldots$ and ΔR is a suitable constant. The first shell S_0 is, by definition, the

sphere centered in $\mathbf{r}_0$ with radius ΔR. The molecular distribution at $t > 0$ predicted by Equation 1 is:

$$C(\mathbf{r},t) \equiv \frac{N}{N_A(4\pi D\, t)^{3/2}} e^{-\frac{r^2}{4D\,t}}$$

Equation 4

where $\mathbf{r} = (x, y, z)$ is the radius vector that identifies the point in space where, at time t, concentration equals C. The concentration corresponding to a number $n(V)$ of molecules in volume V can be computed as

$$C = \frac{1}{N_A}\frac{\partial n}{\partial V},$$

Equation 5

If the units of V are liters, then C is molar concentration (mol/liter, M).

Combining Equation 4 and Equation 5 yields, for the the *i*–th spherical shell, the expression

$$\begin{aligned} n_i(t) &= N_A \int_{R_{i,\text{int}}}^{R_{i,\text{ext}}} C\, dV \\ &\cong N_A \cdot C\left(\overline{R}_i, t\right) \int_{R_{i,\text{int}}}^{R_{i,\text{ext}}} dV \\ &= N_A \cdot C\left(\overline{R}_i, t\right) \cdot V_i \\ &= \frac{N \cdot V_i}{(4\pi D\, t)^{3/2}} e^{-\frac{\overline{R}_i^2}{4D\,t}} \end{aligned}$$

Equation 6

where $\bar{R}_i \equiv (R_{i,\text{ext}} + R_{i,\text{int}})/2$ and, by definition, $R_{0,\text{int}} = 0$. Supplementary Figure 1B, online, compares $n_i(t)$ (red lines) to the number of particles effectively counted in the *i*–th shell as a result of the Monte Carlo simulation (black lines) at corresponding times (shown next to each curve) measured from the onset of the diffusion process. The parameters used in these simulations are: total particles $N = 10^5$, $\Delta R = 0.08$ μm, $D = 200$ μm^{2}s^{-1} and $\Delta t = 10^{-5}$ s. The noise in the random walk plots is a consequence of the random nature of the particle movements and contrasts with the idealized behavior of the C function in Equation 1.

4 Effect of diffusion boundaries

To validate the criterion used to simulate the constraints imposed on diffusion by internal and external impermeable surfaces, we can adopt a procedure similar to the one described above. Specifically, we consider an impermeable cylinder with radius $R_{\text{cyl}} = 1$ μm, symmetry axis coincident with the z–axis and centroid $\mathbf{r}_0 = (0,0,0)$. Cylinder height, $h_{\text{cyl}} = 30$ μm, is comparable to that of a (short) hair cell, but such that $h_{\text{cyl}} >> r_{\text{cyl}}$. The cylinder is assumed to be empty at time $t = 0$, except for its intersection with plane *z*=0, where a homogeneous amount of substance is located (equal to $N = 10^4$ molecules; see Supplementary Figure 1C, online). The particle distribution at $t > 0$ is compared to the solution of the uni–dimensional diffusion equation for an instantaneous point source (see ref. [1]):

$$C(z,t) = \frac{N}{N_A (4\pi D\, t)^{1/2}} e^{-\frac{z^2}{4D\,t}}.$$

Equation 7

The space inside the cylinder is sub–divided in 375 disks with radii $R_{i,\mathrm{cyl}}$ and equally spaced centroids $\mathbf{R}_i = (0,0,i\Delta z) \equiv (0,0,z_i)$, where $-187 \le i \le 187$ and $\Delta z = 0.08$ μm. By analogy to Equation 6, the number of molecules in the *i*–th disk is computed as

$$n_i(t) = \frac{N \cdot V_d}{(4\pi D\, t)^{1/2}} e^{-\frac{z_i^2}{4D\, t}}$$

Equation 8

where $V_\mathrm{d} \cong 0.25$ μm^3 is disk volume. Supplementary Figure 1D, online, compares $n_i(t)$ (red lines) to the number of particles effectively counted in the *i*–th disk as a result of the Monte Carlo simulation (black lines) for $N = 10^5$ and all other parameters as in Supplementary Figure 1A–C.

5 Particles vs. molecules: simulation of chemical reactions

The chemical reactions involving Ca^{2+}, a pool of endogenous buffers (B) as well as one exogenous buffer (F, typically, a fluorescent dye), are represented by the reaction scheme

$$\begin{cases} \mathrm{Ca}^{2+} + \mathrm{B} \underset{k^{\mathrm{B}}_{\mathrm{OFF}}}{\overset{k^{\mathrm{B}}_{\mathrm{ON}}}{\rightleftharpoons}} \mathrm{CaB} \\ \mathrm{Ca}^{2+} + \mathrm{F} \underset{k^{\mathrm{F}}_{\mathrm{OFF}}}{\overset{k^{\mathrm{F}}_{\mathrm{ON}}}{\rightleftharpoons}} \mathrm{CaF} \end{cases}$$

where, $k^{\mathrm{B}}_{\mathrm{ON}}, k^{\mathrm{F}}_{\mathrm{ON}}$ and $k^{\mathrm{B}}_{\mathrm{OFF}}, k^{\mathrm{F}}_{\mathrm{OFF}}$ respectively represent the binding and unbinding rate constants of Ca^{2+} to B and to F. The *law of mass action* identifies the above scheme with the following set of partial differential equations [3]:

$$\begin{cases} \dfrac{\partial[\mathrm{CaB}]}{\partial t} = k_{\mathrm{ON}}^{\mathrm{B}}[\mathrm{Ca}^{2+}]_{\mathrm{i}}[\mathrm{B}] - k_{\mathrm{OFF}}^{\mathrm{B}}[\mathrm{CaB}] \\ \dfrac{\partial[\mathrm{CaF}]}{\partial t} = k_{\mathrm{ON}}^{\mathrm{F}}[\mathrm{Ca}^{2+}]_{\mathrm{i}}[\mathrm{F}\,] - k_{\mathrm{OFF}}^{\mathrm{F}}[\mathrm{CaF}] \end{cases}$$

Equations 9

To satisfy the mass conservation law, Equations 9 are coupled to this following set of equations:

$$\begin{cases} \dfrac{\partial[\mathrm{Ca}^{2+}]_{\mathrm{i}}}{\partial t} = -\dfrac{\partial[\mathrm{CaB}]}{\partial t} - \dfrac{\partial[\mathrm{CaF}]}{\partial t} \\ \dfrac{\partial[\mathrm{B}]}{\partial t} = -\dfrac{\partial[\mathrm{CaB}]}{\partial t} \\ \dfrac{\partial[\mathrm{F}]}{\partial t} = -\dfrac{\partial[\mathrm{CaF}]}{\partial t} \end{cases}$$

Equations 10

At equilibrium, concentrations are not changing, so that

$$\begin{cases} k_{\mathrm{D,B}} \equiv \dfrac{k_{\mathrm{OFF}}^{\mathrm{B}}}{k_{\mathrm{ON}}^{\mathrm{B}}} = \dfrac{[\mathrm{Ca}^{2+}]_{\mathrm{i}}[\mathrm{B}]}{[\mathrm{CaB}]} \\ k_{\mathrm{D,F}} \equiv \dfrac{k_{\mathrm{OFF}}^{\mathrm{F}}}{k_{\mathrm{ON}}^{\mathrm{F}}} = \dfrac{[\mathrm{Ca}^{2+}]_{\mathrm{i}}[\mathrm{F}]}{[\mathrm{CaF}]} \end{cases}$$

Equations 11

where $k_{\mathrm{D,B}}$ and $k_{\mathrm{D,F}}$ are the dissociation constants.

Equations 9 and Equations 10 are solved numerically by subdividing the diffusion volume in cubic voxels of side L comprised between 10 nm and 500 nm, depending on the particular simulation.

At the start of the simulation, each simulated particle of the *i*–th species is taken to represent an integer number of real molecules. We refer to this number as the *mapping factor* χ_i. For example, with a $\chi_i = 12$, a substance distributed within a volume of 1000

μm^3 at a concentration of 1 μM is represented by 50,183 such particles, each particle corresponding to 12 real molecules. Our algorithm is built around the assumption that simulated particles can exchange only integer numbers of real molecules during binding and unbinding reactions. The result of the chemical reactions represented by Equations 9, with the constraints imposed by Equations 10, is obtained by performing the following operations after each random walk time step Δt :

1) real molecules are counted, at time t, within each (occupied) voxel to determine the local reactant concentrations.

2) The result of the chemical reactions within the same voxel is computed from the Taylor's expansion (up to the fifth order) of [CaB] and [CaF], with a time step $\Delta\tau \approx 4 \cdot 10^{-7}$ seconds, i.e.:

$$\Delta[\mathrm{CaB}] \equiv [\mathrm{CaB}]_{t+\Delta\tau} - [\mathrm{CaB}]_t = \frac{\partial[\mathrm{CaB}]}{\partial t}\Delta\tau + \frac{\partial^2[\mathrm{CaB}]}{\partial t^2}\frac{\Delta\tau^2}{2} + \frac{\partial^3[\mathrm{CaB}]}{\partial t^3}\frac{\Delta\tau^3}{6} + \ldots$$

$$\Delta[\mathrm{CaF}] \equiv [\mathrm{CaF}]_{t+\Delta\tau} - [\mathrm{CaF}]_t = \frac{\partial[\mathrm{CaF}]}{\partial t}\Delta\tau + \frac{\partial^2[\mathrm{CaF}]}{\partial t^2}\frac{\Delta\tau^2}{2} + \frac{\partial^3[\mathrm{CaF}]}{\partial t^3}\frac{\Delta\tau^3}{6} + \ldots,$$

(the coefficients of the above expansion are derived from Equations 9).

3) At time $t + \Delta t$, after $n = \Delta t / \Delta\tau = 25$ recursive steps of computation, the numerical results are statistically rounded, for each particle, to integer numbers of real molecules.

4) The number of real molecules corresponding to each particle is updated before generating a new random walk displacement.

In general, the number of particles, and thus the corresponding χ_i factor, remain constant during the simulation. Exceptions are: (1) the complete dissociation of a given particle; (2) its extrusion from the cytosol by Ca^{2+}–pumps of the plasma membrane or by SERCA pumps of the endoplasmic reticulum (ER); (3) Ca^{2+} influx into the cytosol throughout plasma membrane or ER channels.

6 Calcium influx

The mean estimated diameter of a Ca^{2+} active site (Ca^{2+} *hotspot*), $d_{\mathrm{HOT}} \cong 276$ nm [4], is very close to the spatial resolution, $L = 500$ nm , of our whole cell simulations. Thus, for these simulations, we assume the active sites to be point sources (Figure 2B*a* of the Main Text) whose time dependence is dictated by that of the underlying Ca^{2+} current. To determine Ca^{2+} influx (equally distributed on the n_{HOT} active sites) we fit experimental current traces as described in [5] to obtain, using the mapping factor $\chi_{Ca^{2+}}$ of Ca^{2+}, the number $n_{Ca^{2+}}(t)$ of Ca^{2+} particles entered through a single hotspot up to time *t*,

$$n_{Ca^{2+}}(t) = round\left(\frac{Q_{Ca^{2+}}(t)}{2e^{+}\cdot\chi_{Ca^{2+}}\cdot n_{\mathrm{HOT}}}\right),$$

Equation 12

where $Q_{Ca^{2+}}(t)$ is the total charge carried by Ca^{2+} current into the cell and $2e^{+} = 3.2\cdot10^{-19}\mathrm{C}$ is the charge of the Ca^{2+} ion. The Matlab function *round*() is used throughout to approximate the result to the nearest integer number of simulated particles.

The Monte Carlo code is validated by comparing simulation results to the Ca^{2+} steady–state solution in the case of constant Ca^{2+} influx from a point source and unsaturable diffusible Ca^{2+} buffer [6, 7]. The simulation is performed with a random walk time step $\Delta t = 2 \cdot 10^{-8}$ s, a voxel side $L = 13$ nm and $5 \cdot 10^5$ particles. The point source is placed at the base center of a reflective hemisphere, with radius large enough (0.3 μm) that its spherical boundaries cannot influence appreciably the steady–state profile. Under these hypotheses, the internal free Ca^{2+} concentration ($[Ca^{2+}]_i$) depends on the source distance r according to the following approximated formula [6, 7]:

$$\left[Ca^{2+}\right]_i(r) = \left[Ca^{2+}\right]_i^{\infty} + \frac{J_{Ca^{2+}}}{2\pi r D_{Ca^{2+}}} e^{-r/\lambda},$$

Equation 13

where $\left[Ca^{2+}\right]_i^{\infty}$ is the free Ca^{2+} concentration at large distances from the source (i.e. the hemisphere borders), $J_{Ca^{2+}}$ is the local Ca^{2+} influx (mol s^{-1}), $\lambda = \sqrt{D_{Ca^{2+}} \cdot \tau_c}$ is a space constant (nm) and $\tau_c = 1/([B] \cdot k_{ON}^B)$ is the mean capture–time (s) of the buffer. $D_{Ca^{2+}}$ is the free Ca^{2+} diffusion coefficient in the cytoplasm (see Table 1 of the Main Text) and [B] is the free buffer concentration. In this simulation the total buffer concentration equals 1.7 mM, with the k_{ON}^B and k_D^B of BAPTA, and a diffusion coefficient of 70 $\mu m^2 s^{-1}$. To satisfy the condition of unsaturable buffer, a very small current $I_{Ca^{2+}} = 0.46$ pA, compatible with the current flowing through a single L–type Ca^{2+}–channel [8], is introduced into the cell. With these parameter values, whose choice is justified extensively in the Results of the Main Text, $J_{Ca^{2+}} \equiv \frac{I_{Ca^{2+}}}{2F_C} \cong 2.4 \cdot 10^{-18}$ mol $\cdot s^{-1}$, where $F_C =$

9.6485×10^4 C is Faraday's constant, and $\lambda \cong 26.6$ nm. Supplementary Figure 2, online, shows the good agreement between our Monte Carlo simulation and the theoretical prediction based on Equation 13. This example illustrates well the capability of our modeling approach to investigate reaction–diffusion events even at very small, namely nanometer, scales. However, in the rest of this article, we deal with the behavior of the entire cell on much longer time scales (up to 1 s), and much larger L and Δt of 0.5 μm and 10^{-5} s, respectively.

7 Calcium extrusion and storage

During the course of a typical Ca^{2+} transient, various pumps and exchangers remove Ca^{2+} from the cytoplasm. Hair cells rely on mobile Ca^{2+} buffers, the plasma membrane Ca^{2+}–ATPases (PMCAs) and the SERCA pumps of the ER to regulate Ca^{2+} levels [9]. Uptake of Ca^{2+} due to pumps (Figure 1E of the Main Text) can be modeled as an instantaneous function of the cytosolic free Ca^{2+} concentration ($[Ca^{2+}]_i$):

$$\frac{d\left[\mathrm{Ca}^{2+}\right]_\mathrm{i}}{dt} = -V_{\max} \cdot \frac{\left[\mathrm{Ca}^{2+}\right]_\mathrm{i}^{\,\mathrm{m}}}{\left[\mathrm{Ca}^{2+}\right]_\mathrm{i}^{\,\mathrm{m}} + K_\mathrm{M}^{\,\mathrm{m}}}$$

Equation 14

where $V_{\max} = n \cdot \nu$ is the maximum velocity (n is molar concentration of pump molecules and ν the maximal turnover rate in s^{-1}), K_M is the Michaelis constant and the exponent m equals one, for the PMCA pumps, and two for the SERCAs [8, 10-12].

Before Ca^{2+} influx, the equilibrium condition of $[Ca^{2+}]_i$=70 nm in our simulations is maintained by equilibrating the outward action of Ca^{2+}-pumps with an inward Ca^{2+} leakage through the plasma membrane and ER.

8 From particle counts to simulated fluorescence signals

Changes of the $[Ca^{2+}]_i$ can be estimated by fluorescence measurements using single wavelength indicators [13, 14], such as Oregon Green 488 BAPTA–1 (OGB1) and many others. At a given emission wavelength, the measured fluorescence signal f can be expressed as

$$f = S_{\mathrm{CaF}} n_{\mathrm{CaF}} + S_{\mathrm{F}} n_{\mathrm{F}}$$

Equation 15

where n_{CaF} is the number of molecules of dye F buffered to Ca^{2+} and n_{F} is the number of free dye molecules [15]. In general, S_{CaF} and S_{F} depend on a number of parameters of the experimental setup. To compare simulation results to experimental data, we define

$$\alpha = \frac{S_{\mathrm{CaF}}}{S_{\mathrm{F}}} = \frac{f_{\max}}{f_{\min}}$$

Equation 16

where $f_{\max}$ is fluorescence intensity when all dye molecules are bound to Ca^{2+}, whereas $f_{\min}$ is the intensity in the absence of Ca^{2+}. For OGB1, we set α = 5 (measured on our imaging setups), in accord with ref. [16].

Using Equation 15, we can write:

$$f = S_{\mathrm{F}}(\alpha n_{\mathrm{CaF}} + n_{\mathrm{F}})$$

Equation 17

and

$$f_0 = S_{\mathrm{F}}(\alpha n_{\mathrm{CaF},0} + n_{\mathrm{F},0}),$$

Equation 18

where $n_{\mathrm{CaF},0}$ and $n_{\mathrm{F},0}$ are the numbers of dye molecules respectively bound to and free from Ca^{2+} before the onset of depolarization–evoked Ca^{2+} entry. Defining the inverse of the dye mapping factor (see Section 5) as χ_{F}^{-1}, which represents the proportionality constant between the number *n* of real dye molecules and the corresponding number N of simulated particles, from Equation 17 and Equation 18 we obtain

$$f = S_F \chi_F^{-1}(\alpha N_{CaF} + N_F)$$

Equation 19

and

$$f_0 = S_F \chi_F^{-1}(\alpha N_{CaF,0} + N_{F,0})$$

Equation 20

which leads us to the final expression:

$$\Delta f / f_0 = \left[\alpha N_{\mathrm{CaF}} + N_{\mathrm{F}} - \alpha N_{\mathrm{CaF},0} - N_{\mathrm{F},0}\right] / \left(\alpha N_{\mathrm{CaF},0} + N_{\mathrm{F},0}\right)$$

Equation 21

that permits to convert particle counts to simulated fluorescence signals. Note that parameter α that we used to generate the virtual $\Delta f / f_0$ signals (fluorescence change divided by pre–stimulus fluorescence intensity) is relatively insensitive to the experimental conditions, whereas the absolute values of $f_{\max}$ and $f_{\min}$ may vary from

experiment to experiment. Therefore, for a single wavelength Ca^{2+} dye, comparing experimental and simulated $\Delta f / f_0$ signals is more accurate than comparing the $[Ca^{2+}]_i$ or the $\Delta[Ca^{2+}]_i$ values derived by the use of f_{max} and f_{min} (see Equations 1–2 of the Main Text). Simulated and experimental fluorescence signals are compared after computing a sequence of fluorescence images (movie) similar to that acquired by the CCD camera of the experimental apparatus (see Figure 2B*b–c* of the Main Text). Imaging experiments analyzed in this article were performed on a conventional (wide–field) fluorescence microscope, thus each of these images contains not only in–focus information from the region around the focal plane, but also out–of–focus contributions from the remainder of the specimen. To include the effect of the poor axial resolution of wide field microscopy in the model, we consider the relationship between the fluorescence intensity $f(z)$, due to the point source, and the source distance, z, from the focal plane ($z = 0$). In particular, the ratio $f(z)/f(0)$ can be estimated by adapting the data of Ref. [17] to the 90 μm diameter illumination field typical of our experimental apparatus. To simulate the operating conditions of the CCD camera used to acquire the fluorescence images, we integrate numerically the computed fluorescence signal over time intervals of 4.03 ms, corresponding to the actual CCD exposure time. Consecutive integration periods are separated by a delay of 0.1 ms to account for data transfer from the CCD image area to its storage area [18]. This procedure allows us to directly compare the simulated $\Delta f / f_0$ signals to the experimental signals with the sole knowledge of the parameter $\alpha = f_{max} / f_{min}$.

9 Estimating the diffusion coefficients of Ca^{2+} and its buffers

The Einstein–Stokes formula gives the diffusion coefficient D of a spherical particle with radius *r*, which is suspended in a medium with viscosity η [1]:

$$D = \frac{RT}{6\pi r \eta N_A},$$

Equation 22

where N_A is Avogadro's number, $R = 8.314\ \mathrm{J \cdot mol^{-1}K^{-1}}$ is the gas constant and T is temperature (Kelvin). Measured diffusion coefficients of many globular proteins (10–100 kDa) are slightly lower than those estimated from Equation 22 [19] due to [20] hydration, which increases protein effective size beyond the value expected from molecular weight, and irregular shape. Indeed, globular proteins are usually not perfectly spherical, which increases the frictional coefficient and reduces D.

As for the Ca^{2+} ion, we provide below two independent estimates of the Ca^{2+}diffusion coefficient in cytosol assuming, in first approximation, the validity of the Einstein–Stokes relation for the hydrated Ca^{2+} ion.

Estimate 1: Equation 22 predicts the following relationship for viscosity coefficients and diffusion constants of the same molecule in two different media, say water (W) and cytoplasm (C), at the same T:

$$D_W \eta_W = D_C \eta_C .$$

Equation 23

Using $D_W = 790\ \mu m^2 s^{-1}$ [21] and $\eta_C = 1.3\ \eta_W$ as the viscosity of the cytosol (since in cultured fibroblasts $1.2\ \eta_W \le \eta_C \le 1.4\ \eta_W$ [22]) we obtain a value of $D_{Ca^{2+}} \cong 600\ \mu m^2 s^{-1}$

for Ca^{2+} in cytosol. However cytosol is not a homogeneous solvent, thus Ca^{2+} diffusion tortuosity in the cytoplasm should also be considered. Tortuosity increases η_C / η_W to a factor of 2 to 3 [23], yielding $D_{Ca^{2+}} \cong 400\ \mu m^2 s^{-1}$ for $\eta_C / \eta_W = 2$, as in Ref. [8].

Estimate 2: based on Equation 22 the quantity $D\sqrt[3]{M}$ is constant for spherical particles of equal density ρ but different volume V and mass M, as can be easily shown by setting

$$\rho = \frac{M}{V} = \frac{3M}{4\pi r^3}$$

Equation 24

For globular proteins, M/V can be rather safely assumed to be constant [20], which implies constancy of $D\sqrt[3]{M}$. Assuming this constancy also for two small molecules, like Ca^{2+} and IP_3 (both considered hydrated), we can write

$$D_{Ca^{2+}} \sqrt[3]{M_{Ca^{2+}}} = D_{IP_3} \sqrt[3]{M_{IP_3}},$$

Equation 25

yielding the formula:

$$D_{Ca^{2+}} = D_{IP_3} \sqrt[3]{\frac{M_{IP_3}}{M_{Ca^{2+}}}}$$

Equation 26

The *effective diffusive molecular masses* $M_{Ca^{2+}}$ and M_{IP_3} can be taken as the molecular masses of Ca^{2+} and IP_3, respectively 40 Da and 414 Da (the last computed from the IP_3 chemical formula $C_6H_9O_{15}P_3$, Molecular Probes source), plus their first hydration shell.

Molecular dynamics simulations performed by our collaborator Sergio Pantano suggested that the first hydration shells of Ca^{2+} (charge +2) and IP_3 (charge –6) are formed by 6 H_2O molecules for Ca^{2+} [24] and 6.45 H_2O + 1.38 Na^+ molecules for IP_3. This yields hydrated masses of 148 Da and 561.8 Da, respectively. Assuming $D_{IP3} = 283\ \mu m^2 s^{-1}$ at 20 °C [25], Equation 26 yields $D_{Ca^{2+}} \cong 440\ \mu m^2 s^{-1}$, i.e. the value used in our simulations.

Equation 26 was also used to derive the diffusion coefficients for all simulated Ca^{2+} ligand species (see Table 1 of the Main Text). However, unlike Ca^{2+}, the first hydration shell was neglected since the associated mass increase is negligible with respect to the mass computed from the chemical formula. Similarly, the diffusion coefficients of free and Ca^{2+}– bound to buffer are considered almost equal.

10 Estimate of the equivalent endogenous buffer concentration

Many methods have been suggested in the past to estimate the concentration and properties of endogenous buffers from the combination of optical Ca^{2+} measurement and electrophysiological techniques. In particular, the competition between Fura–2 and endogenous Ca^{2+}– buffers is well described in the literature [26-28]. Here, we show how the analysis of the experimental fluorescence traces and patch clamp data can be used to provide an estimate of the equivalent endogenous buffer concentration in the hair cell for the case of a single wavelength Ca^{2+} indicator, such as OGB1. The starting point is Equation 21, which can be written in terms of concentrations instead of number of particles as

$$\frac{\Delta f}{f_0} = \frac{f - f_0}{f_0} = \frac{\alpha[\mathrm{CaF}] + [\mathrm{F}] - (\alpha[\mathrm{CaF}]_0 + [\mathrm{F}]_0)}{\alpha[\mathrm{CaF}]_0 + [\mathrm{F}]_0},$$

Equation 27

where $[\mathrm{F}]$ and $[\mathrm{CaF}]$ are concentrations of free dye and dye bound to Ca^{2+} at time t, $[\mathrm{F}]_0$ and $[\mathrm{CaF}]_0$ are concentrations at time zero, i.e. before the influx of Ca^{2+}, and α is defined in Section 8. In the following, we assume chemical equilibrium of Ca^{2+} with its buffers, both locally and globally (i.e. for the whole cell). After Ca^{2+} influx termination, the new equilibrium is signaled by the settling of the fluorescence trace at a steady state level and, in our simulation with 1.7 mM of BAPTA 29 kDa without the action of Ca^{2+}–pumps (Figure 3A of the Main Text, blue dotted trace), it is attained at $t \cong 1$ s for $\Delta f / f_0 \cong 0.186$. Thus the mass action law permits to write, at this equilibration time:

$$[\mathrm{F}] = [\mathrm{F}]_{\mathrm{TOT}} \cdot \frac{k_{\mathrm{D,F}}}{[\mathrm{Ca}^{2+}]_{\mathrm{i}} + k_{\mathrm{D,F}}},\ [\mathrm{CaF}] = [\mathrm{F}]_{\mathrm{TOT}} \cdot \frac{[\mathrm{Ca}^{2+}]_{\mathrm{i}}}{[\mathrm{Ca}^{2+}]_{\mathrm{i}} + k_{\mathrm{D,F}}},$$

Equations 28

where $[\mathrm{F}]_{\mathrm{TOT}} = 50\ \mu\mathrm{M}$ is the total dye concentration and $k_{\mathrm{D,F}} = 0.206\ \mu\mathrm{M}$ (in Table 1 of the Main Text) is the dissociation constant for the reaction of Ca^{2+} with OGB1. Equation 27 and Equations 28 can be combined to derive the $[\mathrm{Ca}^{2+}]_{\mathrm{i}}$ as

$$[\mathrm{Ca}^{2+}]_{\mathrm{i}} = k_{\mathrm{D,F}} \frac{[\mathrm{Ca}^{2+}]_{\mathrm{i,0}}(\alpha - 1 + \alpha \cdot \Delta f / f_0) + k_{\mathrm{D,F}} \cdot \Delta f / f_0}{k_{\mathrm{D,F}}(\alpha - 1 - \Delta f / f_0) - \alpha \cdot [\mathrm{Ca}^{2+}]_{\mathrm{i,0}} \cdot \Delta f / f_0}.$$

Equation 29

Obtaining numerical values from Equation 29 requires knowledge of the $[Ca^{2+}]_{i,0}$, which we set at 70 nM in our simulations. The estimated $[Ca^{2+}]_i \cong 109.6$ nM is consistent to 1 part in 10^4 with the simulation results.

Equations 28 can be written also in terms of the equivalent endogenous buffer, B, yielding:

$$[B] = [B]_{TOT} \cdot \frac{k_{D,B}}{[Ca^{2+}]_i + k_{D,B}}, \quad [CaB] = [B]_{TOT} \cdot \frac{[Ca^{2+}]_i}{[Ca^{2+}]_i + k_{D,B}},$$

Equations 30

where $k_{D,B} = 0.192$ μM is the dissociation constant of BAPTA 29 kDa and $[B]_{TOT}$ its total concentration, which has to be estimated.

If $\Delta[Ca^{2+}]_{TOT} = 169$ μM is the total amount of Ca^{2+} entering the cell, estimated as the time integral of the calcium current from the patch clamp data (Figure 2A and Figure 4E *bottom* of the Main Text), the mass conservation law for Ca^{2+} imposes the following balance equation:

$$\Delta[Ca^{2+}]_{TOT} = \Delta[Ca^{2+}]_i + \Delta[F] + \Delta[B],$$

Equation 31

where

$$\Delta[Ca^{2+}]_i = [Ca^{2+}]_i - [Ca^{2+}]_{i,0},$$

$$\Delta[F] = [F]_0 - [F]$$

and

$$\Delta[B] = [B]_0 - [B].$$

Equation 31 can now be solved for $[B]_{TOT}$, yielding $[B]_{TOT} = 1.7$ mM, as expected.

When Ca^{2+} pumps are included in the simulations, the $[Ca^{2+}]_i$ tends to return to the resting value of 70 nM (Figure 3A of the Main Text, blue solid trace). Correspondingly, fluorescence traces peak about 0.3–0.4 s after the current onset and thereafter show a tendency to decrease. Substituting $\Delta f / f_0 \cong 0.162$ at $t = 1$ s in Equation 29, we obtain $[B]_{TOT} = 1.97$ mM from Equation 31, i.e. a relatively good approximation to the total buffer concentration of 1.7 mM. The difference, 1.97 mM – 1.7 mM = 0.27 mM, corresponding to ~14 % of the total Ca^{2+}–buffer capacity of the cell (i.e. 1.97 mM), is the buffering power due to the Ca^{2+} ejection activity performed by the Ca^{2+} pumps (SERCAs and PMCAs) in the first ~1 s for the case of a 50 ms depolarization step.

In conclusion, this method provides (1) an independent validation of the (Monte Carlo) generation of the virtual fluorescence $\Delta f / f_0$ and (2) a formula to estimate the total equivalent endogenous buffer concentration from experimental fluorescence data.

REFERENCES

1. Crank J. (1975) The Mathematics of Diffusion. Oxford University Press, London.
2. Segura J, Gil A, Soria B. (2000) Modeling study of exocytosis in neuroendocrine cells: influence of the geometrical parameters. Biophys J, 79, 1771-86.
3. Keener J. S, J. (1998) Mathematical Physiology. Springer-Verlag, New York.
4. Roberts WM, Jacobs RA, Hudspeth AJ. (1990) Colocalization of ion channels involved in frequency selectivity and synaptic transmission at presynaptic active zones of hair cells. J Neurosci, 10, 3664-84.
5. Rispoli G, Martini M, Rossi ML, Rubbini G, Fesce R. (2000) Ca2+-dependent kinetics of hair cell Ca2+ currents resolved with the use of cesium BAPTA. Neuroreport, 11, 2769-74.
6. Roberts WM. (1993) Spatial calcium buffering in saccular hair cells. Nature, 363, 74-6.
7. Neher E. (1986) Concentration profiles of intracellular calcium in the presence of a diffusible chelator. Exp Brain Res, 14, 80-96.
8. Wu YC, Tucker T, Fettiplace R. (1996) A theoretical study of calcium microdomains in turtle hair cells. Biophys J, 71, 2256-75.
9. Mammano F, Bortolozzi M, Ortolano S, Anselmi F. (2007) Ca2+ signaling in the inner ear. Physiology (Bethesda), 22, 131-44.
10. Dumont RA, Lins U, Filoteo AG, Penniston JT, Kachar B, Gillespie PG. (2001) Plasma membrane Ca2+-ATPase isoform 2a is the PMCA of hair bundles. J Neurosci, 21, 5066-78.
11. Goldbeter A, Dupont G, Berridge MJ. (1990) Minimal model for signal-induced Ca2+ oscillations and for their frequency encoding through protein phosphorylation. Proc Natl Acad Sci U S A, 87, 1461-5.
12. Lumpkin EA, Hudspeth AJ. (1998) Regulation of free Ca2+ concentration in hair-cell stereocilia. J Neurosci, 18, 6300-18.
13. Lelli A, Perin P, Martini M, Ciubotaru CD, Prigioni I, Valli P, Rossi ML, Mammano F. (2003) Presynaptic calcium stores modulate afferent release in vestibular hair cells. J Neurosci, 23, 6894-903.
14. Rispoli G, Martini M, Rossi ML, Mammano F. (2001) Dynamics of intracellular calcium in hair cells isolated from the semicircular canal of the frog. Cell Calcium, 30, 131-40.
15. Grynkiewicz G, Poenie M, Tsien RY. (1985) A new generation of Ca2+ indicators with greatly improved fluorescence properties. J Biol Chem, 260, 3440-50.
16. Maravall M, Mainen ZF, Sabatini BL, Svoboda K. (2000) Estimating intracellular calcium concentrations and buffering without wavelength ratioing. Biophys J, 78, 2655-67.
17. Hiraoka Y, Sedat JW, Agard DA. (1990) Determination of three-dimensional imaging properties of a light microscope system. Partial confocal behavior in epifluorescence microscopy. Biophys J, 57, 325-33.
18. Mammano F, Canepari M, Capello G, Ijaduola RB, Cunei A, Ying L, Fratnik F, Colavita A. (1999) An optical recording system based on a fast CCD sensor for biological imaging. Cell Calcium, 25, 115-23.

19. Tanford C. (1961) Physical Chemistry of Macromolecules. John Wiley & Sons, New York.
20. Jackson MB. (2006) Molecular and Cellular Biophysics. Cambridge University Press, New York.
21. Hille B. (2001) Ionic Channels of Excitable Membranes. Sinauer Associates, Sunderland, MA.
22. Fushimi K, Verkman AS. (1991) Low viscosity in the aqueous domain of cell cytoplasm measured by picosecond polarization microfluorimetry. J Cell Biol, 112, 719-25.
23. Kushmerick MJ, Podolsky, R. J. (1969) Ionic mobility in muscle cells. Science, 166, 1297-1298.
24. Bakò I, Hutter J, Palinkas G. (2002) Car-Parrinello molecular dynamics simulation of the hydrated calcium ion. Journal of Chemical Physics, 117, 9838-9843.
25. Allbritton NL, Meyer T, Stryer L. (1992) Range of messenger action of calcium ion and inositol 1,4,5-trisphosphate. Science, 258, 1812-5.
26. Neher E. (1995) The use of fura-2 for estimating Ca buffers and Ca fluxes. Neuropharmacology, 34, 1423-42.
27. Lee SH, Rosenmund C, Schwaller B, Neher E. (2000) Differences in Ca2+ buffering properties between excitatory and inhibitory hippocampal neurons from the rat. J Physiol, 525 Pt 2, 405-18.
28. Neher E, Augustine, GJ. (1992) Calcium gradients and buffers in bovine chromaffin cells. The Journal of Physiology, 450, 273-301.

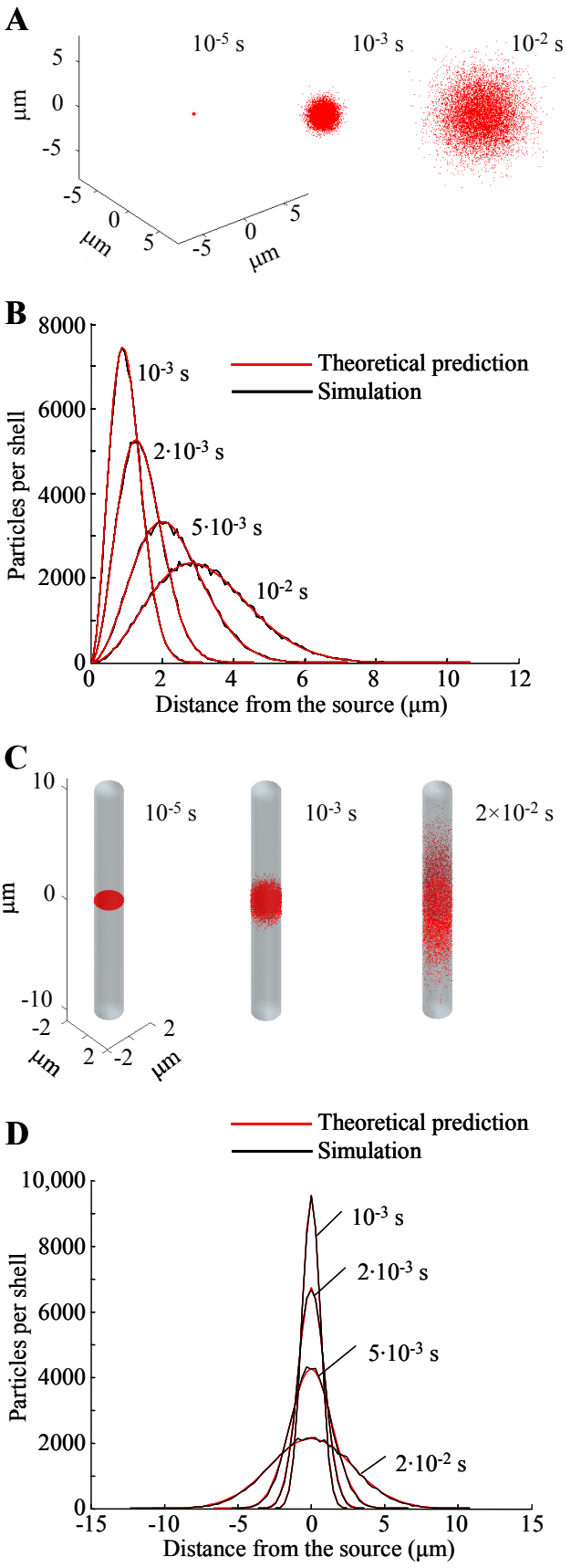

Supplementary Figure 1. Validation of the random walk algorithm.
(A) The diffusion process for 10^4 particles in an unlimited isotropic medium is represented as a sequence of 3D plots of particle positions at increasing times (in seconds). (B) Random walk diffusion simulations for 10^5 particles (black lines) are compared to the analytical solutions of the diffusion equation (red lines) at four different times after the onset of diffusion; ordinates are particle counts within concentric shells centered in the source point and having 80 nm thickness, abscissas are shell mean radii. (C-D) Same as (A-B) for particles diffusing in a thin cylinder having diameter equal to 1 µm and length equal to 30 µm; note that only the central portion of the cylinder is shown to aid visualization of the portion appreciably affected by the diffusion process.

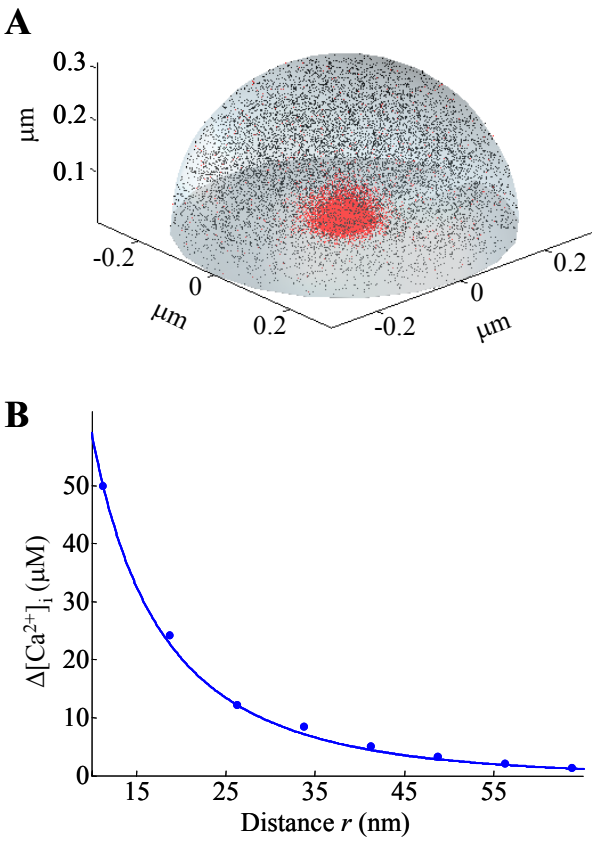

Supplementary Figure 2. $[Ca^{2+}]_i$ steady-state solution in a reflective nano–hemisphere, including Ca^{2+} buffer.

(A) 3-D simulation of the $[Ca^{2+}]_i$ at steady-state in the presence of a 10^4 particles of a mobile Ca^{2+} buffer (black dots). The equilibrium $[Ca^{2+}]_i$ concentration at time $t = 0$ is 70 nM. For $t > 0$, Ca^{2+} particles (red dots) enter as a stochastic current (mean value equal to 0.46 pA) from the point source at the base center of the hemispherical space, diffuse and react with the buffer particles. (B) Comparing simulation results (points) and steady-state theoretical prediction (trace) of $[Ca^{2+}]_i$ change vs. distance r from the point source.

Unitary permeability of gap junction channels to second messengers measured by FRET microscopy

Victor H Hernandez[1,5], Mario Bortolozzi[1,5], Vanessa Pertegato[1,2], Martina Beltramello[1], Michele Giarin[3], Manuela Zaccolo[1,2], Sergio Pantano[1,4] & Fabio Mammano[1,3,4]

Gap junction channels assembled from connexin protein subunits mediate intercellular transfer of ions and metabolites. Impaired channel function is implicated in several hereditary human diseases. In particular, defective permeation of cAMP or inositol-1,4,5-trisphosphate ($InsP_3$) through connexin channels is associated with peripheral neuropathies and deafness, respectively. Here we present a method to estimate the permeability of single gap junction channels to second messengers. Using HeLa cells that overexpressed wild-type human connexin 26 (HCx26wt) as a model system, we combined measurements of junctional conductance and fluorescence resonance energy transfer (FRET) emission ratio of biosensors selective for cAMP and $InsP_3$. The unitary permeabilities to cAMP ($47 \times 10^{-3} \pm 15 \times 10^{-3}$ μm³/s) and $InsP_3$ ($60 \times 10^{-3} \pm 12 \times 10^{-3}$ μm³/s) were similar, but substantially larger than the unitary permeability to lucifer yellow (LY; $7 \pm 3 \times 10^{-3}$ μm³/s), an exogenous tracer. This method permits quantification of defects of metabolic coupling and can be used to investigate interdependence of intercellular diffusion and cross-talk between diverse signaling pathways.

In chordates, intercellular communication based on gap junctions relies on channels formed by protein subunits of the connexin family, whose members are named according to their molecular mass[1]. Connexins have highly conserved sequences with four transmembrane domains separating one cytoplasmic and two extracellular loops, with cytoplasmic carboxy- and amino-terminal ends. Each cell contributes a hexamer of connexins forming a hemichannel, or connexon, which, in the narrow extracellular cleft, interacts and aligns with another connexon from the adjacent cell. Mutations in connexin genes are implicated in various hereditary human diseases, including cardiovascular anomalies, peripheral neuropathies, deafness, skin disorders and cataracts[2].

Several endogenous ions and low-molecular-weight species cross gap junction channels, including all current-carrying anions and cations, glycolytic intermediates, vitamins, amino acids and nucleotides, as well as some of the more important second messengers involved in cell signaling, such as $InsP_3$ and cAMP[3]. $InsP_3$ (molecular mass, 414 Da; charge, –6) is the first and the principal inositol phosphate that is formed by inositol lipid hydrolysis resulting from G protein–linked receptor stimulation of phospholipase C, and it is considered a global messenger molecule[4]. $InsP_3$ molecules diffuse throughout the cell nearly unbuffered, with diffusion coefficient D in cytoplasm on the order of 280 μm²/s and a lifetime up to ~60 s (depending on cell type); when they interact with specific receptors ($InsP_3R$) present in the endoplasmic reticulum, Ca^{2+} is liberated, raising its concentration in the cytosol[5].

Like $InsP_3$, cAMP (molecular mass, 329 Da; charge, –1) is a ubiquitous intracellular second messenger that affects cell physiology by directly interacting with effector molecules, including cAMP-dependent protein kinases (PKA), cyclic nucleotide-gated ion channels (CNG channels), hyperpolarization-activated channels[6] and the guanine exchange factor EPAC[7]. cAMP is generated exclusively at the plasma membrane, but its degradation can occur throughout the cytoplasm, where its lifetime is ~60 s. The D of cAMP has been estimated at 780 μm²/s in Aplysia sensory neurons[8], although this value is probably too high, as the D of Ca^{2+} (40 Da) is 790 μm²/s in water.

The intercellular transfer of ions and endogenous solutes through gap junction channels serves a variety of specific functions. The procedures that have gained wide acceptance in assaying the molecular permeability of connexins, however, are dependent on the introduction into living cells of exogenous markers, which are then traced in their individual intercellular movements[3]. In an 'exotic' assay, the local UV uncaging of NPE-HCCC2 generates fluorescent HCCC2 in one cell to visualize dye transfer to neighboring coupled cells[9]. A more commonly used dye is LY (molecular weight, 443 Da; charge, –2), whose high fluorescence efficiency ensures its detection at minute levels. Studies based on LY and other charged tracers, such as the Alexa series of fluorescent probes, show clearly that the permeability profile of each connexin channel is distinct[3]. As even modest selectivity at cellular junctions could have a great effect on the strength, character and location of the transmitted signal, the mechanisms of such discrimination are of acute biological and medical interest[10]. For

[1]Istituto Veneto di Medicina Molecolare and [2]Istituto Dulbecco Telethon, Fondazione per la Ricerca Biomedica Avanzata, 35129 Padova, Italy. [3]Dipartimento di Fisica 'G. Galilei' dell'Università di Padova and [4]Consorzio Nazionale Interuniversitario per le Scienze Fisiche della Materia, 35131 Padova, Italy. [5]These authors contributed equally to this work. Correspondence should be addressed to F.M. (fabio.mammano@unipd.it).

RECEIVED 2 JANUARY; ACCEPTED 22 FEBRUARY; PUBLISHED ONLINE 11 MARCH 2007; DOI:10.1038/NMETH1031

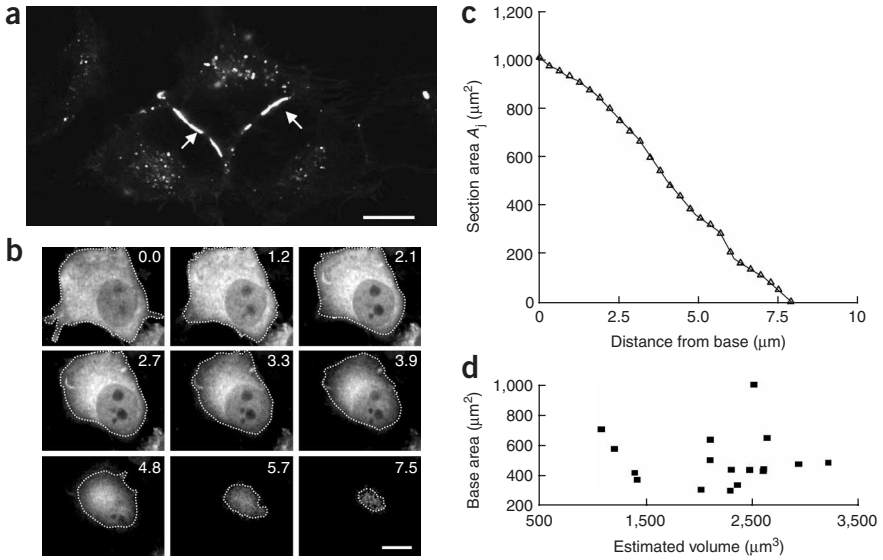

Figure 1 | HeLa cell transfection and cell volume estimate. (**a**) Confocal fluorescence image of three HeLa cells transfected with EYFP-HCx26wt; note junctional plaques (arrows) and fluorescence puncta scattered in the cytoplasm. Scale bar, 10 μm. (**b**) Through-focus optical sections, taken at 0.3-μm intervals, of HeLa cells cotransfected with HCx26wt and the cAMP biosensor H30; numbers on each frame are distance from cell base in μm. Scale bars, 10 μm. (**c**) Cell area section derived from the analysis of the through-focus sequence in **b**, plotted against distance from cell base. (**d**) Scatterplot of cell base area against estimated cell volume for $n = 17$ cells in this study.

instance, defective permeation of cAMP through gap junctions between adjacent cytoplasmic loops of myelinating Schwann cells is thought to underlie certain forms of X-linked Charcot-Marie-Tooth disease[11]. However, extrapolations from dye permeation studies present major difficulties because of the different shapes, flexibilities, charges and charge distributions of these molecules[10]. Thus, how exactly these measurements relate to the selective permeability of endogenous solutes remains obscure.

Measurement of endogenous messengers' transit has been so far problematic mostly owing to lack of direct reporters. For example, to compare the transfer rate of cAMP through gap junction channels formed by different connexins, CFTR-mediated chloride currents[12], Ca^{2+} currents through CNG channels and Ca^{2+} imaging[13] are used as sensors for cAMP. The transfer of $InsP_3$ also is usually detected indirectly[14]. Using Ca^{2+} imaging as the readout for $InsP_3$ dynamics, we recently demonstrated that $InsP_3$ permeability is altered in a deafness mutant of Cx26 (ref. 15).

Here, in an effort to develop direct, quantitative and reproducible means to monitor the flux of cAMP or $InsP_3$ through recombinant gap junction channels, we used novel ratiometric fluorescent biosensors that exploit the phenomenon of FRET for the quantitative monitoring of second-messenger concentrations in single living cells in real time[16,17]. Measurement of junctional conductance, g_j, by the dual whole-cell patch-clamp technique, combined with knowledge of the unitary conductance, γ, of homotypic channels formed by HCx26wt, allowed estimation of the number of active gap junction channels, allowing the determination of the unitary—that is, single-pore—permeability coefficient, p_u, for $InsP_3$ and cAMP. The flux of LY was quantified similarly, for comparison. This approach may have general applicability, as it provides fast and reliable estimates of connexin channel permeability to second messengers and permits the study of their role in the physiology and pathology of cell-cell communication. The method can readily be combined with multispectral imaging of other fluorescent reporters to investigate cross-talk among signaling pathways[18].

RESULTS

Permeability assay development

We performed experiments at room temperature (21–23 °C), following protocols described in the Methods (also see **Supplementary Methods** online). Briefly, we estimated gap junction permeability in HeLa cells transfected with HCx26wt (**Fig. 1a**). All compounds of interest were delivered intracellularly by passive diffusion out of patch pipettes under whole-cell recording conditions. We monitored molecular transfer between cell pairs coupled by homomeric HCx26wt channels with a wide-field fluorescence microscope, directly measuring cell volume, V, by digital optical sectioning[18] (**Fig. 1b–d**). Unless otherwise stated, results are expressed as mean ± s.e.m. and n is the number of transfected cell pairs studied.

Unitary permeability to LY

The estimate of unitary permeability p_u (see **Supplementary Methods**) requires measurement of the junctional transfer rate across the plaque (**Fig. 2**):

$$k_j = \frac{dc_2/dt}{c_1 - c_2}$$

(with units of s^{-1}). In the expression above, c_1 and c_2 indicate intracellular concentrations in cell 1 and cell 2 after delivery of LY to cell 1 (WC_1; see **Fig. 2a**). Concentration has been shown to be directly related to LY fluorescence emission intensity, spatially integrated and divided by V (ref. 19), over a range of ~0–2 mM (ref. 20). This range easily accommodates the values reached in cell 1 and cell 2 as a result of the pipette concentration of 440 μM used for the LY experiments. Therefore, we drew separate regions of interest (ROIs) on the fluorescence images along the contours of each cell at its base, then computed c_1 and c_2 by summing the background-subtracted intensity (gray) levels, F, of all image pixels within each ROI and dividing the result by the volume of the corresponding cell:

$$c_{1,2} \equiv \left(\sum F\right)_{1,2} \Big/ V_{1,2}$$

(with units of gray level per μm^3), where the subscript 1,2 denotes that there are two equations of this form, one for c_1 and one for c_2. After a suitable delay, the whole-cell configuration was achieved in the coupled cell as well (WC_2; **Fig. 2a**), which permitted the measurement of junctional conductance:

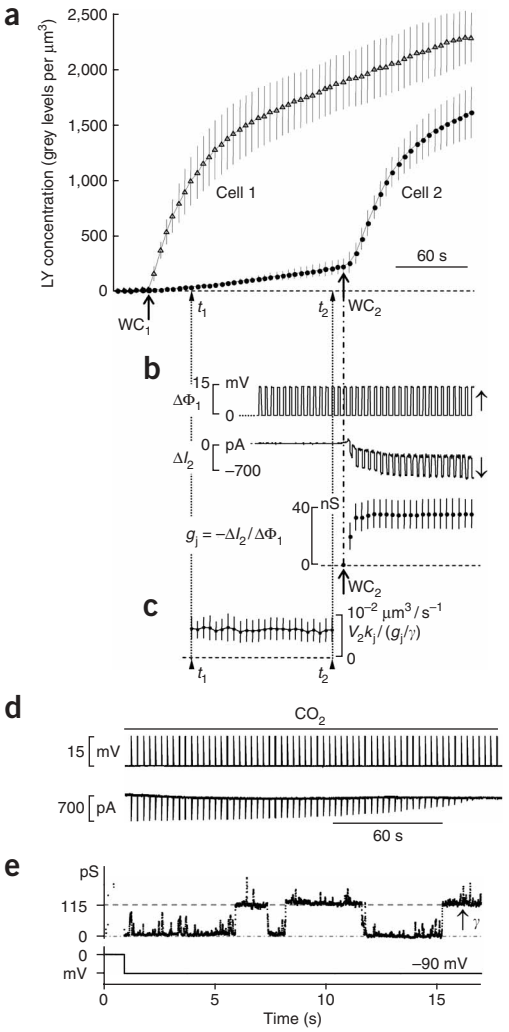

Figure 2 | Estimate of HCx26wt permeability to LY in pairs of transfected HeLa cells. (**a**) Average fluorescence traces ($n = 3$) obtained by illuminating the field at $\lambda_{ex} = 425$ nm to observe LY spread (emission wavelength $\lambda_{em} = 540$ nm). LY (0.44 mM) was delivered to cell 1 under whole-cell recording conditions (WC_1). Ordinates are LY concentration. (**b**) Top trace, voltage steps, $\Delta\Phi_1$, applied to cell 1; middle trace, current changes, ΔI_2, evoked in cell 2 while holding it at a constant potential to measure junctional current $I_j = -\Delta I_2$; bottom trace, average intercellular conductance $g_j = -\Delta I_2/\Delta\Phi_1$ measured after achieving the whole-cell configuration in cell 2 (WC_2). (**c**) Estimated unitary permeability to LY. (**d**) Blockade of junctional current by CO_2. (**e**) Conductance changes (top trace) owing to gating of a single channel, formed by HCx26wt, after application of a transjunctional potential difference $\Phi_j = -90$ mV (bottom trace); estimated unitary conductance $\gamma = 115$ pS (arrow).

$$g_j = -\Delta I_2/\Delta\Phi_1$$

by dual whole-cell current recording (see Methods). Here, ΔI_2 is change in current elicited in cell 2 owing a voltage step $\Delta\Phi_1$ in cell 1 (**Fig. 2b**). In separate control experiments, g_j was stable for time intervals that exceeded the duration of these measurements. Thus, the microscopic parameter p_u (with units of μm³/s), which quantifies the diffusive flow through a single channel, was computed as

$$p_u = V_2 k_j/(g_j/\gamma)$$

(see **Supplementary Methods**), where $\gamma = 115$ pS is unitary conductance of HCx26wt channels (**Fig. 2e**). In the expression above, g_j/γ serves as an estimate for N_{pore}, the number of open gap junction channels in the plaque (see Methods). The unitary permeability p_u estimated from the above formula was constant for the greatest part (interval t_1–t_2) of the interval between the WC_1 and WC_2 events (~2 min), indicating that the method is internally consistent (**Fig. 2c**). In separate control experiments, LY fluorescence in cell 1 reached a steady state within 10 min of the WC_1 event (data not shown).

We routinely applied CO_2 (**Fig. 2d**) to prove that solute transfer occurred through gap junction channels and that cytoplasmic bridges were not responsible for the observed fluorescence changes in the coupled cell[20]. Throughout this study, we retained for analysis only data sets where complete electrical uncoupling by CO_2 was demonstrated at the end of data acquisition. For LY, this procedure yielded an average $p_u = (7 \pm 3) \times 10^{-3}$ μm³/s ($n = 3$).

It could be argued that binding to cytoplasmic and/or nuclear elements[21] might contribute to underestimation of permeability to LY. Indeed, if tracer binding is appreciable and approximately the same in both cells, the time course of this process is indistinguishable from free diffusion with a slower junctional transfer rate. However, our control experiments, performed with a two-photon microscope (see **Supplementary Methods**), confine excess LY fluorescence to no more than 10% (8 ± 1%, $n = 3$; data not shown). This is a consequence of binding (prevalently) nuclear structures; excluding the nucleus from the cell volume in the computation of the p_u for LY yielded a result that overlapped, within the experimental error, that reported above.

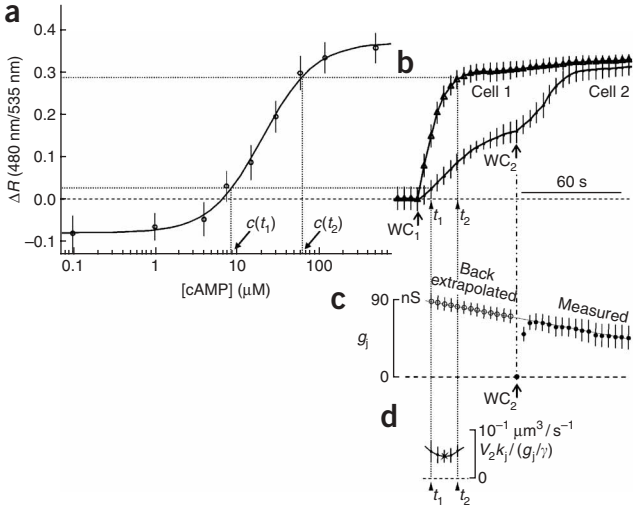

Figure 3 | Estimate of HCx26wt permeability to cAMP in pairs of transfected HeLa cells. (**a**) Concentration-response curve for the cAMP biosensor H30 ($n \geq 5$ cells at each concentration). Ordinates are background-subtracted FRET emission ratio changes ΔR measured from prestimulus ratio R_0. (**b**) Average FRET ratio traces ($n = 5$) obtained by delivery of 120 μM cAMP to cell 1 under whole-cell recording conditions (WC_1), followed by delivery to cell 2 (WC_2). (**c**) Intercellular conductance g_j measured after achieving the whole-cell configuration in cell 2 (filled symbols) and back-extrapolated to the WC_1–WC_2 interval (open symbols). (**d**) Estimated unitary permeability to cAMP.

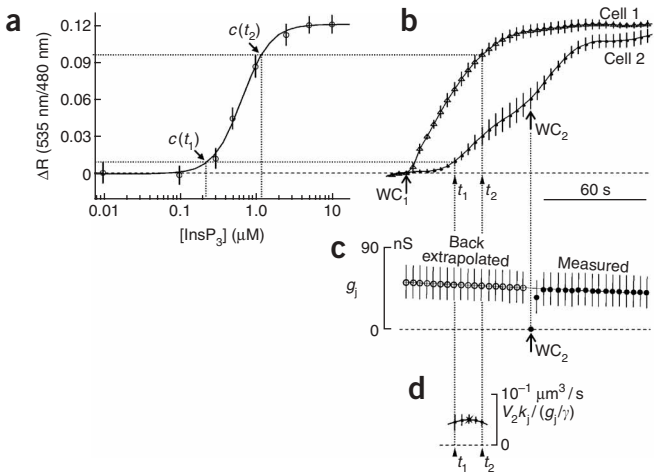

Figure 4 | Estimate of HCx26wt permeability to $InsP_3$ in pairs of transfected HeLa cells. (**a**) Concentration-response curve for the $InsP_3$ biosensor, LIBRA ($n \geq 5$ cells at each concentration). Ordinates are background-subtracted FRET emission ratio changes ΔR measured from prestimulus ratio R_0. (**b**) Average FRET ratio traces ($n = 4$) obtained by delivery of 5 μM $InsP_3$ to cell 1 under whole-cell recording conditions (WC_1), followed by delivery to cell 2 (WC_2). (**c**) Intercellular conductance g_j measured after achieving the whole-cell configuration in cell 2 (filled symbols) and back-extrapolated to the WC_1–WC_2 interval (open symbols). (**d**) Estimated unitary permeability to $InsP_3$.

Fluorescence resonance energy transfer assay

The approach highlighted above can be adapted, in principle, to any solute whose concentration change can be traced back to a fluorescence measurement. To monitor optically the transfer of cAMP (**Fig. 3**), we cotransfected HeLa cells with HCx26wt and a selective ratiometric FRET biosensor, here named H30 (ref. 16). To construct the H30 dose-response curve for cAMP, we patch-clamped transfected cells with various concentrations of cAMP in the pipette. We used ratiometric FRET microscopy (**Supplementary Methods**) to measure the steady-state levels of the background-subtracted FRET ratio signals, which were averaged and plotted against the corresponding pipette concentration. The EC_{50} for cAMP in these cells, 20 μM, is close to the previously reported value[16]. The results (**Fig. 3a**) also indicate that the FRET emission ratio of the H30 biosensor accurately traced cAMP concentration in the range from ~8 μM to ~60 μM. To monitor cAMP transfer through HCx26wt channels, we patch-clamped HeLa cell pairs with pipettes containing 120 μM of this messenger. To quantify p_u, we estimated the junctional transfer rate k_j as

$$k_j \cong \frac{dR_2/dt}{R_1 - R_2}$$

within a subinterval (t_1–t_2) during which the ratiometric FRET signals $R_{1,2}$ evoked by delivery of cAMP to cell 1 (WC_1; **Fig. 3b**) were approximately proportional to the corresponding cAMP concentrations $c_{1,2}$. We then delivered the same intracellular solution to cell 2 (WC_2; **Fig. 3b**) through a second patch-clamp pipette, with the double purpose of appraising the sensitivity of cell 2 to cAMP and measuring the junctional conductance g_j (**Fig. 3c**).

We similarly assayed diffusion of $InsP_3$ through HCx26wt channels using a recently described FRET-based molecular biosensor named LIBRA[17] (**Fig. 4**), which showed submicromolar sensitivity to $InsP_3$, with EC_{50} of 0.64 μM. This estimate agrees with the previously reported EC_{50} value[17] and is consistent with the sensitivity of the $InsP_3$-binding domain of rat type 3 $InsP_3$ receptor[22]. According to the LIBRA dose-response curve to $InsP_3$ (**Fig. 4a**), the FRET emission ratio accurately traced $InsP_3$ concentration in the range from ~0.2 μM to ~1.2 μM. To monitor second-messenger transfer through HCx26wt channels, we delivered $InsP_3$ from patch pipettes at a concentration of 5 μM (**Fig. 4b**).

In these and other preliminary experiments, in which dual patch-clamp recording conditions were maintained for >3 min, g_j tended to decline over time (**Fig. 3c** and **Fig. 4c**). Progressive closure of gap junction channels (chemical gating[23]) is not surprising and can be ascribed to metabolic state alterations resulting from the intracellular solutions used in these experiments (see Methods). Therefore, in each cell pair stimulated with cAMP or $InsP_3$, the values of g_j were back-extrapolated and, for internal consistency, p_u was estimated from the stationary values of $V_2\, k_j / (g_j/\gamma)$ within the t_1–t_2 interval (starred points in **Fig. 3d** and **Fig. 4d**). Results for LY, cAMP and $InsP_3$ are summarized in **Table 1**.

DISCUSSION

Differences in LY permeability among different connexins have been amply documented, yet the analysis is complicated by the fact that selectivity of gap junction channels formed by different connexins does not correlate with channel conductance[3,10]. Indeed, LY has great difficulties traversing channels formed by HCx30wt, despite the main state unitary conductance of the latter ($\gamma = 160$ pS) being larger than the γ of the closely related HCx26wt[15]. The first quantitative study of LY transfer in HeLa transfectants expressing Cx43 channels (main unitary conductance $\gamma = 55$ pS) set p_u at 1.246×10^{-3} μm³/s, corresponding to the flux across a single channel, $J_{pore} = p_u(c_1 - c_2)$, of 0.75 molecule per channel per second, driven by a concentration difference $c_1 - c_2 = 1$ μM; consequently, the dye was placed in the category of relatively impermeable[20]. More recent assays have reported p_u values scattered in a wide range, from 1.28×10^{-3} μm³/s to 34×10^{-3} μm³/s (ref. 19). The reason for the data spread is unclear, but (yet unknown) regulatory mechanisms have been proposed to affect affinities and/or partitioning of permeant molecules into the pore. However, the published mean permeability of Cx43 to LY, $p_u = 6.2 \times 10^{-3}$ μm³/s (ref. 19), is close to our estimate for the HCx26wt channel (**Table 1**), which predicts the transit of 4.2 dye molecules per channel per second for $c_1 - c_2 = 1$ μM.

Table 1 | Properties of LY, cAMP and $InsP_3$ related to permeation through HCx26wt pores

	LY	cAMP	$InsP_3$
Formula	$C_{13}H_9N_5O_9S_2$	$C_{10}H_{12}N_5O_6P$	$C_6H_9O_{15}P_3$
Charge	−2	−1	−6
Molecular mass (Da)	443	329	414
Bulk diffusion coefficient (μm²/s)	200[a]	780[b]	283[c]
Minor crystallographic diameter (Å)	8.5[d]	5.2	7.2
Volume of receiving cell, V_2 (μm³)	1,917 ± 217	1,610 ± 215	2,208 ± 280
Junctional conductance, g_j (nS)	39 ± 9	87 ± 8[e]	54 ± 18[e]
Junctional transfer rate, k_j (10^{-3} s^{-1})	1.1 ± 0.4	23 ± 12	13 ± 5
Unitary permeability, p_u (10^{-3} μm³/s)	7 ± 3[d]	47 ± 15[d]	60 ± 12[d]
n	3	5	4

[a]Reference 21. [b]Reference 8. [c]Reference 5. [d]This work. [e]Back-extrapolated, as in **Figure 3c** and **Figure 4c**.

On the basis of analysis of LY transit, it has been suggested that the selectivity properties of Cx43 channels might exclude the rapid transit of specific solutes such as cAMP and $InsP_3$ (ref. 20). In this vein, studies of mechanically induced calcium waves in rat osteosarcoma cell lines have suggested that gap junction communication mediated by either Cx43 or Cx45 does not allow enough passage of $InsP_3$ to elicit release of intracellular calcium stores in neighboring cells[10]. This conclusion has been challenged, for instance, by an analysis of Ca^{2+} wave propagation in cultures of HeLa cells transfected with Cx43, Cx32 and Cx26, which were reported to have similar permeabilities to the diffusing messenger[24].

Our results show substantially higher p_u for $InsP_3$ or cAMP than for LY in channels formed by HCx26wt (**Table 1**), with mean permeability ratios >6 for both cAMP/LY and $InsP_3$/LY. On the basis of the direct estimate of LY accumulation within the cells, we excluded binding to cytosolic and/or nuclear elements as a confounding factor in our estimate of p_u. Likewise, the LY leak across the plasma membrane in HeLa cells is less than 3% over a 15-min interval[20]; therefore, the nonjunctional permeability of LY was insignificant in our experiments.

Notably, in the presence of a point mutation in the second transmembrane helix, M2, of HCx26wt (valine to leucine at position 84, V84L), both the unitary conductance and the permeability to LY remain basically unaffected, whereas permeability to $InsP_3$ decreases greatly[15]. In fact, the permeant molecules studied here have linear dimensions close to the diameter of the channel pore, estimated from an all-atom model of the HCx26wt connexon (see **Supplementary Discussion** and **Supplementary Fig. 1** online), suggesting the possibility of specific interactions with pore-lining residues. Not withstanding the obvious coarseness of our theoretical structure, this approach has been successfully applied to the analysis of a mutant Cx26 with threonine substituted for methionine at position 34 (M34T)[25].

It is also noteworthy that, on the basis of its size and bulk diffusion coefficients alone, one would expect a lower p_u for $InsP_3$ than for cAMP, whereas the actual difference is not statistically significant (**Table 1**). However, the maximal percentage ratio change $\Delta R/R_0$ recorded with LIBRA is about fourfold smaller than that recorded with H30. Therefore, this estimate might still be considerably improved by use of a cytosolic $InsP_3$ sensor with low $InsP_3$ binding affinity and increased signal-to-noise ratio[26].

It is straightforward to extend these measurements to FRET reporters selective for cGMP[27]. In combination with multispectral imaging of Ca^{2+} fluorescent reporters, this could permit exploration of the mechanisms that regulate local and intercellular diffusion. Ca^{2+}, cAMP, cGMP and $InsP_3$ fluctuations could also be quantified in networks of coupled cells and tissues subject to different stimuli, and under conditions where the diffusion of the second messenger is manipulated or altered by genetic defects.

METHODS

Cell culture and transfection. We cultured a clone of HeLa cells that was essentially devoid of connexins (see Acknowledgments) according to standard procedures, as described[28]. We transfected cells 24 h after plating, using the Lipofectamine transfection protocol (Gibco, Invitrogen), with a previously described EYFP-HCx26wt fusion construct[28], to visualize gap junction plaques (**Fig. 1a**). We then used this construct in experiments involving intracellular delivery of LY, as well as in the measurement of unitary Cx26 conductance, γ, as described below. For intracellular delivery of $InsP_3$ and cAMP (see below), we cotransfected cells with the pcDNA3.1 expression vector carrying the coding region of (untagged) HCx26wt (see Acknowledgments) and an additional expression vector carrying either the $InsP_3$ reporter LIBRA[17] (see Acknowledgments) or the cAMP reporter CFP–Epac(dDEP-CD)–YFP[16] (here called H30 for brevity; see Acknowledgments). Experiments were done at room temperature 24 h after transfection.

Electrophysiology. We transferred HeLa cell cultures transfected with HCx26wt to an experimental chamber mounted on the stage of an upright wide-field fluorescence microscope (BX51, Olympus Optical Corporation) equipped with an infinity-corrected water-immersion objective (60×, 0.90 NA, LUMPlanFl, Olympus). We continuously superfused cells at 2 ml/min in a standard extracellular solution (ECS), which contained 150 mM NaCl, 5 mM KCl, 1 mM $MgCl_2$, 10 mM HEPES, 2 mM $CaCl_2$, 2 mM pyruvate and 5 mM glucose (pH 7.4). Patch pipettes were filled with an intracellular solution (ICS) containing 120 mM potassium aspartate, 10 mM tetraethylammonium chloride, 1 mM $MgCl_2$, 10 mM HEPES, 10 mM CsCl, 0.3 mM GTP-sodium and 3 mM ATP-potassium (adjusted to pH 7.2 with KOH), and filtered through 0.22-μm pores (Millipore). Pipette resistances were 3–5 MΩ when immersed in the bath.

To measure junctional conductance g_j, we maintained each cell of an isolated pair under whole-cell patch-clamp conditions with one of two List EPC-7 amplifiers and kept the two at the same holding potential, Φ_h. By stepping the voltage in one cell (cell 1) while keeping the potential of cell 2 at Φ_h, thus establishing a 15-mV transient transjunctional voltage $\Phi_j \equiv \Phi_1 - \Phi_2 = \Delta\Phi_1$, we measured junctional current, I_j, directly as a change in current in the unstepped cell ($I_j = -\Delta I_2$) (**Fig. 2b**).

To detect single–gap junction channel events and thus measure the unitary conductance, γ, we transiently switched the superfusion medium to ECS saturated with 100% CO_2 to produce carbonic acid (H_2CO_3). In its undissociated form, H_2CO_3 is membrane permeant and causes a rapid closure of the gap junction channels (**Fig. 2d**). We detected the current flowing through single gap junction channels owing to a Φ_j of –80 to –100 mV as discrete step-like events while the cells recovered from cytoplasm acidification during washout of the CO_2 (**Fig. 2e**).

Intracellular delivery of permeant molecules. For molecular transfer assays, we dissolved LY in ICS at a concentration of 440 μM. We added cAMP (120 μM, Sigma-Aldrich) to ICS together with IBMX (100 μM, Sigma-Aldrich), a phosphodiesterase inhibitor; dideoxyadenosine (1 μM, Calbiochem), a noncompetitive adenylate cyclase inhibitor; and thapsigargin (1 μM, Sigma-Aldrich), a blocker of the SERCA pumps. We added $InsP_3$ (5 μM, Calbiochem) to ICS together with diphosphoglyceric acid (3.5 mM, Sigma-Aldrich), a competitive inhibitor of $InsP_3$ phosphomonoesterases[29] that convert $InsP_3$ into $InsP_2$; and $InsP_3$-kinase inhibitor (20 μM, Calbiochem), a competitive inhibitor of the $InsP_3$ kinase that catalyzes the conversion of $InsP_3$ to $InsP_4$. All solutions were adjusted to pH 7.2 with KOH and filtered through 0.22-μm pores.

For $InsP_3$, we obtained recordings from cells superfused in ECS (see above) supplemented with 200 μM suramin, a

broad-spectrum P2Y receptor antagonist, to inhibit paracrine amplification of $InsP_3$ signals. We tested the efficacy of suramin in control experiments by exposing HeLa transfectants, loaded with fura-2, to ATP (50 μM). No detectable Ca^{2+} signals were evoked under these conditions. Methods used for these controls have been described previously[15].

In all permeability assays, both cells were approached by pipettes containing identical intracellular solutions and maintained in the cell-attach configuration. A few seconds after the onset of the recording, we ruptured the patch of membrane under the pipette sealed to cell 1 while leaving the seal intact (whole-cell recording conditions for cell 1, WC_1), allowing the compound of interest to fill the cell by passive diffusion from the patch pipette. To monitor access and membrane resistance and to synchronize image acquisition to electrical recordings, we used the 5-V pulse (FVAL) that signals active exposure of the charge-coupled device (CCD) camera used to observe the preparation. The FVAL signal was scaled down to 15 mV and fed to the patch-clamp amplifier connected to cell 1 (ref. 30). By the end of the recording interval, we also established whole-cell recording conditions for cell 2 (WC_2), which permitted an assay of its reaction to direct delivery of the compound (**Fig. 2a**) and measurement of g_j in response to scaled FVAL pulses (**Fig. 2b,c**). We then applied CO_2 to prove that transfer occurred through gap junction channels. Only cell pairs that showed complete uncoupling by the CO_2 (**Fig. 2d**) were retained for the analysis.

In separate control experiments, we monitored g_j for time intervals up to 3 min, corresponding to the duration of a standard permeability assay. With LY in the patch pipettes, g_j was constant over this time span; we therefore estimated the number of open channels $N_{pore} = g_j/\gamma$ in the interval between the WC_1 and WC_2 events from the average of g_j in a 1-min interval after the WC_2 event (excluding transients owing to incomplete seal openings). In contrast, similar control experiments revealed a progressive decline of g_j that was more pronounced for cAMP (average rate of loss 0.37 ± 0.04 nS/s, $n = 10$) than for $InsP_3$ (0.07 ± 0.03 nS/s, $n = 8$). Therefore, g_j values collected in a 1-min interval after the WC_2 event (excluding transients) were used to extrapolate back to the WC_1–WC_2 interval (**Fig. 3c** and **Fig. 4c**).

Additional methods. A description of the theoretical framework for the permeability assays, fluorescence imaging, measurement of cell volumes, estimation of permeant molecule concentration and estimation of transfer rate and unitary permeability is available in the **Supplementary Methods**.

Note: Supplementary information is available on the Nature Methods website.

ACKNOWLEDGMENTS

This work was funded by grants from Telethon Italy (GGP05131) and the European commission FP6 Integrated Project EuroHear (LSHG-CT-20054-512063) under the Sixth Research Frame Program of The European Union (to F.M.) and from Fondazione CARIPARO (to S.P.). M.Z. is supported by Telethon Italy (TCP00089, GGP05113), the Italian Cystic Fibrosis Research Foundation, the Fondazione Compagnia di San Paolo and the HFSPO (RGP1/2005). We thank K. Willecke (University of Bonn), R. Bruzzone (Institute Pasteur), K. Jalink (The Netherlands Cancer Institute) and A. Tanimura (Health Sciences University of Hokkaido) for the gifts of HeLa cells, HCx26wt, H30 and LIBRA, respectively, and T. Pozzan (University of Padova) for helpful discussions and constructive criticism.

COMPETING INTERESTS STATEMENT

The authors declare no competing financial interests.

Published online at http://www.nature.com/naturemethods
Reprints and permissions information is available online at http://npg.nature.com/reprintsandpermissions

1. Sosinsky, G.E. & Nicholson, B.J. Structural organization of gap junction channels. *Biochim. Biophys. Acta* **1711**, 99–125 (2005).
2. Gerido, D.A. & White, T.W. Connexin disorders of the ear, skin, and lens. *Biochim. Biophys. Acta* **1662**, 159–170 (2004).
3. Goldberg, G.S., Valiunas, V. & Brink, P.R. Selective permeability of gap junction channels. *Biochim. Biophys. Acta* **1662**, 96–101 (2004).
4. Irvine, R.F. 20 years of Ins(1,4,5)P3, and 40 years before. *Nat. Rev. Mol. Cell Biol.* **4**, 586–590 (2003).
5. Allbritton, N.L., Meyer, T. & Stryer, L. Range of messenger action of calcium ion and inositol 1,4,5-trisphosphate. *Science* **258**, 1812–1815 (1992).
6. Zaccolo, M., Filippin, L., Magalhaes, P. & Pozzan, T. Heterogeneity of second messenger levels in living cells. *Novartis Found. Symp.* **239**, 85–95, 150–159 (2001).
7. Bos, J.L. Epac: a new cAMP target and new avenues in cAMP research. *Nat. Rev. Mol. Cell Biol.* **4**, 733–738 (2003).
8. Bacskai, B.J. *et al.* Spatially resolved dynamics of cAMP and protein kinase A subunits in Aplysia sensory neurons. *Science* **260**, 222–226 (1993).
9. Dakin, K., Zhao, Y. & Li, W.H. LAMP, a new imaging assay of gap junctional communication unveils that Ca2+ influx inhibits cell coupling. *Nat. Methods* **2**, 55–62 (2005).
10. Harris, A.L. Emerging issues of connexin channels: biophysics fills the gap. *Q. Rev. Biophys.* **34**, 325–472 (2001).
11. Oh, S. *et al.* Changes in permeability caused by connexin 32 mutations underlie X-linked Charcot-Marie-Tooth disease. *Neuron* **19**, 927–938 (1997).
12. Qu, Y. & Dahl, G. Function of the voltage gate of gap junction channels: selective exclusion of molecules. *Proc. Natl. Acad. Sci. USA* **99**, 697–702 (2002).
13. Bedner, P. *et al.* Selective permeability of different connexin channels to the second messenger cyclic AMP. *J. Biol. Chem.* **281**, 6673–6681 (2006).
14. Saez, J.C., Connor, J.A., Spray, D.C. & Bennett, M.V. Hepatocyte gap junctions are permeable to the second messenger, inositol 1,4,5-trisphosphate, and to calcium ions. *Proc. Natl. Acad. Sci. USA* **86**, 2708–2712 (1989).
15. Beltramello, M., Piazza, V., Bukauskas, F.F., Pozzan, T. & Mammano, F. Impaired permeability to Ins(1,4,5)P3 in a mutant connexin underlies recessive hereditary deafness. *Nat. Cell Biol.* **7**, 63–69 (2005).
16. Ponsioen, B. *et al.* Detecting cAMP-induced Epac activation by fluorescence resonance energy transfer: Epac as a novel cAMP indicator. *EMBO Rep.* **5**, 1176–1180 (2004).
17. Tanimura, A., Nezu, A., Morita, T., Turner, R.J. & Tojyo, Y. Fluorescent biosensor for quantitative real-time measurements of inositol 1,4,5-trisphosphate in single living cells. *J. Biol. Chem.* **279**, 38095–38098 (2004).
18. Bastianello, S., Ciubotaru, C.D., Beltramello, M. & Mammano, F. in *Three-Dimensional and Multidimensional Microscopy: Image Acquisition and Processing XI* (ed. Conchello, J.-A.) Vol. 5324, 265–274 (San Jose, California, USA, 2004).
19. Eckert, R. Gap-junctional single-channel permeability for fluorescent tracers in mammalian cell cultures. *Biophys. J.* **91**, 565–579 (2006).
20. Valiunas, V., Beyer, E.C. & Brink, P.R. Cardiac gap junction channels show quantitative differences in selectivity. *Circ. Res.* **91**, 104–111 (2002).
21. Brink, P.R. & Ramanan, S.V. A model for the diffusion of fluorescent probes in the septate giant axon of earthworm: axoplasmic diffusion and junctional membrane permeability. *Biophys. J.* **48**, 299–309 (1985).
22. Patel, S., Joseph, S.K. & Thomas, A.P. Molecular properties of inositol 1,4,5-trisphosphate receptors. *Cell Calcium* **25**, 247–264 (1999).
23. Peracchia, C. Chemical gating of gap junction channels; roles of calcium, pH and calmodulin. *Biochim. Biophys. Acta* **1662**, 61–80 (2004).
24. Paemeleire, K. *et al.* Intercellular calcium waves in HeLa cells expressing GFP-labeled connexin 43, 32, or 26. *Mol. Biol. Cell* **11**, 1815–1827 (2000).
25. Bicego, M. *et al.* Pathogenetic role of the deafness-related M34T mutation of Cx26. *Hum. Mol. Genet.* **15**, 2569–2587 (2006).
26. Matsu-ura, T. *et al.* Cytosolic inositol 1,4,5-trisphosphate dynamics during intracellular calcium oscillations in living cells. *J. Cell Biol.* **173**, 755–765 (2006).
27. Nikolaev, V.O., Gambaryan, S. & Lohse, M.J. Fluorescent sensors for rapid monitoring of intracellular cGMP. *Nat. Methods* **3**, 23–25 (2006).
28. Beltramello, M. *et al.* Permeability and gating properties of human connexins 26 and 30 expressed in HeLa cells. *Biochem. Biophys. Res. Commun.* **305**, 1024–1033 (2003).
29. Downes, C.P., Mussat, M.C. & Michell, R.H. The inositol trisphosphate phosphomonoesterase of the human erythrocyte membrane. *Biochem. J.* **203**, 169–177 (1982).
30. Mammano, F. *et al.* An optical recording system based on a fast CCD sensor for biological imaging. *Cell Calcium* **25**, 115–123 (1999).

SUPPLEMENTARY METHODS

Theoretical framework for the permeability assays

Let *dm* denote the *net molar amount* of solute transferred during a time interval *dt* from cell 1 to cell 2 through a gap junction plaque, treated as a porous membrane of thickness h_m pierced by small cylindrical openings ("pores"). Conservation of mass requires that

$$\frac{dm}{dt} = N_{\text{pore}}\ J_{\text{pore}}$$

Equation 1

where N_{pore} is the number of open gap junction channels in the plaque and J_{pore} (mol/s) is the *net flux of solute* through a single pore. According to Fick's first law [1, 2], it is equal to

$$J_{\text{pore}} = -A_{\text{pore}}\ D_e\ \frac{\partial c}{\partial x}$$

Equation 2

Where A_{pore} is pore section area (μm^2), D_e is the effective diffusion coefficient (μm^2/s), c is *solute concentration* (mol/μm^3) and x (μm) is spatial coordinate along the pore axis. Assuming that

$$\frac{\partial c}{\partial x} = -\frac{c_1 - c_2}{h_m}$$

Equation 3

where c_1 is concentration in cell 1 and $c_2 < c_1$ is concentration in cell 2 (ref. 2) we can re-write Eq.2 as

$$J_{\text{pore}} = p_u\left(c_1 - c_2\right)$$

Equation 4

where the proportionality constant is the *unitary permeability*, i.e. the permeability of the single pore (in μm^3/s)

$$p_u \equiv A_{\text{pore}} D_e / h_m .$$

Equation 5

This is the critical parameter we sought to derive from the experiments by monitoring optically the time course of the fluorescence changes in the injected cell (cell 1) and recipient cell (cell 2). Due to influx through the gap junction channels, the concentration in cell 2 increases at a rate

$$\frac{dc_2}{dt} = \frac{1}{V_2}\frac{dm}{dt}$$

Equation 6

where V_2 is the volume of cell 2. By combining the above equations and solving for p_u we obtain

$$p_u = \frac{V_2}{N_{\text{pore}}}\frac{dc_2/dt}{c_1 - c_2}.$$

Equation 7

Thus the estimate of p_u based on Equation 7 requires the measurement of N_{pore}, V_2, c_1 and c_2. The methods used to perform these measurements are described hereafter.

Fluorescence imaging

To monitor optically the transfer of the injected compound from cell 1 to cell 2 we used fluorescence imaging in combination with patch clamp recordings. Image acquisition on the BX51 microscope was performed using software developed in the laboratory [3]. For LY, illumination was set at a wavelength of 425 nm by a fast switching monochromator (Polychrome IV, TILL Photonics, Martinsried, Germany) and directed onto the sample through a dichromatic mirror (440dclp, Chroma, Rockingham, VT, USA). Fluorescence emission was selected around 540 nm using a D540/40m filter (Chroma) to form fluorescence images on a scientific grade CCD camera (SensiCam, PCO Computer Optics GmbH, Kelheim, Germany). Image sequences were stored on disk and processed off-line using the Matlab 7.0 software package (The MathWorks, Inc., Natick, MA, USA), as described below.

To quantify the error due to LY binding to cytosolic and–or nuclear elements, we performed control experiments taking advantage of the intrinsic optical sectioning capabilities of our two-photon microscope (Radiance 2100, Biorad/Carl Zeiss MicroImaging GmbH, Gottingen, Germany) powered by a Tsunami pulsed laser (Spectra Physics/Newport Corporation, Irvine, CA, USA). HeLa cells were loaded through patch pipettes containing 440 µM LY in the presence of an equal concentration of the dye in the bathing solution. After equilibration of the intracellular concentration (approximately 10 min), LY fluorescence emission, excited at 835 nm in a thin optical slice (thickness < 1 µm), was compared to fluorescence from the surrounding medium in the same focal plane.

For $InsP_3$ or cAMP, Fluorescence Resonance Energy Transfer (FRET) images [4] were acquired by interposing a custom-made image-forming beamsplitter between the microscope output optical port and the CCD camera. The beamsplitter was equipped with a dichromatic mirror (515dcrx, Chroma) and emission filters (d480/40 and hq535/30, Chroma) for CFP-YFP emission separation, following CFP excitation at 430 nm. Sequences of image pairs were acquired synchronously at the two emission wavelengths and stored on disk for off-line processing.

In all fluorescence experiments, the effects of photobleaching were rendered virtually negligible by carefully selecting the most appropriate inter-frame interval while controlling illumination with a mechanical shutter triggered by the FVAL signal.

Measurement of cell volumes

Immediately after the end of each intracellular delivery experiment, a through-focus sequence of fluorescence images of the patch-clamped cell pair was acquired by stepping the objective along the optical (z) axis of the microscope with a resolution Δz of 250 nm or 300 nm. We obtained digital confocal sections by multi-neighbour deconvolution using a direct estimate of the microscope point-spread function (PSF), as described in ref.3. Cell section area A_j in the *j*-th deconvolved image was measured by identifying boundaries with the *Canny* edge detection algorithm [5] (Fig. 1b). Finally, we computed cell volume as

$$V = \Delta z \sum A_j$$

(Fig. 1c). In the population sampled in this study, cell base area A_1 = 500±176 μm^2 and volume V = 2190±594 μm^3 (mean ± standard deviation, n=17 in both cases) were not correlated (Fig. 1d).

Estimate of permeant molecule concentration

For LY, $c_{1,2}$ were estimated from the single-wavelength background-subtracted fluorescence emission intensities (F). For each pixel of the 12-bit CCD camera used in this study, F is an integer number comprised between 0 and 4095 (gray levels). Since F signals collected through a wide field fluorescence microscope, and integrated over cell volume, are proportional to the number of fluorescent molecules in each cell [6], pixel gray values were summed within ROIs drawn on the fluorescence images along the contours of each cell at its base. Division by cell volume then yielded an estimate of LY concentration in units of gray levels / μm^3 (see Results and Fig.2a).

For cAMP (or $InsP_3$) FRET images at the two emission wavelengths were divided pixel-by-pixel to generate an emission ratio at each sampled point. A well known advantage of dual-wavelength over single-wavelength imaging is that the rationing operation cancels out most or all of the possible variability due to the instrument efficiency and content of the fluorescent molecular sensor [7]. Thus the ratio of the fluorescence emission images yields a non-linear function of the cAMP (or $InsP_3$) concentration within the cell. Average ratio values for the FRET signals were obtained by encompassing the image of each cell within a ROI drawn along the contours of the cell base, and averaging pixel ratios within each ROI. To calibrate these spatially averaged ratio signals, R, known amounts of cAMP (or $InsP_3$) were delivered to single transfected HeLa cells through patch pipettes filled with the same solutions used for the permeability assays. Dose-response curves (Fig. 3a and Fig. 4a) are shown as ratio changes,

$$\Delta R = R - R_o,$$

vs. pipette concentration. Here R_o is pre-stimulus ratio, measured prior to achieving the whole-cell configuration (1.11±0.01, n = 6 LIBRA transfectants; 0.81±0.05, n = 6 H30 transfectants). The steady-state R values used for the dose-response curves were obtained by maintaining the whole-cell configuration for a time long enough to permit equilibration with the pipette content by passive diffusion. This time varied between few

minutes (at saturating concentrations) to more than 10 minutes (at the lowest concentrations). Throughout this process, cell viability was monitored electrophysiologically by verifying that access resistance, membrane resistance, cell capacitance and zero-current potential stayed within 10% of their initial values. Only cells meeting these multiple criteria were retained for the analysis. Dose-response data at each concentration are averages of $n \geq 5$ cells.

Estimate of transfer rate and unitary permeability

Knowledge of the dose-response curves permits to estimate the unitary permeability p_u by converting FRET ratios $R_{1,2}$ to the corresponding concentrations $c_{1,2}$ of Equation 7. Mathematically, this is equivalent to inverting the dose-response function, but in practice this operation is subjected to controllable errors only in a limited range near the inflection point, where approximate proportionality between c and R occurs. Thus unitary permeability was computed as

$$p_u = V_2 k_j / g_j / \gamma$$

where k_j indicates the junctional transfer rate that was estimated as

$$k_j \cong \frac{dR_2 / dt}{R_1 - R_2}.$$

Since p_u is a constant, internal consistency implies that the only data which ought to be retained for the analysis are those acquired during a sub-interval (t_1, t_2) of the recording period in which the time derivative of

$$V_2 k_j / g_j / \gamma$$

approaches zero (starred points in Fig. 3d and Fig. 4d).

References

1. Fick, A. Ueber diffusion. *Poggendorff's Annalen der Physik und Chemie* **94**, 59-86 (1855).
2. Benedek, G., Villars, FMH in Biological Physics Series, Vol. 2, STATISTICAL PHYSICS, Edn. Second edition. (ed. E. Greenbaum) 91-261 (Springer-Verlag New York, Inc., New York; 2002).
3. Bastianello, S., Ciubotaru, C.D., Beltramello, M. & Mammano, F. in Three-Dimensional and Multidimensional Microscopy: Image Acquisition and Processing XI, Vol. 5324, 265-274, San Jose, California; 2004).

4. Periasamy, A. & Day, R.N. in Green Fluorescent Proteins, Vol. 58. (ed. K.F. Sullivan) (Academic Press, San Diego; 1999).
5. Canny, J. A computational approach to edge detection. *IEEE Trans. Pattern Analysis and Machine Intelligence* **8**, 679-714 (1986).
6. Eckert, R. Gap-junctional single-channel permeability for fluorescent tracers in mammalian cell cultures. *Biophys J* **91**, 565-579 (2006).
7. Grynkiewicz, G., Poenie, M. & Tsien, R.Y. A new generation of Ca2+ indicators with greatly improved fluorescence properties. *J Biol Chem* **260**, 3440-3450 (1985).

SUPPLEMENTARY DISCUSSION

Structural models of HCx26wt and permeant molecules

To gain further insight into the permeation mechanism, we constructed an atomic model of the trans-membrane portion of the HCx26wt connexon (Supplementary Figure 1) starting from the Cα model of mouse Cx32 [1]. Molecular dynamics (MD) simulations were used to achieve structural relaxation of the model, in which the tilting of the pore-lining α helices is responsible for the narrowing of the pore at the boundary with the extracellular gap (Supplementary Figure 1, b), with a major diameter $2a \approx 17.5$ Å.

Diffusion through porous membranes can been modelled by an equation due to Renkin [2], which predicts

$$p_u = D\frac{\pi a^2}{\Delta x}\left(1-\frac{r}{a}\right)^2 \cdot \left[1-2.1\left(\frac{r}{a}\right)+2.09\left(\frac{r}{a}\right)^3-0.95\left(\frac{r}{a}\right)^5\right]$$

Here r is molecular radius, D is diffusion coefficient in the bulk (see Table 1, main text) and Δx is pore length (9 nm in our model, based on Ref. 3). The above equation has been tested experimentally for r/a values in the range from ~0.05 to ~0.32 [4]. The minor crystallographic diameter of cAMP, $2r \approx 5.2$ Å (Supplementary Figure 1, c), is such that $r/a \approx 0.3$ and the prediction is $p_u = 44.1\times10^{-3}$ μm^3/s, close to our experimental estimate ($47\pm15 \times10^{-3}$ μm^3/s). We refrained from extending these considerations to $InsP_3$ or LY, for which $r/a \approx 0.41$ and 0.49, respectively.

Computational details

The atomic model of the trans-membrane (TM) portion of HCx26wt connexon was constructed on the basis of the Cα model of mouse Cx32 reported by Fleishman et al. [1] (PDB entry code 1TXH). The sequence of HCx26wt was aligned to that of the Cx32 using T-COFFEE [5] and the coordinates of the matching Cα atoms were mapped. Additionally, charged residues next to the TM segments were added to consider electrostatic interactions that may potentially modify the conformation of the molecule. The final TM fragments in the HCx26wt subunits corresponded to: Ser19 to Glu42

(TM1), Arg75 to Ala96 (TM2), Leu132 to Val153 (TM3) and Glu187 to Leu209 (TM4). After Cα mapping from Cx32 to HCx26wt, all the atoms of the amino acids were added using their canonical conformation with the XLEAP module of the AMBER 8.0 software suite (http://amber.scripps.edu/). All chains were capped with N-methyl and acetyl groups, respectively, in order to avoid the spurious effects of terminal zwitterionic charges. This protocol yielded an atomic model with a large number of steric clashes and internal tensions that were relaxed using energy minimization (EM) and MD. Simulations were performed in the presence of implicit solvent with the Generalized Born approach [6] as implemented in AMBER 8.0 using the Amber94 force field [7]. A cutoff distance of 18 Å, a salt concentration of 0.15 M and a dielectric constant of 78 were adopted. The simulations used the Amber94 force field keeping the temperature at 100 K using Langevin dynamics with a collision frequency of 2 ps^{-1}. The *shake* algorithm was used to constraint all the chemical bonds. After full EM, the system underwent 50 ps MD with harmonic constraints applied on the Cα carbons. During this time interval, the positional constraints were decreased from 1 [kcal/mol-$Å^2$] to 0. Subsequently, 450 ps of free MD were performed. The stabilization of the root mean square deviations (RMSD) from the initial positions measured on the Cα atoms was taken as a criterion for structural relaxation of the model. RMSD reached stabilization after 250 ps, thereafter oscillating around a value of about 3 Å [8]. The diameter of the pore (17.5 Å) was measured on a structure averaged over the last 100 ps and fully minimized.

The molecular structures of $InsP_3$ and cAMP (in its *anti* conformation), were obtained from the PDB structures 1N4K [9] and 1Q5O [10], respectively. Since the structure of LY has not yet been solved by experimental techniques, structural models were constructed using WebLab ViewerPro (Accelerys). Molecular graphics and measures were performed with VMD [11].

References

1. Fleishman, S.J., Unger, V.M., Yeager, M. & Ben-Tal, N. A Calpha model for the transmembrane alpha helices of gap junction intercellular channels. *Mol Cell* **15**, 879-888 (2004).
2. Renkin, E.M. Filtration, diffusion, and molecular sieving through porous cellulose membranes. *J Gen Physiol* **38**, 225-243 (1954).

3. Unger, V.M., Kumar, N.M., Gilula, N.B. & Yeager, M. Three-dimensional structure of a recombinant gap junction membrane channel. *Science* **283**, 1176-1180 (1999).
4. Benedek, G., Villars, FMH in Biological Physics Series, Vol. 2, Statistical Physics, Second edition. (ed. E. Greenbaum) 91-261 (Springer-Verlag New York, Inc., New York; 2002).
5. Notredame, C., Higgins, D.G. & Heringa, J. T-Coffee: A novel method for fast and accurate multiple sequence alignment. *J Mol Biol* **302**, 205-217 (2000).
6. Tsui, V. & Case, D.A. Theory and applications of the generalized Born solvation model in macromolecular simulations. *Biopolymers* **56**, 275-291 (2000).
7. Cornell, W.D., P. Cieplak, C. I. Bayley, I. R. Gould, K. M. M. Jr., K. M. Ferguson, D. M. Spellmeyer, T. Fox, J. W. Caldwell, P. A. Kollman. A 2nd generation force-field for the simulation of proteins, nucleic acids, and organic-molecules. *J. Am. Chem. Soc.* **117**, 5179–5197 (1995).
8. Bicego, M. et al. Pathogenetic role of the deafness-related M34T mutation of Cx26. *Hum Mol Genet* **15**, 2569-2587 (2006).
9. Bosanac, I. et al. Structure of the inositol 1,4,5-trisphosphate receptor binding core in complex with its ligand. *Nature* **420**, 696-700 (2002).
10. Zagotta, W.N. et al. Structural basis for modulation and agonist specificity of HCN pacemaker channels. *Nature* **425**, 200-205 (2003).
11. Humphrey, W., Dalke, A. & Schulten, K. VMD: visual molecular dynamics. *J Mol Graph* **14**, 33-38, 27-38 (1996).

SUPPLEMENTARY FIGURE 1

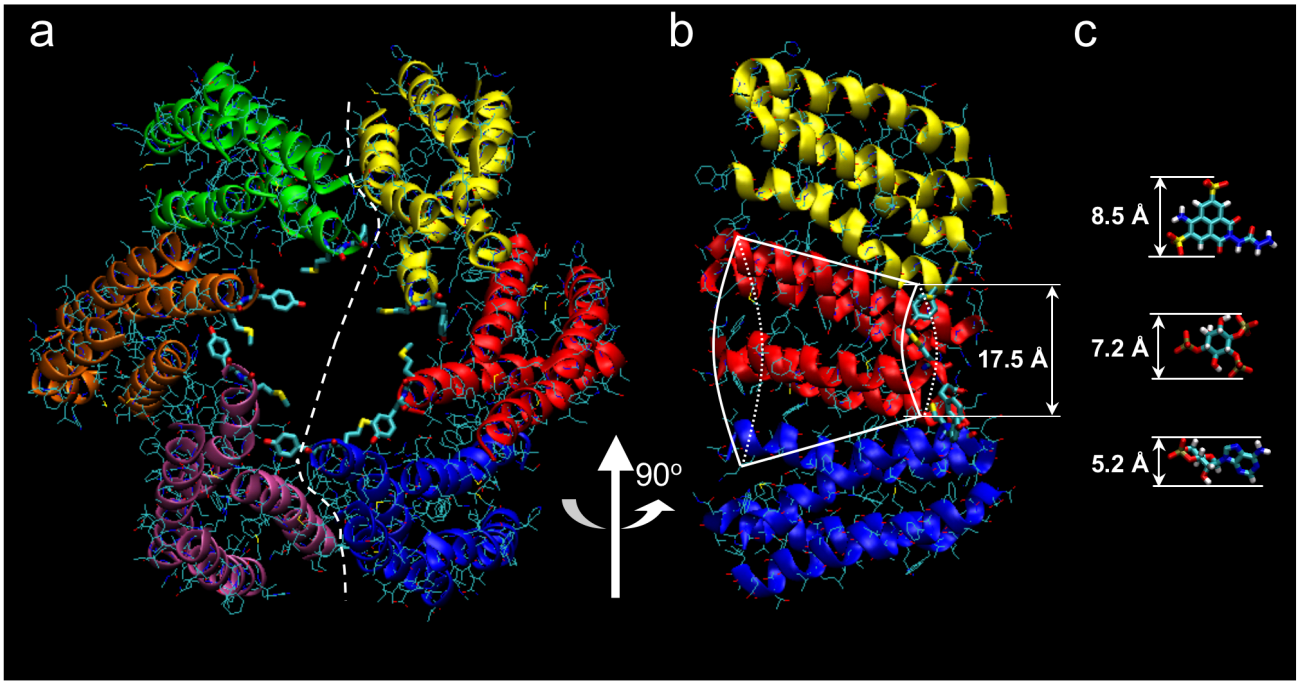

Supplementary Figure 1 Structural models of the HCx26wt connexon and permeant molecules. **(a)** Extracellular view of the atomistic model of the transmembrane part of the HCx26wt connexon. The differently colored ribbons indicate the diverse connexin proteins forming the connexon. Only heavy atoms are shown for visual clarity in line representation. Residues Met151 and Tyr152 that determine the maximum constriction belt are depicted with thick lines. The white dashed line indicates the dissection surface of the cross section of the model, shown in (**b**). (**c**) Molecular structures of LY, $InsP_3$ and cAMP (from top to bottom). The structures of the protein complex and permeating molecules are presented at the same scale to provide a comparative view. Minimal dimension are shown beside each molecule.